Neotectonics of major faults in the Canadian Cordillera

by

Theron Douglas Finley

B.Sc., University of Victoria, 2017
M.Sc., University of Alberta, 2020

A Dissertation Submitted in Partial Fulfillment of the
Requirements for the Degree of

DOCTOR OF PHILOSOPHY

in the School of Earth and Ocean Sciences

We acknowledge and respect the Lək̓ʷəŋən (Songhees and Xʷsepsəm/Esquimalt) Peoples on whose territory the university stands, and the Lək̓ʷəŋən and W̱SÁNEĆ Peoples whose historical relationships with the land continue to this day.

Neotectonics of major faults in the Canadian Cordillera

by

Theron Douglas Finley

B.Sc., University of Victoria, 2017
M.Sc., University of Alberta, 2020

Supervisory Committee

Dr. Edwin Nissen, Co-Supervisor
(School of Earth and Ocean Sciences)

Dr. John F. Cassidy, Co-Supervisor
(School of Earth and Ocean Sciences & Geological Survey of Canada)

Dr. Kristin D. Morell, Departmental Member
(School of Earth and Ocean Sciences & University of California Santa Barbara)

Dr. Andrew Schaeffer, Departmental Member
(School of Earth and Ocean Sciences & Geological Survey of Canada)

Dr. Christopher Bone, Outside Member
(Department of Geography)

Abstract

The Canadian Cordillera is an 800 to 1000 km-wide accretionary orogen comprised of numerous terranes and crustal fragments, which are bounded and crosscut by major, mature fault zones. Despite being most active during Mesozoic to early Cenozoic mountain building, the Cordillera continues to be tectonically active in the present, with elevated seismicity and strain rates compared to the stable continental interior. The role of the major faults within the Cordillera in accommodating ongoing deformation has remained unclear, in part due to sparse seismic and geodetic instrumentation, but also due to the challenging surficial environment (i.e., recent glaciation, high precipitation, dense vegetation) that has hindered tectono-geomorphic and paleoseismic studies.

In this thesis, I leverage a recent expansion of high-resolution topographic data coverage across the Canadian Cordillera to investigate the geomorphic signature of faulting in the landscape. I make use of new airborne lidar (light detection and ranging) data made available by provincial and territorial governments, and I also collect new lidar using a novel drone system – the first of its kind applied to tectonic geomorphology. In addition, I take advantage of the new ArcticDEM dataset, derived from optical satellite imagery, and covering all regions north of the 60th parallel. These datasets enable the mapping of subtle fault scarps, as well as the glacial landforms that constrain the timing of past ruptures.

I focus on three major fault zones: the Tintina fault in northern Yukon, the Eastern Denali fault in southwestern Yukon, and the Southern Rocky Mountain Trench fault in southeastern British Columbia. The Tintina fault is a major, ~1000-km-long fault that has accommodated over 400 km of dextral offset in the Eocene but is generally not considered active today. I show that it has in fact ruptured numerous times throughout the Quaternary, is capable of future large earthquakes (>M_w 7.5), and may be late in a seismic cycle, representing a major seismic hazard to the region. The Southern Rocky Mountain Trench fault is thought to have been a locus of significant extensional deformation in the Eocene. Using new airborne lidar, surficial mapping, and shallow geophysical surveys, I provide evidence of multiple extensional surface ruptures in the Holocene. A potential decrease in slip rate through time is speculated to be related to glacial isostatic adjustment. The Eastern Denali fault, a major terrane-bounding fault, is already known to be a potential seismogenic source, however its kinematics and the level of tectonic activity have remained topics of debate. Using a new, comprehensive lidar dataset covering nearly the entire fault, I demonstrate that its kinematics are dominantly dextral despite being in an overall compressive setting, highlighting the role of inherited fault geometry.

The results of this work have significant implications for seismic hazard assessments in Canada. Much of Canada's National Seismic Hazard Model is based on historical and instrumental records of seismicity to define probabilities of shaking over broad areas. My work will enable the inclusion of additional discrete fault sources in the hazard model. In addition to seismic hazard, these geomorphic studies shed light on the driving mechanisms and characteristics of neotectonic deformation across the Cordillera and provide broader insight into how pre-existing, mature faults behave in regions of moderate to low strain.

Preface

The body of this dissertation comprises three main chapters in the format of scientific journal publications, as well as introductory and concluding chapters that tie the main studies together. Each of the body chapters therefore have their own abstract, introduction, detailed methods, discussion, conclusions, and supporting information formatted for the journal to which they were, or are soon to be, submitted.

Chapter 1 describes the motivation behind this thesis, and a summary of the scientific questions that unite the various studies I conducted over the course of my PhD. It also provides an overview of some of the main methodological approaches common to all the chapters.

Chapter 2 is focused on the Quaternary activity of the Tintina fault (TF) in northwestern Yukon Territory. Using ArcticDEM data and a targeted drone lidar survey, combined with surficial mapping and an array of geochronological constraints, I show that the Tintina fault represents a major, previously unrecognized seismic hazard. This chapter is currently in revision for *Geophysical Research Letters*.

Chapter 3 is focused on the Southern Rocky Mountain Trench fault (SRMTF), in southeastern British Columbia (BC). Using new airborne lidar data made available by the BC government, detailed surficial mapping, and geophysical surveys, I examine a potential surface rupture near Columbia Lake. I demonstrate the possibility of multiple earthquakes through the Holocene, and a potential temporal shift in slip rate related to glacial rebound. This chapter will soon be submitted to the *Journal of Geophysical Research: Solid Earth.*

Chapter 4 is focused on the Eastern Denali fault (EDF) in southwestern Yukon Territory. Despite being one of Canada's most significant onshore active faults, the EDF is understudied and there is ongoing debate surrounding its kinematics and the level of activity. With the support of the Yukon Geological Survey, I collected data along several sections of the EDF using a novel drone-based lidar system. The preliminary results from these surveys are published in *Yukon Exploration and Geology* (Finley et al., 2022b). Recognizing a need for lidar along more remote segments of the EDF, I led a successful NSERC Alliance grant that funded the acquisition of crewed airborne lidar along the entire EDF to the Alaska border. Chapter 4 represents my final analyses and interpretations from the new datasets, which will ultimately be submitted to the *Journal of Geophysical Research: Solid Earth.*

Chapter 5 provides a brief conclusion, summarizing the main findings of my work, and discussing potential avenues of future work.

In addition to the main projects that I have led, and which constitute the body chapters of this thesis, I have been involved in several other related projects as a collaborator and coauthor. These papers are not included in this thesis, though many of the methodological concepts are touched on in the introduction (Chapter 1).

The first is a paleoseismic trench study of the XEOLXELEꝀ – Elk Lake fault (XELF) on southern Vancouver Island. I played a leading role in organizing the logistics of the complex trench excavation, which occurred in a popular regional park, and during a time of COVID-related restrictions. I also made significant contributions to the interpretations and analyses of our paleoseismic and geophysical data. I am second author on the resulting paper – now published in *Tectonics* – led by my colleague Nicholas Harrichhausen (Harrichhausen et al., 2023).

The second is a methodological paper on the use of drone based lidar for mapping fault morphology. My projects on the EDF, TF, and SRMTF served as the proving grounds for the drone lidar system, and I spent a great deal of time during my PhD operating the drone, establishing best practices, and processing the data it collected. My colleague Guy Salomon led a paper detailing the operation and performance of the drone lidar system. This paper, on which I am second author, is now published in *Seismica* (Salomon et al., 2024).

The third is a review paper on active fault research in western Canada. This paper is being led by Tiegan Hobbs at the Geological Survey of Canada, and is motivated by the recent surge of paleoseismological research in the Canadian Cordillera, driven by the expansion of lidar data availability. It provides a summary of all paleoseismological studies on intraplate/crustal faults that have taken place in Canada, and I have contributed summaries of fault systems that I have specific expertise on (i.e., Eastern Denali, Tintina, Rocky Mountain Trench, and XEOLXELEꝀ – Elk Lake faults). This paper will be submitted in 2025.

Table of Contents

List of Tables

List of Figures

Acknowledgements

The University of Victoria is situated on the traditional territory of the Lekwungen peoples. The Songhees, Esquimalt and W̱SÁNEĆ peoples also have important historical relationships with this land that continue to this day. Field research conducted as part of this thesis spans a large region, crossing the traditional territories of the Ktunaxa, Secwépemc, Dakelh, Tse’khene, Kluane, Champagne & Aishihik, White River, Tr’ondëk Hwëch’in, and Na-Cho Nyäk Dun First Nations. I am grateful to community members from several of these Nations for their engagement and support of our field studies on their traditional lands.

Funding for my work was provided by the Natural Sciences and Engineering Research Council, the Yukon Geological Survey, Polar Knowledge Canada, and generous scholarships established in memoriam of Dr. Margaret Perkins Hess, John and Myrtle Tilley, and Geoffrey Bradshaw.

I consider myself incredibly fortunate to have been surrounded by so many supportive colleagues during my PhD. First and foremost, I am deeply appreciative of the mentorship and guidance provided by my co-supervisors, Edwin Nissen and John Cassidy, who both were sources of limitless positive encouragement, and taught me so much about the many facets of earthquake science. I truly cannot imagine a more enriching and inspiring PhD experience than the one Ed and John provided to me.

There are many others in my broader network of academic colleagues who I need to thank. Kristin Morell and Lucinda Leonard have both been incredible mentors and sources of scientific inspiration for nearly my entire career in geoscience. I also deeply appreciate the support and guidance Andrew Schaeffer has offered over the course of my PhD, and the many opportunities to participate in research projects at the GSC. Major thanks are due to Chris Bone for taking the time to serve on my supervisory committee, and to Roger Stephen for sharing his encyclopedic knowledge of lidar, drones, and the combination of the two. I am also grateful to Brian Menounos, Duane Froese, Brendan Miller, and Veronica Prush for contributing their surficial geology and tectonic geomorphology expertise to my work.

Many people find their PhD journey to be lonely, and I am so thankful to have been part of a wonderful, collaborative research group. Though our lab’s unofficial name was Tectonics, Earthquakes, And Remote Sensing (TEARS), real tears were seldom shed. Grace, Guy, Roger, Élyse, Sarah, Fengzhou, Siyu, Madison, Peter, Meg, Anna, Taryn, Lekima, and many others at UVic and the GSC with whom I have shared discussions, fieldwork, and fun: thank you!

Finally, I am forever grateful for the unwavering love and support offered by my family and friends during my long journey through academia. In particular, thank you to my partner Braeden for being my rock over these last four years – I couldn’t have done it without you!

Chapter 1: Introduction

1.1 Context and Motivation

1.1.1 Seismic Hazard and Risk

Earthquakes are among the most destructive natural disasters facing society and, unlike many other kinds of natural disasters that have precursory signals, the exact location, timing and size of earthquakes cannot be predicted (Kanamori, 2003). Furthermore, earthquake-related deaths have increased substantially in the last century due to a rapidly expanding population and associated urban development – building collapse being a primary cause of fatalities (Bilham, 2009). This problem is especially acute for earthquakes on crustal or intraplate faults, which are generally closer to built infrastructure than plate boundary faults (e.g., Kanaori and Kawakami, 1996; Gledhill et al., 2011). Shaking-related damage from intraplate faults can be particularly severe, and surface rupture can also directly sever infrastructure built across the fault.

The most effective way to mitigate earthquake losses is to build resilience into our communities. The primary mechanism to do so are seismic building codes, which are informed by seismic hazard models. The most common type of seismic hazard models are known as Probabilitistic Seismic Hazard Analysis (PSHA) models, which estimate the probability that a given region will exceed specified thresholds of shaking over set time frames (Figure 1.1). These models are based on seismic, geodetic, and geologic data that provide information about locations, rates, kinematics, and possible magnitudes of future earthquakes (Morell et al., 2020). Typically, models are divided into area or volume sources with differing rates of seismicity or geodetic strain. In some cases, discrete fault sources – 3D representations of a fault plane – can also be included if there is sufficient information to warrant doing so (Morell et al., 2020).

Historically, Canada's National Seismic Hazard Model (NSHM) has been based mostly upon area sources defined by the instrumental and written record of seismicity (Adams, 2019). Notable exceptions include the Cascadia megathrust fault, the Queen Charlotte fault, and the Leech River fault, which are included as discrete fault sources with paleoseismic data (Halchuk et al., 2019; Kolaj et al., 2020). Generally though, the records used to construct the NHSM are only complete for the past century or so and are therefore very short on geological time scales. However, the intervals between large earthquakes on individual intraplate faults can be on the order of thousands of years, and the hazard is therefore not fully represented by the instrumental record (Morell et al., 2020). Seismic hazard models address this issue by using frequency-magnitude scaling relationships that estimate the probability of a large earthquake based on the occurrence of smaller earthquakes (Youngs and Coppersmith, 1985). However, this approach may not be appropriate or accurate for faults in low strain rate regions, that host very little seismicity between rare, large events.

To address this limitation of seismic hazard models, we must turn to the record of pre-historic earthquakes preserved in the landscape and the geologic record. When intraplate faults rupture Earth's surface, they typically produce a linear step or scar in the landscape known as a fault scarp. By examining fault scarps, and the surficial sediment they displace, we can determine key input parameters for seismic hazard models such as the recurrence interval, slip rate, kinematics, and maximum credible magnitude. Moreover, by mapping the specific faults anticipated to host large earthquakes, we can generate more detailed seismic hazard models that specify the source of greatest hazard. In addition, fault mapping enables another kind of seismic hazard model known as Probabilistic Fault Displacement Hazard Assessment (PFDHA), which considers the probability of specific amounts of lateral or vertical offset across a fault during a surface rupturing earthquake (Youngs et al., 2003). Rather than considering the potential for damaging shaking, PFDHA considers the potential for damaging shearing, which is especially important for critical infrastructure such as pipelines, dams, railways and highways, and any structures built across a fault.

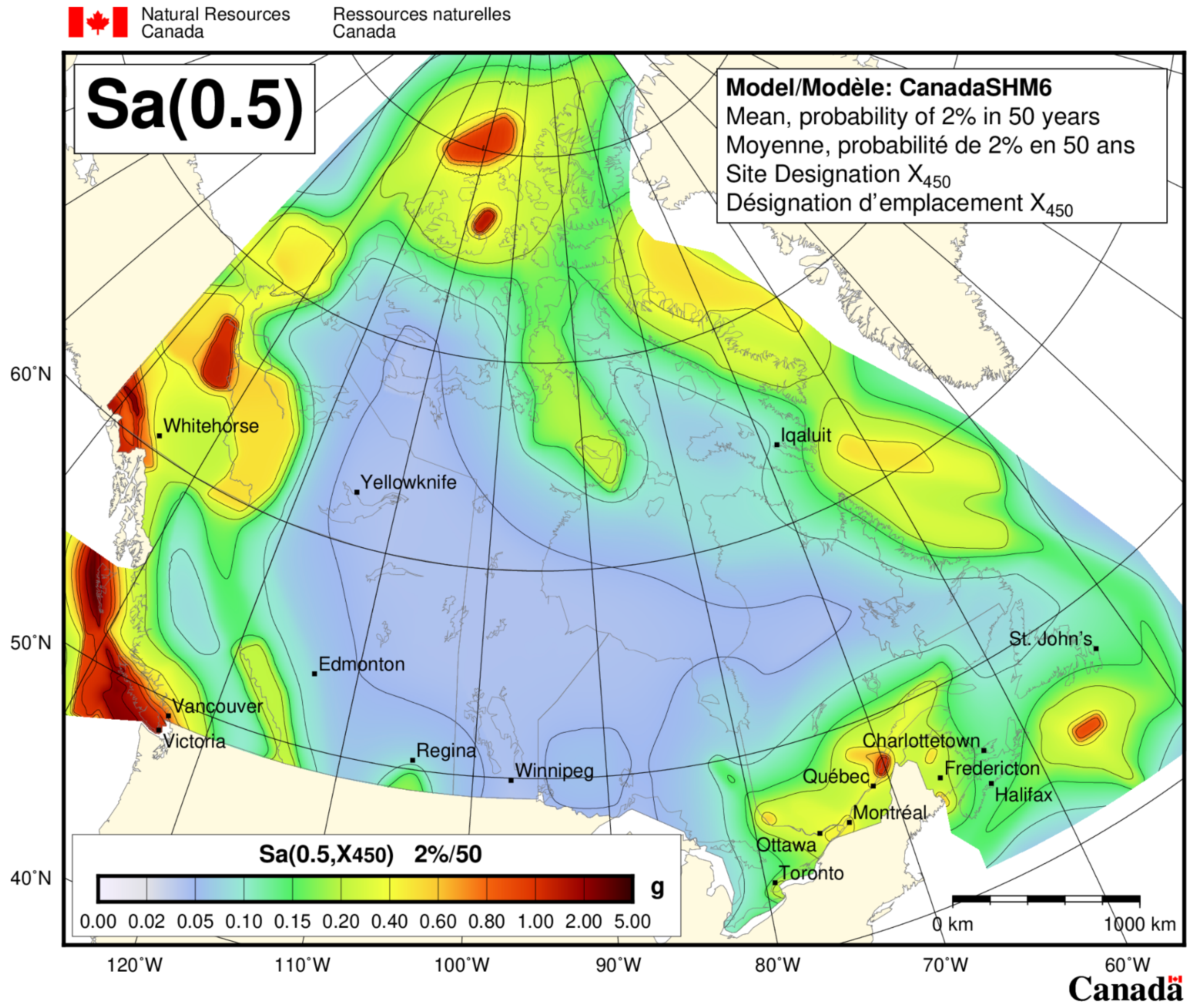

Figure 1.1. Example of Canada's National PSHA Model showing spectral acceleration at a period of 0.5 seconds with a 2% probability of exceedance over 50 years (Kolaj et al., 2020). With the exception of the Cascadia Subduction Zone, Leech River fault, Queen Charlotte fault, and Eastern Denali fault, the majority of the model is based on area sources and historical seismicity.

Until recently, paleoseismic research has been limited in Canada, in large part due to the many challenges posed by its geography and recent glacial history (see Section 1.1.4). However, the recent availability of high-resolution topographic data (see Section 1.2.1) necessary to identifying fault surface ruptures has contributed to an acceleration of research and discovery (e.g., Morell et al., 2017, 2018; Harrichhausen et al., 2021, 2023). This thesis is motivated by the expanding access to this critical data. The results of each of the three chapters are anticipated to trigger changes in Canada’s NSHM, enabling the inclusion of additional discrete fault sources, and improving estimates of fault slip rate, kinematics, and maximum magnitude.

1.1.2 Regional Tectonics and Intraplate Fault Behaviour

In addition to the mitigation of seismic hazard and risk, a second goal of this thesis is to gain an improved understanding of what drives intraplate faulting, and how intraplate faults respond to regional stresses. Ultimately, these questions are relevant to understanding seismic hazard, but they contribute to formal seismic hazard analyses in less tangible ways. Efforts to understand regional tectonic processes are often based upon the rates and kinematics of earthquakes and crustal deformation as recorded by seismic and geodetic networks (e.g., Leonard et al., 2008; Mazzotti et al., 2008; Schmeelk et al., 2017; McConeghy et al., 2022). Paleoseismic and tectonogeomorphic studies offer an alternative source of data from which to make inferences about crustal deformation.

In the western Canadian context, geodetic networks broadly indicate that the interior of the Canadian Cordillera is undergoing northeast directed shortening (Leonard et al., 2007; Mazzotti et al., 2008; Ojo et al., 2021), and crustal stress orientations derived from earthquake focal mechanisms are generally indicative of a reverse faulting regime (Ristau et al., 2007; Kao et al., 2012; Lund Snee and Zoback, 2020). Taken at face value, the regional deformation field indicates that many of the major faults that run the length of the Cordillera should accommodate a significant component of shortening. However, geomorphic studies add important nuance. For example, on the Tintina fault (Chapter 2) and Eastern Denali fault (Chapter 4) the geomorphic signature of surface ruptures instead indicates nearly pure strike-slip kinematics, potentially indicating some degree of strain partitioning as a consequence of inherited fault geometry. On the Southern Rocky Mountain Trench fault (Chapter 3), the geomorphic evidence points to extensional faulting, in a region that is inferred to be under compression based on instrumental data. Though these discrepancies may be related to the sparsity of instrumentation in these regions, they underscore the importance of including geomorphic and geologic data to gain a full picture of regional deformation patterns.

A related line of enquiry is how pre-existing, mature faults accommodate stress in relatively low strain rate environments. An accretionary orogen, the Canadian Cordillera is comprised of numerous terranes and crustal fragments bounded and crosscut by major faults. These faults have accrued tens to hundreds of kilometers of offset, likely slipped at much faster rates than they do today, and are therefore end members in terms of their structural maturity (Dolan and Haravitch, 2014; Manighetti et al., 2021; Thakur and Huang, 2021). It is not entirely clear how these mature faults behave under the present-day lower strain rates. Do they continue to localize significant strain even if not optimally oriented in the stress field? Are they still capable of large earthquakes? Do those earthquakes occur quasi-periodically as is common among mature faults (Berryman et al., 2012; Thakur and Huang, 2021), or aperiodically as is common among low-slip-rate faults (Nicol et al., 2016; Griffin et al., 2020)? The major faults of the Canadian Cordillera offer excellent natural laboratories to answer these questions.

1.1.3 Faults as Geothermal Energy Resources

A third motivation behind this thesis is the exploration of major faults as potential geothermal energy resources. Geothermal systems require three main ingredients: a source of heat, a fluid (usually groundwater) to transport that heat, and the necessary permeability to allow for the circulation of the fluid (Grasby et al., 2012; Moeck, 2014). The Canadian Cordillera has relatively high heat flow, and over 130 thermal springs, and is considered to have high potential for geothermal energy development (Davis and Lewis, 1984; Grasby and Hutcheon, 2001; Grasby et al., 2012; Finley et al., 2022a). Faults are thought to act as the permeable conduits that facilitate deep circulation and heating of groundwater, that can then be harnessed for direct heating and electricity (Bense et al., 2013; Moeck, 2014). Active faults in particular are more likely to remain permeable, as earthquakes prevent the buildup of impermeable mineral precipitate in the fault zone (Curewitz and Karson, 1997). In addition, the orientation of crustal stress relative to the fault zone exerts a major control on fault permeability (Meixner et al., 2016), and specific structural settings are shown to be more conducive to geothermal upwelling (Faulds and Hinz, 2015). There have been a number of studies examining potential fault-controlled geothermal resources throughout the Cordillera, and the Eastern Denali, Tintina, and Rocky Mountain Trench faults have been specifically targeted (Grasby and Hutcheon, 2001; Allen et al., 2006; Mira Geoscience, 2015; Witter, 2020, 2022; Tschirhart et al., 2022; Finley et al., 2022a; Lee et al., 2024). This thesis builds on those studies in a number of ways: First, it identifies where the active strands of these faults are; second, it provides information about fault geometry and complexity, which both play a role in localizing geothermal upwellings; and third, it provides information about the present-day stress orientations and fault kinematics that control fault permeability.

1.1.4 Challenges to Studying Active Faults

The identification and characterization of active faults in western Canada is hindered by many challenges posed by the region's geography, climate, glacial history and tectonic setting. In the interior of the Canadian Cordillera, strain rates are relatively low (<2mm/yr) compared to plate boundary regions (Mazzotti et al., 2008; Ojo et al., 2021). Active faults therefore do not develop strong topographic expressions, and likely rupture infrequently and irregularly (Yuan et al., 2018). Exacerbating this issue, the Late Pleistocene Fraser glaciation (Ryder et al., 1991; Clague and James, 2002) reset much of the Cordilleran landscape, and low-slip-rate faults have therefore had limited time to develop distinct surface expressions. Another consequence of the recent glaciation is that postglacial rebound has the potential to perturb the stress field sufficiently to trigger – or at least modulate the rate of – seismicity (Muir-Wood, 1989; Thorson, 2000; Steffen et al., 2014; Brooks and Adams, 2020), and this effect is difficult to distinguish from a tectonic driving mechanism when examining a potentially active fault. Additionally, geomorphic features such as sackungen – which develop as a result of gravitational settling of over-steepened slopes common to glaciated terrain – are challenging to distinguish from tectonic faults (McCalpin et al., 2011). Moreover, much of Western Canada is host to dense forests that hide fault surface ruptures, requiring the use of expensive remote sensing techniques such as lidar (light detection and ranging) over lower-cost alternatives like aerial photogrammetry (Salomon et al., 2024). Finally, much of western Canada is mountainous, inaccessible, and sparsely populated. Collectively, these challenges are responsible for the relatively small number of paleoseismic fault studies in Canada, and the reliance on seismicity-based area sources in Canada's National Seismic Hazard Model. However, new, widespread high resolution topographic data promise to significantly increase fault discoveries and our understanding of the hazard they represent.

1.2 Key Methodologies

1.2.1 High Resolution Topographic Data

Fault surface ruptures are typically 10s to 100s of kilometers long, but less than ~10 m tall and wide. As such, they are challenging to identify and characterize in the absence of remotely-sensed data with sufficient spatial resolution to distinguish features of this scale. As discussed above, this issue is particularly true in young landscapes where faults have had limited time to accrue large offsets, and in heavily vegetated landscapes where the barren ground surface cannot be observed directly or via aerial or satellite images. Until recently, much of western Canada has been covered by topographic datasets with a 30 m pixel size (e.g., the Shuttle Radar Topography Mission – SRTM), which would be insufficient to reveal even the largest tectonic scarps studied in this thesis. High resolution topographic (HRT) data – herein defined as topographic datasets with pixel sizes of 2 m or less – are a necessity for the study of active faults. This thesis capitalizes on the rapid expansion of HRT coverage in western Canada. Below, I detail the three main HRT datasets utilized in this thesis.

1.2.1.1 Satellite-based Elevation Models

Some satellite-derived HRT datasets – which have the advantage of continuous coverage over wide areas – offer sufficient resolution to image fault surface ruptures. Most relevant to this thesis is ArcticDEM (Porter, 2023), which covers the entire polar region north of 60° latitude, and is therefore applicable to my work on the Tintina fault (Chapter 2) and the Eastern Denali fault (Chapter 4). ArcticDEM has a spatial resolution of 2 m and is constructed from stereoscopic image pairs from the WorldView and GeoEye satellites (which themselves have spatial resolutions of 0.32 to 0.5 m). The digital elevation mode (DEM) is extracted from the imagery using the Surface Extraction by TIN-based Search space Minimization (SETSM) algorithm (Noh and Howat, 2017) and provided to end users as a gridded raster. Though not truly "bare earth", ArcticDEM performs well in high latitudes where vegetation is relatively sparse. Thus, in most cases it provides sufficient resolution to map features such as fault scarps and other geomorphic features of similar scale, though care must be taken where foliage is dense as the canopy can create artificial bumps in the DEM.

1.2.1.2 Airborne Lidar Data

Lidar data play a key role in all of my projects. Lidar instruments emit laser pulses at high rates (~100 kHz) and measure their return times to obtain the distance to an object from the precisely known position of the sensor. Multiple returns can be distinguished from the same laser pulse, and dedicated software can filter out returns from trees and other above-ground objects to obtain a high-resolution DEM of the bare earth surface, more specifically known as a digital terrain model (DTM). This ability to "see through" the trees is especially important for mapping tectonic features in forested terrain like the Pacific Northwest, where these features would otherwise be practically invisible from the air and on the ground (Haugerud et al., 2003; Meigs, 2013).

Lidar instruments are typically mounted to small, crewed, fixed-wing aircraft, which are flown at an altitude of ~1-2 km above the ground, in order to collect individual or overlapping swaths of data ~1-2 km wide. Crewed airborne lidar surveys are expensive to operate (10s to 100s of thousands of dollars per survey), which hinders widespread coverage. Some jurisdictions have committed to obtaining lidar coverage over their entire landmass (e.g., Washington State) and it is a stated goal of the BC government to attain full coverage by the end of this decade. Currently, only a patchwork of freely available lidar exists, covering a small fraction of the province. There is also a great deal of privately-held lidar data, and the negotiation of data-sharing agreements is often required to gain access. Having freely available, province- and territory-wide lidar coverage will be revolutionary in our efforts to map faults in the Canadian Cordillera (e.g., Haugerud et al., 2003; Meigs, 2013).

1.2.1.3 Drone Lidar Data

As the capabilities of consumer grade drones have rapidly expanded in recent years, they have become important tools in geological field studies. Lidar scanners have also become small enough and light enough to mount on drone platforms and have begun to see use in a variety of scientific applications (Risbøl and Gustavsen, 2018; Resop et al., 2019). In 2019 our group at the University of Victoria began the development a drone lidar platform for the purpose of studying tectonic geomorphology in the Canadian Cordillera. The studies undertaken for my thesis have served as a proving ground for the UVic drone lidar system. For the Tintina fault study in

Chapter 2, the drone allowed for a quick, inexpensive, targeted survey of a site previously only covered by lower resolution ArcticDEM data. For the Southern Rocky Mountain Trench study in Chapter 3, though crewed airborne lidar coverage existed, the higher spatial resolution lent increased confidence to kinematic interpretations. The Denali fault, presented in Chapter 4 and in Finley et al. (2022b) tested the utility of the drone in a more widespread application, and also benefitted from the higher resolution data.

Below, I provide a brief overview of the drone system, survey methodology, and data processing steps. I also briefly discuss the utility of drone lidar in comparison to conventional lidar. A more thorough description of the lidar drone and its capabilities are provided by Salomon et al. (2024).

1.2.1.3.1 Drone Lidar Methodology

The UVic drone lidar system (Figure 1.2) is comprised of a DJI M600 Pro drone mounted with a Riegl miniVUX 1UAV lidar scanner. The position and orientation of the platform are concurrently logged with an Applanix APX-20 UAV GNSS-Inertial system. A Trimble R12 Real-Time Kinematic Global Navigation Satellite System (GNSS) records a static base station position on the ground during the survey, and a rover unit is used to measure the position of reflective, 120 × 120 cm “harlequin cross” style targets for the purpose of ground control.

Survey patterns are designed using Universal Ground Control Station (UgCS) software developed by SPH engineering. The size of each survey flight is limited by both the battery life and Transport Canada regulations that require the drone to remain within Visual Line of Sight (VLOS). In practice, this means that each individual flight is less than 20 minutes long, and the drone rarely goes beyond ~1.5 km from the launch point. The data from multiple flights can later be merged in post-processing to create a larger seamless dataset. The manufacturer-recommended altitude for the lidar scanner is 80 m above ground level, and the drone is programmed to follow terrain using an existing lower-resolution elevation model, such as SRTM, as a baseline. Through experimentation we have found that a flight speed of 4-6 m/s over ground offers the best balance between survey speed, area covered, and point density (Salomon et al., 2024).

Figure 1.2. The UVic drone lidar platform conducting a survey on the Eastern Denali fault in the Yukon.

The drone lidar data processing workflow is summarized in Figure 1.3. The static base station position is refined using Natural Resource Canada's Precise Point Positioning tool, and the positions of the ground control points recorded with the rover are corrected accordingly. Using the refined base station position, Applanix's POSPac UAV software is used to generate a smoothed best estimate of the drone trajectory. Riegl's RiProcess software is then used to generate an initial point cloud from the laser data and drone trajectory, which can be georeferenced more precisely using the ground control points. The LAStools software package (Isenburg, 2021) is used for point classification and raster generation. The resulting point clouds have ground point densities of between ~10 and 70 pts/m^2, much higher than is common in traditional airborne lidar surveys (Figure 1.4). In practice this range in point density is amenable to producing DTMs with pixel resolutions of 30 to 50 cm (Salomon et al., 2024).

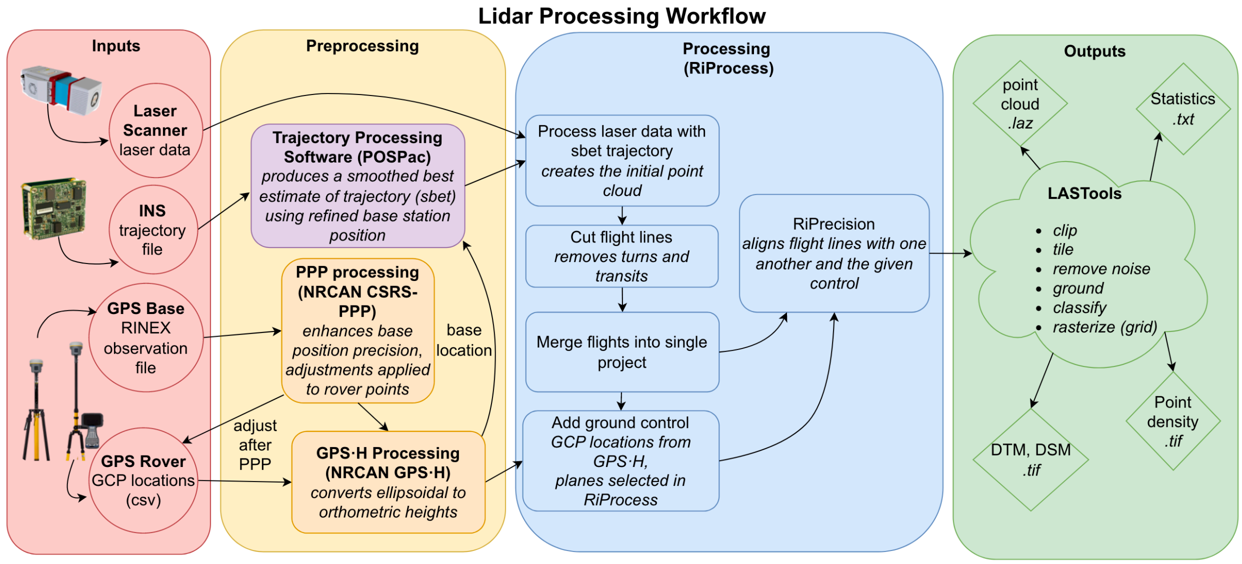

Figure 1.3. Drone lidar data processing flowchart from Salomon et al. (2024).

1.2.1.3.2 Drone Lidar Strengths and Limitations

The extremely high spatial resolution of drone lidar (Figure 1.4) enables greater confidence in mapping and interpretation of subtle geomorphic features. The importance of higher resolution lidar was previously demonstrated by Lin et al. (2013), who found that sub-meter pixel sizes were critical to the identification of subtle fault features in a heavily vegetated landscape in Japan. In our experience, the higher resolution was not critical to identifying fault scarps, as the features examined in this thesis were of sufficient size to be distinct in at traditional resolutions. However, the added detail was useful in distinguishing small lateral offsets across faults (Chapter 4), or lack thereof (Chapter 3).

Drone lidar data come at a relatively low cost compared to traditional airborne lidar. The upfront cost of purchasing the system can be in the 10s to 100s of dollars, similar to the cost of a single crewed survey. Thus, drone lidar is well suited to small, targeted studies of features that would otherwise be cost-prohibitive to survey (e.g., Chapter 2). It is also very useful for repeat surveying in changing landscapes, whether that be for the study of creeping faults, pre- and post-earthquake differencing, or the monitoring of other related geohazards such as landslides. Our research group has ongoing projects focused on these applications.

The small size of drone lidar surveys (Figure 1.5) is a significant limitation that will only be overcome through innovations in battery life, and changes in regulations that restrict beyond-VLOS flight. Moreover, because the necessary equipment is too bulky to deploy on foot (Figure 1.5), the VLOS requirement essentially precludes deployment of the drone over remote sites without vehicle access. Transport Canada has recently announced changes to drone regulations that will reduce the restrictions on low-risk beyond-VLOS flight, and new gas-electric hybrid drones as well as the continual advancement of battery technology promise to extend possible flight times, thereby increasing the utility of drones for geological research.

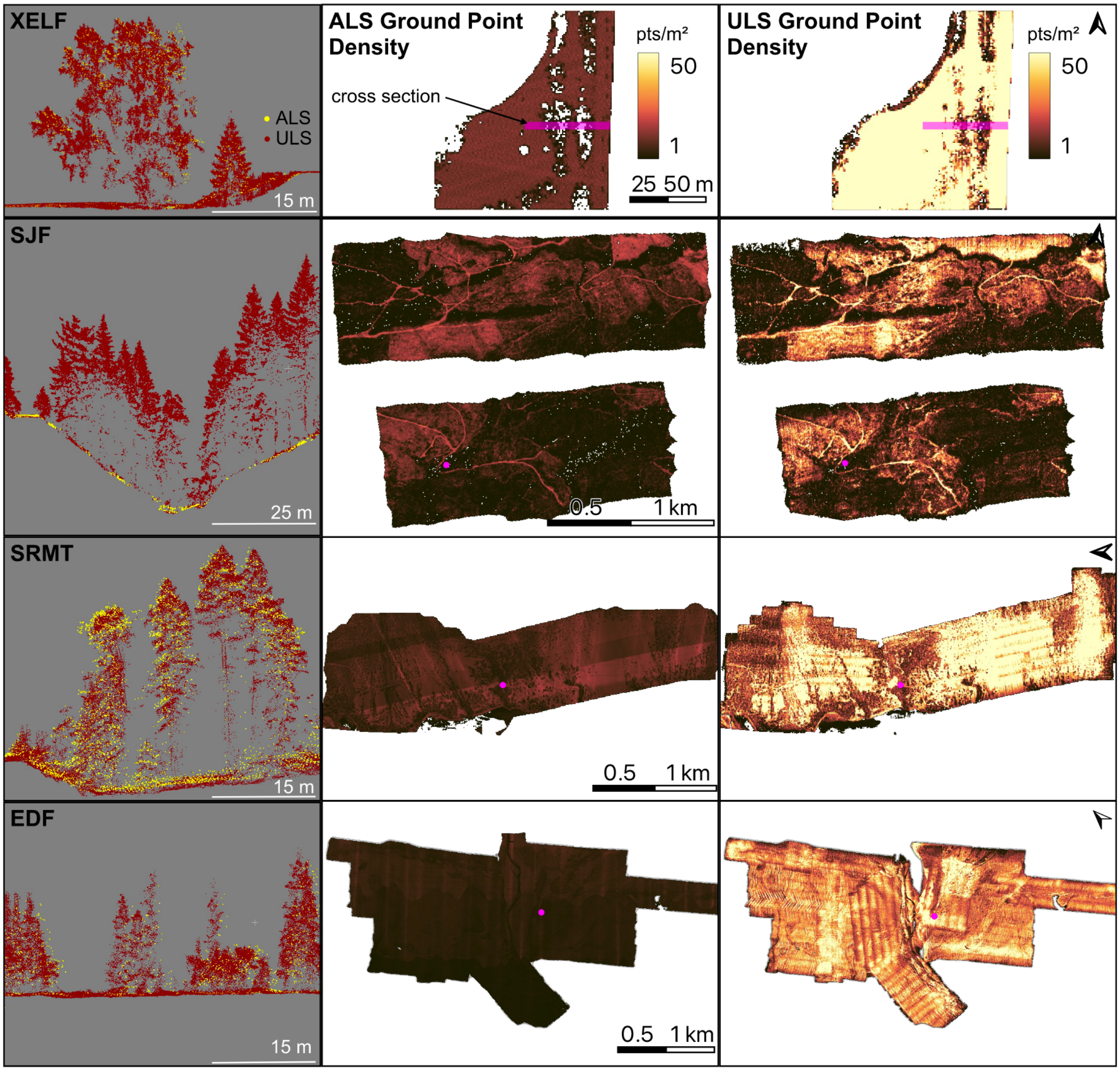

Figure 1.4. Comparison of point densities between conventional airborne lidar scanning (ALS) and Uncrewed lidar scanning (ULS) methods at study sites on the XEOLXELE~~K~~ Elk Lake Fault (XELF), San Juan Fault (SJF), Southern Rocky Mountain Trench (SRMT), and Eastern Denali faults. Figure is from Salomon et al. (2024). Locations of the representative cross sections through lidar point clouds are indicated by the pink markers. Map views in second and third columns are at the same scale.

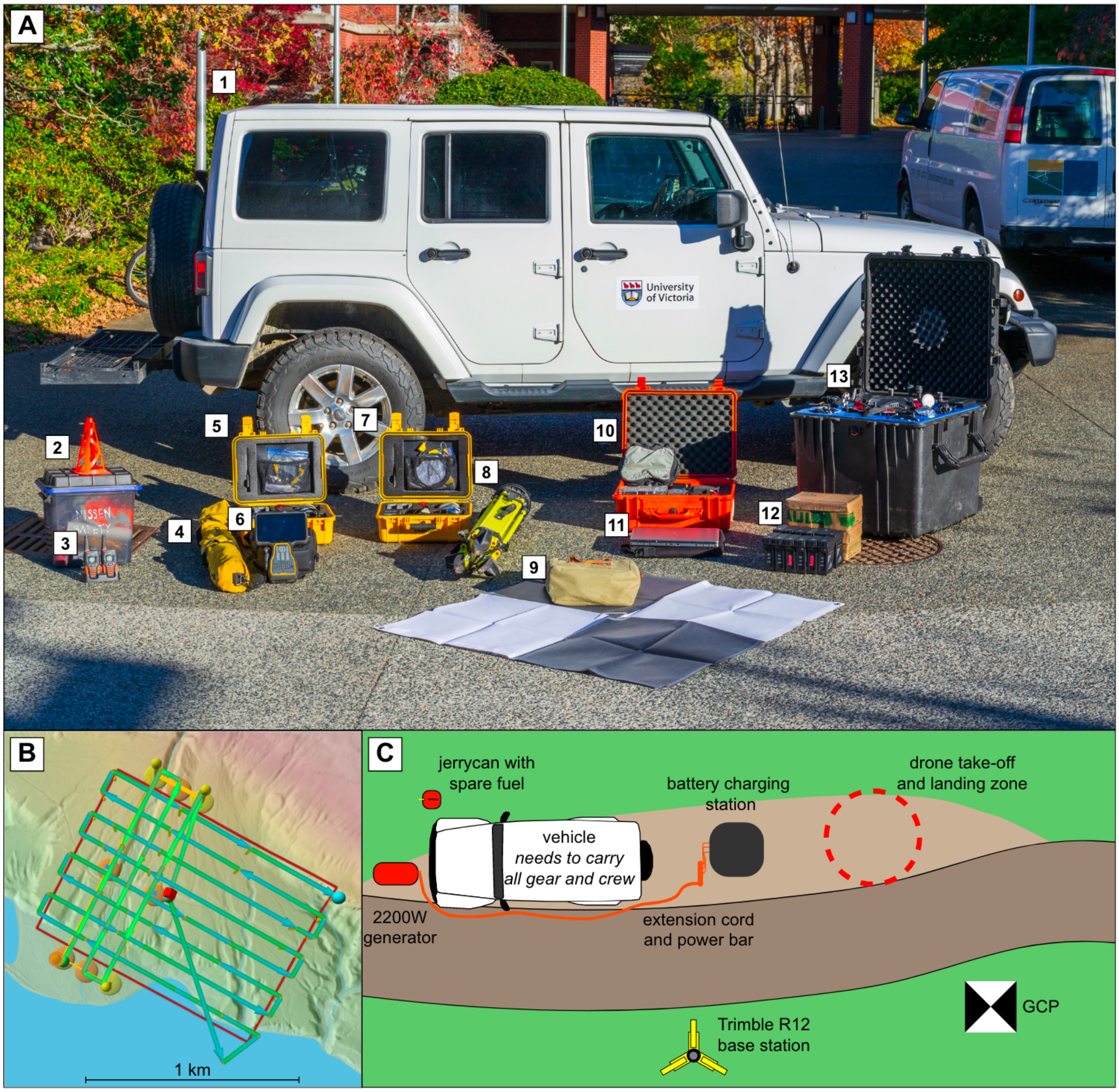

Figure 1.5. (a) Full ensemble of equipment required for a lidar drone survey. (b) Example of a UgCS flight plan for a ~1 km^2 lidar survey at the Columbia Lake site (Chapter 3). This particular survey would require at least 5, individual, ~20 minute flights and at least half a day of overall field time. (c) Schematic of a typical base station setup. Figure is from Salomon et al. (2024).

1.2.2 Geomorphic Mapping

The HRT datasets discussed above facilitate the identification and measurement of fault scarp morphology, as well as detailed surficial mapping to constrain earthquake age and slip rate. The identification of fault scarps is primarily a manual, visual task, and a combination of elevation, hillshade, slope-angle, and slope-aspect maps can be used to aid the process. Fault scarps are primarily identified on the basis of their linearity and spatial scale (multiple kilometers long, several meters wide and tall). Care must be taken to distinguish fault scarps from other linear features of similar scale, including river terrace risers, raised beaches, glacial striations, landslide headscarps and sackungen, all of which are common in the recently deglaciated landscape of the Canadian Cordillera. Once identified, it is also important to determine the age of surficial material that the scarp offsets or deforms; scarp-like features that offset pre-Quaternary bedrock offer little information about the neotectonic activity of a fault whereas scarps offsetting Quaternary sediment and surficial features are key indicators of active faulting. It is also important to establish that some fault displacement – lateral or vertical – has occurred across the scarp: for example, lateral offset of linear features (e.g., creeks), or vertical offset of a planar surface (e.g., river terrace). A variety of software tools can then be used to extract robust measurements of these vertical and lateral offsets (e.g., Zielke and Arrowsmith, 2012; Stewart et al., 2018; Wolfe et al., 2020).

HRT data also enable detailed mapping of different surficial units and, when tied with measurements of fault offsets and any available geochronological constraints (see next section), this can provide crucial information about fault slip rate. A solid understanding of Quaternary stratigraphy and especially glacial and paraglacial geomorphology is necessary: In Canada, the majority of geomorphic landforms are related to Late Pleistocene deglaciation (Ryder et al., 1991; Clague and James, 2002), and provide a maximum age of faulting, from which a minimum slip rate can be calculated.

Mapping of Quaternary stratigraphy and fault geometry can be extended into the subsurface using a variety of shallow geophysical techniques. This approach is especially useful where ground disturbance (i.e., paleoseismic trenching) is not easily permitted. The main geophysical technique used in this thesis is Electrical Resistivity Tomography (ERT). ERT is well suited to glacial environments, as glacial sediments have a wide range of electrical properties (Palacky, 1987) and are readily distinguished in resistivity inversions. Several previous paleoseismic studies in western Canada have made use of an Advanced Geosciences Inc. (AGI) MiniSting instrument (Graham, 2018; Harrichhausen et al., 2023), which is capable of 80 m-long profiles, resolving features to depths of up to ~16 m. In this thesis (Chapter 3), I make use of an AGI SuperSting system, which is capable of profiles up to 1000 m long, with depth penetration of several 100 m. Though much more labour-intensive to deploy, this larger system proved critical in providing evidence of active faulting, as it was able to image clear vertical offsets to Quaternary stratigraphy well below the ground surface.

1.2.3 Quaternary Geochronology

Combining geomorphic mapping with chronological constraints allows for the determination of fault slip rate, which is a key input into seismic hazard models. In this thesis I do not produce new geochronological data, but leverage existing studies and datasets of direct and relative age constraints. In the Canadian Cordillera, the timing of deglaciation following the Late Pleistocene Last Glacial Maximum (LGM), provides a primary constraint on landscape age. I make extensive use of the recently released North American Deglacial Isochrone (NADI-1) database (Dalton et al., 2023), which provides a comprehensive catalog of direct age constraints on deglacial timing along with continent-wide interpretations of ice retreat patterns through time. The main direct dating methods compiled in NADI-1 include: 1) radiocarbon dating, which generally provides the timing of ice free conditions as recorded by the presence of organic matter and plant life; 2) optically stimulated luminescence (OSL) dating, which indicates the time since a sediment was last exposed to sunlight, and 3) terrestrial cosmogenic nuclide dating, which indicates the length of time a surface (e.g., an alluvial fan) has been exposed to cosmic ray bombardment from an open sky. I addition to these techniques I make use of a variety of other age constraints from the broader literature including tephrochronology, magnetostratigraphy, and soil weathering. In general, because these dating techniques, and the landforms they are applied to, constrain the timing of deglaciation and not faulting, they can only provide a minimum slip rate.

Chapter 2: Exceptionally long intervals between large earthquakes on the Tintina fault, Yukon

2.1 Article Information

Theron Finley[1], Edwin Nissen[1,2], John F. Cassidy[3,1], Guy Salomon[1], Lucinda Leonard[1,] Duane Froese[4]

[1]School of Earth and Ocean Sciences, University of Victoria, BC, Canada

[2]College of Earth, Atmospheric, and Ocean Sciences, Oregon State University, Corvallis, OR, USA

[3]Pacific Geoscience Centre, Geological Survey of Canada, Sidney, BC, Canada

[4]Department of Earth and Atmospheric Sciences, University of Alberta, Edmonton, AB, Canada

This article is currently under revision for *Geophysical Research Letters.* I was the first to identify and map the Tintina fault scarp using ArcticDEM data, and I acquired grant funding to conduct fieldwork. I led two separate fieldwork trips to the Yukon to acquire additional drone lidar data and ground truth interpretations of the surficial geology. I also led the processing and interpretation of data, writing of the text, and creation of figures. Dr. Edwin Nissen co-supervised this work, assisted with data interpretation and manuscript preparation, and provided additional fieldwork funding. Dr. John Cassidy co-supervised this work, assisted with manuscript preparation, and provided additional funding. Dr. Guy Salomon assisted with drone lidar acquisition and minor manuscript edits. Dr. Lucinda Leonard contributed expertise on regional tectonics and edited the manuscript. Dr. Duane Froese contributed expertise on regional surficial geology and geochronology.

2.2 Abstract

New geomorphic evidence indicates successive large surface-rupturing earthquakes occurred throughout the Quaternary on the Tintina fault in the Yukon Territory, northwestern Canada. A ~130 km-long series of bedrock lineations, scarps, and pressure ridges, offset Pleistocene landforms, indicating a dextral slip rate of ~0.6 mm/yr. However, early Holocene terraces are undeformed across the fault, implying that the elapsed time since the most recent earthquake is >12 kyrs and that the fault may be nearing the end of a long seismic cycle. A minimum slip deficit of 6.1 m can be assumed to have accrued since the last major surface rupture, and future earthquakes could exceed Mw 7.5, presenting a major, previously unrecognized seismic hazard. These results highlight the hazard of earthquakes on mature, low-slip-rate intraplate faults, which may have exceptionally long recurrence intervals, elude instrumental networks, and lack a distinct surface expression due to landscape resetting.

2.3 Plain Language Summary

The Tintina fault is a major ~1000-km-long geologic fault in the Yukon Territory of northwestern Canada. It was previously believed to have last been active over 30 million years ago, though some have speculated it remains capable of generating large earthquakes. Using new high resolution topographic data collected from satellites, airplanes, and drones, we have identified a 130-km-long segment of the fault where 2.6 million-year-old, and 130 thousand-year-old geological formations are laterally shifted across the fault by ~700 m and 70 m respectively. From this, we are able to estimate that the Tintina fault has ruptured in numerous large earthquakes in the relatively recent geologic past, and that it continues to accumulate strain at an average rate of 0.6 mm/yr. We further show that the fault has not ruptured in a major earthquake for at least 12 thousand years, and it is still capable of generating large earthquakes of at least magnitude 7.5 in the future. The Tintina fault therefore represents a major, previously unrecognized, seismic hazard to the region.

2.4 Introduction

Identifying and characterizing seismogenic faults in slowly deforming regions is a major challenge for seismic hazard analysis. Microseismicity often does not align (or even exist) along active fault planes, geodetic networks commonly lack the precision to resolve sub-millimeter/year slip rates, and low strain rate regions are generally a low priority for dense instrumentation. Recurrence intervals between large earthquakes on low-slip-rate faults can be both long and irregular (Nicol et al., 2016; Yuan et al., 2018; Griffin et al., 2020; Bollinger et al., 2021), and consequently, multi-event paleoseismic and tectono-geomorphic records are rare. This issue is exacerbated in young landscapes reset by icesheets or other climatic factors, where faults have not had time to accrue offset of the youngest surfaces. Seismic hazard models in these regions typically rely on area sources based on historical seismicity alone, which may not capture the maximum credible earthquake or the potential for surface rupture. Notably, low-slip-rate faults are shown to produce larger magnitude earthquakes with greater static stress drops than faster slipping faults with comparable rupture lengths, underscoring the importance of characterizing them (Anderson et al., 2017).

In this paper we examine the Tintina fault, a major, structurally-mature fault, that occupies a pronounced, northwest-trending, ~1000-km-long valley known as the Tintina Trench in the Yukon Territory of northwestern Canada (Figure 2.1.; Gabrielse et al., 2006). To the northwest it connects to the Kaltag fault in Alaska, and to the southeast, the Rocky Mountain Trench fault system in British Columbia. The Tintina fault is shown to have accrued ~430 km of cumulative dextral offset, largely in the Eocene (Gabrielse et al., 2006), and may have had slip rates as high as 13 mm/yr (Ryan et al., 2017), making it an end member in terms of structural maturity. However, its activity has since waned. There are low levels of diffuse seismicity along it (Drooff and Freymueller, 2023) with ~2 earthquakes ≥ M_w3.0 per year (Figure 2.1.). Summing the seismic moment yields a slip rate of 0.5 (+0.9/-0.3) mm/yr (Leonard et al., 2008), and geodetic block models struggle to resolve any slip (Leonard et al., 2007; Elliott and Freymueller, 2020). Strain from the ongoing Yakutat collision in southeast Alaska is transmitted across the entire northern Cordillera (Figure 2.1.; Mazzotti and Hyndman, 2002), and some have suggested that the Tintina fault may still be capable of large surface-rupturing earthquakes (Mortensen and Von Gaza, 1992; Duk-Rodkin et al., 2001). However, while potential large earthquakes (up to M_w7.8) are included in a broad seismic source area covering >3×10^5 km^2 of the central Yukon Territory in Canada’s National Seismic Hazard Model, the Tintina fault is not currently recognized as a discrete seismogenic fault source (Adams et al., 2019; Kolaj et al., 2023).

The landscape in northwestern Yukon is among the oldest in Canada, with high potential for the preservation of tectonic landforms. Much of northwestern Yukon – aside from a few isolated ice fields in the Ogilvie Mountains – remained ice-free during the most recent Late Pleistocene (late Wisconsinan), Marine Isotope Stage (MIS) 2 glaciation, locally referred to as the McConnell glaciation, which otherwise covered most of the Canadian Cordillera (Figure 2.1.) between ~24 and 12 ka (Stroeven et al., 2010; Dalton et al., 2023). Several older and more spatially extensive glaciations did advance into northwestern Yukon (Duk-Rodkin, 1999): these are the late-Middle Pleistocene Reid glaciation (MIS 6), which ended at ~132 ± 18 ka (Demuro et al., 2012), and several Late Pliocene-Early Pleistocene Pre-Reid glaciations, which occurred at 2.64 (+0.20/-0.18) Ma (Hidy et al., 2013). Pro-glacial sedimentation at the margins of these icesheets left moraines and glaciofluvial deposits with distinctive soils on their surfaces (Smith et al., 1986; Tarnocai et al., 1985) that, together with the absolute ages, provide constraint on the slip rate and timing of ruptures on the Tintina fault (Figure 2.1.).

Using new high resolution topographic data (ArcticDEM and drone lidar), surficial mapping, and geochronological constraints (see Supplemental Text), we provide the first conclusive evidence of large surface ruptures on the Tintina fault in the Quaternary (2.6 Ma to present). We further show that despite rupturing numerous times throughout the Pleistocene (2.6 Ma to ~12 ka), the Tintina fault has not ruptured in a large event in the Holocene (~12 ka to present) and may be late in its seismic cycle, which has significant seismic hazard implications. Our findings highlight a pitfall of relying on the short Holocene paleoseismic record in seismic hazard analysis and show that in low strain rate regions, existing, mature faults can accommodate strain via large earthquakes with recurrence intervals on the order of >10^4 years.

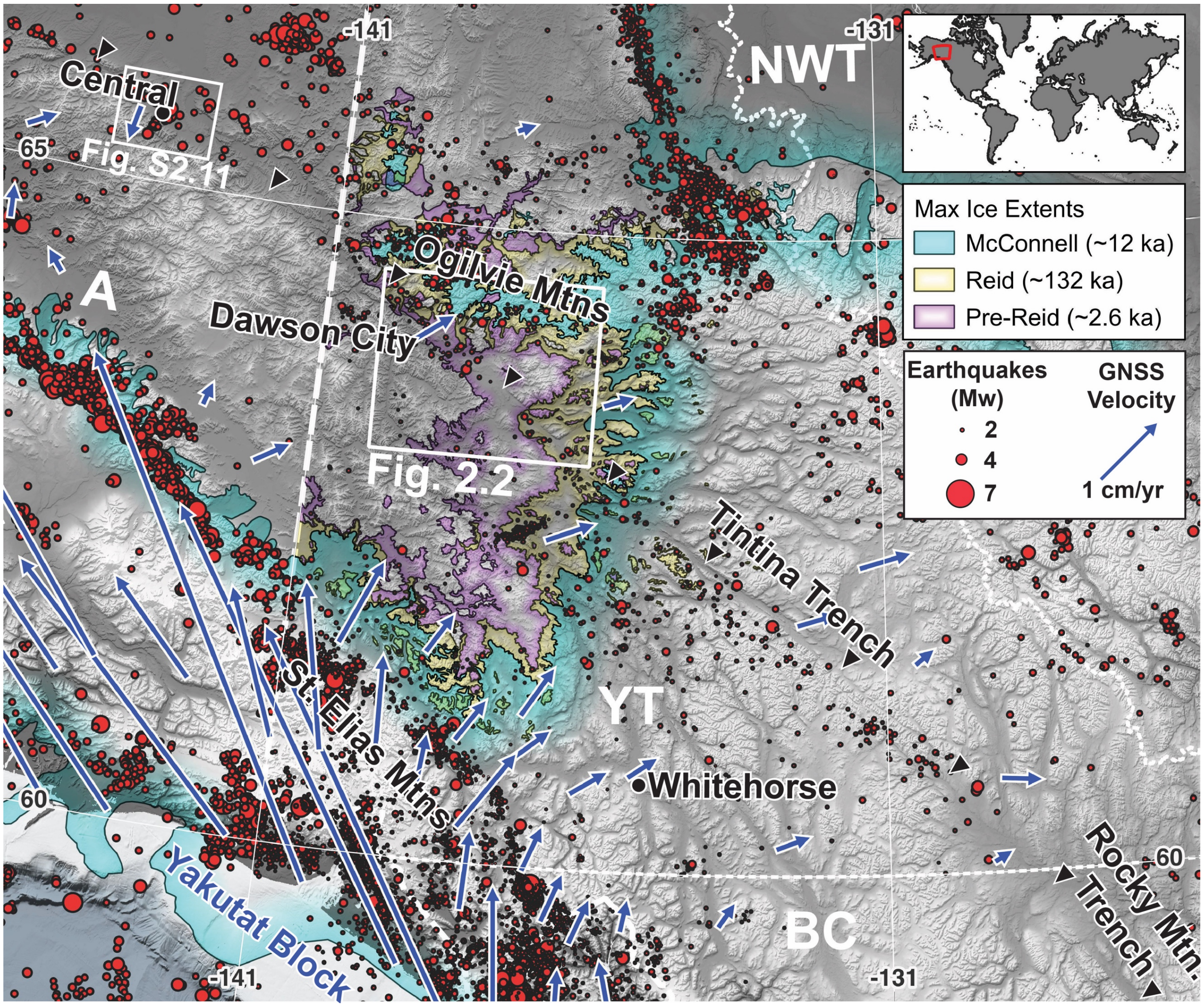

Figure 2.1. Physiography and seismotectonics of the Yukon Territory. Hillshade highlights the conspicuous topographic form of the Tintina Trench. Ice limits for the McConnell, Reid and Pre-Reid glaciations (Duk-Rodkin, 1999; Dalton et al., 2023) are shown. Reid and Pre-Reid limits are not mapped beyond the Yukon Territory. Seismicity (Natural Resources Canada, 2024) and a subset of GNSS velocities relative to stable North America (Elliott and Freymueller, 2020) demonstrate a slow rate of deformation in the Cordilleran interior.

2.5 Geomorphic Evidence of Pleistocene Surface Ruptures on the Tintina Fault

We map a series of semi-continuous lineations and scarps for a total length of 130 km along the Tintina Trench (Figure 2.2). The mapped fault traces offset and deform glacial and paraglacial sediments and surfaces of Reid (132 ka) and Pre-Reid (2.6 Ma) ages. Below, we describe three distinct segments of the fault, here named the Flat Creek, Dempster, and Dawson segments.

2.5.1 The Flat Creek Fault Segment

The Flat Creek fault segment extends for 52 km across a broad plain southwest of the Klondike Highway (Figure 2.3). Here, a scarp up to 20 m high, and a series of en-echelon mounds and depressions that we interpret as positive and negative flower structures, deform outwash gravels and till deposited during the 2.6 Ma Pre-Reid glaciation. A shallow test pit on one of the mounds (blue star; Figure 2.3) confirms that it is composed of clast-supported pebble-cobble gravel, weathering to reddish brown, consistent with Pre-Reid glaciofluvial deposits (Tarnocai et al., 1985; Smith et al., 1986). The pull-apart features are commonly occupied by small lakes (sag ponds). The push-up structures are on the order of 300 m long, 50 m wide, and 20–40 m high. These are at least an order of magnitude larger than traditional coseismic "mole tracks" observed in continental strike-slip earthquake surface ruptures (Rizza et al., 2015; Choi et al., 2018; Little et al., 2021). However, they closely resemble larger push-up structures and pressure ridges observed along the Kunlun fault in northern Tibet (Fu et al., 2003; Lin et al., 2004), and the Eastern Denali fault in southwestern Yukon (Haeussler et al., 2017; Blais-Stevens et al., 2020; Finley et al., 2022b), which are interpreted to record cumulative mole-track-style deformation as a result of transpression. Tibet and the Yukon both have semi-continuous permafrost at present, and such surface deformation may be a consequence of the rheological properties of ground ice in thick, unconsolidated surficial sediments. In addition to the push-up structures being indicative of dextral transpression, we interpret a set of subdued, arcuate, northwestward-convex ridges, as Pre-Reid terminal moraines; these are dextrally offset by ~700 (+300/-200) m (Figure 2.3 and S2.6). The Flat Creek valley riser is dextrally offset by 1500 (+100/-200) m, though this may overestimate the true tectonic displacement as the riser could have been reworked by the creek immediately north of the fault.

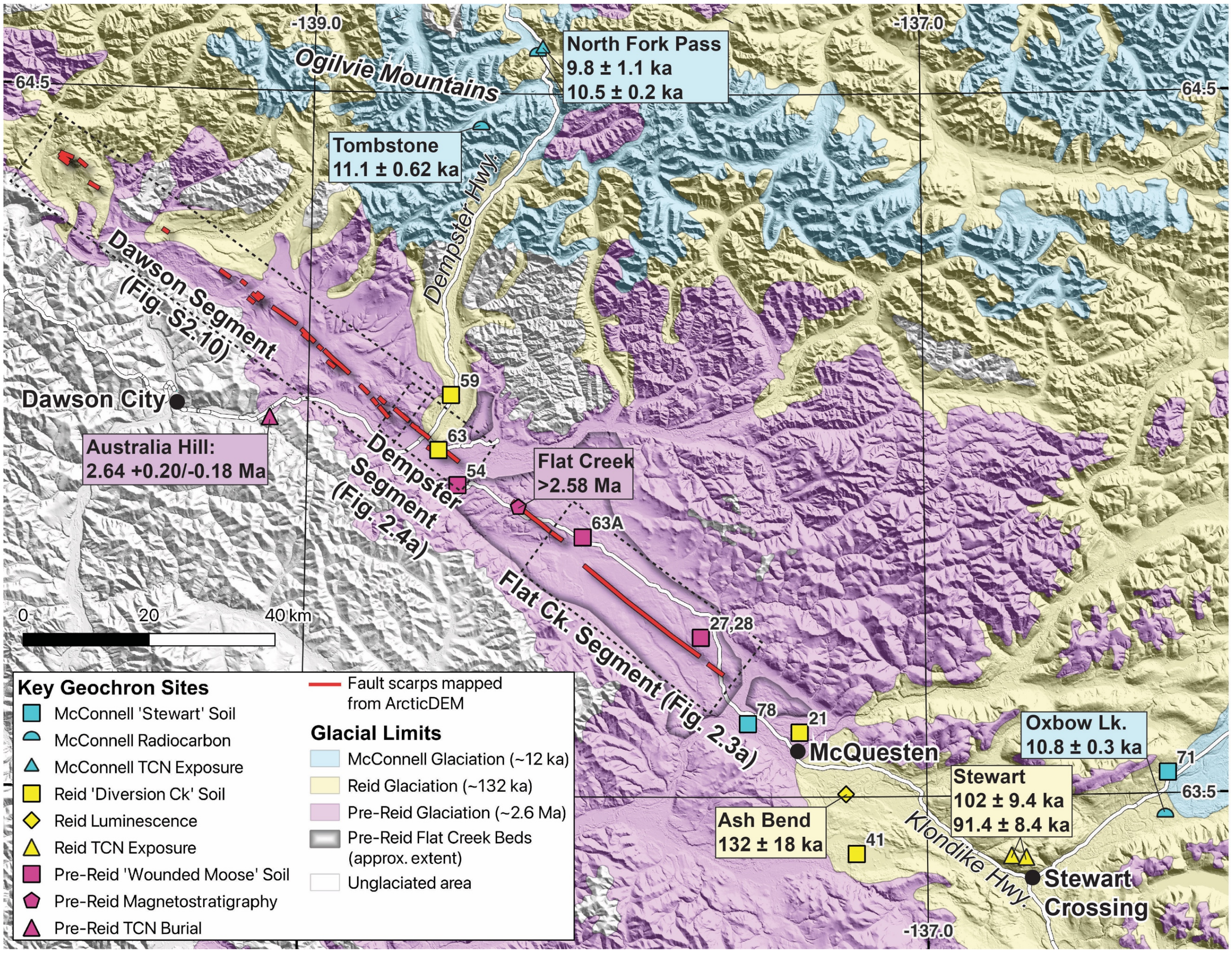

Figure 2.2. Map of Quaternary fault scarps (130 km total length) along the Tintina Trench in the Klondike region. Limits of the McConnell, Reid, and Pre-Reid ice (Duk-Rodkin, 1999) and geochronological sample locations from the literature (see Table S2.1) are shown. Some sample sites occur on glaciofluvial outwash terraces and are therefore beyond the ice limit of the corresponding glaciation. Basemap is ArcticDEM version 4 (Porter et al., 2023).

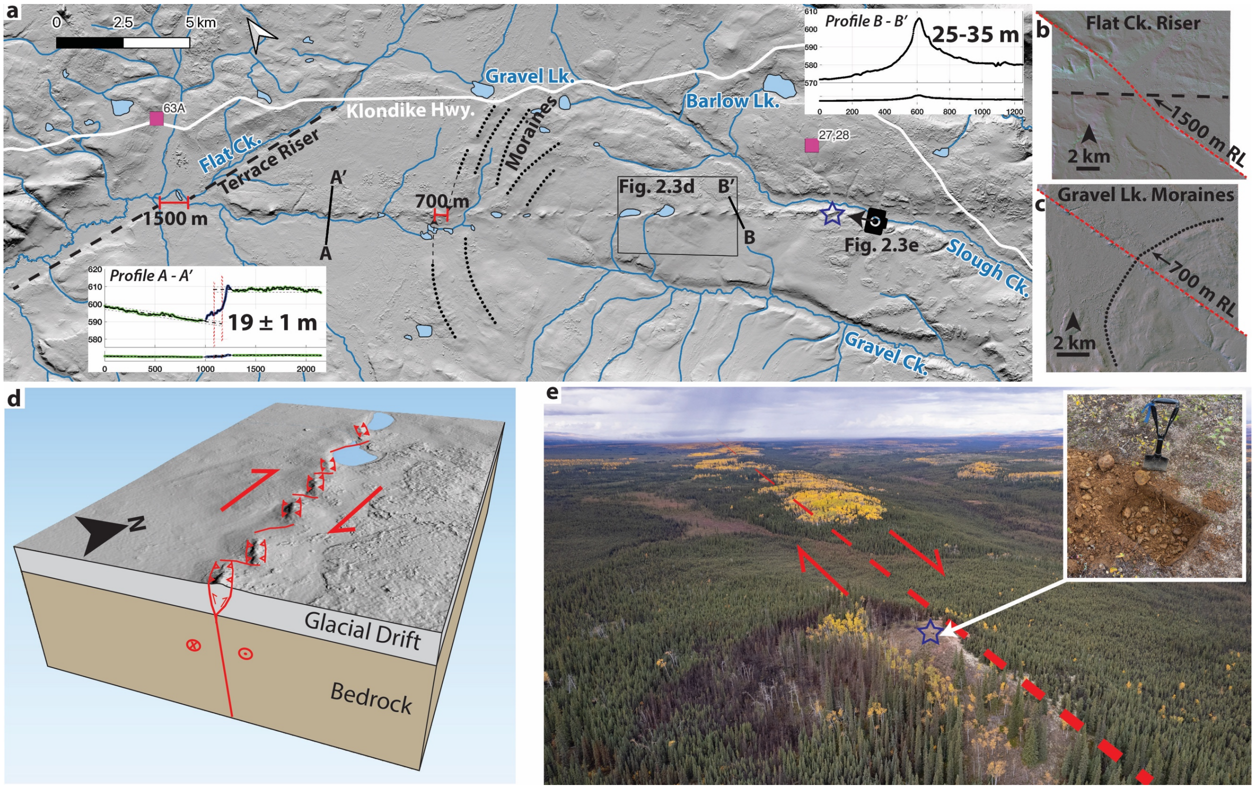

Figure 2.3. Detailed view of the Flat Creek fault segment. (a) ArcticDEM (Porter et al., 2023) hillshade showing the scarp cross-cutting the 2.6 Ma Flat Creek Beds. See Figure 2.2 for map extent. Topographic profiles are shown with both 1:1 scale (lower) and a vertical exaggeration (upper). (b,c) LaDiCaoz restoration of 1500 m right lateral offset of Flat Creek riser and 700 m right lateral offset of Gravel Lk. Moraines. (d) 3D model and kinematic interpretation of the en-echelon push-ups. (e) Drone photo looking northwest along fault trace showing dense boreal forest cover. Push-up structures are highlighted by groves of yellow birch trees. Inset image shows subrounded cobble gravel and reddish-brown soil characteristic of Pre-Reid "Wounded Moose" paleosol in test pit located at blue star at top of push-up.

2.5.2 The Dempster Fault Segment

The Dempster fault segment extends for 7.7 km, crossing the Dempster Highway northeast of its junction with the Klondike Highway. A fault scarp clearly offsets terraces of Reid age (Gt-R), but does not deform terraces of McConnell age (Gt-M), nor the modern floodplain of the Klondike and North Klondike Rivers (Figure 2.4 and S2.7). The scarp has a consistent northeast-side-up vertical separation of 3.3 ± 2.5 m (Figure S2.9). A discontinuous terrace riser, interpreted as late-Reid because it merges with a Reid-age outwash channel (rather than incising it), is dextrally offset by 72.5 ± 2.5 m (Figure 2.4). This riser may have been trimmed or reworked, but this would have occurred primarily on the upstream side of the fault and our offset measurement would therefore be an underestimate. We consider this riser the most reliable offset marker available and use it as a primary constraint on slip rate. Two additional features with apparent dextral offsets of 200 and 130 m are shown in Figure 2.4 and S2.7 respectively; while providing supporting evidence, we consider these less clearly defined features to be less reliable for the purposes of slip rate calculation.

2.5.3 The Dawson Fault Segment

The Dawson segment extends for a further 70 km northwest, passing within 20 km of Dawson City (Figure 2.2 and S2.9). This section of the fault has more topographic relief than the Flat Creek and Dempster segments; colluvial and mass wasting processes are more dominant, contributing to poorer scarp preservation. We map a series of discontinuous lineaments and scarps, the majority of which exhibit northeast-side-up separation and no evidence of lateral offset. These scarps deform surfaces mapped as glaciofluvial terraces, till plains, and till veneers of both Reid and Pre-Reid age (Duk-Rodkin, 1996). We attribute the lack of observable lateral offset on the Dawson segment to the fact that channel offsets are not well preserved on low-slip-rate faults over long time periods, as the channels will tend to avulse to a straighter path (Dascher-Cousineau et al., 2021; Reitman et al., 2022). Cumulative lateral offsets are better preserved by static geomorphic features on flat terrain, such as the terrace risers and moraines on the Flat Creek and Dempster segments. Thus, we are confident with our interpretation of predominantly strike-slip kinematics on the Tintina fault despite the preservational record being biased towards the relatively minor dip-slip component.

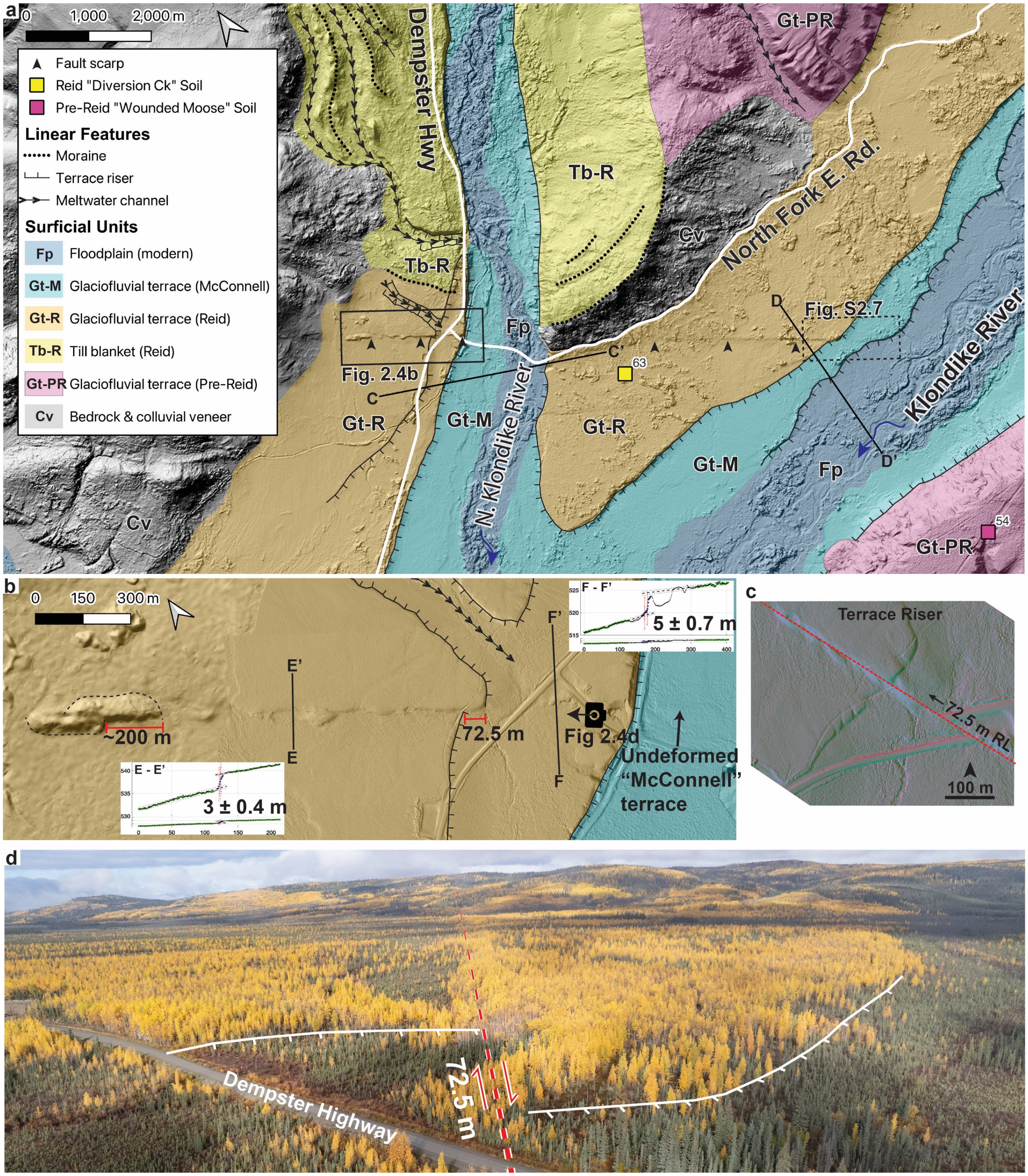

Figure 2.4. Detailed view of the Dempster fault segment. (a) Surficial map of the Dempster fault segment, based on existing maps (Thomas and Rampton, 1982; Duk-Rodkin, 1996; Froese, 2005a, 2005b; McKenna and Lipovsky, 2014) and augmented with new high resolution topography. See Figure 2.2 for map extent. Topographic profiles C-C' and D-D' are provided in Figure S.2.8. (b) Detailed map of the Dempster fault segment. Base map is drone lidar data. The ~132 ka Reid-age terrace surface is vertically offset by 3.3 ± 2.5

m, and dextrally offset by 72.5 m ± 2.5. (c) LaDiCaoz restoration of 72.5 m right lateral offset of terrace riser. (d) Drone photo looking northwest along fault trace, with annotation showing dextrally offset riser.

2.6 Analyses and Implications

2.6.1 A Low Slip Rate and a Long Recurrence Interval

Our measurements of deformed and undeformed Quaternary landforms indicate that the modern kinematics of the Tintina fault are dominantly right-lateral, the slip rate is low, and the average recurrence interval is exceptionally long. The lack of deformation on McConnell-age terraces suggests that there has been no surface rupture or aseismic slip at least since the McConnell ice sheet receded from the Ogilvie Mountains ≥ 12 ka (Stroeven et al., 2010; Menounos et al., 2017; Dalton et al., 2023). We acknowledge the possibility that a Holocene flood event could potentially have erased evidence of a fault scarp on McConnell-age terraces, but note that modern channel of the Klondike River is in places 10 m below these terraces (Figure S2.8). Thus, if the total 72.5 ± 2.5 m right-lateral offset of a Reid-aged terrace riser occurred between the ends of the Reid and McConnell glaciations, we estimate a closed-interval slip rate of 0.62 (+0.13/-0.11) mm/yr (Figure 2.5). This slip rate is consistent within uncertainty both with a longer-term closed-interval slip rate of 0.41 (+0.11/-0.18) mm/yr that can be estimated from the 700-1500 m right-lateral offsets to the Pre-Reid (ca. 2.6 Ma) Flat Creek beds (Figure 2.5), and with slip rate estimates of 0.5 (+0.9/-0.3) mm/yr from seismic moment summation (Leonard et al., 2008). There have been no documented changes in the overall tectonic regime in the northern Cordillera during the Quaternary, so it is inferred that the lack of surface rupture through McConnell-aged and younger deposits is due to a current (open) recurrence interval of at least 12 kyr, rather than waning tectonic activity.

The 72.5 m offset of the Reid-age terrace riser on the Dempster fault segment could not have been accomplished by a single rupture. Low-slip-rate faults are known to have variable inter-event times between earthquakes with differing average slip (Nicol et al., 2016; Yuan et al., 2018; Griffin et al., 2020), though this behaviour may be moderated by the high structural maturity of the Tintina fault (Berryman et al., 2012; Thakur and Huang, 2021). It is therefore challenging from surface morphology alone to determine how many earthquakes are preserved in the landscape. However, most large strike-slip ruptures globally have < 10 m slip (Wesnousky, 2008), so we can infer that the Dempster fault segment likely records at least ~7 major earthquakes. The 700-1500 m dextral offsets on the Flat Creek segment potentially record >100 individual earthquakes throughout the entire Quaternary Period.

2.6.2 The Potential for Large Earthquakes

Using empirical scaling relations between maximum surface slip, surface rupture length, and moment magnitude (Wesnousky, 2008) we find that the Tintina fault is capable of large earthquakes despite its low slip rate. The total surface rupture length of ~130 km corresponds to a moment magnitude of 7.4 (Figure 2.5), but we view both the rupture length and associated magnitude as underestimates given the inferred long open interval and consequent likelihood that parts of the scarp have been substantially eroded, particularly in sloped terrain. Taking 12 kyr as a minimum recurrence interval, at a minimum slip rate of 0.51 mm/yr the fault will have accumulated at least 6.1 m of slip deficit since its last rupture (Figure 2.5), a value within the range of modern strike-slip surface ruptures (Wesnousky, 2008). Coseismic slip of 6.1 m empirically predicts a rupture length of 181 km and moment magnitude of 7.5 (Figure 2.5). The highly linear Tintina fault trace is likely conducive to long surface rupture lengths, with minimal steps and bends to arrest rupture (Wesnousky, 2006). Critically, our estimate of M_w7.5 is a minimum, as the coseismic slip and corresponding rupture length could be larger (and the recurrence interval longer). The resemblance of the Tintina scarp morphology – particularly on the Flat Creek segment – to large push-up structures along major faults in Central Asia that have hosted M_w>7.8 ruptures (Fu et al., 2003; Lin et al., 2004; Rizza et al., 2015; Choi et al., 2018) further supports the notion that the Tintina fault may be capable of similarly large earthquakes.

The fate of a potential 181+ km surface rupture beyond the 130 km-long scarp currently preserved is not known, but we note that Reid-age terraces directly along strike to the southeast near Stewart Crossing (Figure 2.2) are not visibly faulted. The remainder of the surface rupture may instead extend northwestward into Alaska where the more mountainous terrain may be less conducive to scarp preservation. A rupture extending to the northwest raises the possibility of a link with the active Preacher-Medicine Lake segment of the Tintina fault, near the hamlet of Central, Alaska (Figure 2.1. and S2.10), ~210 km northwest of the termination of scarps we map

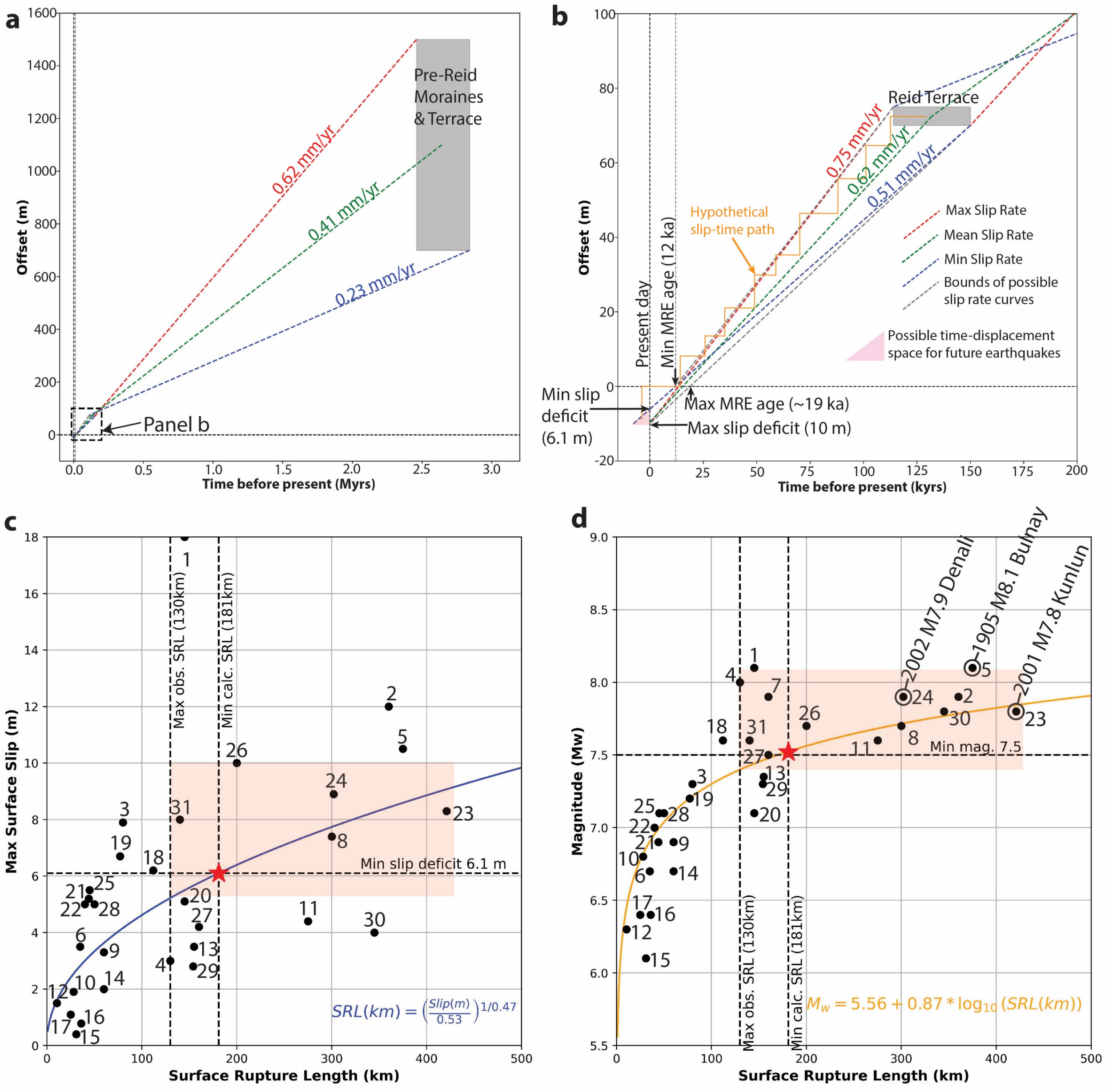

Figure 2.5. Slip rate and magnitude calculations. (a,b) Range of closed-interval slip rates calculated from offsets to Pre-Reid-age moraines and terraces, Reid-age terrace riser, and the inferred most recent event (MRE) >12 ka (see supplemental methods). Grey boxes indicate range of uncertainty in offset amount and feature age. Slip deficits are projected into the open interval to define range of possible time-displacement positions for future earthquakes. (c) Empirical power-law scaling relation between maximum surface slip and surface rupture length (Wesnousky, 2008) including datapoints from historical, instrumentally recorded strike-slip earthquakes (indexed in Table S2.2). A minimum slip deficit of 6.1 m corresponds to a surface rupture length of 181 km (red star). Orange rectangle indicates full range of plausible values. (d) Empirical

scaling relation between surface rupture length and moment magnitude (Wesnousky, 2008). A 181 km surface rupture length corresponds to a minimum moment magnitude of 7.5 (red star).

in the Klondike region. It exhibits a ~5-m-high north-side-up scarp that offsets a 18-12 ka surface of loess (Haeussler et al., 2024), though it lacks any clear lateral offsets.

2.6.3 Seismic Hazard Implications

Our results have significant implications for seismic hazard in the Yukon Territory and neighbouring Alaska. If ≥12 kyr have elapsed since the last major earthquake, the fault may be at an advanced stage of strain accumulation. Notably, viscoelastic models show that geodetically-derived strain rates will appear low across faults near the end of long recurrence intervals, with most of the strain having accumulated early in the seismic cycle (Wang et al., 2021). This modelling result is consistent with the fact that strain accumulation on the Tintina fault is currently unresolvable with GNSS (Leonard et al., 2007; Elliott and Freymueller, 2020). An earthquake of $M_w \geq 7.5$ would cause severe shaking in Dawson City (population ~1600), located < 20 km from the mapped fault trace (Figure 2.2), and could also cause damage to important highways and nearby mines. Moreover, it has been shown that for equivalent rupture lengths, low-slip-rate faults tend to host larger earthquakes with greater stress drops than those on faster slipping faults (Anderson et al., 2017). Compounding the shaking hazard, the Klondike region is prone to landslides, which could be seismically triggered. In particular, the Moosehide Slide immediately north of Dawson City, and the newly-discovered Sunnydale landslide directly across the Yukon River, both show ongoing signs of instability (Brideau et al., 2007; Bodtker et al., 2023). More work is needed to determine the impact of revising seismic hazard models to include the Tintina fault as a discrete fault source; due to its low slip rate and long recurrence time, changes to computed hazard values may only be marginal. However, the fact that the fault is late in an open interval highlights the importance of time-dependent seismic hazard models (Petersen et al., 2007) and the need for more paleoseismic data.

Owing to its position outside the bounds of Late Pleistocene glaciation, the segments of the Tintina fault examined herein likely represent the longest tectono-geomorphic record of active faulting in Canada, and among the longest globally. Had this area been glaciated in the Late

Pleistocene, no record of surface-rupture would be preserved, and instrumental networks would provide little indication of the potential for large earthquakes. Our results therefore suggest that the paucity of fault surface ruptures observed in other low strain rate regions of the Canadian Cordillera is due – at least in part – to a preservation problem arising from extensive Late Pleistocene glaciation (Figure 2.1.) rather than a true absence of paleoseismic activity. These findings should motivate future paleoseismic studies of potentially active faults, particularly pre-existing, mature structures that may localize strain in slowly-deforming regions.

2.7 Acknowledgements

This work occurred on the traditional territory of the Tr'ondëk Hwëch'in and Na-Cho Nyäk Dun First Nations. We thank Jordan Ross and Hussain Malik of the Tr'ondëk Hwech'in Government for their support of our fieldwork. Maurice Colpron, Panya Lipovsky, Kristen Kennedy and Derek Cronmiller of the Yukon Geological Survey provided helpful discussions and logistical support. Paul Sanborn is thanked for providing XRD data for soil profiles in the Yukon. Braeden Clark provided field assistance. T.F. was supported by an NSERC CGS-D scholarship, a Dr. Margaret Perkins Hess Graduate Fellowship, and a Geoffrey Bradshaw Memorial Scholarship. Additional research funding came from NSERC Discovery Grants awarded to E.N. and J.C., a Canada Research Chair to E.N., and a Polar Knowledge Canada Northern Scientific Training Program grant awarded to T.F. Our drone lidar system was developed with support from the Canada Foundation for Innovation John Evans Leadership Fund (CFI JELF) and BC Knowledge Development Fund (BCKDF). Nadine Reitman and an anonymous reviewer provided helpful peer reviews of this manuscript, and Andrew Schaeffer provided a GSC internal review.

2.8 Open Research

ArcticDEM version 4 (Porter et al., 2023) is publicly available online (https://www.pgc.umn.edu/data/arcticdem/). Our drone lidar data are hosted by Open Topography (https://doi.org/10.5069/G9MG7MR9). The Government of Yukon lidar collection is available at https://maps.mcelhanney.com/Vertisee/YukonGovLidar/. Our fault scarp traces are provided in ESRI shapefile format in the supplement.

2.9 Supporting Information

This supplement includes additional text on our methodological approach, figures that support our conclusions, and tabulated data presented in maps and plots in the main text. Text S1 (Section 2.9.1) provides details on the high-resolution topographic data we used, the sources and interpretation of our geochronological data, our approach to surficial mapping and fault scarp characterization, and our slip rate and magnitude calculations. Figure S2.6 shows the output of LaDiCaoz lateral offset calculations. Figure S2.7 is a detailed map of a lateral offset measurement site not shown in the main text. Figure S2.9 is a graph of along-strike vertical separation. Figure S2.10 is a surficial map of the Dawson fault segment discussed in the text. Figure S2.11 is a map of the Preacher-Medicine Lake fault scarp in Alaska, which is mentioned in the text. Figure S2.12 is a series of soil profiles for geomorphic surfaces of different ages in the Yukon. Table S2.1 summarizes the geochronological data cited in the text. Table S2.2 is an index to the earthquake rupture length, maximum surface slip, and moment magnitude data presented in Figure 2.5 in the main text. Additionally, we provide a description of Dataset S1, a Shapefile of our mapped Quaternary scarps along the Tintina fault. All works cited here in the supplement are included in the reference section of the main text.

2.9.1 Text S1: Data and Methodological Details

2.9.1.1 High Resolution Topographic Data

The primary topographic dataset used in this paper is the ArcticDEM version 4 (Porter, 2023), which has a spatial resolution of 2 m and is constructed from stereoscopic image pairs from the WorldView and GeoEye satellites. Though not truly “bare earth” it performs well in high latitudes where vegetation is relatively sparse. Thus, in most cases it provides sufficient resolution to map features such as fault scarps with < 10 m heights and widths, though care must be taken where foliage is dense as the canopy can create artificial bumps in the Digital Elevation Model (DEM). We reviewed ArcticDEM data covering the entire length of the Tintina fault in the Yukon Territory and only found evidence of Quaternary faulting on the 130 km-long section discussed in this paper.

To augment the regional ArcticDEM coverage, we collected several lidar surveys using a novel drone platform (Salomon et al., 2024). This produces bare-earth Digital Terrain Models (DTMs) with 0.3 m spatial resolution, enabling high-confidence interpretation of subtle tectonic landforms and fault offsets. The drone lidar datasets used in this study are available for download from OpenTopography (Finley et al., 2024). We also used conventional airborne lidar (1 m resolution) collected on behalf of the Yukon Government in 2013 along the Dempster Highway corridor (Government of Yukon Lidar collection, 2013).

2.9.1.2 Geochronological Constraints

To constrain the ages of surficial units and the timing of faulting, we adopt the numerous existing geochronological constraints from the literature that have guided past surficial mapping of the area (Figure 2.2 and Table S2.1). The ages of the various stratigraphic units are anchored by direct dating methods (optically stimulated luminescence (OSL), terrestrial cosmogenic nuclides (TCN), radiocarbon) at select locations, as well as chronostratigraphic constraints (tephrochronology, and magnetostratigraphy). During the McConnell glaciation, several isolated ice sheets developed in the Ogilvie Mountains north of our study area. Deglaciation occurred between 12 and 14 ka, based on radiocarbon and cosmogenic nuclide exposure ages (Beierle, 2002; Stroeven et al., 2010; Dalton et al., 2023). The extent of the penultimate Reid Glaciation is relatively well constrained on the basis of glacial landforms recognizable in airphotos and topographic maps (Duk-Rodkin, 1999). The timing of the Reid glaciation is best constrained by OSL samples above and below Reid till at the 'Ash Bend' site on the Stewart River (Figure 2.2), which give ages of 132 ± 18 ka and 158 ± 18 ka, respectively, indicating a MIS 6 age (Demuro et al., 2012). The Reid deglacial age is corroborated by a bed of the 140 ± 10 ka Old Crow tephra – identified by major element chemistry – that occurs near the top of Reid deposits along the Pelly River ~100 km southeast of our study area (Ward et al., 2008). The extent of the antepenultimate Pre-Reid glaciation is inferred from scattered outcrops of glacial drift known as the Klondike Gravel, which occurs in elevated terraces throughout the Klondike region. A large outcrop of Klondike Gravel, known as the Flat Creek Beds, occupies the center of the Tintina Trench southeast of Dawson City (Figure 2.2). The Klondike Gravel at the 'Flat Creek' stratigraphic site (Figure 2.2) is normally-magnetized and therefore correlated with the late Pliocene Gauss chron (>2.58Ma; Froese et al., 2000). A terrestrial cosmogenic nuclide burial age of 2.64 +0.20/-0.18 Ma for the Klondike Gravel at the 'Australia Hill' site (Figure 2.2) corroborates the magnetostratigraphy (Hidy et al., 2013).

In addition to the direct and stratigraphic age constraints, McConnell, Reid, and Pre-Reid surfaces can be regionally correlated based on soil development and weathering. Characteristic soil weathering profiles, known as the Stewart, Diversion Creek, and Wounded Moose paleosols, are observed on McConnell, Reid, and Pre-Reid deposits, respectively (Figure S2.12; Smith et al., 1986; Tarnocai et al., 1985). The Stewart soil (McConnell glaciation) is a shallow, weakly developed brunisol with minor clay content typical of Holocene soils in the Yukon. The Diversion Creek paleosol (Reid glaciation) exhibits brunisols and weakly developed luvisols indicative of moderately temperate conditions (similar to modern soils of southern boreal forest regions) in the subsequent interglacial. Diversion Creek soils in central Yukon indicate weathering through the last interglaciation (MIS 5, *sensu lato*) and distinguish these deposits from the younger MIS 4 and MIS 2 drift surfaces, and the older Wounded Moose paleosol surfaces. The Wounded Moose paleosol (Pre-Reid glaciation) is the most strongly and deeply weathered, with B-horizons to 2 m depth exhibiting a well-developed luvisol with a distinctive reddish-brown colour and high clay content consistent with a warm and moist climate through the Early Pleistocene (Smith et al., 1986). All Wounded Moose paleosols described and sampled in central Yukon are reversely magnetized indicating an age of >780 kyrs (Duk-Rodkin et al., 2001). Each of the soil profiles exhibits a characteristic clay weathering curve, as measured by X-Ray Diffraction (XRD) analysis of soil samples (Figure S2.12; Paul Sanborn pers. comm.), which adds confidence in stratigraphic unit assignment distant from sites with direct or stratigraphic age control. Geochronological sample site locations key to constraining modern activity on the Tintina fault are shown in Figure 2.2.

2.9.1.3 Surficial Mapping

Our surficial mapping was founded upon existing surficial geology maps produced by federal and territorial geological surveys in 1982 (Thomas and Rampton, 1982), 1996 (Duk-Rodkin, 1996), 2005 (Froese, 2005b, 2005a), and 2014 (McKenna and Lipovsky, 2014). These maps are at scales between 1:25k and 1:250k, and each uses a slightly different categorization scheme for surficial units. However, the depiction of McConnell, Reid and Pre-Reid-aged terrace levels is consistent between them. We do not adapt existing maps for the Flat Creek and Dawson fault segments. The Flat Creek segment is entirely underlain by the Pre-Reid “Flat Creek Beds” and required no refinement for the purposes of our analyses (Froese, 2005b, 2005a). The Dawson fault segment is largely inaccessible, limiting our ability to improve significantly upon existing maps (Duk-Rodkin, 1996; McKenna and Lipovsky, 2014). For the Dempster segment, which offered the best opportunity to improve constraint on fault kinematics and timing, we augmented and adapted the existing maps with our own field observations, satellite and drone imagery, and the new high resolution topographic data (lidar, ArcticDEM), which were not available to previous surficial mappers. Our most significant changes were slight modifications to the positions of unit boundaries (i.e., terraces), which are more clearly resolved in the new DEMs. It is worth noting that a short fault scarp was depicted near the Dempster Highway on many of the existing surficial maps (Thomas and Rampton, 1982; Duk-Rodkin, 1996; Froese, 2005a), but received little attention or detailed study.

We distinguish 6 different lithological units and features on the basis of their geomorphology (form, expression, and topographic relief) evident in lidar and ArcticDEM data, and stratigraphy and sedimentology observed in outcrop. Unit 1 (Cv) is bedrock draped by a thin veneer of colluvium and/or till. This unit is extensive in the hills to the northwest of the Dempster Highway. Unit 2 (Gt-PR) is a glaciofluvial outwash terrace inferred to be related to Pre-Reid glaciation. This age assignment is based on the high topographic level of the terrace (above the Reid terraces), and similar morphology to the well-studied Flat Creek Beds 10 km to the southeast across the Klondike River. Soil profile site #54 (Smith et al., 1986) supports this age assignment. Unit 3 (Tb-R) is a till blanket inferred to have been deposited sub-glacially by a lobe of Reid-aged ice incised into Gt-PR. A series of arcuate terminal and recessional moraines are observed within this unit, as well as deeply incised outwash channels. Soil profile site #59 (Smith et al., 1986) supports this Reid age assignment. Unit 4 (Gt-R) comprises mid-level glaciofluvial terraces mapped as Reid in age on the basis of soil profile site #63. Regionally, terraces of similar form and elevation appear to emanate from other mapped lobes of Reid-age ice/moraine position (Figure 2.2). Unit 5 (Gt-M) is a series of lower-level glaciofluvial terraces which are inset 10-20 m below the level of the Reid-age terraces and can be traced northward for 40-50 km along the flanks of the modern floodplain of the North Klondike River to the terminus of McConnell-age ice caps in the Ogilvie Mountains (Figure 2.2). Unit 6 (Fp) is the modern floodplain of the Klondike and North Klondike Rivers.

2.9.1.4 Fault Scarp Morphology

We measure dip-slip separation across scarp features using the Monte Carlo Slip Statistics Toolkit (MCSST) (Wolfe et al., 2020). This tool samples uncertainty distributions for the fault dip, fault position on the scarp, and topographic slopes of the hanging wall and foot wall to account for overall uncertainty in the measurement of vertical separation and/or net slip. The uncertainty distributions for fault dip and fault position are user-defined, and in our case we assign trapezoidal distributions, wherein the wide base of the trapezoid defines the entire range of possible values, and the narrow top of the trapezoid represents the range of most likely values. We allow for a steeply-dipping fault ranging between 75° NE and 75° SW, with the highest probability between 85° NE and 85° SW. We allow for a fault-scarp intersection over the entire width of the scarp, but assign the highest probability to a fault-scarp intersection between 1/3 and 2/3 of the scarp width. The along-strike distribution of vertical separation values (and uncertainties) are shown in Figure S2.9.

We measure strike-slip separation using version 2 of the Lateral Displacement Calculator (LaDiCaoz) tool (Zielke and Arrowsmith, 2012; Haddon et al., 2016), which enables back-slipping of fault-parallel profiles across drainages and other piercing points. LaDiCaoz performs a grid search to find the best fitting offset. Using the result of the grid search as a starting point we then visually assessed uncertainties by producing a range of backslips. Our minimum estimates represent a threshold at which the fault still appears to have a small discernible amount of right-lateral offset, and our maximum estimates represent a threshold where the fault begins to have a small discernible amount of left-lateral offset. Backslipping results are shown in Figure S2.6. None of our scarp sites appear to have significant oblique slip, the slopes they occur on are low-angle and oriented close to fault-normal, and the fault dips are inferred to be steep, so we deem a 2D approach to offset measurement appropriate; more advanced 3D methods (Mackenzie and Elliott, 2017) are not necessary and would be difficult to implement with such a low density of offset landforms.

2.9.1.5 Slip Rate Calculations

Our slip rate calculations are based on dextral offsets of 700-1500 m to Pre-Reid (2.6 Ma) features, and of 70-75 m to Reid (132 ka) geomorphic features. Because each of these intervals contain >>5 earthquakes, we consider the resulting slip rate measurements robust as any temporal variability in slip will effectively be averaged out (Styron, 2019). Moreover, although slip rates can be biased negatively or positively depending on the timing of past ruptures relative to dated landforms, this effect is minimized when slip rates are calculated over numerous earthquake cycles (Styron, 2019). We calculate closed-interval slip rates for the period between the Pre-Reid and Reid features, as well as between the Reid features and the most recent event (MRE). The MRE must have occurred at 12 ka at the latest and we calculate a minimum slip rate (blue line, Figure 2.5b) based on this constraint. However, we do not have a maximum MRE age from which to calculate a maximum slip rate. We therefore estimate maximum slip rate based on a plausible upper limit of slip deficit of 10 m accrued in the present, and the youngest possible age and largest possible offset of the Reid terrace (red line, Figure 2.5b). The 10 m slip value is based upon the maximum coseismic slip observed in the largest intraplate strike-slip fault events such as the 2002 M_w7.8 Denali and the 1905 M_w8.1 Bulnay earthquakes. Similarly, using a 10 m maximum slip deficit and the oldest possible age and smallest possible offset of the Reid terrace, we calculate a lower bound of possible slip rate paths (not a minimum slip rate), corresponding to a maximum MRE age of 19 ka (grey line, Figure 2.5b). Our mean slip rate (green line, Figure 2.5b) is based upon the mean age and offset of the Reid age terrace, and an MRE age of 15.5 ka (halfway between our minimum MRE age of 12 ka and maximum MRE age of 19 ka).

We acknowledge that there are two features with 200 and 130 m of apparent dextral offset, shown in Figures 4b and S2, respectively. These features could be interpreted as indicators of a higher slip rate, especially considering that the upstream side of the 72.5m offset of the Reid-age terrace riser may have been trimmed and would thus only represent a minimum slip rate. However, there are several reasons we do not place high confidence on these larger offset measurements.

For the first site with 200 m offset in Fig 4b, our main reason for rejecting it as a reliable constraint on the amount of slip is that we do not know for certain what this feature is, nor how old it may be. We visited this location in the field and determined that the mound is not bedrock, but is made up of unconsolidated glaciofluvial gravel. Because it is elevated well above the Reid terrace level, it must either be a push-up mound similar to those observed on the Flat Creek segment (Figure 3), and/or perhaps a remnant of an older, higher Pre-Reid terrace. If it is indeed a push-up mound, the 200 m offset would still only be a minimum slip measurement, as the mound would have had to be built up through multiple seismic cycles prior to being offset. Further, if this feature is of Reid age (132 ka), the minimum measurement of 200 m offset would imply a slip rate of at least ~1.5 mm/yr. At this rate, the fault will have accrued a slip deficit of at least 18 meters since 12 ka, which is more than double the maximum surface slip of most large strike-slip earthquakes globally. Taken together, the evidence points to this feature being older than the surrounding Reid terrace surface; however, lacking strong control on its age we do not consider it a reliable slip rate constraint.

For the site with 130 m offset in Fig S2, our main reason for rejecting it is as a reliable constraint is that the apparent right-lateral offset to the terrace riser is more gently curved and could potentially be explained as a bend in the river. Additionally, the terrace riser intersects with the fault at an oblique angle, making accurate measurement of offset subject to higher error. In contrast, the 72.5 m terrace offset is sharp and at a right angle to the fault scarp. Finally, we do not have high resolution lidar data at this site (only ArcticDEM), and were unable to visit this site in person to verify observations.

For these reasons, we prefer to retain the more conservative estimate of minimum slip rate from the 72.5 m offset terrace riser, which is also more internally consistent with our observation that the fault has not ruptured since at least 12 ka and slip deficit has been accumulating since then. However, these two sites – though unreliable for slip rate – are still useful observations that corroborate our interpretation of right-lateral kinematics, in an environment where lateral offsets are not well preserved.

2.9.1.6 Magnitude Estimation

We use empirical fault scaling relations for strike-slip earthquakes (Wesnousky, 2008) to estimate paleo-earthquake magnitude. These relations are derived from a dataset of 21 historical, large, continental surface-rupturing earthquakes for which there are instrumental moment magnitudes along with maps of surface rupture length (SRL) and coseismic slip along strike. We supplement this dataset with 10 additional earthquakes that were not included in the original scaling relation (Table S2.2). We do not recalculate the scaling equation, and the additional data are provided only as additional points of comparison. The logarithmic relation between moment magnitude and fault SRL for strike-slip faults is given by:

$$(1)\ M_w = A + B\ * \log(SRL\ (km))$$

where A and B are constants 5.56 and 0.87 respectively. We use 130 km as our minimum SRL, as this is the total length of our mapped lineaments that deform Reid and Pre-Reid surfaces. We suspect the entire surface rupture is not necessarily preserved in the landscape, and we use the power law relation between SRL and maximum surface slip on strike slip faults given by:

$$(2)\ SRL\ (km) = \left(\frac{slip(m)}{C}\right)^{\frac{1}{D}}$$

Where C and D are constants 0.53 and 0.47 respectively. We note that there are also linear and logarithmic scaling curves for surface rupture length and slip, but we opt for the power law relation as it best fits the empirical data (Wesnousky, 2008). Based on our minimum slip rate (see above), we estimate a minimum slip deficit of 6.1 m since the last rupture, which gives a higher surface rupture length (181 km) than the 130 km mapped. We suggest that a scaling relation using maximum surface slip is more appropriate than using the average surface slip, as for our estimated single event slip (6.1 m), the latter predicts an SRL of 930 km, more than double the maximum strike-slip SRL ever observed globally (Fu et al., 2003). The 181 km length derived from equation 2 can be used to calculate an upper estimate of magnitude (M_w7.5) using equation 1. Both the slip deficit of 6.1 m and total surface rupture length of 181 km are minima, and the magnitude could plausibly be higher.

2.9.2 Figures S2.6 to S2.11

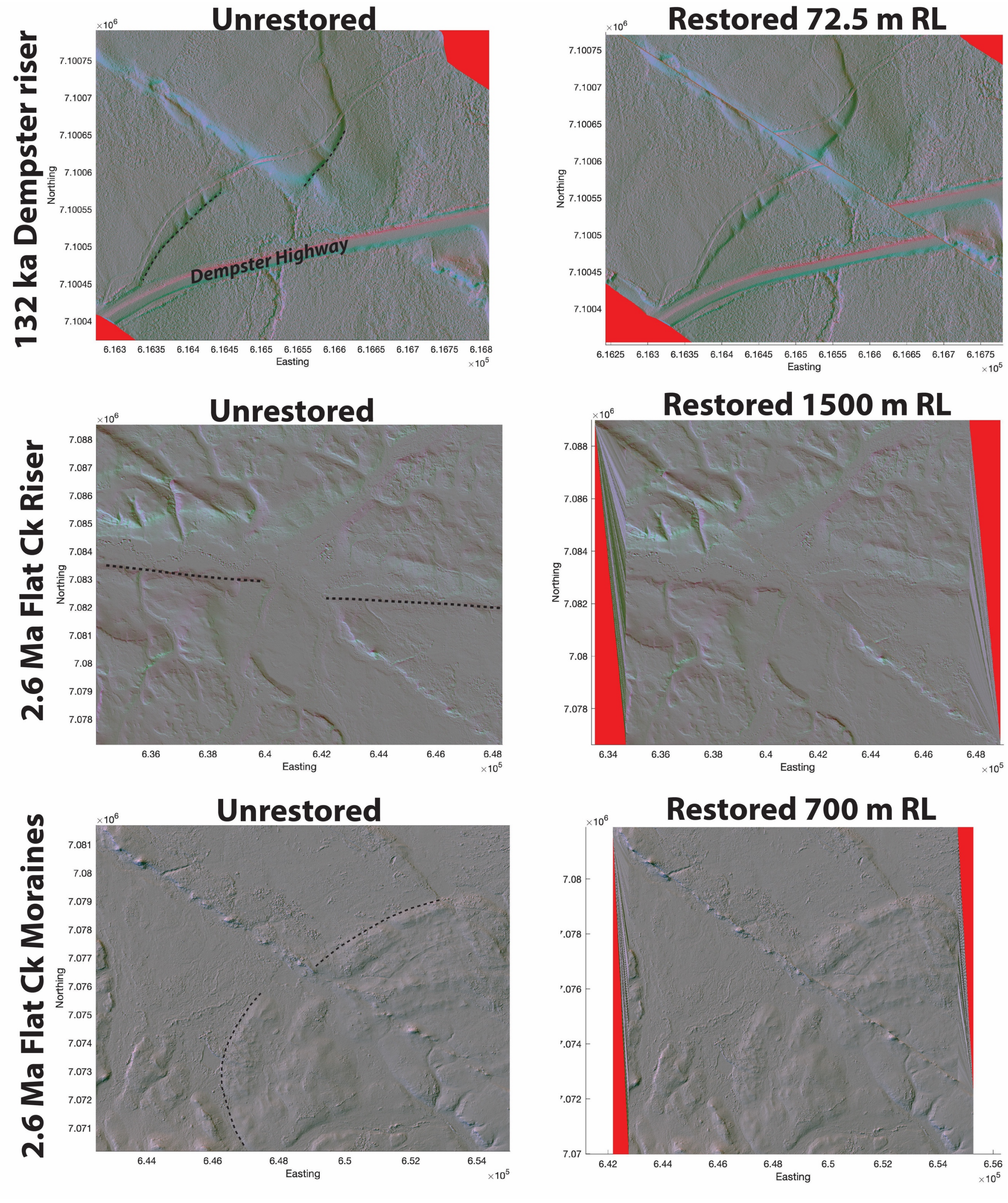

Figure S2.6. LaDiCaoz backslipping results from three key sites. Left column shows unrestored modern landscape with dashed lines delineating selected piercing points. Right column shows optimal restoration determined with LaDiCaoz.

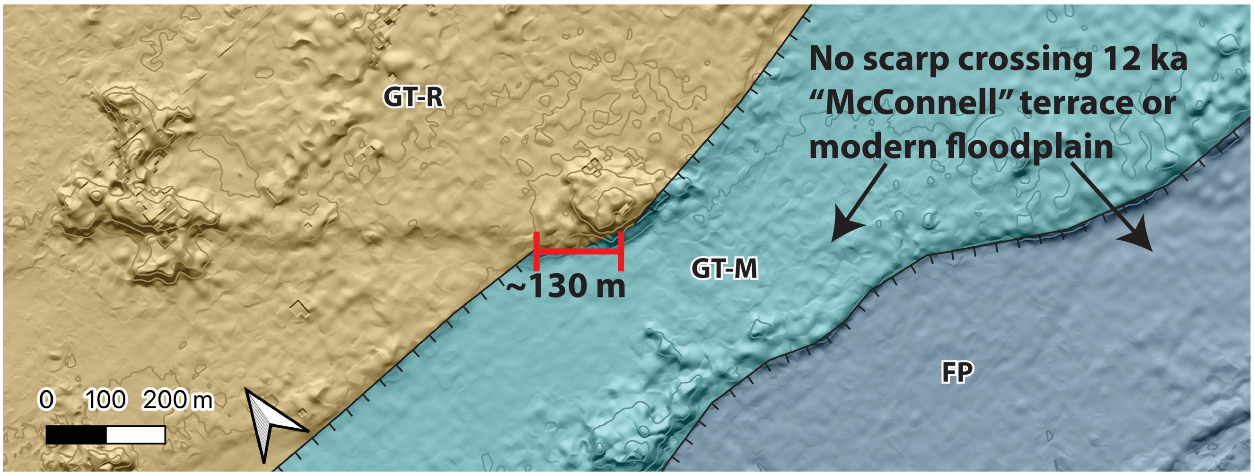

Figure S2.7. Further evidence of dextral offset and lack of Holocene rupture on Dempster fault segment. Surficial map of Klondike River terrace 6 km southeast of Dempster highway showing ~130 m dextral offset to GT-R riser, but no deformation of GT-M and FP units. See Figure 2.4 in main text for legend and location. Riser may have been reworked and is therefore an unreliable lateral offset measurement. Basemap is ArcticDEM.

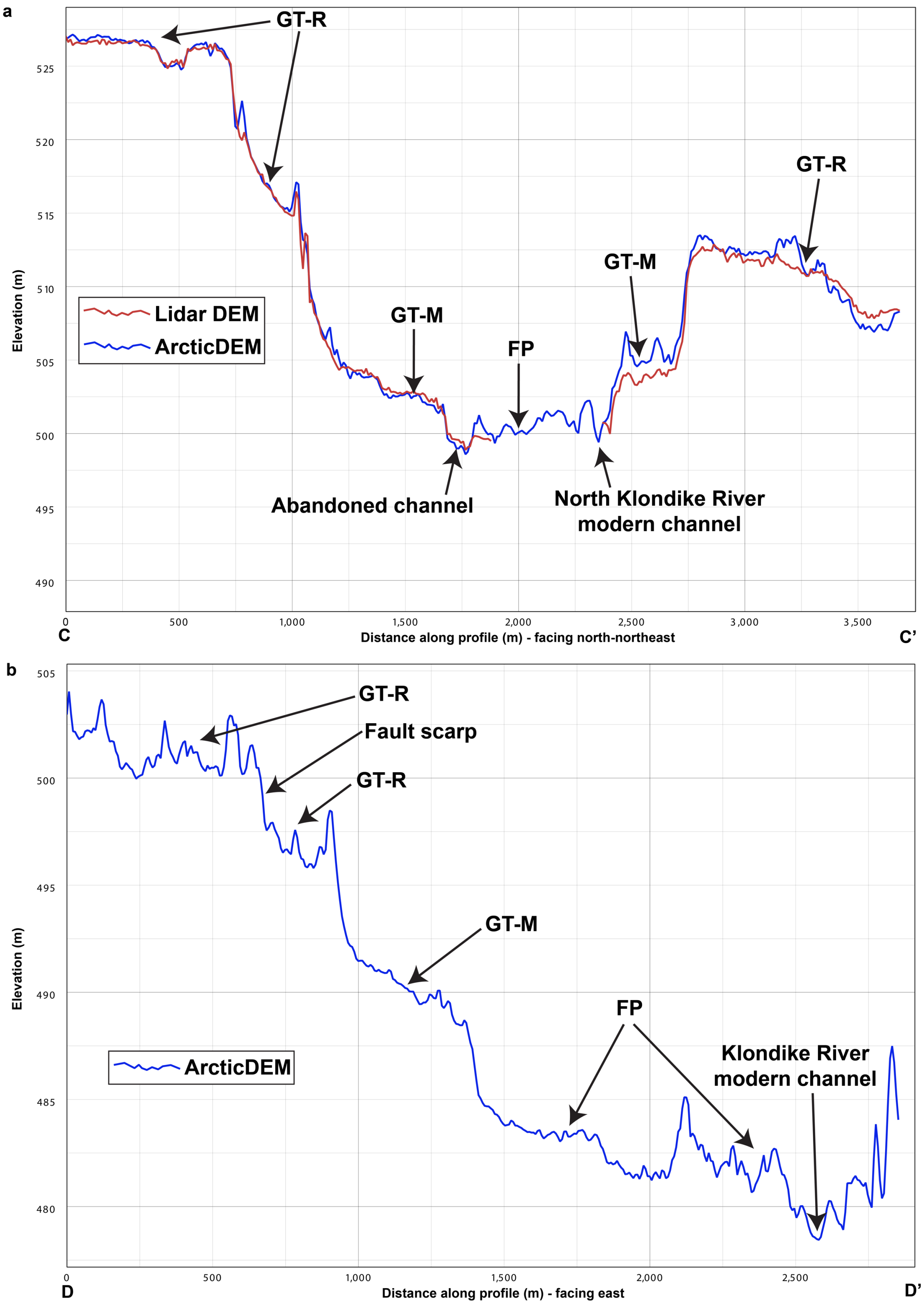

Figure S2.8. Topographic profiles extracted from lidar and ArcticDEM data across (a) the North Klondike River and (b) the Klondike River. See Figure 2.4a for profile locations.

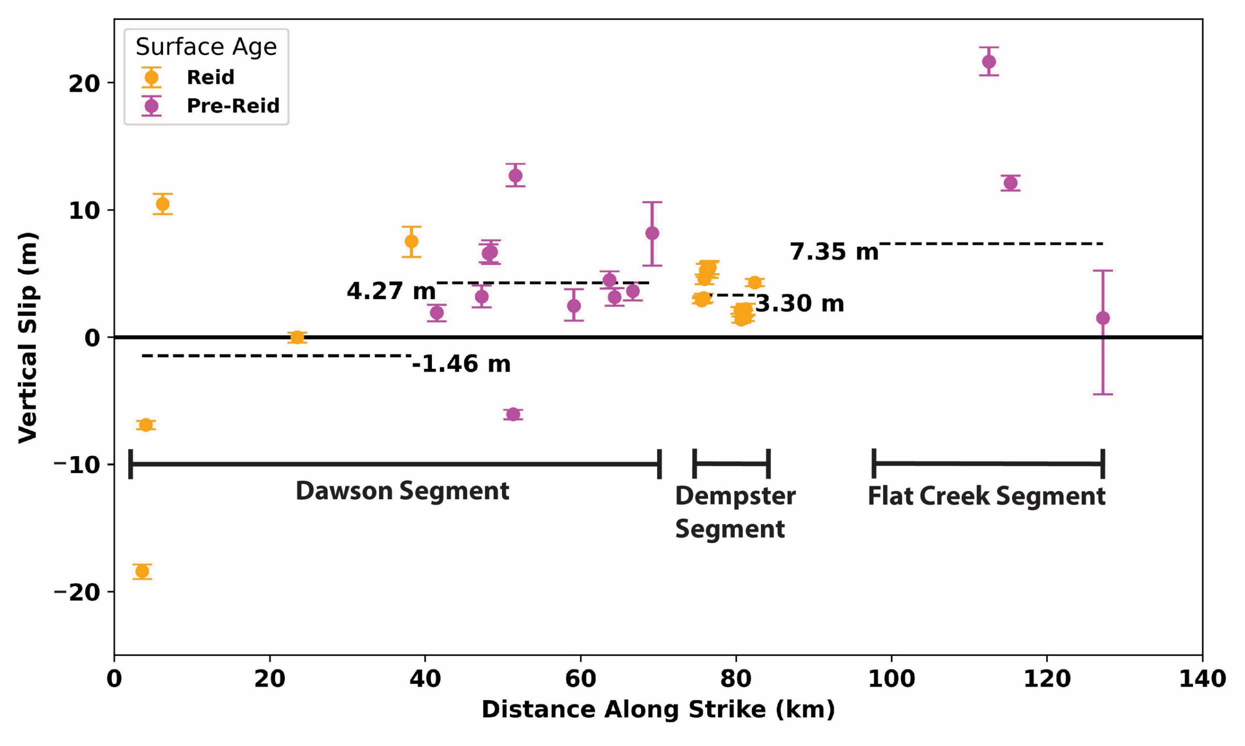

Figure S2.9. Vertical slip distribution along strike as measured with MCSST. Black dashed lines indicate average vertical slip for surfaces of Reid and Pre-Reid ages within each of the three main fault segments.

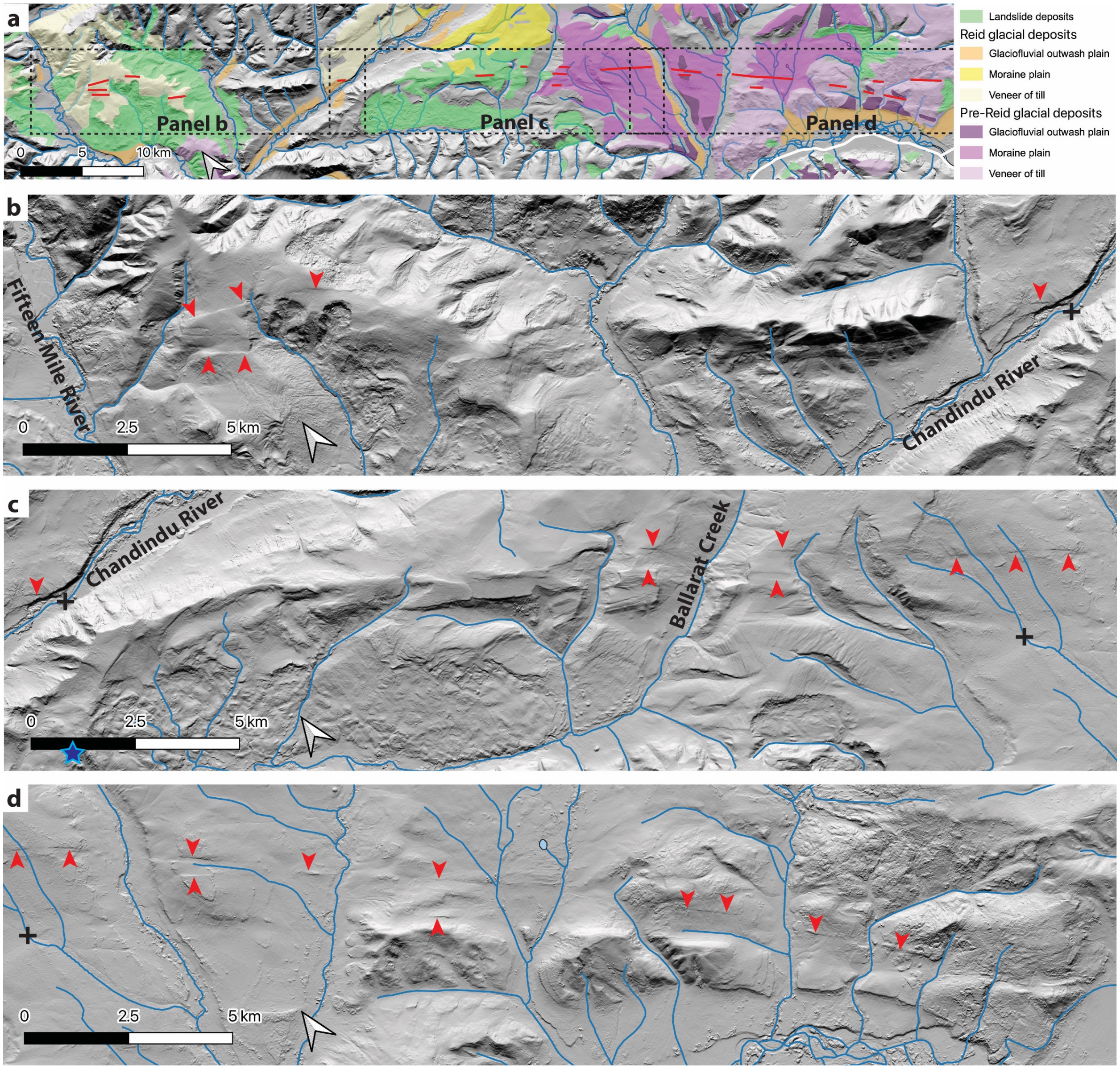

Figure S2.10. The Dawson fault segment. (a) Surficial map of Reid and Pre-Reid deposits along the Dawson fault segment (Duk-Rodkin, 1996). See Figure 2.2 in text for figure extent. (b, c, & d) detailed views with red arrows highlighting discontinuous scarps. Black crosses are tie points between panels.

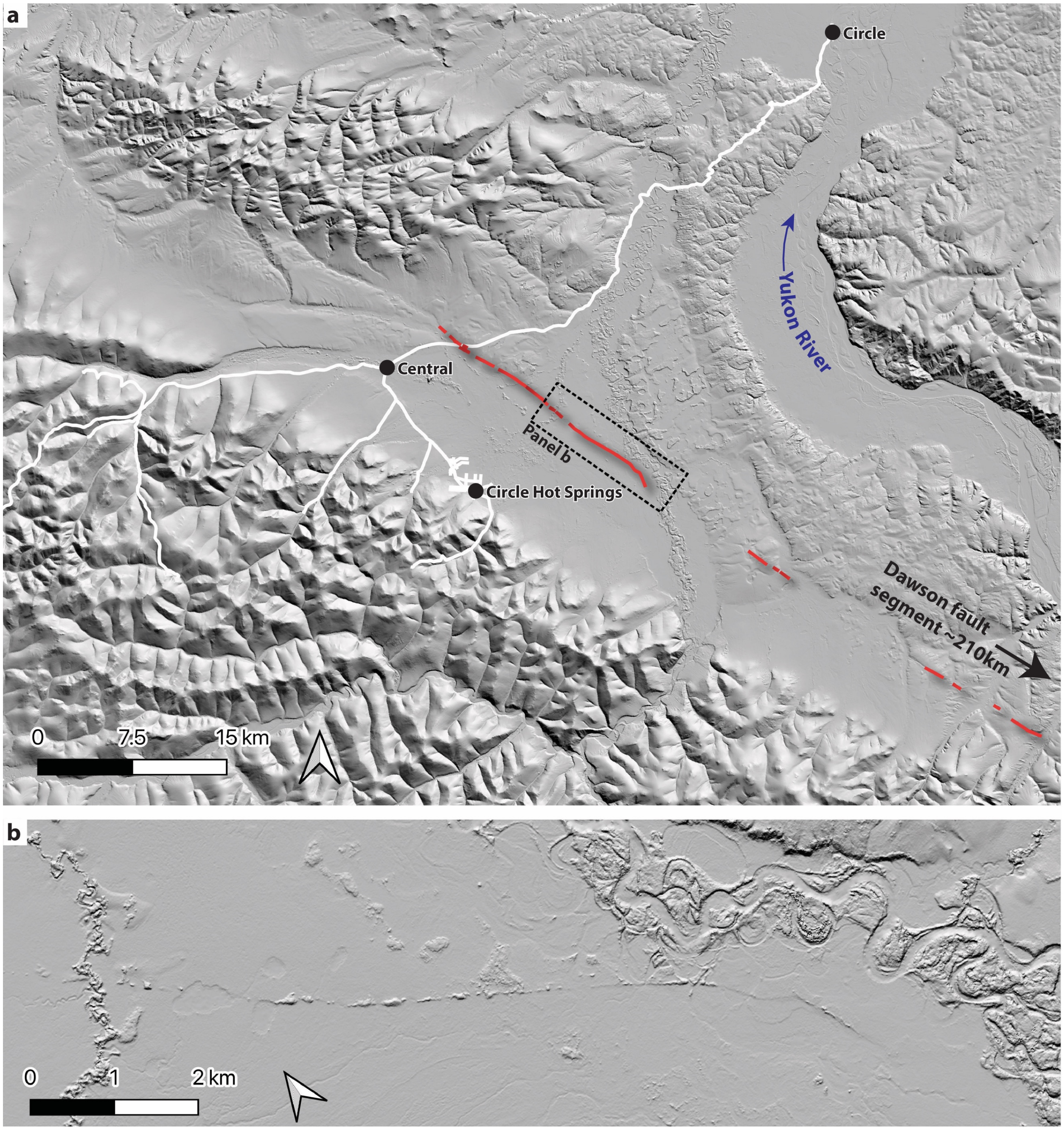

Figure S2.11. Preacher-Medicine Lake fault scarp near Central, AK. (a) Regional view of the Preacher-Medicine Lake fault scarp near Central, AK, ~210 km northwest of termination of Dawson fault segment. (b) detailed view of a section of the fault scarp, vertically offsetting a flat-lying plain.

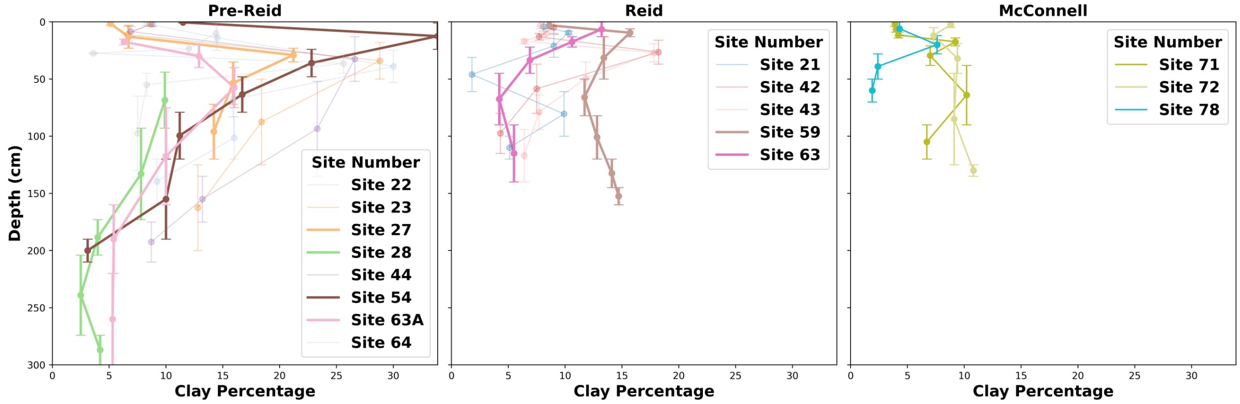

Figure S2.12. Characteristic soil profiles of the Pre-Reid, Reid, and McConnell glacial deposits (Smith et al., 1986). Key sites that support our surficial unit assignments (27, 28, 54, 59, 63, 63A) are bolded. Other sites in the region are provided in the background for comparison.

2.9.3 Tables S2.1 and S2.2, and Dataset S1.

Table S2.1. Direct and chronostratigraphic age constraints for McConnell (blue), Reid (yellow), and Pre-Reid (pink) glacial deposits in the Klondike region.

Site	Data Type	Description	Age	Glaciation	Reference
Tombstone Range	Radiocarbon	Basal radiocarbon age from bog	11.12 ± 0.62 ka	McConnell	(Dalton et al., 2023)
Oxbow Lake	Radiocarbon	Basal age from lake core	10.79 ± 0.28 ka	McConnell	(Beierle, 2002; Dalton et al., 2023)
North Fork Pass	Radiocarbon	Twigs at base of core in lake at North Fork terminal moraine	10.5 ± 0.2 ka	McConnell	(Beierle, 2002; Dalton et al., 2023)
North Fork Pass	Terrestrial Cosmogenic Nuclide Exposure Age	Boulders in moraine at North Fork Pass	9.8 ± 1.1 ka 9.5 ± 0.9 ka	McConnell	(Stroeven et al., 2010)
Ash Bend	Optically Stimulated Luminescence	Samples extracted from gravel above and below till inferred to be Reid age	Upper: 132 ± 18 ka; Lower: 158 ± 18 ka	Reid	(Demuro et al., 2012)
Pelly River	Tephrochronology	Tephra layer near top of glacial deposits.	140 ± 10 ka	Reid	(Ward et al., 2008)
Stewart Crossing	Terrestrial Cosmogenic Nuclide Exposure Age	Bedrock exposures immediately north of Stewart Crossing	91.4 ± 8.4 ka 102.0 ± 9.4 ka	Reid	(Stroeven et al., 2010)
Australia Hill	Terrestrial Cosmogenic Nuclide Burial Age	Sample extracted from base of Klondike Gravel	2.64 (+0.20/-0.18) Ma	Pre-Reid	(Hidy et al., 2013)
Flat Creek, Australia Hill	Magnetostratigraphy	Samples extracted from base of Klondike Gravel	>2.58 Ma	Pre-Reid	(Froese et al., 2000)

Table S2.2. Key to earthquake data shown in Figure 2.5.

ID	Year	Earthquake Name	Length (km)	Max Slip (m)	Mw	Reference
1	1855	Wairarapa, NZ	145	18	8.1	(Rodgers and Little, 2006; Manighetti et al., 2020)
2	1857	Fort Tejon, CA, USA	360	12	7.9	(Wesnousky, 2008)
3	1891	Neo-Dani, Japan	80	7.9	7.3	(Wesnousky, 2008)
4	1905	Tsetserleg, Mongolia	130	3	8	(Wesnousky, 2008)
5	1905	Bulnay, Mongolia	375	10.5	8.1	(Choi et al., 2018; Rizza et al., 2015)
6	1930	Kita-Izu, Japan	35	3.5	6.7	(Wesnousky, 2008)
7	1931	Fuyun, Mongolia	160	-	7.9	(Klinger et al., 2011)
8	1939	Erzincan, Turkey	300	7.4	7.7	(Wesnousky, 2008)
9	1940	Imperial, CA, USA	60	3.3	6.9	(Wesnousky, 2008)
10	1942	Erbaa-Niksar, Turkey	28	1.9	6.8	(Wesnousky, 2008)
11	1943	Tosya, Turkey	275	4.4	7.6	(Wesnousky, 2008)
12	1943	Tottori, Japan	10.5	1.5	6.3	(Wesnousky, 2008)
13	1944	Gerede-Bolu, Turkey	155	3.5	7.35	(Wesnousky, 2008)
14	1967	Mudurnu, Turkey	60	2	6.7	(Wesnousky, 2008)
15	1968	Borrego Mtn, CA, USA	31	0.4	6.1	(Wesnousky, 2008)
16	1979	Imperial Valley, CA, USA	36	0.78	6.4	(Wesnousky, 2008)
17	1987	Superstition Hills, CA, USA	25	1.1	6.4	(Wesnousky, 2008)
18	1990	Luzon, Philippines	112	6.2	7.6	(Wesnousky, 2008)
19	1992	Landers, California	77	6.7	7.2	(Wesnousky, 2008)
20	1999	Izmit, Turkey	145	5.1	7.1	(Wesnousky, 2008)
21	1999	Hector Mine, CA, USA	44	5.2	6.9	(Wesnousky, 2008)
22	1999	Duzce, Turkey	40	5	7	(Wesnousky, 2008)
23	2001	Kunlun, China	421	8.3	7.8	(Wesnousky, 2008)
24	2002	Denali, AK	302	8.9	7.9	(Wesnousky, 2008)
25	2010	Darfield, NZ	45	5.5	7.1	(Elliott et al., 2012)
26	2013	Balochistan, Pakistan	200	10	7.7	(Avouac et al., 2014)
27	2018	Palu, Indonesia	160	4.2	7.5	(Jaya et al., 2019)
28	2019	Ridgecrest, CA, USA	50	5	7.1	(DuRoss et al., 2020a)
29	2021	Maduo, Tibet	154	2.8	7.3	(Ren et al., 2022)
30	2023	Kahramanmaras, Turkey	345	4	7.8	(Kozaci et al., 2024)
31	2023	Elbistan, Turkey	140	8	7.6	(Akciz et al., 2024)

Chapter 3: Holocene intraplate faulting in the Southern Rocky Mountain Trench; orogenic collapse modulated by glacial unloading?

3.1 Article Information

Theron Finley[1], Edwin Nissen[1,2], Lucinda Leonard[1], John F. Cassidy[3,1], Veronica Prush[4], Brendan Miller[5]

[1]School of Earth and Ocean Sciences, University of Victoria, BC, Canada

[2]College of Earth, Atmospheric, and Ocean Sciences, Oregon State University, Corvallis, OR, USA

[3]Pacific Geoscience Centre, Geological Survey of Canada, Sidney, BC, Canada

[4]Department of Earth and Environmental Science, New Mexico Institute of Mining and Technology Socorro, NM, USA

[5]British Columbia Ministry of Forests, Prince George, BC, Canada

This article will soon be submitted to the *Journal of Geophysical Research: Solid Earth.* I led the initial systematic review of lidar data covering the Rocky Mountain Trench and identified the potential fault scarp at Columbia Lake. I led two fieldwork trips to acquire drone lidar, conduct surficial mapping, and collect Electrical Resistivity Tomography data. I led data processing and interpretation, wrote the manuscript, and made all the figures. Dr. Edwin Nissen co-supervised this project, provided field funding, and assisted with fieldwork, data interpretation, and manuscript preparation. Dr. Lucinda Leonard led the ERT surveying aspect of fieldwork, and contributed to manuscript preparation. Dr. John Cassidy co-supervised this project, provided funding, and contributed to manuscript preparation. Dr. Veronica Prush contributed to the initial systematic lidar review to identify this fault, and assisted with data interpretation and manuscript preparation. Mr. Brendan Miller provided additional non-public lidar data to include in our review of the Rocky Mountain Trench, and made several contributions to the data interpretation and manuscript preparation.

3.2 Abstract

The Southern Rocky Mountain Trench (SRMT) is a conspicuous valley in the eastern Canadian Cordillera. It lies above a sharp change in lithospheric strength and thickness and is occupied by a normal fault thought to have last been active in the Eocene. However, its geomorphic prominence, the occurrence of diffuse regional seismicity including notable early instrumental earthquakes, and a subtle geodetic strain gradient, have hinted that it is still active, raising the possibility of large, surface-rupturing earthquakes. Using new high resolution topographic data, surficial mapping, scarp morphology analysis, and shallow geophysics, we provide evidence of multiple Holocene surface ruptures on the SRMT near Columbia Lake, British Columbia. A paraglacial fan surface is vertically offset by ~3 m, whereas younger channels on the fan surface are only offset by ~1 m, implying that the fan records cumulative offset from multiple earthquakes. Electrical Resistivity Tomography data confirm that a fault continues to depth beneath the scarp, and a resistivity horizon in the subsurface beneath the scarp is offset by ~10 m. Regional geochronological constraints on paraglacial sedimentation constrain the fault slip rate to have been > 1 mm/yr in the early Holocene, decreasing to < 1 mm/yr in the late Holocene. This temporal variation in slip rate is consistent with fault activity being modulated by glacial isostatic adjustment following the last glacial maximum. However, the underlying cause of tectonism may be gravitational collapse of the Cordillera. We suggest the SRMT represents a northern extension of the Intermountain Seismic Belt of the western US, which has hosted damaging normal fault earthquakes in recent decades.

3.3 Introduction

In the Cordillera of northwestern North America, active deformation and seismicity occurs over an ~800 to 1000 km-wide belt inboard of the plate boundary. As an accretionary orogen, it is comprised of numerous terranes and crustal fragments bounded and crosscut by several major fault zones. How and where the moderate rates of strain across the Cordillera are accommodated on these faults remains unclear. It is not well established whether the pre-existing, mature faults serve to localize the majority of the strain budget in single, rare, large earthquakes, or whether strain is more distributed. Moreover, the driving mechanisms of deformation in the interior of the Cordillera are debated, with possible candidates being: (1) far-field strain transfer from the plate boundaries (Mazzotti and Hyndman, 2002), (2) lateral gradients in gravitational potential energy (Mazzotti et al., 2011; Fraser et al., 2021), (3) basal tractions from mantle flow (Faccenna and Becker, 2010; Becker et al., 2015), or (4) some combination of the three (Humphreys and Coblentz, 2007; Finzel et al., 2014; Schmeelk et al., 2017; Lund Snee and Zoback, 2020; McConeghy et al., 2022; Cao and Liu, 2024). In addition, the effects of Glacial Isostatic Adjustment (GIA) due to the removal of Late Pleistocene ice sheets may also play a significant role in driving regional deformation (Mazzotti et al., 2005; Sella et al., 2007).

The Southern Rocky Mountain Trench (SRMT) is a conspicuous series of broad, deep valleys that extend for ~800 km along the length of the southeastern Canadian Cordillera. Widely thought to be occupied by a normal fault last active during post-orogenic collapse in the Eocene (van der Velden and Cook, 1996), the occurrence of diffuse seismicity along some sections (Mazzotti et al., 2008; Purba et al., 2021), several notable historical earthquakes (Rogers and Ellis, 1979; Rogers et al., 1980, 1990), and a subtle strain gradient measured by Global Navigation Satellite System (GNSS; Mazzotti et al., 2008), suggest that it may still be active. Moreover, the SRMT is situated above a significant vertical boundary in lithospheric thickness and strength (Currie and Yu, 2023). A similar feature is observed beneath the Intermountain Seismic Belt (ISB), which defines the eastern boundary of active deformation in the western United States and which has hosted numerous Quaternary, historical and instrumental surface rupturing earthquakes (Ostenaa et al., 1995; Hofmann et al., 2006; Johnson et al., 2018; DuRoss et al., 2020b; Bello et al., 2022).

Instrumental data have not been sufficient to classify the SRMT as an active structure, and there has, thus far, been minimal paleoseismic work in the Cordillera as a whole. The SRMT is not included as a discrete fault source in Canada’s National Seismic Hazard Model; a large region encompassing the SRMT is treated as an area source based on seismicity rates, as is common for seismic hazard modelling across much of Canada (Kolaj et al., 2023). Determining whether large paleoseismic events have occurred along the SRMT is critical not only for the safety of the >100,000 people who live in communities along it, but also for critical infrastructure (dams, pipelines, highways, and rail corridors) that cross or are adjacent to it. Like much of Canada, however, the paleoseismic record along the SRMT is deprecated by the effects of Late Pleistocene glacial erosion and deposition. Here, we examine newly available high resolution topographic data and provide the first geomorphic evidence of Quaternary surface rupture along the SRMT. Our results provide insight into the tectonic processes driving deformation in the eastern Cordillera, and highlight the hazard of inherited faults in orogenic belts.

3.4 Background

3.4.1 Physiography and Structure of the SRMT

The first recognition of the SRMT as a significant geological and physiographic feature in the southern Cordillera was by Dawson (1885), and the name "Rocky Mountain Trench" was first coined by Daly (1912). Daly (1912) used the term “trench” rather than “valley” because it is occupied by multiple major contemporary river systems – the Fraser, Columbia, and Kootenay – flowing in different directions, rather than a single watershed. Multiple hypotheses on its origin were proposed in the following decades, with the main question being whether the trench is controlled by faulting or whether it is simply a product of glacial and fluvial erosional processes (North and Henderson, 1954, and Crickmay, 1964).

It is now widely accepted that the SRMT is occupied by a major normal fault (the SRMT fault), active predominantly in the Eocene (Clague, 1974; van der Velden and Cook, 1996). In the southernmost Canadian portions of the SRMT, Clague (1974) concluded that the distribution and orientation of the Miocene St. Eugene formation (silts, sands, and gravels of flood plain and fan facies) was related to the formation of a half-graben along a major west-dipping normal fault on the eastern valley wall. Seismic reflection surveys across the SRMT fault between Canal Flats and the Canada-U.S. border confirm this interpretation, indicating up to 12 km of normal displacement locally (van der Velden and Cook, 1996). Offset is thought to decrease to the north, though there is a dearth of literature and mapping pertaining to the SRMT fault between Canal Flats and Golden (Figure 3.1). 100 km north of Golden, Gal and Ghent (1990) proposed 2 km of normal displacement on the SRMT based on restoration of metamorphic isograds across the fault. McDonough and Simony (1988) estimated less than 2 km of normal displacement near the town of Valemount. At this latitude, the kinematics begin to transition to dextral faulting, with various authors allowing for the possibility of ~55-60 km of strike-slip separation (Murphy, 1990; McMechan, 2000; Finley et al., 2022a; Lee et al., 2024). Thermochronological modeling by Fraser et al. (2021) provides evidence of a complex history of variable cooling rates on either

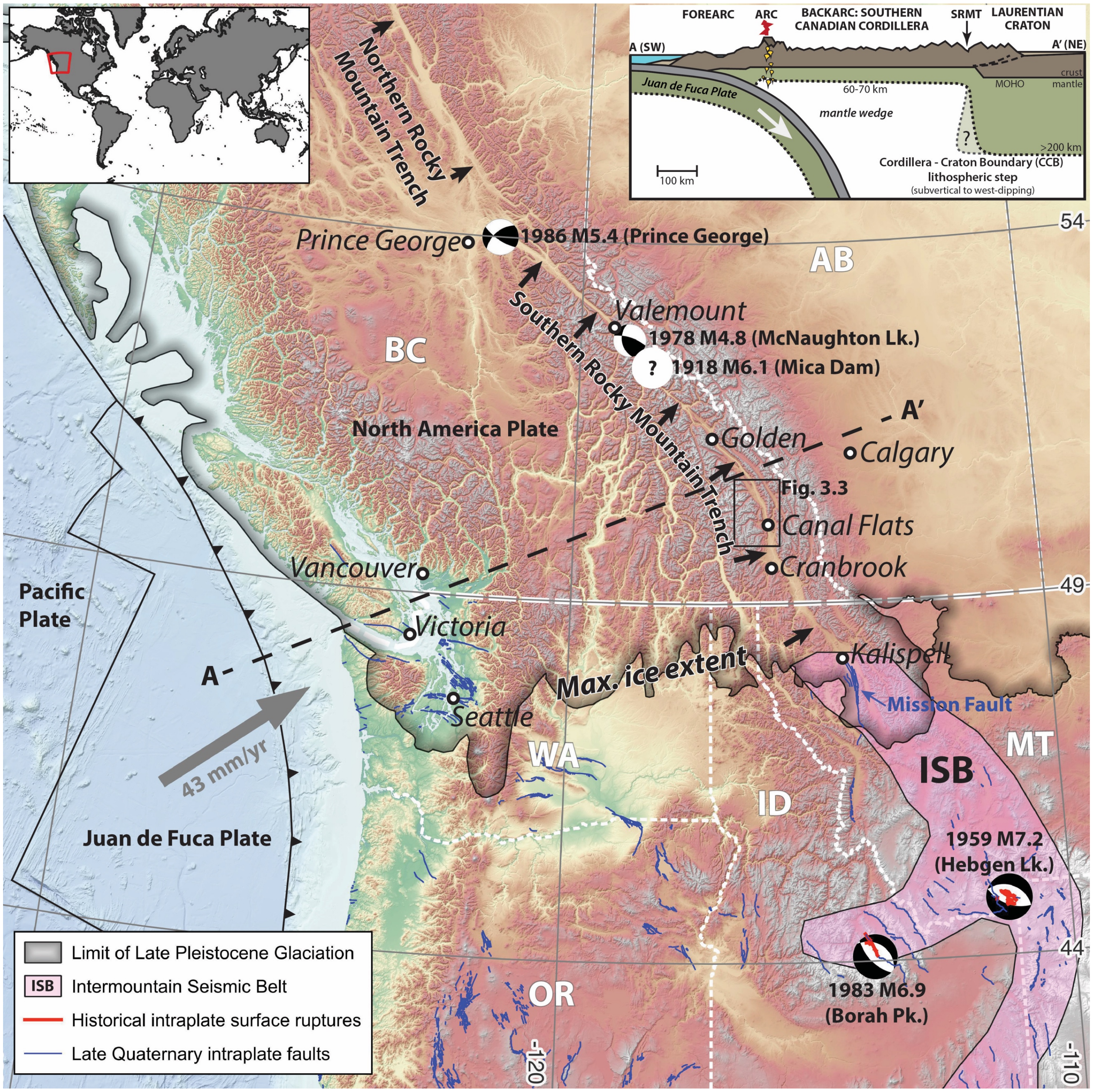

Figure 3.1. Physiography and tectonic setting of western North America. The conspicuous trace of the Southern Rocky Mountain Trench is indicated with black arrows. The grey shaded region indicates the diachronous maximum extent of the Cordilleran Ice Sheet reached between 19 and 16.5 ka (Dalton et al. 2023), which largely reshaped the landscape in the Late Pleistocene. The approximate extent of the Intermountain Seismic Belt (ISB) is shown in pink. Focal mechanisms of notable historical earthquakes along the ISB and SRMT are from Rogers and Ellis (1979), Rogers et al. (1980, 1990), Doser (1985), Doser and Smith (1985). Quaternary fault traces (U.S. only) are compiled from the USGS Quaternary Fault and Fold database, Harrichhausen et al. (2023), Morell et al. (2018), and Lynch (2023). Inset is a schematic cross-section of the lithospheric structure of the Cordillera adapted from Currie and Yu (2023).

side of the fault from the Eocene to the present. Farther north, the SRMT connects to the Northern Rocky Mountain Trench and Tintina faults, which both accommodated over 400 km of dextral offset, also largely in the Eocene (Gabrielse, 1985; Gabrielse et al., 2006).

The SRMT surface expression corresponds to a sharp change in geophysical properties. Hyndman and Lewis (1999) show that crustal heat flow markedly decreases eastward across the SRMT. Many authors have shown a subvertical step-change in seismic velocity across the SRMT (Schaeffer and Lebedev, 2014; Audet et al., 2019; Chen et al., 2019; Estève et al., 2020; Yu et al., 2022; Currie et al., 2023; Currie and Yu, 2023), as well as in electrical conductivity (Rippe et al., 2013). The step is thought to correspond to the boundary between thin and hot Cordilleran lithosphere to the west and thick and cold cratonic lithosphere to the east (Figure 3.1 inset). A number of hypotheses have been proposed to explain the existence of thin lithosphere beneath the high topography of the Cordillera, including: (1) rifting of the Rodinian supercontinent in the Neoproterozoic, (2) a Late Cretaceous suture between ancestral North America and accreted terranes, and (3), lithospheric delamination in the Eocene (Currie and Yu, 2023). A clear causal relationship between the conspicuous topography of the SRMT and the significant geophysical transition beneath it has not been established. However, in the western United States, the strength and buoyancy contrasts across the transition are thought to be a primary cause of seismicity in the ISB (Lowry and Smith, 1995; Levander and Miller, 2012).

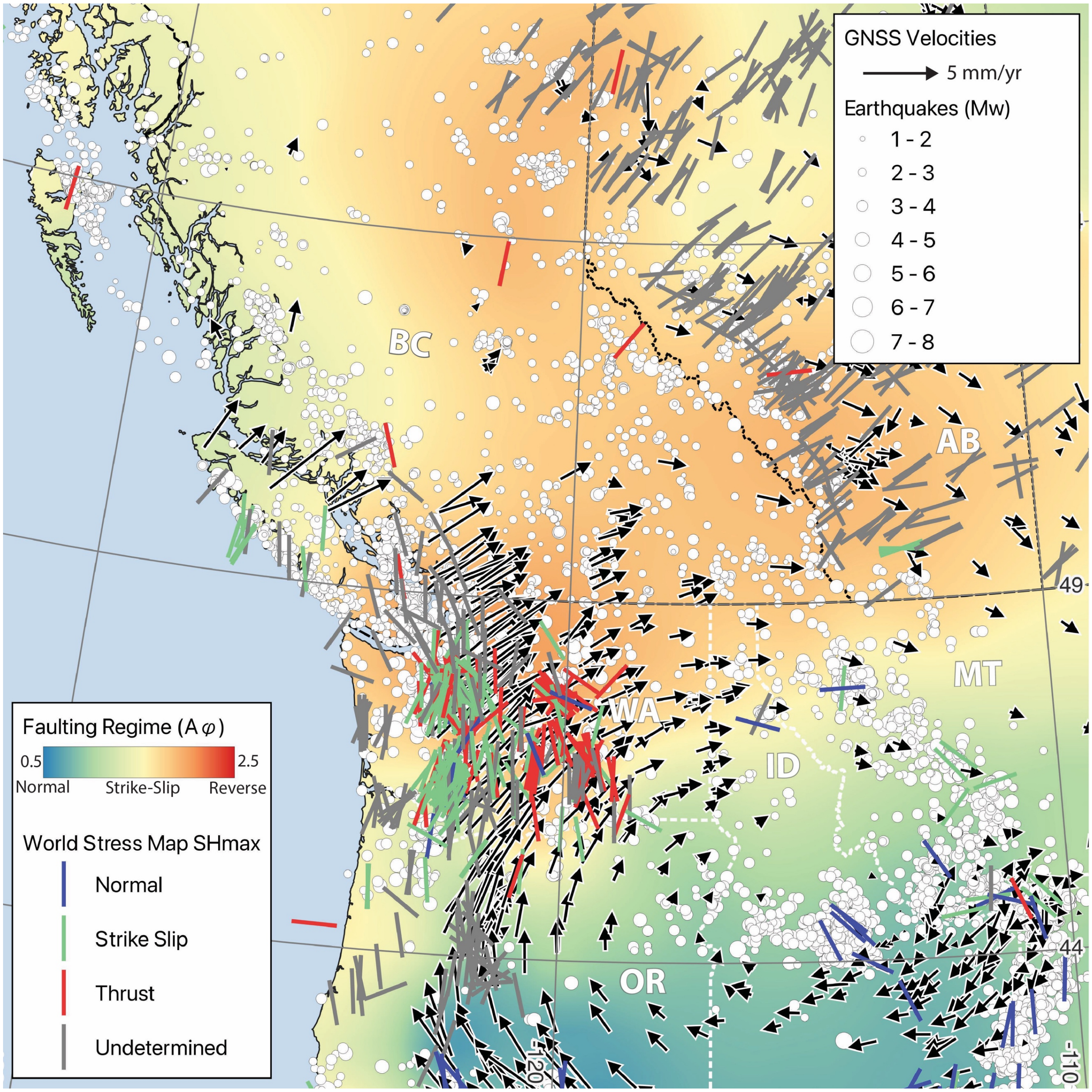

Figure 3.2. Seismicity and crustal strain across the Cordillera (same extent as Fig. 1). Epicentres are from the official catalogs used for the Canadian and U.S. National Seismic Hazard Models (Halchuk et al., 2015; Mueller, 2018). Both catalogs are clipped at the Canada-US border to minimize duplication, and exclude offshore events. SHmax orientations are from the World Stress Map project (Heidbach et al., 2018) and the style of faulting (Aϕ) – based on relative stress magnitudes – is from Lund Snee and Zoback (2020). GNSS velocities are from Ojo et al. (2021) and are relative to the ITRF2014 reference frame, with the modelled effects of Cascadia subduction zone interseismic locking removed.

3.4.2 Seismicity, Stress, Strain, and Surface Rupture, in the Vicinity of the SRMT

There is an average of ~6 events in the M_w 2-4 range every year in a 100-km-wide-swath along the SRMT, though there is no clear alignment of seismicity along a discrete fault plane. Focal depths in the region are generally poorly constrained due to sparse instrument density, but a dense portable array deployed near the town of Valemount in 2017 found that the majority of microseismicity along the SRMT occurs at depths less than 15 km (Purba et al., 2021). Three historical earthquakes of note have occurred close to the trace of the SRMT (Figure 3.1). On February 4, 1918, a significant earthquake occurred somewhere north of Golden, BC, though it was poorly studied at the time. This earthquake, which remains the largest to have been recorded in the eastern Canadian Cordillera, was re-examined by Rogers and Ellis (1979) who assigned it a magnitude (Mb_{Lg}) of 5.6 to 6.1, and a location in the vicinity of the present day Mica Hydroelectric Dam. On May 14, 1978, a magnitude (M_L) 4.8 earthquake occurred along the SRMT south of the town of Valemount at a shallow depth of ~10 km (Rogers et al., 1980). It was thoroughly investigated at the time due to concerns of induced seismicity from the filling of the McNaughton Lake (now Kinbasket Lake) hydroelectric reservoir, and a transpressional focal mechanism was determined from P-wave polarities (Rogers et al., 1980). On March 21, 1986, a magnitude (M_B) 5.4 earthquake occurred near the city of Prince George, causing minor damage, also with a transpressional focal mechanism (Rogers et al., 1990). A portable array deployed immediately following the earthquake recorded aftershocks at depths between 9 and 16 km. Ristau et al. (2007) compiled regional moment tensor solutions for all of western Canada and showed a broad pattern of northeast-southwest compression as indicated by P-axis orientations. This stress pattern is also evident in borehole breakouts compiled in the World Stress Map project (Figure 3.2; Heidbach et al., 2018).

A small geodetic strain gradient has been observed across the eastern Canadian Cordillera using geodetic GNSS data (Figure 3.2). Mazzotti et al. (2008) integrate GNSS and seismicity data to estimate between 0-1 mm/yr of convergence between central BC and Alberta, and attribute this to far-field strain transfer from the Cascadia subduction zone. With an additional decade of data, Ojo et al. (2021) showed a broad pattern of transpression and a decreasing strain gradient from SW to NE. Notably, both Mazzotti et al. (2008) and Ojo et al. (2021) show that the geodetic moment rate in the Cordillera significantly exceeds the seismic moment rate, which may imply that there is some degree of aseismic deformation, or that large earthquakes with long recurrence intervals are not captured in the seismic catalog.

It has previously been demonstrated that the SRMT hosted large surface rupturing earthquakes in the Holocene at its southern termination in Montana. On the east side of the Flathead Valley south of Kalispell (Figure 3.1), a west-facing 3- to 6-m-high scarp known as the Mission fault extends for at least 45 km along the base of the Mission Range; a dam safety study involving multiple paleoseismic trenches on the Mission fault established at least two normal faulting earthquakes occurred in the late Quaternary, with the most recent occurring around 7.7 ka (Ostenaa et al., 1995). Hofmann et al. (2006) further suggest a late Pleistocene average slip rate of 0.64 mm/yr, decreasing to 0.17 mm/yr through the Holocene. Ostenaa et al. (1995) suggest that the Flathead region defines the northernmost occurrence of regional extension in the ISB (Smith and Sbar, 1974; Cao and Liu, 2024). Further south in the ISB, there have been two historical surface rupturing earthquakes (Figure 3.1): the 1959 M_w 7.2 Hebgen Lake earthquake was one of the world's largest recorded continental normal faulting events, and killed 28 people (Johnson et al., 2018); and the 1983 M_w 6.9 Borah Peak normal fault earthquake is the second largest historical rupture to have occurred in the ISB, and caused two deaths and several millions of dollars of damage to buildings and infrastructure (Bello et al., 2022). Numerous other Quaternary fault scarps, mostly with extensional kinematics, are mapped throughout the ISB (Figure 3.1; U.S. Geological Survey, 2017).

3.4.3 Quaternary Geology of the Cordillera

The geomorphic expression of the Canadian Cordillera has been heavily shaped by Late Pleistocene glaciation (Figure 3.1). The young landscape is not conducive to the preservation of geomorphic signatures related to tectonic activity, making it challenging to find and characterize these features, particularly those formed by low-slip-rate faults (e.g., Morell et al., 2017; Harrichhausen et al., 2023). The timing of deglaciation is often the sole geochronological constraint available for determining the timing of faulting and provides minimum slip rate constraints. It is therefore critical to understand the glacial record. The Late Pleistocene (late Wisconsinan) Fraser glaciation diachronously reached its maximum extent between ~19 and 16.5 ka (Figure 3.1), before collapsing and achieving an ice extent similar to the present day by 10 ka

(Dalton et al., 2023). The thickest ice (up to 2 km) was situated over the interior plateau (Intermontane Belt) of central BC. Ice streams drained the ice sheet along valleys, including a southward-flowing trunk glacier in the SRMT (Ryder et al., 1991; Eyles et al., 2018). Paraglacial landforms developed in the dynamic and unstable period of warming climate and deglaciation, including large proglacial lakes and alluvial fan complexes (e.g., Ryder, 1971a,b; Ballantyne, 2002). These paraglacial features have the potential to further constrain the timing of tectonic activity, as their depositional record potentially extends on the order of 100s or 1000s of years beyond the period of ice sheet retreat. However, they also hinder the identification of tectonic features, as they further shorten the timeframe available for the accrual of surface offset.

3.5 Methods and Study Site

3.5.1 Systematic Review of Lidar Data Along the SRMT

We compiled and systematically reviewed all available high resolution topographic data covering the SRMT. Most data (by total area) are from the LidarBC Data Portal (https://lidar.gov.bc.ca/), which, at the time of writing cover most of the SRMT from the U.S. border to Golden, BC. These data were largely collected for Public Safety Canada's National Disaster Mitigation Program. Bare earth Digital Terrain Models (DTMs) and derivative hillshade, slope, and aspect maps were used to identify potential fault scarps. Primarily, we looked for locations where young, unconsolidated surficial sediments appeared to be offset or deformed along linear traces or scarps. We distinguished tectonic fault scarps from sackung features (which are common in glaciated terrain) using the geomorphic criteria summarized by McCalpin (1999). In our review, we only identify with confidence one site with a potential fault scarp, located on the east side of Columbia Lake, 20 km south of Invermere (Figure 3.3). This scarp was first observed in aerial photographs by Sawicki (1990), who hypothesized that it could be a fault or the head-scarp of a rotational landslide but was unable to conclusively prove either origin. The Columbia Lake site forms the main focus of our paper.

3.5.2 Geologic Setting of Columbia Lake

3.5.2.1 Surficial Geology

Columbia Lake is situated in a shallow depression in the floor of the SRMT between the towns of Canal Flats and Fairmont Hot Springs (Figure 3.3). During the late Wisconsinan Fraser glaciation, the SRMT was locally occupied by a south-flowing trunk glacier/ice stream, which deposited a drumlinized basal till known as the Wycliffe Till (Clague, 1975; Sawicki and Smith, 1992; Eyles et al., 2018). At the end of the glaciation, the ice retreated northward along the SRMT (Sawicki and Smith, 1992). The timing of ice-free conditions in the SRMT are inferred from a radiocarbon age of 11.30 ± 0.10 cal kyr BP from a sediment core in Cleland Lake (Figure 3.3), 70 km north of Columbia Lake (Mihindukulasooriya et al., 2015; Dalton et al., 2023). Another 70 km farther north near Golden, an age of 11.59 ± 0.41 cal kyr BP extracted from peat (Fulton, 1971; Dalton et al., 2023) is consistent with the inferred rapid northward retreat of the SRMT trunk glacier. At Flathead Lake, Montana, 280 km south of Columbia Lake, a charcoal age of 14.67 ± 0.50 cal kyr BP is reported from a sediment core (Smith et al., 2018; Dalton et al., 2023), indicating the earliest stages of ice retreat in the SRMT. Several other radiocarbon ages at North Star Glacier, Dog Lake and Burstall Lake (Figure 3.3), indicate that the mountains to the east and west of the SRMT may have remained glaciated for ~1000 years longer than the valley bottom.

As the SRMT trunk glacier receded north beyond the Kootenay-Columbia drainage divide near Canal Flats, a narrow proglacial lake – glacial Lake Invermere – developed in front of the ice (Sawicki and Smith, 1992). Extensive glaciolacustrine clay and silt deposits from glacial Lake Invermere are observed over a total length of 210 km from south of Canal Flats to north of Golden. The deposits form cliffs up to 50 m high, and are believed to be over 60 m thick in some locations (Sawicki and Smith, 1992). Glacial Lake Invermere was relatively short-lived, ultimately draining to the north when the retreating trunk glacier receded beyond the present Columbia River drainage near Mica Dam, 270 km north of Columbia Lake (Figure 3.1).

3.5.2.2 Structural Geology

The exact trace of the SRMT fault in the Columbia Lake region is not well located. It appears on geological maps south of Canal Flats on the east wall of the SRMT (Cui et al., 2017), where its geometry is constrained by seismic reflection profiles (Figure 3.4; van der Velden and Cook, 1996). The SRMT fault is generally not depicted in large-scale (small area) maps north of Canal Flats (Henderson, 1954) but does appear in most small-scale (large area) regional maps covering the SRMT. Instead, many maps depict the late Mesozoic Purcell Thrust fault occupying the

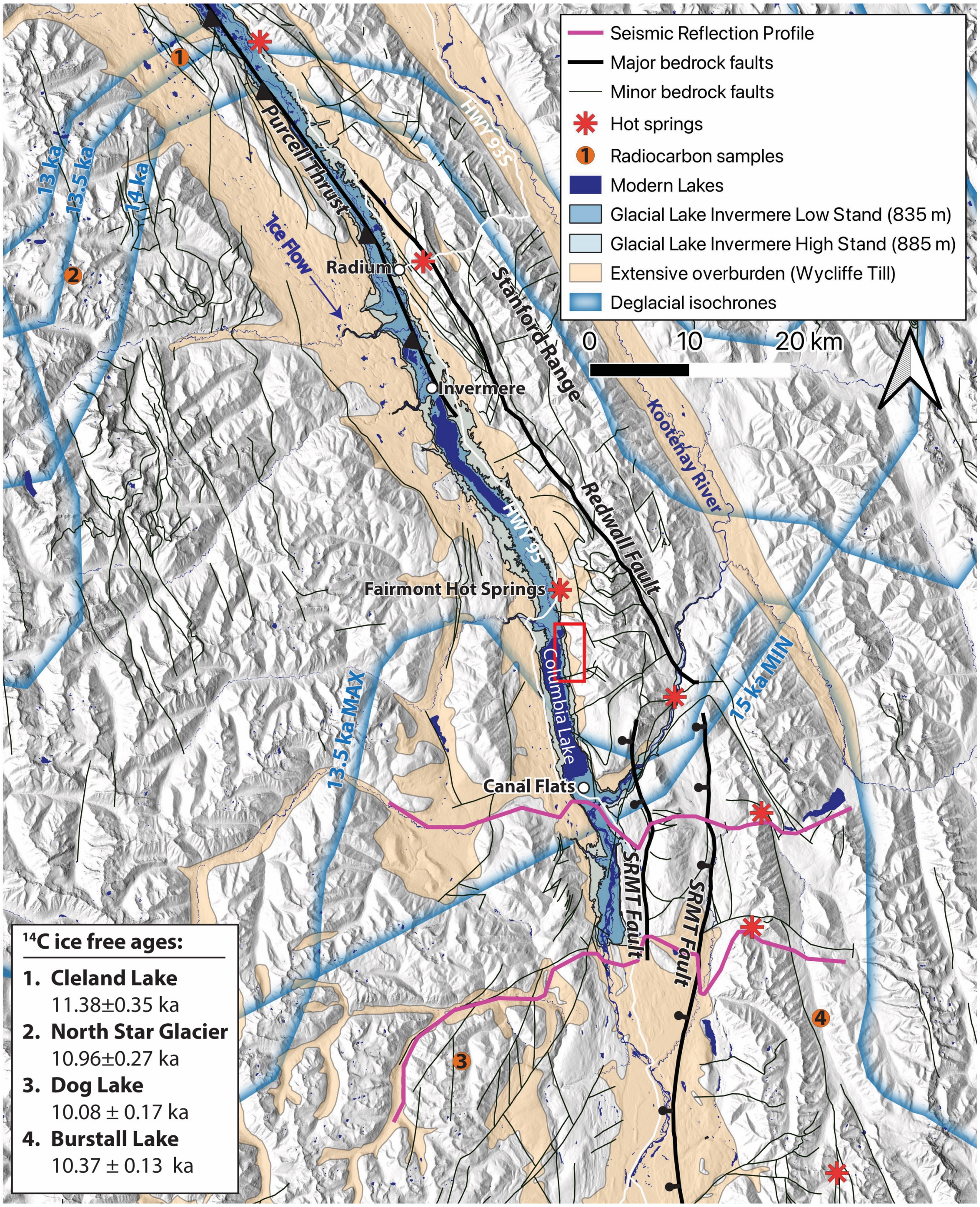

Figure 3.3. Physiographic setting of the SRMT. Approximate low and high stand contours of Glacial Lake Invermere are based on mapping by Sawicki and Smith (1992). Quaternary overburden extent and bedrock faults are from the British Columbia Digital Geology database (Cui et al., 2017). Deglacial isochrones and radiocarbon dates in calendar years are from Dalton et al. (2023). Traces of previously collected seismic reflection profiles shown in Figure 3.4 are from van der Velden and Cook (1996). Red box shows extent of Figure 3.5.

trench floor in this segment, with the SRMT fault reappearing north of Golden. The exact reason for its exclusion from maps is unclear, but likely results from the thick surficial deposits, lack of bedrock exposure, and lack of subsurface data (geophysics) that collectively prevent detailed study, rather than a true absence of the SRMT fault.

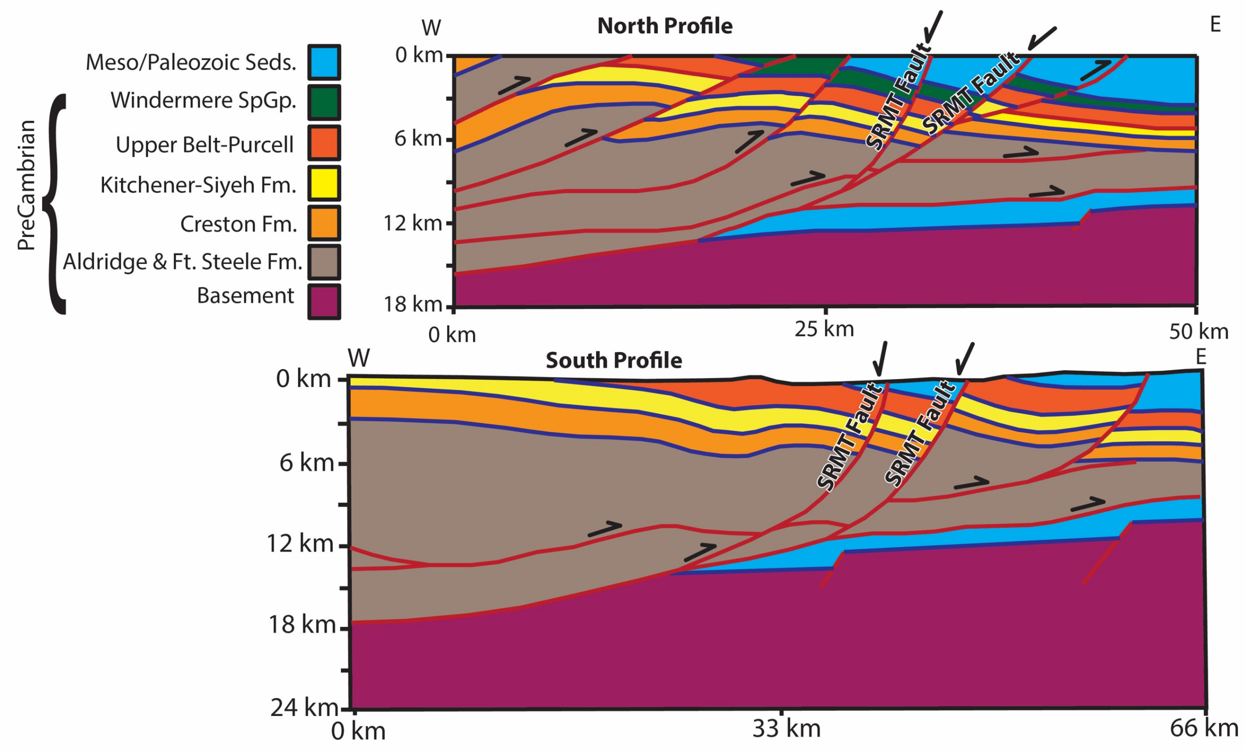

Figure 3.4. Interpretation of seismic reflection profiles across the SRMT modified from van der Velden and Cook (1996); see Figure 3.3 for cross section locations. Note that the SRMT fault splays are interpreted to be listric and steeply west dipping. Older Mesozoic thrust faults are also broadly west-dipping.

The bedrock underlying the mountainous Stanford Range immediately east of Columbia Lake was first mapped in detail by Henderson (1954) and Foo (1979). The range is underlain by a series of imbricate south-verging thrust-fault blocks with boundaries at high angle to the overall north-south structural grain of the Cordillera. The dominant lithologies are dolostone, limestone and shale, ranging from Precambrian to Devonian in age. Structural measurements from Henderson (1954) and our own mapping are shown in Figure 3.5. Henderson documents no evidence of trench-parallel faults in bedrock exposures on the western boundary of the Stanford Range along the edge of the SRMT, but does identify the Redwall fault as a major structural boundary within the Stanford Range and suggests that its kinematics may be the same as the obscured SRMT fault.

3.5.3 Drone Lidar and Surficial Mapping

To aid with mapping and measurement of scarp morphology at the Columbia Lake site, we supplemented the LidarBC data with high resolution lidar collected using a novel drone lidar system (Salomon et al., 2024). This platform produces Digital Terrain Models (DTMs) with 30 cm spatial resolution, allowing for high confidence in our measurements and interpretations of geomorphic and tectonic features. The drone lidar datasets used in this study are available for download from OpenTopography (Finley et al., 2023).

We map the surficial geology of the Columbia Lake site in detail to constrain the age of faulting. No detailed surficial maps exist for the Columbia Lake area, so we used broader studies of glacial (Clague, 1975), pro-glacial (Sawicki, 1990; Sawicki and Smith, 1992), and paraglacial (Ryder, 1971a) sedimentation in the southeastern Canadian Cordillera as the basis for our mapping interpretations. We identify five major stratigraphic units (Figure 3.5) on the east side of Columbia Lake. Unit 1 is diamict, inferred to be the Wycliffe till (Clague, 1975) associated with the last glaciation. It is semi-consolidated, bluff forming, and occurs discontinuously on the hillsides above the alluvial fans. Unit 2 is a finely laminated silt, inferred to have been deposited in glacial Lake Invermere (Sawicki and Smith, 1992). It is evident in ~20 m high bluffs along the shore of Columbia Lake, and is capped by Unit 3: pebble to cobble gravel paraglacial fan deposits (Figure 3.5). Unit 4 is a fine silt, inferred to be loess, which is presumably regionally extensive but is locally most evident near the apex of the fan and in a pre-existing gravel pit excavation. Unit 5 is comprised of coarse gravels associated with the 8-10-m-deep entrenched channel and fan of the modern Warspite Creek. The surface of the fans is also dissected by numerous headless drainages interpreted to be liquefaction flow slides (e.g., Miller et al., 2021).

3.5.4 Electrical Resistivity Tomography

We use Electrical Resistivity Tomography (ERT) to image deformed paraglacial sediments in the shallow subsurface. The ERT method is non-invasive and therefore useful in locations where a trench excavation is not easily permitted (i.e., within Provincial Parks). Additionally, ERT allows for the imaging of sediments deeper than a typical trench, and glacial/paraglacial sediments are well resolved in ERT profiles due to their wide variance in electrical properties (e.g., Harrichhausen et al., 2023). Unconsolidated clays and silts generally have resistivity values ranging between 1 and 100 Ωm, tills range between 100 and 1,000 Ωm, and sands and gravels exhibit values between 1,000 and 10,000 Ωm (Palacky, 1987). Carbonate sedimentary rocks have a wide range of resistivities from 1,000 and 100,000 Ωm.

We used an Advanced Geosciences Inc. (AGI) SuperSting instrument, which has 112 electrodes and a maximum survey length of ~1370 m. Constrained by the width of the fan, we conducted three surveys: a 650-m-long survey across the scarp near its maximum offset, a 325-m-long, higher-resolution survey superimposed on the first, and a 400-m-long survey on the southern end of the main scarp where the access road is not at the scarp base. These surveys allowed us to image to depths of between 100 m and 200 m. We used a dipole-dipole array configuration to maximize resolution of lateral variations in subsurface structure (e.g., Neyamadpour et al., 2010). In a dipole-dipole array, current is induced in the ground between a pair of electrodes and the potential difference, measured between a second electrode pair, is used to calculate the average (apparent) resistivity of the subsurface between the two electrode pairs. Each measurement uses a different set of 4 electrodes; different electrode spacings and positions will measure the apparent resistivity at different depth ranges and locations along the profile. The apparent resistivity for each measurement is mapped to a location halfway between the pairs, and to a depth of half the distance between the pairs. The contoured pseudosection of all apparent resistivity measurements is inverted to model the true sub-surface resistivity structure. The inversion is performed with AGI's proprietary EarthImager software, using manufacturer-recommended parameters (Table S1) and a smooth model inversion method. Apparent resistivity measurements with individual RMS error of more than 50% are removed to improve the overall fit of the inversion. The relative elevation of each electrode strongly influences the inversion, and a Trimble R12 RTK GNSS system was used to precisely survey each electrode position to allow for terrain correction.

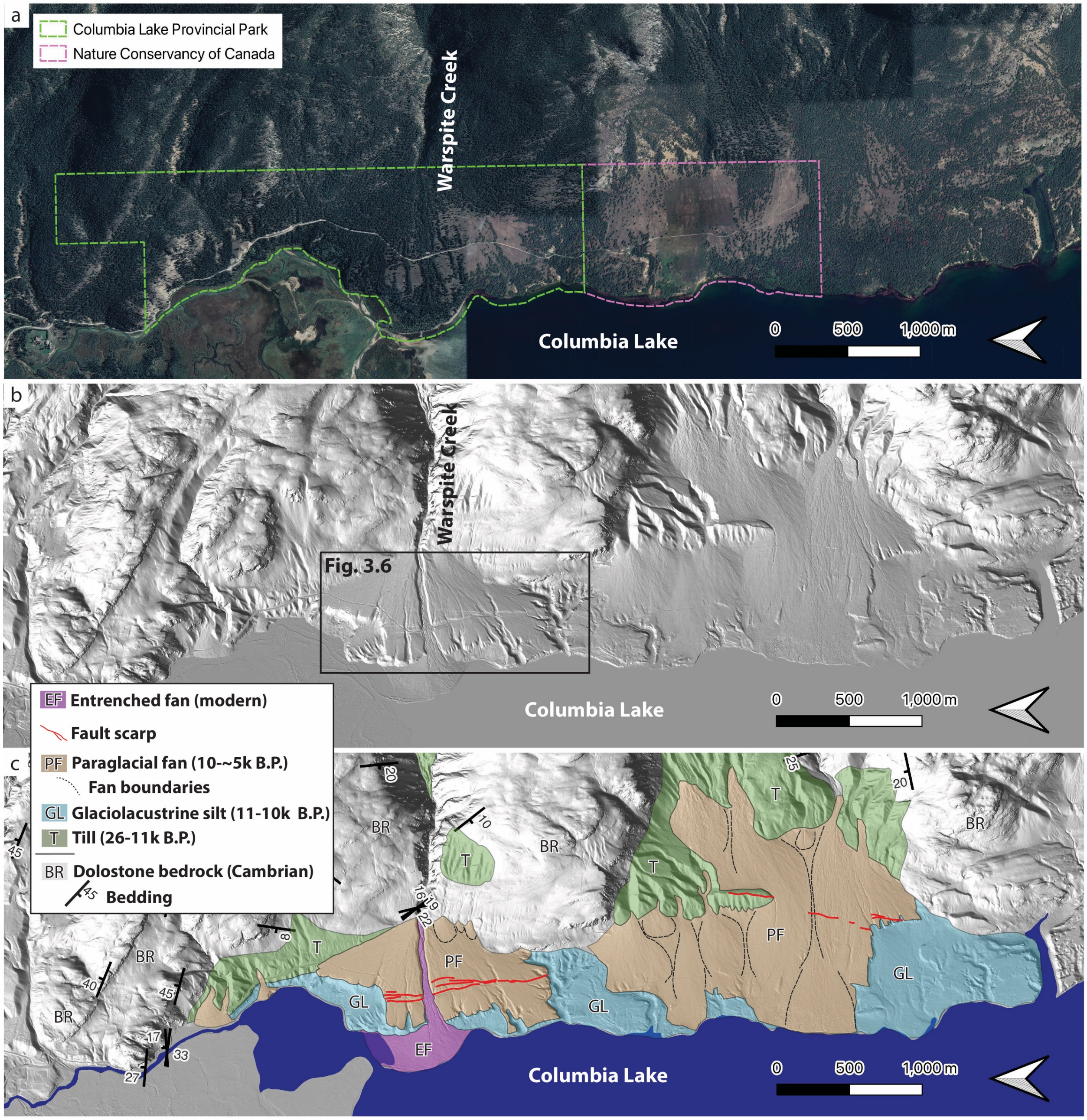

Figure 3.5. (a) Satellite imagery (2025 Google, CNES/Airbus) of the study area on the east side of Columbia Lake. (b) Bare earth lidar hillshade of the same area. (c) Our surficial mapping of the area. Bedrock structural measurements include our own and those from Henderson (1954). See Figure 3.3 for location.

3.5.5 Offset Measurements

Within the study area, there are no discernible lateral offsets across the scarp, only dip-slip offsets. We measure dip-slip offsets using the Monte Carlo Slip Statistics Toolkit (MCSST) developed by Wolfe et al. (2020) and our high resolution drone lidar DTM. The MCSST tool samples uncertainty distributions for the fault dip, fault position on the scarp, and topographic slopes of the hanging wall and foot wall to account for overall uncertainty in the measurement of vertical separation and/or net slip. We are careful to exclude a narrow gravel road constructed along part of the foot of the scarp from our estimates of the lower surface slope. The uncertainty distributions for fault dip and fault position are user-defined. We assign trapezoidal distributions, wherein the wide base of the trapezoid defines the entire range of possible values, and the narrow top of the trapezoid represents the range of most likely values. We use our ERT profiles as well as regional seismic reflection profiles (Figure 3.4; van der Velden and Cook, 1996) to constrain the dip of the fault in the subsurface. The linear fault trace and the lack of deflection with respect to topographic contours suggest a steeply dipping fault. In our offset calculations, we therefore allow for a fault with a steep dip ranging between 75° NE and 75° SW, with the highest probability between 85° NE and 85° SW. We allow for a fault intersection over the entire width of the scarp (width is measured perpendicular to strike), but assign the highest probability to a fault-scarp intersection between 1/3 and 2/3 of the scarp width. Uncertainties on offset measurements are reported as 95% confidence intervals (Figure 3.6).

3.6 Results and Analysis

3.6.1 Scarp Morphology

The west-facing scarp at Columbia Lake vertically displaces the surfaces of a series of overlapping paraglacial fans (Figure 3.5 and 3.6). The fans are completely vegetated by grassland and pine forest (Figure 3.5 and 3.7) and show no evidence of recent activity (channel avulsions or debris flow deposits). The scarp is most prominent on the fan emanating from Warspite Creek but can be traced intermittently to the south for a total length of 3.6 km across the adjacent fan complex. It is not well preserved in surface exposures of glaciolacustrine silt (Unit 2), which has been dissected by numerous drainage channels and liquefaction flow slides. The northern end of the scarp branches into three splays, with the largest offset on the lower

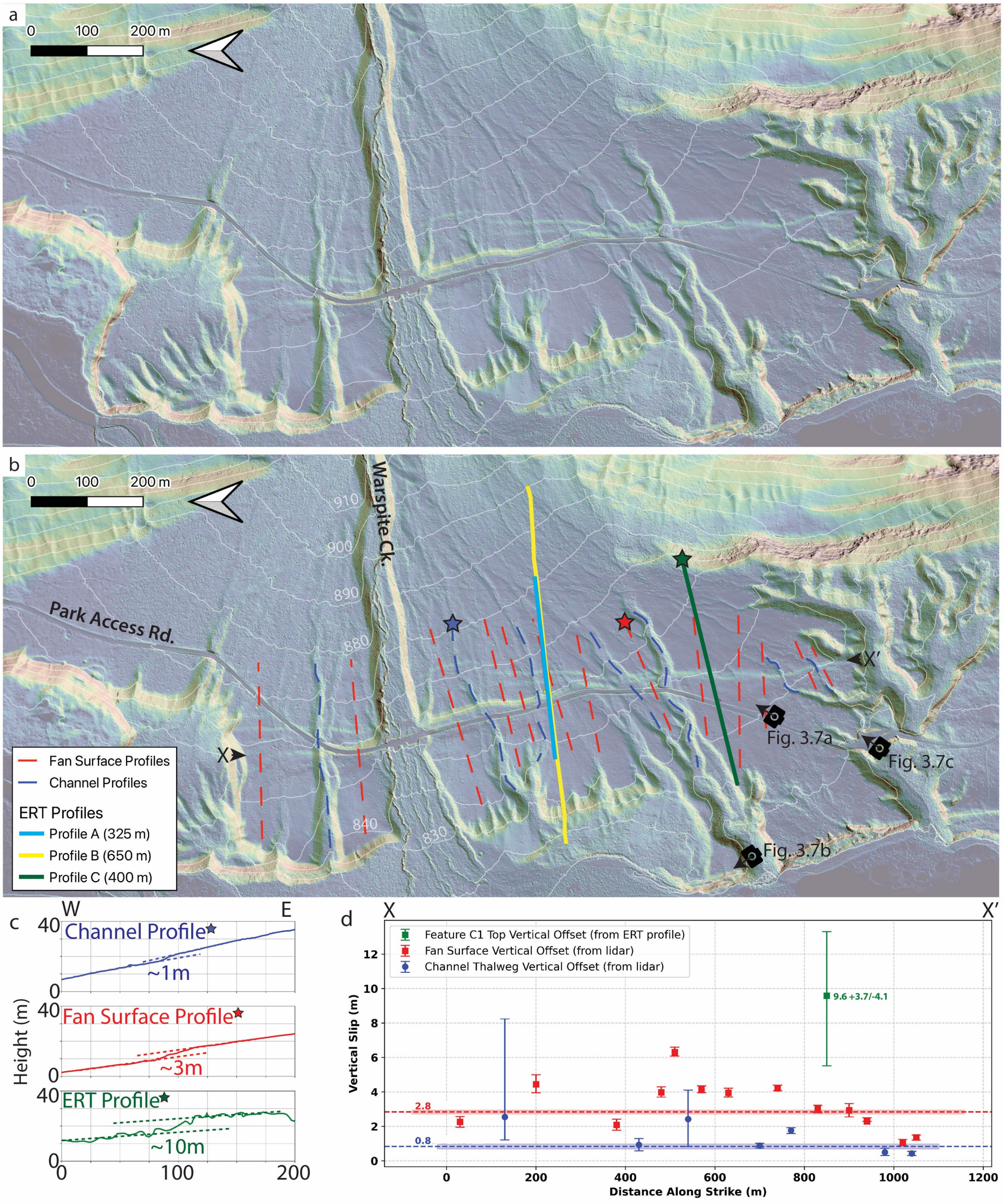

Figure 3.6. (a,b) Unannotated and annotated detailed view of scarp on Warspite Creek fan (see Figure 3.5 for location). Hillshade/slope angle basemap is high resolution drone lidar (Finley et al., 2023; Salomon et al., 2024). Topographic profiles and ERT survey lines are shown. (c) representative topographic profiles in a

channel thalweg, on the fan surface, and along the top of feature C1 in ERT Profile C (see Figure 3.8) illustrating progressively larger vertical offsets on older surfaces. (d) Distribution of vertical separation measurements from channels, fan surface, and ERT profile along strike from X to X'.

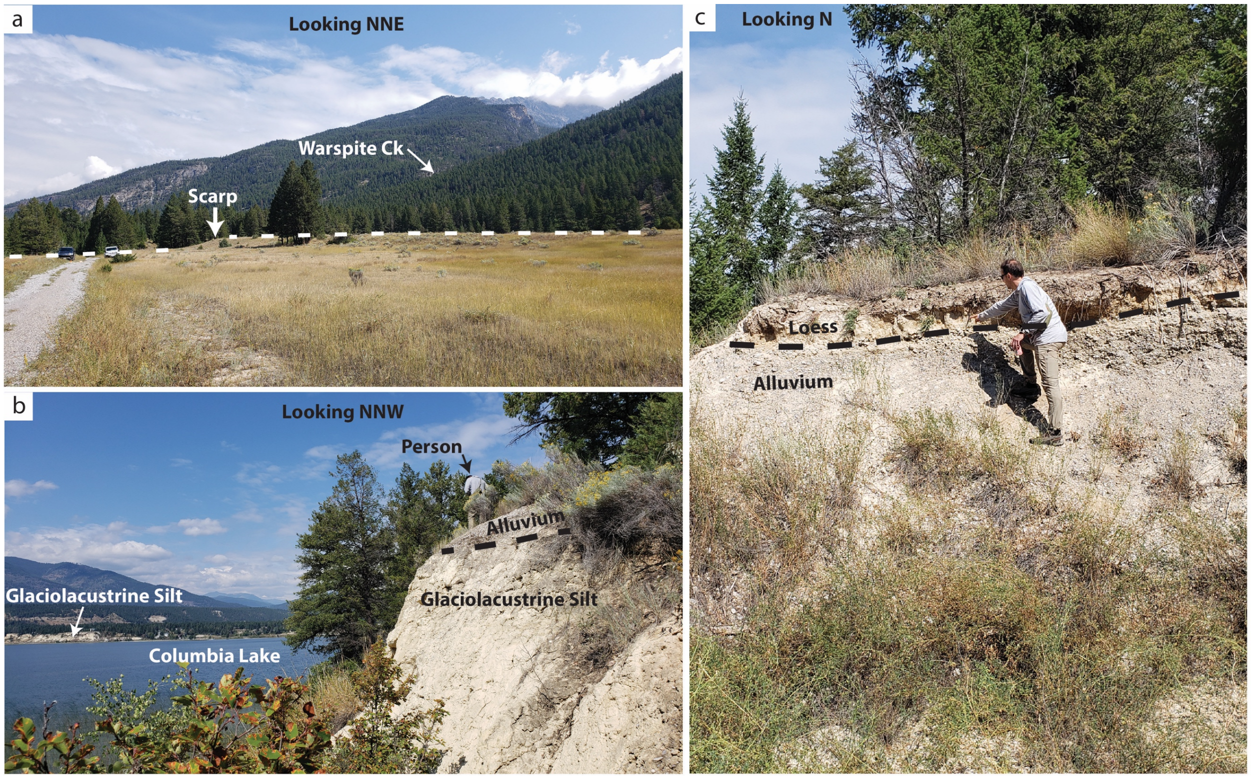

Figure 3.7. Field photos of Warspite Creek fan - see Figure 3.6 for camera locations. (a) View NNE of fan surface displaced by scarp indicated by white arrows. (b) View NNW near Columbia Lake shoreline showing finely laminated silt overlain by coarser alluvial gravel. (c) View N in small gravel pit on south edge of Warspite Ck. fan, showing ~30 cm layer of loess blanketing alluvium.

(western) splay. We measure dip-slip offsets both of the fan surface and of channel thalwegs that incise the fan surface. Where the scarp is multi-stranded, we report the cumulative vertical offset of all strands. The 13 fan surface cumulative vertical offsets range between 1 and 6 m, with a mean value of 2.8 m. The 7 channel profiles have systematically smaller vertical offset of between 0.4 and 2.5 m with a mean of 0.8 m (Figure 3.6). The scarps preserved in channels are aligned with the scarp on the fan surface and have a similar wavelength, indicating that their lower height is not related to knickpoint migration and associated scarp diffusion. The active channel of Warspite Creek itself does not preserve a vertical offset.

3.6.2 ERT Profiles of Subsurface Structure

The ERT surveys results show notable conductive and resistive features which are correlative between profiles, labelled as C# and R#, respectively in Figure 3.8. In Profile A, a highly resistive feature (R1) at the east end of the profile is interpreted to be dolostone bedrock, which is observed to crop out at the surface directly along strike (Figure 3.9a). The >70 m-thick conductive feature C1 is interpreted to be the glaciolacustrine clays and silts of glacial Lake Invermere. The subvertical contact between C1 and R1 is interpreted to be a steep shoreline rather than a fault contact. Feature C1 is, however, bisected by a sub-vertical zone of slightly higher resistivity directly below the surface scarp. Features R1 and C1 are overlain by a ~20 m thick high-resistivity layer (R2) which we interpret to be the coarse alluvium of the Warspite Creek fan. This in turn is capped by a thin low-resistivity layer (C2), interpreted to be fine loess. Profile B is superimposed on Profile A, providing greater detail in the shallow subsurface. The vertical disruption of feature C1 (glaciolacustrine silt) directly beneath the surface scarp is also evident in this profile. Feature R2 (alluvium) is also vertically offset. In Profile C, feature R1 is again interpreted to be bedrock, which outcrops at the east end of the profile. Feature C1 (glaciolacustrine silt) is 20-30 m thick, and both the top and bottom of the feature are clearly vertically offset. Using the MCSST tool, with lines fit to the upper contact of C1, we estimate a vertical separation of 9.6 +3.7/-4.1 m. Feature R2 (alluvium) is thinner than in profile A and is not capped by a layer of low-resistivity loess.

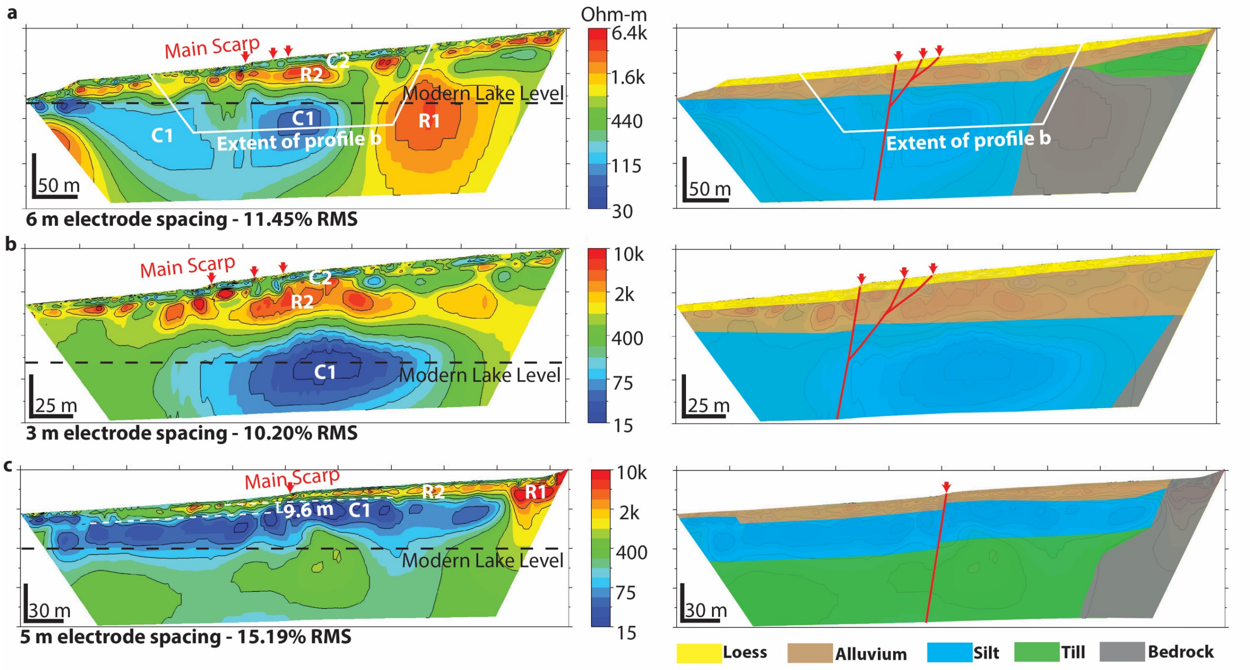

Figure 3.8. ERT Profiles A (a), B (b), and C (c) across the Columbia Lake scarp. Left column shows inversion results, and right column shows geological interpretation. Surface trace locations of profiles are shown in Figure 3.6.

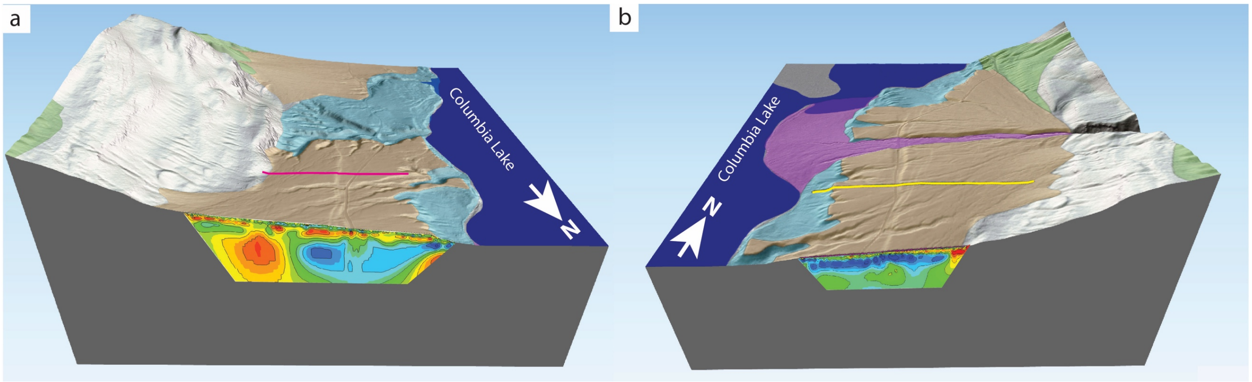

Figure 3.9. 3D models of ERT Profiles superimposed on 3D model of lidar DTM and surficial map. (a) View south at Profile A (reflected from Figure 3.8). Vertical discontinuity bisecting feature C1 is directly beneath surface scarp. Vertical contact between C1 and R1 is directly along-strike from bedrock outcrop. Pink line shows trace of Profile C. (b) View north at Profile C. 10 m vertical offset of feature C1 is directly beneath 3-m-high surface scarp. Yellow line shows trace of Profile A.

3.7 Discussion

3.7.1 Scarp Origin: Tectonic or Geomorphic?

Our lidar analyses and ERT profiles suggest that the scarp is most likely tectonic, rather than of erosional or mass wasting origin. The scarp crosses topographic contours rather than following them, ruling out the possibility that the feature is a wave-cut bench of a higher stand of Columbia Lake or other prehistoric lake. Sawicki (1990) suggested that the scarp might be the headscarp of either a rotational or translational landslide rooted in weak glaciolacustrine silts and clays deposited in glacial Lake Invermere. However, our lidar analysis does not support a landslide origin for this feature. There is no graben or back-rotated blocks, lateral scarps, or minor scarps (Cruden and Varnes, 1996) evident downslope of the scarp. Our lidar analysis reveals sites that have not been impacted by fan activity since the formation of the scarp (i.e., channels cutting into the scarp face). The scarp does not have a cuspate surface trace as is typical of landslide head scarps and its position at the base of a buttressed, low-angle slope, (without any unsupported slope down-slip of it) is incongruous with it being a landslide. Further, our ERT profiles show that a vertical discontinuity directly beneath the surface scarp extends to depths of 40-100 m below surface, which is well below the present level of Columbia Lake's bottom (surveyed maximum depth of 4.6 m; BC Department of Recreation and Conservation, 1958). Finally, both the top and bottom contact of glacial Lake Invermere silts (feature C1) appear to be vertically offset in our ERT profiles. For these reasons, we suggest that the scarp is related to a tectonic fault rather than a surficial geomorphic feature (i.e., a landslide). In the remainder of the discussion, we continue with the assumption that it is a fault.

3.7.2 Fault Geometry and Kinematics

Based on the vertical offsets observed on the surface and in ERT profiles and the lack of lateral offsets to channels incised into the fan surface, it is evident that the fault is purely dip-slip. The vertical discontinuity observed at depth in ERT profiles appears to dip steeply west, which is more consistent with normal than with reverse kinematics. If the fault were east-dipping, it would cut through the middle of feature C1 in ERT Profiles A and B, rather than passing through the subvertical zone of elevated resistivity. Furthermore, where imaged in seismic reflection profiles farther south, the main SRMT fault is shown to be listric, with a steep westward dip near surface (Figure 3.3; van der Velden and Cook, 1996), and the overall structural fabric of the region is also characterized by west-dipping faults. Thus, based on the scarp morphology observed with lidar, subsurface geometry observed in ERT profiles, and the regional structural setting observed with seismic reflection and geological mapping, we infer that the fault has normal kinematics.

3.7.3 Earthquake Timing and Slip Rate

Our topographic and subsurface elevation profiles (Figure 3.6b) indicate that the scarp may have hosted multiple earthquakes since deglaciation in the Late Pleistocene. Topographic profiles across the Warspite Creek fan surface exhibit systematically larger vertical separation than those within abandoned channels. Assuming the channels are, on average, younger than the surface of the fan, they may record only one event, whereas the fan surface records the cumulative displacement of two or three events. This inference is speculative, but a similar phenomena has been used as evidence of multiple Holocene earthquakes on the Leech River fault in the forearc region of the Cordillera (Morell et al., 2017). Furthermore, ERT Profile C shows that the vertical offset of the top of feature C1 is greater than the vertical separation of the fan surface, and that the paraglacial fan sediments (R2) are thicker on the downthrown (western) side of the fault. This observation suggests that there may have been multiple ruptures postdating the existence of glacial Lake Invermere, but predating the cessation of channel activity on the Warspite Creek fan.

Paleoseismic trenching and geochronology will be required to rigorously test the hypothesis of multiple earthquakes, but we can make some inferences about the timing of ruptures even without those constraints. Glacial Lake Invermere is thought to have drained when the trunk glacier occupying the SRMT receded beyond the Columbia River drainage 135 km northwest of Golden (Sawicki and Smith, 1992). The deglacial isochrones of Dalton et al., (2023) suggest that the ice sheet retreated past this position between 13 and 12 ka. A radiocarbon age of 11.59 ± 0.41 cal kyr BP from peat deposited 26 km northwest of Golden records ice-free conditions and provides a minimum surface age (Fulton, 1971; Dalton et al., 2023). We therefore assume that glacial Lake Invermere drained at approximately 12 ± 1 kyr BP, and that 9.6 +3.7/-4.1 m of vertical displacement occurred after that time.

Paraglacial fans (like the Warspite Creek fan) in British Columbia were most active in the early Holocene immediately following deglaciation, as glacial drift deposits mantling hillsides were reworked (Ryder 1971a, 1971b). For example, in the Thompson-Okanagan region of south-central British Columbia (~300 km west of Columbia Lake), a set of paraglacial fans are inferred to have been most active prior to the deposition of the Mazama Ash at 7.6 cal kyr BP (Ryder, 1971b; Egan et al., 2015). This period of activity appears to be relatively consistent for paraglacial fans across much of the southern Canadian Cordillera (Ballantyne, 2002). For example, Eyles and Kocsis (1988) constrain the construction of a paraglacial fan along the Fraser River to between 11 and 7 kyr BP, Lian and Hickin (1996) found that paraglacial sedimentation in the Seymour Valley (North Vancouver) was largely complete by 9 ka, and Friele et al. (2000) similarly showed that the Cheekye Fan near Squamish was most active prior to 9 ka. East of the SRMT, Roed and Wasylyk (1973) showed that alluvial fans in the Bow River valley near Banff were largely inactive prior to deposition of the Mazama ash, and Beaudoin and King (1994) make a similar observation near Jasper. We therefore make the conservative assumption that the Warspite Creek fan ceased to be significantly active at 7 ± 2 kyr BP and that ~6.8 m of vertical offset occurred before that time, and an additional 2.8 m occurred afterwards. As fan activity waned, and the average valley base levels became lower, many fans in BC were modified and incised by their distributary streams (Ryder, 1971b). We suggest that many of the minor abandoned channels on the Warspite fan may have developed during the later stages of fan activity. We therefore suggest that the ~1 m vertical offset of the minor channels likely occurred sometime after 7 kyr BP. It is challenging to constrain the minimum age of channel formation, however, they must predate the 8-10 m deep entrenchment of the present course of Warspite Creek, which would serve to limit channel avulsions. The timing of the most recent rupture could postdate channel entrenchment, with the high sediment flux quickly obscuring any scarp or knickpoint.

Despite the large uncertainties on the timing of various depositional events, we can derive approximate estimates of slip rate (Figure 3.10). Considering our estimates of both the vertical separation and age of the fan surface as our most robust constraints, we derive a minimum, open interval slip rate of 0.41 +0.18/-0.11 mm/yr. Closed interval slip rates potentially reveal a pattern of decreasing slip through time. To achieve the 9.6 +3.7/-4.1 m of total vertical separation observed in ERT Profile C, the slip rate must have been 1.35 +3.94/-1.03 mm/yr between the draining of glacial Lake Invermere and the cessation of paraglacial fan activity. Although the lower end of this range is consistent with a steady sub-millimeter slip rate throughout the Holocene, the middle to high end of this range is indicative of a significant decrease in slip rate between the early and late Holocene (Figure 3.10). Our age constraints on the minor channels are poor: if they are late Holocene features, they may be consistent with the open interval slip rate of 0.41 mm/yr; if they are early Holocene features, then the slip rate may have slowed even further.

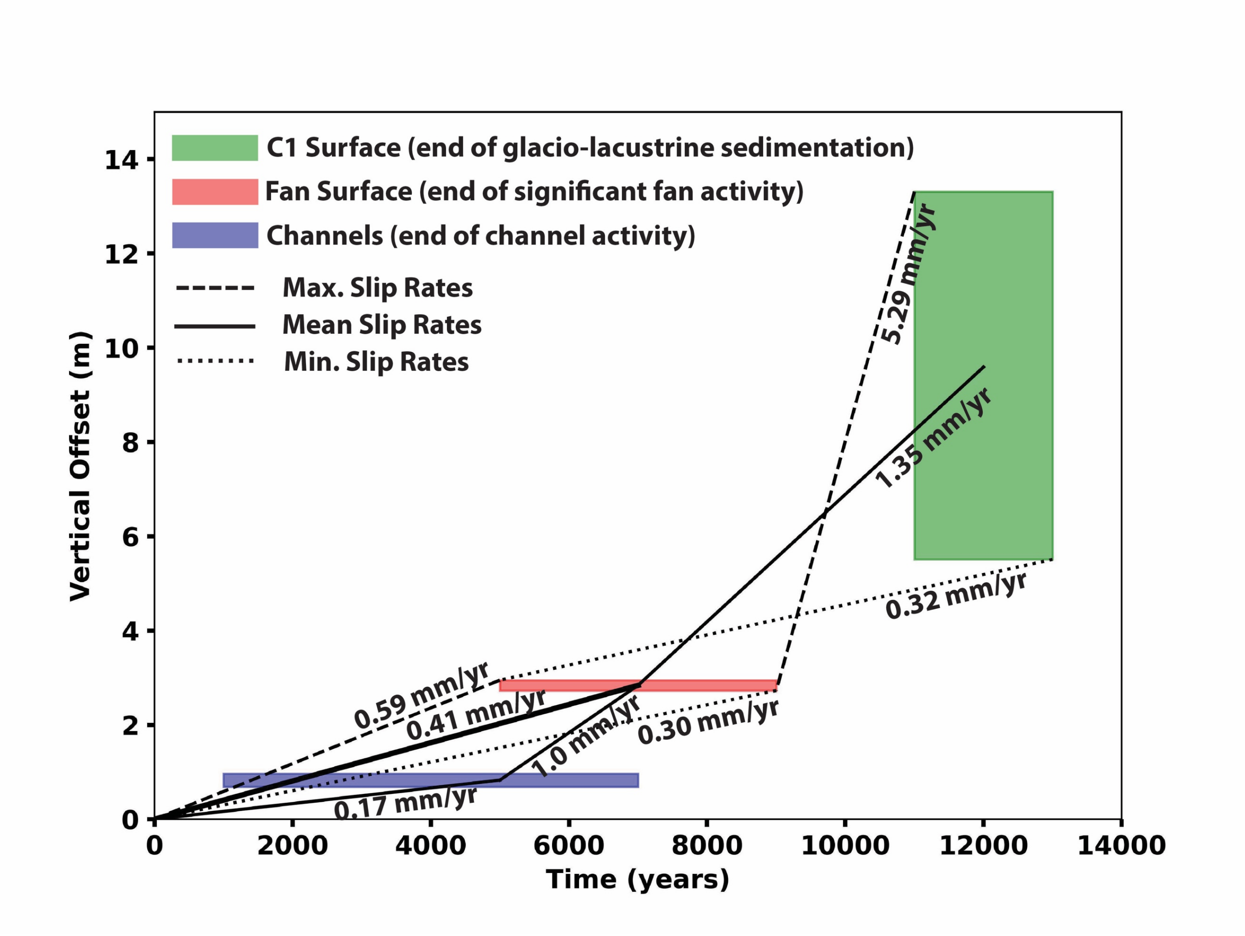

Figure 3.10. Vertical slip rates calculated from offsets to abandoned channels, the fan surface, and the top of the C1 feature (glaciolacustrine silt).

3.7.4 Driving Mechanism and Regional Neotectonics

There are many proposed driving mechanisms for deformation in the interior of the northern North American cordillera, including mantle convection, far field stress transfer, gravitational collapse, and GIA (Hyndman et al., 2005; Mazzotti et al., 2008; Becker et al., 2015; Hurtado and Gallen, 2024). Here, we discuss whether our geomorphic results are compatible with these various mechanisms and the geophysical data that underpin them.

The extensional kinematics we observe are seemingly inconsistent with the modern instrumentally measured stress and strain regime. Mazzotti et al. (2008) estimate ~1 mm/yr of shortening across the southern Rocky Mountains, and Ojo et al. (2021) show transpression in this region—but these geodetic strain estimates are based on very sparse datapoints (Figure 3.2). Earthquake focal mechanisms in the southeastern Cordillera are sparse, but generally exhibit northeast-southwest P-axes, transitioning from right-lateral transpression west of the Rockies to pure-thrust mechanisms in the foreland basin of Alberta (Rogers et al., 1980, 1990; Ristau et al., 2007; Kao et al., 2012).

The Warspite Creek scarp could plausibly be related to glacio-isostatic adjustment (GIA), which is thought to have caused large surface-rupturing earthquakes in other previously glaciated regions (Muir-Wood, 1989; Brooks and Adams, 2020). It is difficult to discriminate between a potential glaciotectonic and tectonic origins based upon the form of the fault scarp alone. However, variations in fault slip rate are a potential indicator of GIA-induced faulting, with an increased rate of seismicity anticipated to correspond with the period of greatest isostatic rebound (Steffen and Steffen, 2021); in western Canada, this was in the early Holocene (Clague and James, 2002). GIA-induced slip can manifest in a wide variety of fault kinematics that are dependent on the ambient stress field and faulting regime (Steffen et al., 2014; Steffen and Steffen, 2021). Modelling has shown that rupture can occur on non-optimally oriented faults (Steffen and Steffen, 2021), and that the stress perturbation caused by the ice sheet can lead to release of strain accumulated over much longer time periods than the glacial cycle (Craig et al., 2016). Some studies have shown that postglacial rebound was responsible for increased rates of early Holocene normal faulting on the Wasatch fault system in Utah (Hetzel and Hampel, 2005) and in the Sangre de Cristo Mountains of Colorado (Hurtado and Gallen, 2024). Hofmann et al.

(2006) found evidence of a Holocene decrease slip rate on the Mission fault at the south end of the SRMT, and though they made no inferences about the potential effect of GIA the similarity of their results to ours are notable. GNSS data indicate minimal, present-day GIA-induced vertical motion in the southeastern Cordillera, and the Columbia Lake site is near a hinge-line between uplift in the previously ice-loaded region and subsidence in the ice-marginal forebulge (Sella et al., 2007; van der Wal et al., 2009). However, the modern GNSS velocities do not necessarily reflect the long-term pattern of GIA. Our observation of a marked early to late Holocene decrease in vertical slip rate on the Warspite Creek scarp will require further paleoseismic work to confirm. However, if true, it points to a potential GIA driver to elevated rates of seismicity in the early Holocene. Although the slip rate may have slowed in the late Holocene, the fault still represents a seismic hazard.

Gravitational collapse of the cordilleran orogen may be a driver of deformation in the longer term. Thermochronological data along the SRMT in the Valemount area (~360 km north of Columbia Lake) indicates west-side-down normal faulting from 10 Ma to present (Fraser et al., 2021). Fraser et al (2021) attribute the extensional kinematics to gravitational collapse of the eastern Canadian Cordillera, which exhibits high topography in conjunction with a negative Bouguer gravity anomaly (Jobin et al., 2017), and thus high gravitational potential conducive for orogenic collapse. Mazzotti et al. (2008) calculated gravitational potential energy across several transects in the Cordillera and similarly suggest that gravitational forces may be responsible for extension in the interior Cordillera. That this extension is not captured by GNSS networks could simply be due to the sparsity of the network in this region. Copley et al. (2009) describe a comparable scenario in the mountains of Albania, where a thrust faulting regime is present on the edge of the orogen, whereas subparallel normal faults are observed in the interior, driven by gravitational forces.

3.7.5 Correlation with Thermal Spring Activity

The Canadian Cordillera is host to over 130 hot springs, the locations of which are thought to be controlled by faults (Grasby and Hutcheon, 2001; Finley et al., 2022a). The southeastern Cordillera in particular is host to a cluster of springs, seven of which occur along or near the traces of the SRMT, Redwall Fault, and Purcell Thrust Fault (Figure 3.3). Fairmont Hot Springs, the hottest of the seven, is less than 4 km north along strike of the Warspite Creek scarp. In the Basin and Range province of Nevada (which is bound to the east by the ISB), range-bounding normal faults act as conduits of geothermal fluid (e.g., Craig et al., 2021). Recency of faulting is a key predictor of the presence of geothermal systems (Faulds et al., 2015). We therefore suggest that the presence of the Fairmont Hot Spring may be a direct consequence of surface rupture at Warspite Creek. Moreover, the ~165-km-long section of the SRMT with hot springs (Figure 3.3) may delineate a more active, or more recently active, segment of the SRMT fault system.

3.7.6 Seismic Hazard and Risk Implications

The total 3.6 km length of the mapped scarp indicates a rupture corresponding to an earthquake with a moment magnitude of 6.4 using magnitude – rupture length scaling relation for normal faults from Wesnousky (2008). However, scaling relations between fault slip and rupture length suggest that the preserved scarp does not represent the full rupture length: assuming that the ~1 m of offset preserved in abandoned channels represents average slip from only one earthquake, the Wesnousky (2008) slip-rupture length scaling relation for normal faults gives a rupture length of 33 km. Taking this value as the true rupture length allows for a moment magnitude of 6.8. It is unlikely that the entire scarp length is preserved or exposed in the dynamic geomorphic environment of the Canadian Cordillera.

Although the surface rupture we map is only 3.6 km long, and the total estimated rupture length 33 km, surface-rupturing earthquakes may be possible anywhere along the SRMT. Rates of modern seismicity are relatively constant along the SRMT, as is the position of the deep lithospheric boundary beneath it (Currie and Yu, 2023), which may localize strain. To the south of Columbia Lake, the ~90 km-long Mission fault surface rupture (Ostenaa et al., 1995) demonstrates the SRMT is capable of large earthquakes. To the north, several major historical earthquakes are indicative of ongoing activity. In particular, the 1918 M6.1 Eastern British Columbia earthquake (Rogers and Ellis, 1979) is large enough for there to potentially be an associated surface rupture, which may have gone unnoticed due to its remoteness. The connections between these major events is unclear and will require further paleoseismic work.

The 1959 M_w 7.2 Hebgen Lake and 1983 M_w 6.9 Borah Peak earthquakes in the northern ISB of Montana and Idaho are of comparable kinematics and magnitude to inferred events on the

SRMT, and offer some insight into the potential impact of such an event. The Hebgen Lake earthquake triggered a major landslide that dammed a river, as well as a seiche wave in the Hebgen Lake reservoir; these events collectively killed 28 people (Johnson et al., 2018). Property damage was estimated to be around \$11 million (equivalent to ~\$119 million in 2024). The position of the Warspite Creek scarp near the shore of Columbia Lake may allow for similar wave generation that would pose a risk to residential properties and infrastructure on the shore of the lake. The steep slopes on the eastern side of the SRMT above Columbia Lake may also pose a shaking-induced landslide risk. The Borah Peak earthquake caused two deaths due to the failure of a brick façade on a storefront (Reavely, 1985). Additionally, the earthquake caused numerous landslides, and extensive liquefaction of nearby flood plain sediment. The total cost of property damage was estimated to be around \$12 million (~\$38 million in 2024).

Considerable population centres and critical infrastructure are at risk from future large earthquakes on the SRMT. The SRMT valley is populated by approximately 105,000 people, primarily in the towns of Cranbrook (20,000), Invermere (4,000), Golden (4,000), Valemount (1,000), and Prince George (76,000). The smaller hamlets of Canal Flats (800) and Fairmont Hot Springs (800) are within 14 and 4 km of the Warspite Creek fault scarp, respectively. The SRMT is also crossed by numerous pieces of critical infrastructure for which fault displacement hazard may need to be considered. A branch of the Canadian Pacific Railway is on the opposite shore of Columbia Lake from Warspite Creek, and only a few meters above the lake level. Farther north, the SRMT is crossed by the Transmountain Pipeline, several highways and major railways, providing critical transport and supply chain connections to the west coast. Several hydroelectric dams are also in close proximity to the SRMT. In particular, the Mica Hydroelectric Dam impounds the Kinbasket Lake reservoir, which occupies a 185 km stretch of the SRMT between Golden and Valemount.

3.8 Conclusion

One of the most prominent lineaments in North America, the SRMT has long been an enigmatic structure. We have shown here that, in addition to being a locus of major normal faulting in the Eocene, it may continue to exhibit localized deformation. Although the scarp feature we identify at Columbia Lake is limited in its surface expression, our analysis of its surficial morphology and subsurface structure point to a tectonic origin. In particular, our ERT profiles show that a vertical discontinuity extends to depths well below what would be expected for a translational landslide. Despite being in an overall compressive regional stress regime, we suggest that the scarp is most likely a normal fault related to gravitational collapse of the Cordillera. We find that offsets to buried stratigraphic horizons, the fan surface, and younger channel thalwegs are progressively smaller, indicating multiple surface ruptures, and a possible decrease in slip rate from >1 mm/yr in the early Holocene to < 1 mm/yr in the late Holocene. This finding suggests that seismicity may have been modulated by GIA, a phenomenon that has been observed on several other range-bounding normal faults in the North American cordillera. The presence of several thermal springs near the Holocene trace of the SRMT may be related to the recency of faulting on this segment and could be an indicator of ongoing earthquake hazard. Future paleoseismic studies are necessary to assess the risk to critical infrastructure and communities along the entire SRMT.

3.9 Acknowledgements

This research occurs on the traditional territory of the Ktunaxa and Secwépemc peoples, who regard the east side of Columbia Lake as having particularly high cultural significance. We sincerely thank Dustinaya Duteau, Kris Belanger, and colleagues at the Ktunaxa Nation Council, and Joshua Martin of the Shuswap Band (Secwépemc Nation) for their engagement with our field studies at Columbia Lake. Darin Welch at BC Parks, as well as Richard Klafki and Kate Mackenzie at the Nature Conservancy of Canada, further assisted with access to the field site. Tracy Brennand and B-Jae Kelly at Simon Fraser University provided and coordinated rental use of their AGI SuperSting ERT system. We benefitted from discussions about glacial Lake Invermere with Ozzie Sawicki. Thanks to Claire Currie for providing the cross section of the Cordillera in Figure 3.1. Stipend support for T.F. was provided by an NSERC CGS-D scholarship and a Dr. Margaret “Marmie” Perkins Hess Graduate Fellowship. Additional funding for research came from NSERC Discovery Grants awarded to E.N. and J.C. and a Canada Research Chair to E.N. Our drone lidar system was developed with support from the Canada Foundation for Innovation John Evans Leadership Fund (CFI JELF), and BC Knowledge Development Fund (BCKDF). All maps were created using the free and open source QGIS software.

3.10 Supporting Information

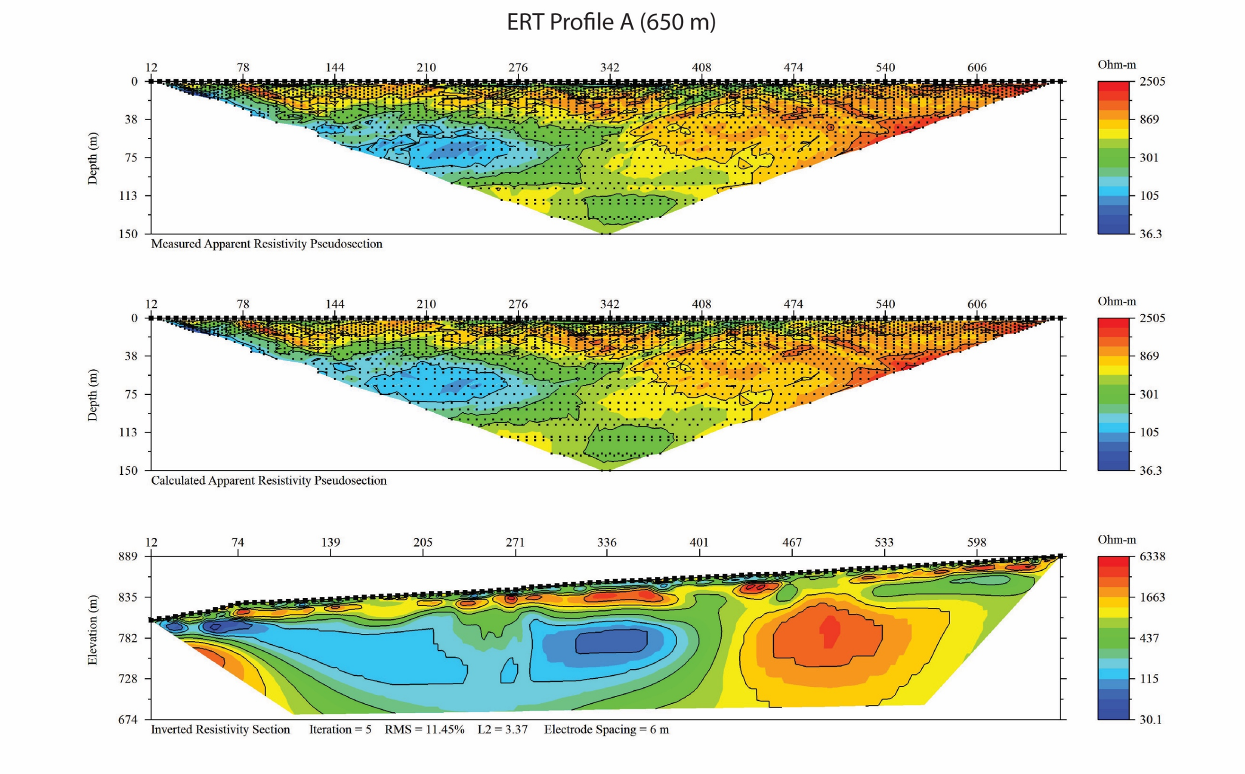

Figure S3.11. Apparent resistivity pseudosection, calculated apparent resistivity pseudosection, and inverted resistivity profile for ERT Profile A (650 m). Note that the sections are vertically compressed.

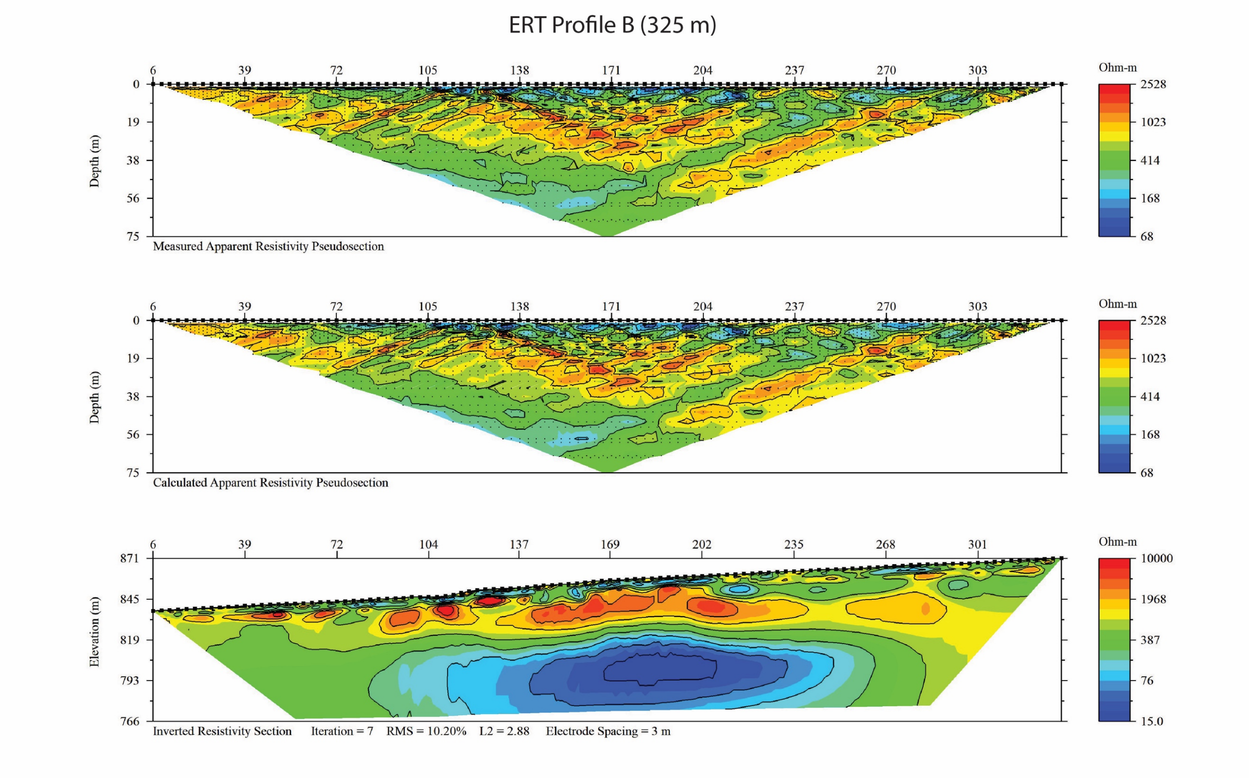

Figure S3.12. Apparent resistivity pseudosection, calculated apparent resistivity pseudosection, and inverted resistivity profile for ERT Profile B (325 m). Note that the sections are vertically compressed.

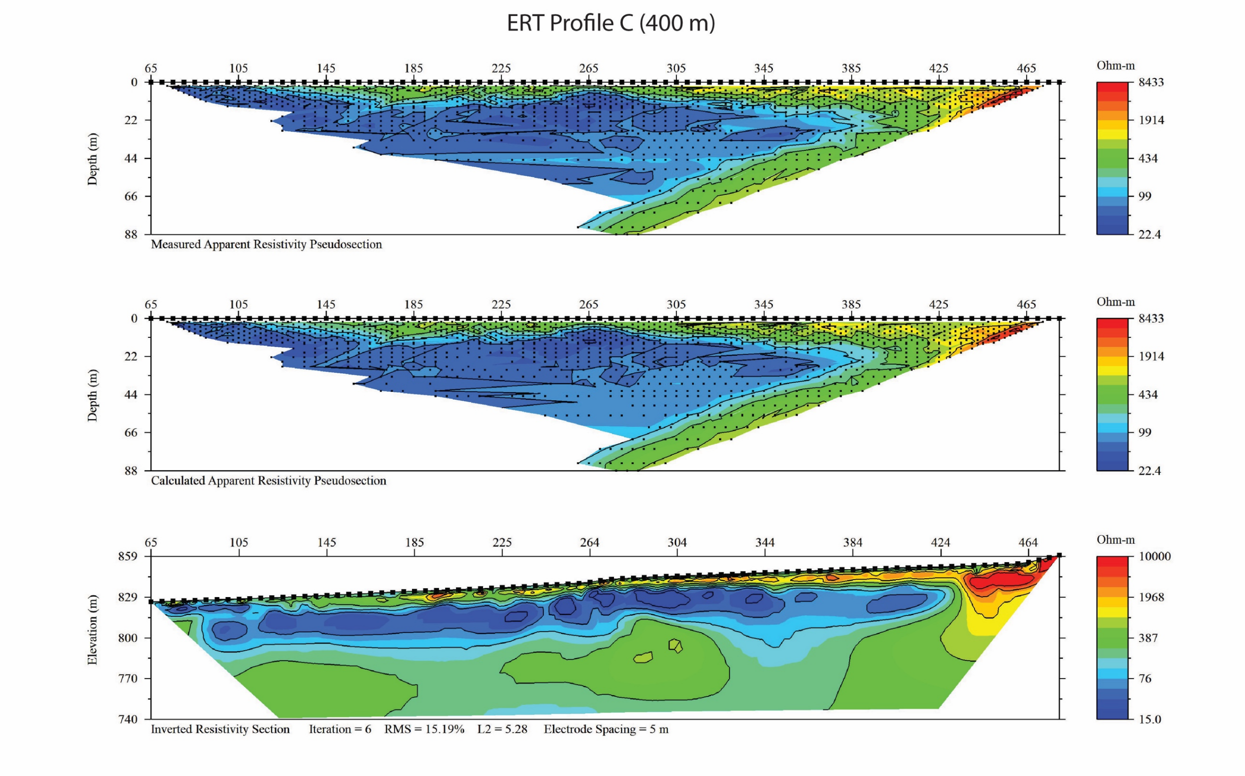

Figure S3.13. Apparent resistivity pseudosection, calculated apparent resistivity pseudosection, and inverted resistivity profile for ERT Profile C (400 m). Note that the sections are vertically compressed.

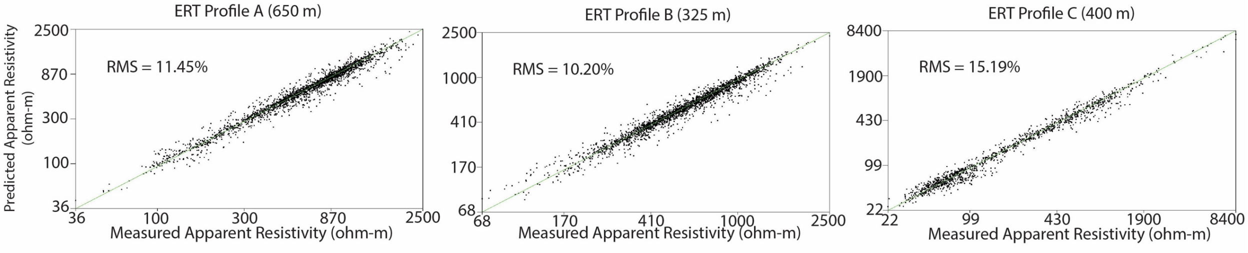

Figure S3.14. Cross-correlation plots for ERT inversions.

Table S3.1. Key settings and parameters for AGI EarthImager resistivity inversion. Parameters not shown here were set to default.

Parameter	Value	Note
Min. Voltage	-1 mV	
Min. V/I	0.001	
Min. Apparent Resistivity	1 Ω-m (absolute)	
Max. Apparent Resistivity	100000 Ω-m	
Max. Repeat Error	10 %	
Max. Reciprocal Error	10 %	
Remove Neg. Apparent Res.	Yes	
Inversion Method	Smooth Model Inversion	
Forward Modelling Method	Finite Element	
Forward Modelling Solver	Cholesky Decomposition	
Number of Iterations	15	Stop if reached first
Max. RMS Error	3	Stop if reached first
Min. Error Reduction	5 %	Stop if reached first
Min. Resistivity	15 Ω-m	
Max. Resistivity	100000 Ω-m	
H/V Ratio	0.5	

Chapter 4: Dextral strike-slip rupture of the Eastern Denali fault, a mature terrane bounding fault in a compressive setting

4.1 Article Information

Theron Finley[1], Guy Salomon[1], Edwin Nissen[1], John F. Cassidy[2,1], Brian Menounos[3], Roger Stephen[4], Jeremy Gosselin[2], Kristin Morell[5]

[1]School of Earth and Ocean Sciences, University of Victoria, BC, Canada

[2]Pacific Geoscience Centre, Geological Survey of Canada, Sidney, BC, Canada

[3]Department of Geography, Earth, and Environmental Sciences, University of Northern British Columbia, Prince George, BC, Canada

[4]Department of Geography, University of Victoria, BC, Canada

[5]Department of Earth Sciences, UC Santa Barbara, CA, United States.

This article will soon be submitted to the *Journal of Geophysical Research: Solid Earth.* I conceptualized this study and created research partnerships (primarily via the NSERC Alliance Grant program) between the Yukon Geological Survey, Geological Survey of Canada, Hakai Institute, University of Northern British Columbia, Yukon University, and University of Victoria to fund and undertake this project. I led several field campaigns, and led data processing, and interpretation. I wrote the manuscript and created all figures. Guy Salomon assisted with multiple field campaigns, contributed to data processing analysis, and provided minor manuscript edits. Dr. Edwin Nissen and Dr. John Cassidy co-supervised this project, assisted with funding acquisition, and contributed to data interpretation and manuscript preparation. Dr. Brian Menounos directed the collection of the majority of crewed airborne lidar used in this study and made minor manuscript edits. Roger Stephen made major contributions to fieldwork and data processing. Dr. Jeremy Gosselin provided crustal stress data from earthquake focal mechanisms. Dr. Kristin Morell contributed to data interpretation and manuscript preparation.

4.2 Abstract

The Denali fault is one of North America's longest active strike-slip faults, but the kinematics and earthquake potential of its eastern section in Canada remain poorly understood. Using a new, near-continuous airborne lidar dataset, we map the ~350-km-long surface trace of the Eastern Denali fault (EDF), and measure dip-slip and strike-slip offsets to constrain its kinematics. Though the EDF is situated within a nearly fault-perpendicular, compressive strain field, we show that it is dominantly a dextral strike-slip fault with only a minor reverse component. We also provide new slip rate estimates of 3.8 mm/yr that are slightly higher than previously reported for the Yukon segment of the EDF. Our structural analysis constrains the fault dip to >80º, and, using a new crustal stress catalog we show that the maximum shear stress resolved on this steeply-dipping fault plane would produce dominantly strike-slip motion, consistent with the geomorphic offsets. We hypothesize that strain in this overall convergent setting is partitioned between small thrust earthquakes, and large, infrequent strike-slip earthquakes, which facilitate overall shortening by way of northwestward tectonic escape of the St. Elias Mountains. Despite being a minor component of the slip vector, the vertical offsets correspond to topographic patterns in the hanging wall and footwall, implying that the fault plays a role in regional landscape evolution. Using empirical earthquake scaling relations, we show that our measured offsets of young fluvial terraces as well as the continuity of the scarp are consistent with large strike-slip ruptures (M_w 7.4 to 8.0), underscoring the seismic hazard to regional communities, natural resource development projects, and critical infrastructure.

4.3 Introduction

In the continents, many of the very largest earthquakes with moment magnitudes (M_w) of around 8 occur on 100s of km-long, structurally-mature, strike slip faults (Barka and Eyidoğan, 1993; Wald et al., 1993; Özalaybey et al., 2002; Klinger et al., 2005; Choi et al., 2018; Goldberg et al., 2023). The >2000 km-long Denali fault is one such fault, and one of only a few in North America. It is subdivided into a western section that strikes northeastward across western Alaska, a central section that curves eastwards through the Alaska ranges, and an eastern section that bends southeastwards across SW Yukon and NW British Columbia and into the Alaska panhandle. The central section, known as the Central Denali fault (CDF), hosted the largest modern earthquake in continental North America, the 2002 M_w 7.9 Denali earthquake (Eberhart-Phillips et al., 2003; Kayen et al., 2004; Haeussler et al., 2004). In contrast, the eastern section, termed the Eastern Denali fault (EDF), has a poorly defined earthquake potential despite its proximity to the eastern end of the 2002 rupture, and its clear, continuous surface trace. The purpose of this paper is to constrain this earthquake potential.

Though the EDF has been relatively seismically quiescent during the ~150 yr-long written and historical period, a conspicuous post-glacial scarp provides evidence of surface rupture, and paleoseismic investigations suggest up to five strike-slip, surface-rupturing earthquakes in the past 6800 years at a single central trenching site (Blais-Stevens et al., 2020). However, crustal maximum horizontal stress orientations and GNSS velocities are near-perpendicular to the fault (Figure 4.1) and only limited seismicity occurs along its trace, leading to suggestions that it is no longer active, or at least waning in activity (Marechal et al., 2015; Choi et al., 2021). Moreover, the modern kinematics of the EDF are not well defined. The scarp is generally northeast-facing (south-west-side up), leading many to infer dominantly reverse slip (Bostock, 1952; Clague, 1979; Marechal et al., 2018; Choi et al., 2021). Others have interpreted an enigmatic series of sediment mounds and depressions observed along the fault as a series of positive and negative flower structures associated with dominantly strike-slip movement (Haeussler et al., 2017; Blais-Stevens et al., 2020).

The magnitudes of past earthquakes are also not rigorously constrained. It remains uncertain whether a similar size and style of earthquakes to the 2002 M_w7.9 CDF rupture have occurred on the Canadian segment of the EDF in the past, and how they are related to large ruptures on the CDF in space and time. Examining the Denali-Totschunda intersection, Schwartz et al., (2012) speculated that the only reason the 2002 rupture deviated from the CDF onto the Totschunda is because more time had elapsed (and more strain had accumulated) since the previous rupture on the Totschunda fault. This observation highlights the possibility of a direct linkage between ruptures on the CDF and EDF. Blais-Stevens et al. (2020) estimated magnitudes of >M6 based on the observation that mole-track features – as occur along the EDF – only develop in large >M6 earthquake ruptures globally. However, given the extreme length and continuity of the Holocene scarp, it is critical to consider whether the entire EDF and CDF have ruptured together in single large “end member” events, or in multiple smaller, segmented events.

To address these outstanding questions, we surveyed and compiled a near-continuous 400-km-long swath of airborne lidar data along the fault scarp from the Denali-Totshunda fault intersection in Alaska, southeast to near Haines Junction, Yukon (Figure 4.2). These surveys are the first widespread acquisition of lidar along the EDF. Using the high resolution lidar data, we map the scarp in detail and examine its morphology to gain a better understanding of fault geometry, kinematics, and rupture behaviour. We show that despite the fault being oriented at a high angle to the maximum strain and principal stress, geomorphic offsets are indicative of dominantly dextral strike-slip motion. We further show that the fault must be steeply-dipping (>80°), and via kinematic analysis we demonstrate that the current stress field would produce nearly pure strike-slip motion when applied to this fault geometry. Our findings challenge the notion that the EDF is no longer active as a consequence of its orientation within the stress field (e.g., Choi et al., 2021). Instead, strain is evidently partitioned between large strike-slip earthquakes on the inherited steeply-dipping geometry of the EDF, and smaller thrust events occurring diffusely within the fault damage zone and on other faults within the St. Elias Mountains.

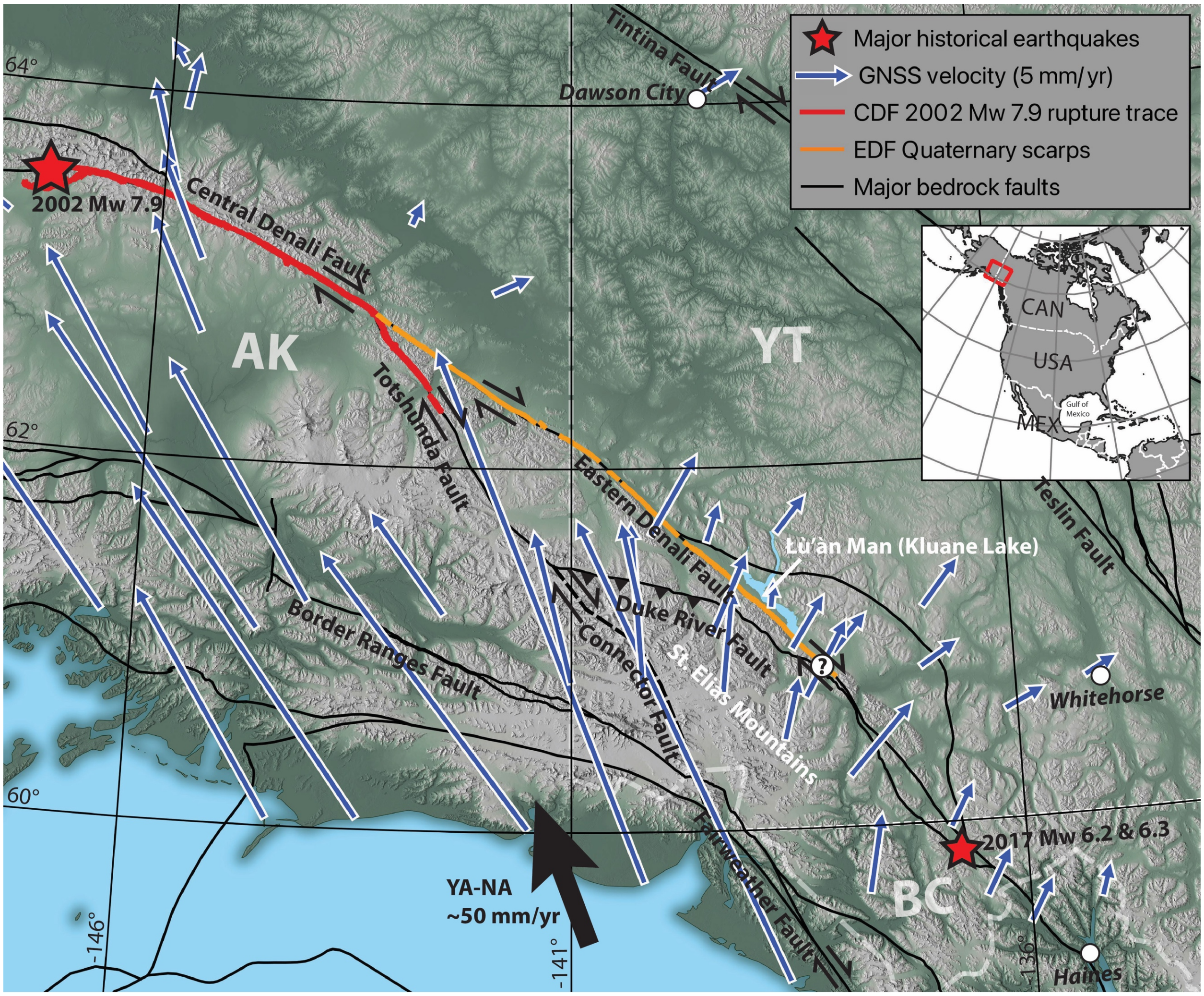

Figure 4.1. Tectonic setting of the EDF. A subset of GNSS velocities relative to stable North America from Elliott and Freymueller (2020) illustrate the inboard transfer of strain from the oblique subduction of the Yakutat block.

4.4 Background

4.4.1 Regional Tectonics and Geology

The >2000 km-long Denali fault strikes northeastward through central Alaska before curving southeastward through SW Yukon, NW British Columbia and the Alaska panhandle. Originally a Cretaceous accretionary suture between insular and intermontane superterranes (Colpron et al., 2007), the neotectonic activity of the EDF is largely a consequence of the flat slab subduction of the Yakutat microplate in southeastern Alaska (McDermott et al., 2019), which drives strain far inboard of the plate boundary (Figure 4.1). Waldien et al. (2021) estimate a total dextral offset of ~465 km since 52 Ma on the basis of offsets between the McClaren and Kluane Schists, making the Denali fault an end member in terms of structural maturity (Manighetti et al., 2007; Dolan and Haravitch, 2014; Thakur and Huang, 2021). The possibility of larger offset on an older proto-Denali fault is also recognized (Wahrhaftig et al., 1975; Waldien et al., 2021). Kinematic indicators from rare bedrock exposures of the fault zone are consistent with dominantly strike-slip motion, but indicate a component of fully partitioned reverse slip as well (Caine et al., 2024). Thermochronological data appear to indicate that the EDF acts as a tectonic backstop, as Cenozoic exhumation rates are much greater on the southwest side of the fault compared to the northeast (Enkelmann and Falkowski, 2021).

4.4.2 Quaternary Geology

The EDF lies near the maximum extent of Late Pleistocene (late Wisconsinan) Marine Isotope Stage (MIS) 2 glaciation, which covered much of the Canadian Cordillera, substantially reshaping the landscape and thus providing a primary constraint on fault slip rate (Figure 4.3). Several short segments of the westernmost, Alaskan portion of the EDF were last ice-covered during the MIS 6 Reid glaciation, which receded at ~132 ± 18 ka (Demuro et al., 2012). The majority of the EDF disrupts the Late Pleistocene glaciated surface, from which ice began to recede around 18.5-16.5 cal kyr B.P. and was likely completely ice free by 12.5 cal kyr B.P. (Dalton et al., 2023). The main ice sheet in the St. Elias Mountains was drained by a NW-flowing ice stream in the Shakwak Valley (in which the EDF trace lies), and the landscape is broadly characterized by a series of NW trending, ~2-3 km-long, mega-scale glacial lineations (MSGLs) that are subparallel to the trace of the EDF (Eyles et al., 2018). The Alaskan portion of the EDF was crossed by several piedmont lobes emanating from the Chisana, Nabesna, and other minor river valleys. As the Late Pleistocene ice retreated, paraglacial sedimentation caused a series of large debris fans to form from drainages in the Kluane Ranges. As with many paraglacial fans in the Cordillera (Ballantyne, 2002), these have become less active during the late Holocene with most flows restricted to their central channels (Koch et al., 2014).

4.4.3 Active Tectonics

The EDF exhibits less seismicity than neighbouring faults to the SW (Figure 4.4), which has led to debate regarding its modern activity. Slip rates derived from geodetic, seismic, and geomorphic studies are markedly lower on the EDF than on the CDF in central Alaska (Leonard et al., 2008; Marechal et al., 2015; Haeussler et al., 2017). It is apparent that a large portion of strain from the Yakutat collision is accommodated instead on the more westerly Totshunda fault, and a hypothesized "Connector Fault" (Figure 4.1) that links the Totshunda fault with the Fairweather fault through a heavily glaciated and inaccessible region of the St. Elias Mountains (Spotila and Berger, 2010; Doser, 2014; Marechal et al., 2015; Elliott and Freymueller, 2020; Biegel et al., 2024). The Duke River fault also appears to take up a significant portion of northeast directed shortening, and is host to a high rate of seismicity (Marechal et al., 2018; Biegel et al., 2024).

In 2016, a M_w 6.2 and 6.3 earthquake doublet occurred near the southern end of the EDF (Feng et al., 2019). Choi et al. (2021) found that the epicentres of the mainshocks and a cluster of aftershocks were located closer to the Duke River fault, which is parallel to, and less than 10 km from the trace of the EDF at this location. They found that maximum principal stress orientations calculated from the main events and a cluster of aftershocks were oriented near-perpendicular to the EDF and on this basis, concluded that the EDF is no longer a significantly active fault, further suggesting that seismic hazard assessments for the region be revaluated.

In contrast to these studies that broadly downplay activity on the EDF, the existence of a major Quaternary fault scarp along its trace indicates that large earthquakes are possible. This scarp feature was first recognized by Bostock (1952) and studied in more detail by Clague (1979), who determined that the EDF had likely ruptured in the early and mid-Holocene, but not more recently than 500 years ago. Three paleoseismic trenches were excavated on the EDF near Shắr Ndü Chù (the Duke River) but the results were not formally published beyond conference abstracts (Seitz et al., 2008; Lipovsky et al., 2009). Blais-Stevens et al. (2020) re-excavated these trenches and integrated other data from lake sediment cores and exposures of Holocene sediment, ultimately concluding that up to four >M_w 6 events have occurred in the last 6000 years.

4.4.4 Geothermal Energy Exploration

In addition to its seismic hazard, there is interest in the EDF as a geothermal energy exploration target (Witter, 2020; Tschirhart et al., 2022), with the goal of providing heating and potentially electricity to the Kluane First Nation community of Burwash Landing. Geothermal conditions in Yukon are generally favourable; terrestrial heat flow is in the range of 80-100 mW m^{-2} over a broad area of the territory and curie point depth mapping indicates a particularly steep geothermal gradient (40ºC/km) in southwestern Yukon (Witter et al., 2018; Gaudreau et al., 2019). Additionally, warm water has been encountered in several groundwater wells adjacent to the EDF (EBA Engineering Consultants, 2004; Tetra Tech, 2017), and a warm spring with outlet temperatures of 16ºC and estimated maximum temperatures at depth of ~100ºC exists near the fault at the Jarvis River (Crandall and Sadlier-Brown, 1976; KGS Group, 2016). It has been speculated that the EDF might provide the necessary permeability to allow thermal fluid to ascend to the near surface where it might be economically accessible via drilling (Witter, 2020). There are several related factors that contribute to fault permeability, the most important of which are fault age (timing of last activity), slip rate, stress orientation, and kinematics (Faulds and Hinz, 2015; Faulds et al., 2015). Young, seismically active faults are generally more permeable due to episodic refracturing of mineral precipitate that would otherwise seal the fault (Curewitz and Karson, 1997). A maximum principal stress oriented perpendicular to a fault will tend to “clamp” the fault shut, whereas an oblique or fault-parallel (extensional) stress field will cause slip or dilation and maintain permeability (Meixner et al., 2016). Thus, determining these key parameters is not only important for seismic hazard analyses, but also for geothermal energy exploration.

4.5 Data and Methods

4.5.1 Lidar Surveys and Fault Trace Mapping

We compile lidar data from several major survey campaigns to cover 400 km of the EDF from the Totshunda fault intersection to Haines Junction (Figure 4.2). The first dataset is the 2008 EarthScope Alaska lidar survey (https://doi.org/10.5069/G9QN64NF) of the northwestern 90 km of the fault, southeast of the Totshunda fault junction. The second dataset is a 70 km-long survey collected in 2018 by the Hakai Airborne Coastal Observatory platform along the southwestern side of Łù’àn Mā̀n (Kluane Lake). The third, flown in 2024, is comprised of two segments, a 125 km-long survey from the Alaska border to the north end of Łù’àn Mā̀n (Kluane Lake), and a 74 km-long segment from the south end of Łù’àn Mā̀n (Kluane Lake) to the headwaters of the Alsek River west of Haines Junction. We also make use of a small area of lidar collected by the Yukon Department of Highways and Public Works at the southeast end of Łù’àn Mā̀n (Kluane Lake) near Män Shìè’aya (Silver City). All airborne lidar surveys resulted in digital terrain models (DTMs) with pixel resolutions of 1 m. A 40 km segment of the fault west of the Yukon-Alaska border is not covered by lidar, and we rely on version 4 of the ArcticDEM dataset (Porter, 2023), which offers 2 m pixel resolution. We further complement these datasets with higher resolution drone-based lidar surveys over select, road-accessible segments of the fault in the summers of 2021 and 2022. The drone system achieved an average point density of 98 pts/m^2 with a ground return density of 45 pts/m^2, resulting in a bare earth DTM with a 30 cm pixel size. For details of the drone lidar platform and surveying procedures, see Finley et al. (2022b) and Salomon et al. (2024).

Using these high resolution topographic datasets and their derivatives (hillshade, slope, and aspect), we map the entire surface trace of the EDF in detail, improving on past efforts that were limited to lower resolution datasets (Bender and Haeussler, 2017; Haeussler et al., 2017; Marechal et al., 2018). We assign the fault traces qualitative confidence ratings of “high”, “moderate”, and “low” to reflect our certainty of fault position. We assign a rating of “inferred” where the fault scarp is not evident, but the fault can reasonably be assumed to be continuous between two aligned traces (e.g., where the fault trace disappears while it crosses an active stream channel, and reappears, in alignment, on the other side). We do not draw a fault trace where no scarp is observed and its position cannot be easily inferred. Thus, our fault trace represents the continuity of the Holocene rupture, which may have implications for fault segmentation.

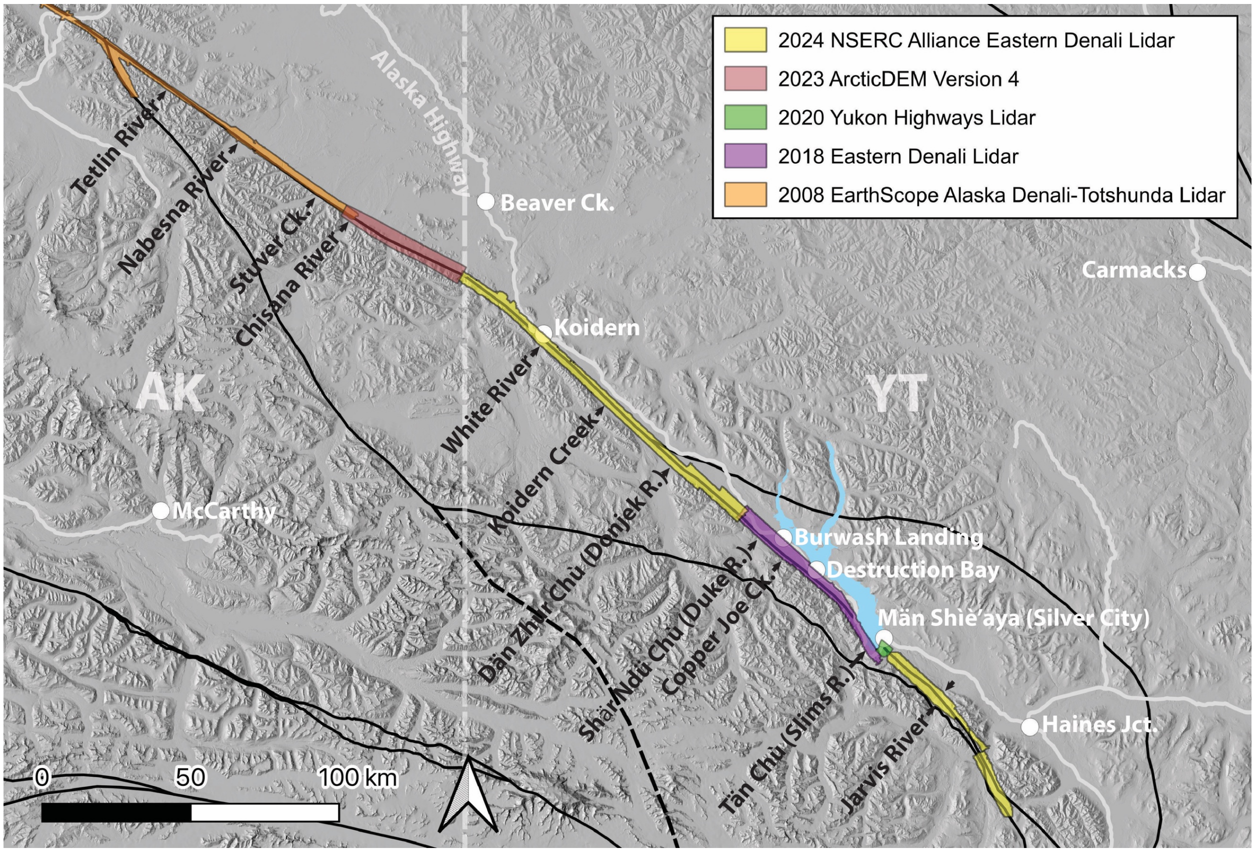

Figure 4.2. Extent of recent lidar and ArcticDEM data coverage compiled along the EDF for this study. Drone lidar survey footprints are too small to be shown at this scale.

4.5.2 Surficial Mapping and Geochronological Constraints

We use the new lidar data to map the surficial geology along the EDF trace, guided by regional surficial mapping of the area by the Yukon Geological Survey (Kennedy, 2013; Kennedy and Ellis, 2020; Ackerson et al., 2025). For essentially its entire length, the EDF cuts across unconsolidated Quaternary deposits with very few cross-sectional exposures. We distinguish two major surficial units relevant to the slip rate and timing of past ruptures on the EDF. The first is a morainal blanket deposited during the last glacial maximum. This surface is characterized by megascale glacial lineations (MGSLs) that indicate northwestward ice flow of an ice stream in the Shakwak Valley (e.g., Figures 4.8 and 4.9). Cross-sectional exposures of this unit are rare, however a bluff on the north side of Shä́r Ndü Chù (the Duke River) reveals a thin (<5 m) veneer of morainal deposits (till) overlying a >50 m sequence of stratified glaciofluvial outwash gravel.

The second major surficial unit is a series of fluvial fan deposits associated with major drainages emanating from the Kluane Ranges. These fans incise 10s of meters into the morainal and outwash deposits, and the large, outermost riser makes their boundaries relatively clear in lidar. Several of these fans have been previously dated using dendrochronology and tephrochronology, which indicate they were most active during the late Pleistocene to early Holocene immediately after deglaciation (Koch et al., 2014). Within each fan, there are typically multiple internal terrace levels and the modern rivers and creeks are typically restricted to relatively narrow channels with limited flood plains. The majority of fans are blanketed with the White River Ash (~1900 and 1250 years B.P.; Lerbekmo, 2008), indicating that there have been limited channel avulsions since this time (Koch et al., 2014). At several accessible locations on the Shä́r Ndü Chù (Duke River) and Nines Creek fans we excavated pits to test for the presence or absence of these two prominent ash layers on faulted and unfaulted terrace levels, in an attempt to constrain late Holocene slip rate.

To estimate the longer term late Quaternary slip rate based on offsets to the glaciated surface, we use existing chronostratigraphic constraints on the age of deglaciation. Specifically, we rely on the North American Deglacial Isochrone (NADI-1) database (Dalton et al., 2023), which provides a thorough compilation of age constraints from the literature, and interpreted deglacial isochrones in calendar years based on that data. The primary dataset used in the NADI-1 ice sheet reconstruction are terrestrial cosmogenic nuclide (TCN) exposure ages of moraine features, which directly record the removal of ice cover. Radiocarbon ages generally indicate the establishment of vegetation, and therefore lag behind deglaciation, providing a more indirect constraint. Radiocarbon ages are converted (by Dalton et al. 2023) to calendar years using the IntCal20 calibration curve (Reimer et al., 2020). Figure 4.3 shows the key TCN and radiocarbon ages from NADI-1, constraining deglacial timing in the vicinity of the EDF. With the exception of short segments of the fault in Alaska, the majority of the EDF fault trace was covered by ice during the Late Pleistocene last glacial maximum (LGM). Based on NADI-1, much of the Alaskan portion of the EDF was ice-free by 16.5 cal kyr B.P. The Yukon portion of the EDF was likely ice covered until 14.5 cal kyr B.P. Fully ice-free conditions are recorded by several radiocarbon ages averaging 12.5 cal kyr B.P.

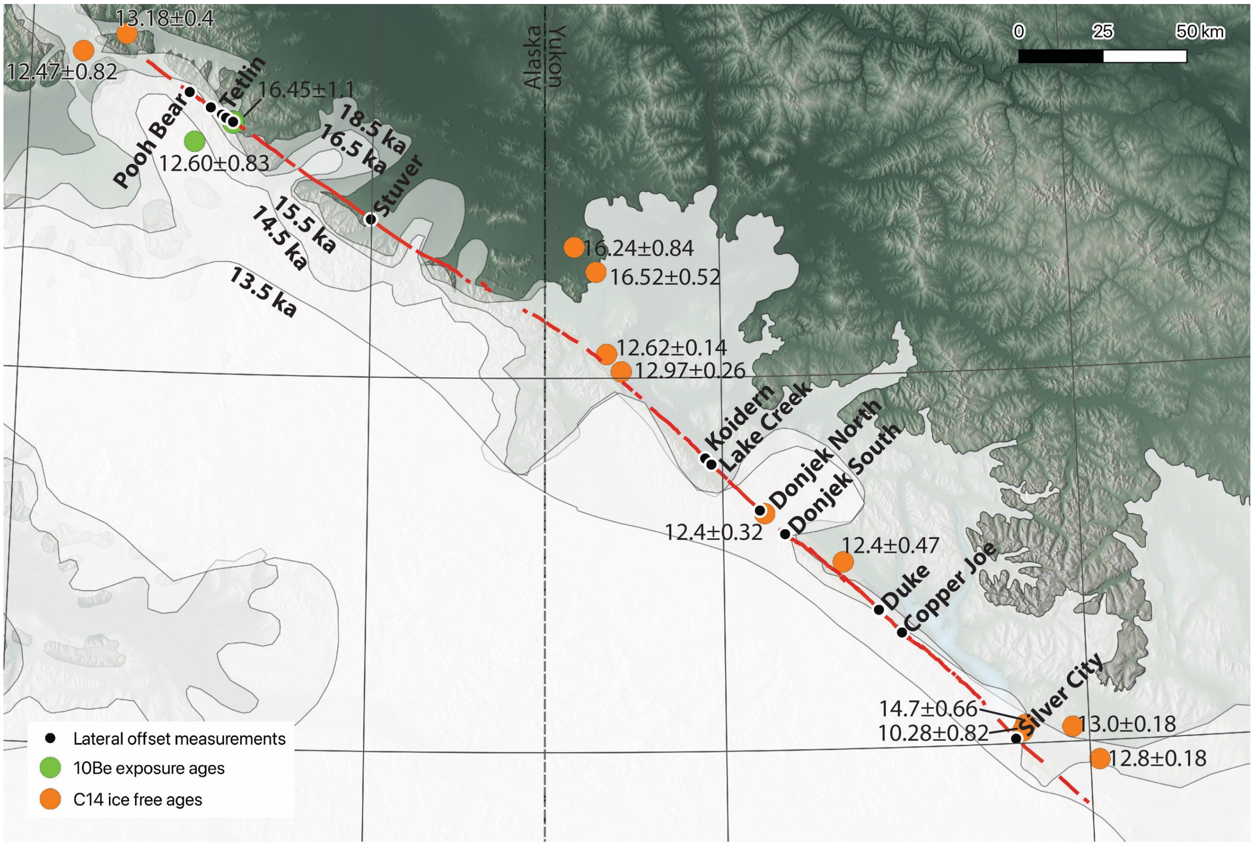

Figure 4.3. Constraints on deglacial timing from Dalton et al. (2023) and references therein. Maximum glacial limits in the Yukon are based on geomorphic mapping by Duk-Rodkin (1999). Maximum limits in Alaska are based on the Alaska PaleoGlacier Atlas (Kaufman et al., 2011).

4.5.3 Fault Dip and Dip-Slip Offset

To analyze dip-slip offset across the EDF scarp we used the Monte Carlo Slip Statistics Toolkit (MCSST) developed by Wolfe et al. (2020) following methods established by Thompson et al. (2002). Applied to fault-perpendicular topographic profiles, MCSST samples uncertainty distributions for the fault dip, fault position on the scarp, and topographic slopes of the hanging wall and foot wall to arrive at a probability density function of dip-slip offset. We assign trapezoidal distributions to represent uncertainty in fault dip, wherein the wide base of the trapezoid defines the entire range of possible values, and the narrow top of the trapezoid represents the range of most likely values. For much of the fault length, its surface trace is subparallel to topographic contours, making it challenging to estimate fault dip. However, south of Łù’àn Mān (Kluane Lake), the EDF scarp climbs over a broad pass, returning to a similar elevation at the Jarvis River. The fault strike is near-perpendicular to the topographic contours and its surface trace remains linear, implying a near-vertical dip. Using structure contours, we show that with fault dips any less than 80º, the fault trace would deviate significantly from the observed surface trace. A steep fault dip is also supported by fault plane measurements from rare bedrock outcrops of the main EDF at Telluride and Kimberley Creeks (Figure 4.11; Caine et al., 2024), and our own structural measurements of fault planes exposed in Nines Creek, Duke River, and Burwash Creek, ~2-4 km southwest of the main fault trace. Based on this analysis, we allow for a steeply-dipping fault in our MCSST analyses, with the highest probability between 85° NE and 85° SW, and lower probability extending to 75° NE and 75° SW. We assign the highest probability to a fault-scarp intersection between 1/3 and 2/3 of the scarp width, but allow for a fault-surface intersection over the entire width of the scarp.

We apply MCSST to 151 topographic profiles extracted across the fault at hand-picked locations (Figure 4.5). Profiles are placed where the scarp shows a clear facing direction, and the land surface on either side shares a similar morphology and slope. This approach excludes locations where there is no apparent vertical offset across the scarp, but such locations are rare, and the scarp generally has an obvious facing direction. We combine the probability density functions of each measurement to produce cumulative offset probability distributions (COPD) of dip-slip offset of the Late Pleistocene glacial surface, and Holocene fluvial/paraglacial fans (Figure 4.5).

4.5.4 Strike-Slip Offsets

To measure lateral offsets, we use the LaDiCaoz (Version 2) tool (Zielke and Arrowsmith, 2012; Haddon et al., 2016), which uses back-slipping of DEMs to restore offset drainages and other piercing points. The tool includes an automated grid search function which attempts to minimize the misfit between fault-parallel topographic profiles by shifting them laterally and vertically, and stretching them. However, along the EDF, we find that most offset features are too complex for successful automated back-slipping, so we use the manual back-slipping function and assess results and uncertainties visually. Our minimum estimates represent a threshold at which the fault still appears to have a small discernible amount of right-lateral offset, and our maximum estimates represent a threshold where the fault begins to have a small discernible amount of left-lateral offset.

In total, we identify 14 sites at which convincing lateral offsets can be measured (Figure 4.6). Piercing points include morainal deposits, megascale glacial lineations, terrace risers, and channel thalwegs. We recognize that obtaining the true 3D slip vector for faults with oblique slip can be subject to high error, particularly where slopes angles are steep, slope aspects are at low angle to fault strike, and fault dip is shallow (e.g., Mackenzie and Elliott 2017). The majority of the fault trace mapped here, however, cuts across slope angles of less than 10°, and slope aspects are generally within 40° of fault-normal. As discussed above, the fault dip is also inferred to be steep, which minimizes the error introduced by oblique slip. Thus, a 2D approach is deemed sufficient.

4.5.5 Crustal Stress and Kinematic Analysis

We use a new focal mechanism catalog compiled by Gosselin et al. (2024) to evaluate the modern crustal stress field in which the EDF is situated. This catalog contains 363 crustal (<30 km deep) events in southwestern Yukon and neighbouring Alaska from between 2010 and 2022 (Figure 4.4) and represents the most complete set of focal mechanisms in the region. Gosselin et al. (2024) rely on double-difference-relocated hypocentral locations from Biegel et al. (2024) and use P-wave first motion polarities to determine focal mechanisms using the Bayesian Earthquake Analysis Tool (BEAT; Vasyura-Bathke et al., 2020). This probabilistic approach provides better quantification of uncertainties compared to other focal mechanism inversion methods, and therefore provides higher confidence in interpretations of the regional stress field.

The P-, M-, and T-axes of individual focal mechanisms can be poor approximations for regional principal stress orientations (McKenzie, 1969). Formal stress inversions assume that tectonic stress is uniform over some spatial extent and seek to find the minimum misfit between the resolved shear traction and the observed slip vectors for a group of focal mechanisms. Here, we use the STRESSINVERSE program developed by Vavryčuk (2014) to invert for stress at 50 km intervals along the surface trace of the EDF, using focal mechanisms from 100×100 km bins aligned to the strike of the fault. Each bin contains a minimum of 10 events and overlaps by 50 km with the neighbouring bin. We then use the “Stress on Plane” function in the FaultKin 8 software (Marrett and Allmendinger, 1990) to calculate the expected kinematics of the EDF. The program takes as inputs the trend, plunge, and relative magnitudes (stress ratio) of σ_1 and σ_3, and calculates the traction, normal, and shear stresses acting on a user-specified plane. This analysis is based on the principle that a fault will slip in the direction of the maximum shear stress resolved on the fault plane (Wallace, 1951; Bott, 1959). We calculate the expected kinematics for each 50 km bin along the fault, using a steep dip of 80°, and the average fault strike within that bin.

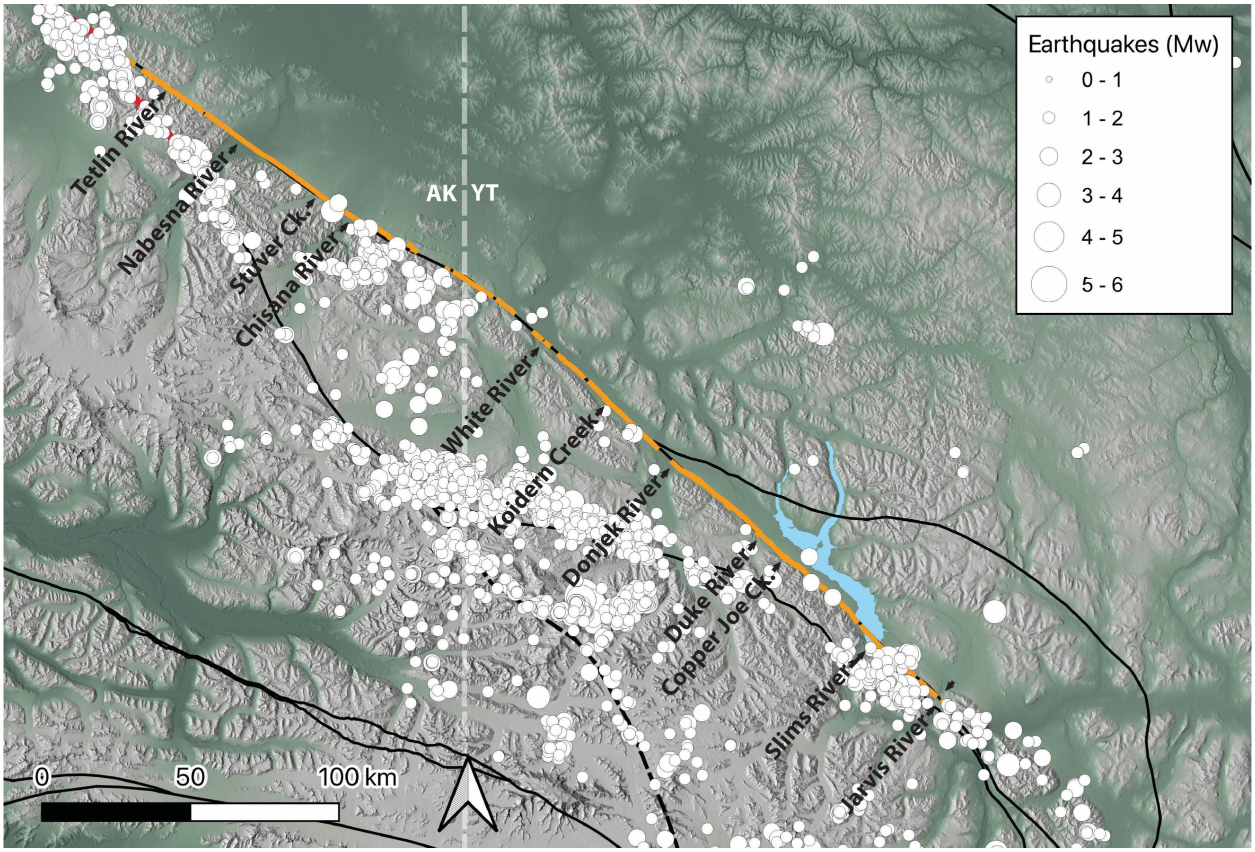

Figure 4.4. Relocated epicentres from Biegel et al. (2024), used in stress inversion by Gosselin et al. (2024) and this paper. Orange line indicates the Quaternary scarp on the EDF.

4.6 Results

4.6.1 Fault Trace Morphology

The fault trace is mostly linear and relatively unsegmented, consistent with the high structural maturity of the fault (e.g., Manighetti et al., 2007). Our full fault trace is provided as a shapefile in the supplement (Dataset S1). Detailed views of select segments are provided in Figure 4.7-4.11. Deformation appears to be highly localized to the main fault trace (e.g., Figure 4.7), with relatively limited off-fault deformation. In a few locations, short subparallel scarps (< 1 km long) occur within 1 km of the main fault trace (e.g., Shä́r Ndü Chù/Duke River, Figure 4.9). Identifying subsidiary fault strands is confounded by the fact that streamlined glacial landforms (MSGLs) are largely sub-parallel to the fault trace and share similar geometry (e.g., Figure 4.9).

At its northwest end, the scarp is directly connected with the CDF at the Totshunda fault intersection. For 100 km east of this point, the fault trace is highly linear, striking 125°, and is conspicuous, allowing for high confidence in mapping. At the Chisana River, the fault trace deviates 5° counterclockwise, then forms a broad right-hand bend, ultimately straightening to a 135° trend at the White River. In this curved segment between the Chisana and White Rivers, the fault scarp trace is less distinct and apparently less continuous, which is reflected in our sparse vertical and lateral offset measurements on this segment. We note that the first 40 km of this is not covered by lidar, only ArcticDEM so our confidence in identifying its trace is lessened; however, even where lidar coverage returns, the scarp is not well expressed. The scarp becomes more conspicuous south of the White River, and continues on a 135° trend for approximately 50 km, until it makes a 1000 m wide left-hand step via a series of four 200-400 m wide steps (Figure 4.8). From there, the scarp is continuous and easily traceable to the south end of Łù'àn Mǟn (Kluane Lake) where it is obscured by a series of young alluvial fans before crossing under the lake where it has been imaged with subbottom profiler (Clague, 1979). South of Łù'àn Mǟn (Kluane Lake) near Män Shìè'aya (Silver City), the fault trace climbs over a broad plateau (Figure 4.10), and ultimately appears to terminate abruptly in the vicinity of the Jarvis River (Figure 4.11). Our lidar surveys extend along the mapped bedrock fault trace of the EDF for a further 45 km in the mountainous regions west of Haines Junction (Figure 4.2), but reveal no compelling evidence of a Holocene fault scarp. Thus, we constrain the full length of the Holocene surface rupture of the EDF to be 354 km.

For much of its length, and especially on the segment of the fault between Łù’àn Mā̀n (Kluane Lake) and White River, the fault trace is characterized by a series of sediment mounds with dimensions on the order of ~100 m, and heights of 10 m (e.g., Figure 4.7 and 4.8). These features, which were previously identifiable in aerial imagery due to the preferential growth of White Spruce on them, have been interpreted as a series of en-echelon positive flower structures, or push-ups between Riedel shears (Haeussler et al., 2017; Blais-Stevens et al., 2020). Our lidar data adds new insight into the formation of these enigmatic features. First, it is clear that these mounds are caused by tectonic motion rather than fluvial dissection of a northeastward-facing scarp, as they are consistently elevated above the planar glacial surface on both sides of the fault trace. We distinguish two specific types of mounds. The first occur along linear segments of the fault with no apparent step-overs or bends in the overall fault trace. In some cases, these mounds demonstrate a preferred long axis orientation, and in others they are essentially circular in planform (Figure 4.7). These topographic features resemble push-ups observed in analog models of strike-slip faulting where deformation from a basement fault propagates through a thick sequence of weak or unconsolidated overburden (Richard et al., 1991; Schellart and Nieuwland, 2003; Dooley and Schreurs, 2012). In such models, the mounds develop under pure strike slip and do not necessarily require a component of transpression. Notably, similar aligned mounds are observed on the Tintina fault, a major Quaternary-active dextral fault in northwestern Yukon (Chapter 2), and on major strike-slip ruptures in central Asia (Baljinnyam, 1993; Fu et al., 2003; Rizza et al., 2015). The second form of mound occur at left-stepping bends in the fault trace and are generally larger than the aligned mounds, implying greater shortening across them. These mounds resemble push up features in analog sandbox models of restraining bends on strike-slip fault with weak sedimentary cover (e.g., McClay and Bonora, 2001). The Dän Zhǜr Chù (Donjek River) locality (Figure 4.8) offers a good example of both types of mounds in proximity. The vertical dimensions of the mounds require that they have been constructed over several earthquake cycles.

4.6.2 Dip Slip Offsets and Slip-Rate

The dip slip distribution along the EDF is shown in Figure 4.5. Broadly, the scarp is northeast-facing (southwest-side-up), with some exceptions. The first 25 km of the fault southeast of the Totshunda intersection has a variable facing direction, with several sites exhibiting northeast-side-up displacement. A ~2-km-long segment of the fault at Shär Ndü Chú (Duke River) is southwest facing (Figure 4.9), and the same is true of the southeasternmost 15 km of the fault near the Jarvis River (Figure 4.11). Where the scarp is northeast-facing, there is a dominant COPD peak of ~7 m of dip slip offset of the glaciated surface, and a more minor peak at 15 m, with some surfaces exhibiting offsets as high as 20 m. Southwest-side-up vertical separations on fluvial terrace surfaces, such as Koidern Creek (Figure 4.7) and Shä́r Ndü Chù (Duke River; Figure 4.9), are systematically smaller than the glaciated surface, yielding a COPD peak in dip slip offset of around 1.5 m. Taking 14.5 kyr as the average age of deglaciation, we calculate a mean dip slip rate of 0.5 mm/yr (southwest-side-up) on the basis of the dominant 7 m COPD peak. The dip slip rate may be as high as 1.0 mm/yr based on the 15 m COPD peak.

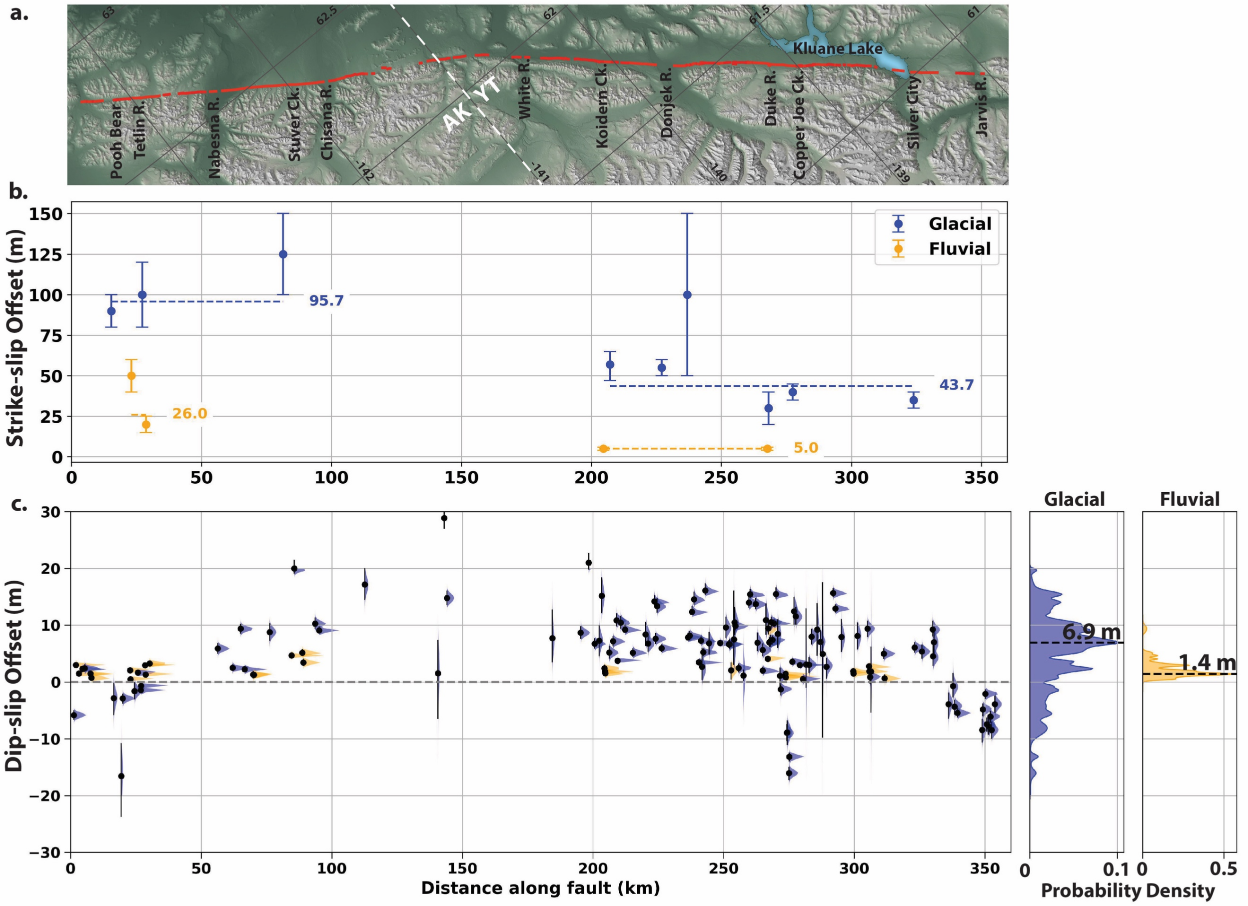

Figure 4.5. Lateral and dip slip offset distributions along the EDF. (a) Reference map of the EDF trace. (b) Lateral offsets based on LaDiCaoz analyses. Measurements are coloured according to whether they are from the Late Pleistocene glaciated surface (blue) or Holocene fluvial/paraglacial fans (yellow). (b) Dip slip offset distribution based on MCSST analyses. Panels on right show COPD peaks for measurements taken on glacial surfaces (blue) and fluvial/paraglacial fans (yellow).

4.6.3 Lateral Offsets and Slip-Rate

We identify fourteen locations that demonstrate compelling evidence of dextral offset. Offset features include braided channels and bars on Holocene fans, creeks and associated terrace risers incising the glacial surface, mega-scale glacial lineations, and paleo-lake shorelines (Figure 4.6 and Table 4.1). Lateral offsets to braided river channels and bars inferred to be Holocene age at Tetlin, Tetlin South B, Koidern Creek, and Shä́r Ndü Chù (the Duke River), are systematically smaller than those on adjacent Late Pleistocene glacial features. In general, offsets to both fluvial and glacial features are greater near the northwest end of the EDF and lower towards the southeast (Figure 4.5).

Our slip rate estimates are based on deglacial timing, which occurred diachronously along the EDF, with slightly older deglacial ages on the northwest end of the fault. On the northernmost segment of the EDF, a TCN age of 16.5±1.1 kyr in a moraine at the Tetlin South C site provides a maximum age of deglaciation (Matmon et al., 2006; Dalton et al., 2023). The oldest ice-free age from the vicinity of the EDF is 14.7±0.66 cal ka from organic matter in a kettle at the south end of Łù'àn Mā̈n (Kluane Lake) (Denton and Stuiver, 1967; Dalton et al., 2023), and this serves as a primary constraint on the timing of deglaciation on the southern segment of the fault. The majority of other ice-free ages are on average ~12.5 ka (Figure 4.3). We discuss each of the lateral offset sites from northwest to southeast, and constraints on slip rate, in detail below.

4.6.3.1 Pooh Bear (Buck Creek)

The Pooh Bear locality (also known as Buck Creek) is one of the most unambiguous lateral offsets on the EDF (Figure 4.6). An alluvial fan is incised by the modern creek, and the main riser is offset at a right angle across the fault. This site was examined by Haeussler et al. (2017) who estimated 75 ± 8 m of dextral offset and a slip rate of 2.7 ± 0.3 mm/yr, based on a TCN exposure age of 27.8 ± 3.1 ka which they acknowledge may be unrealistically old. Using LaDiCaoz, we estimate a slightly larger offset of 90 ± 10 m. We make the assumption that the alluvial fan and subsequent channel incision are both post-glacial as the fan deposits would have been eroded by overriding ice. We therefore estimate a minimum slip rate of 5.5 ± 0.9 mm/yr on the basis of the oldest realistic post-glacial TCN exposure ages (16.45 ± 1.1 ka) in the vicinity (Figure 4.3).

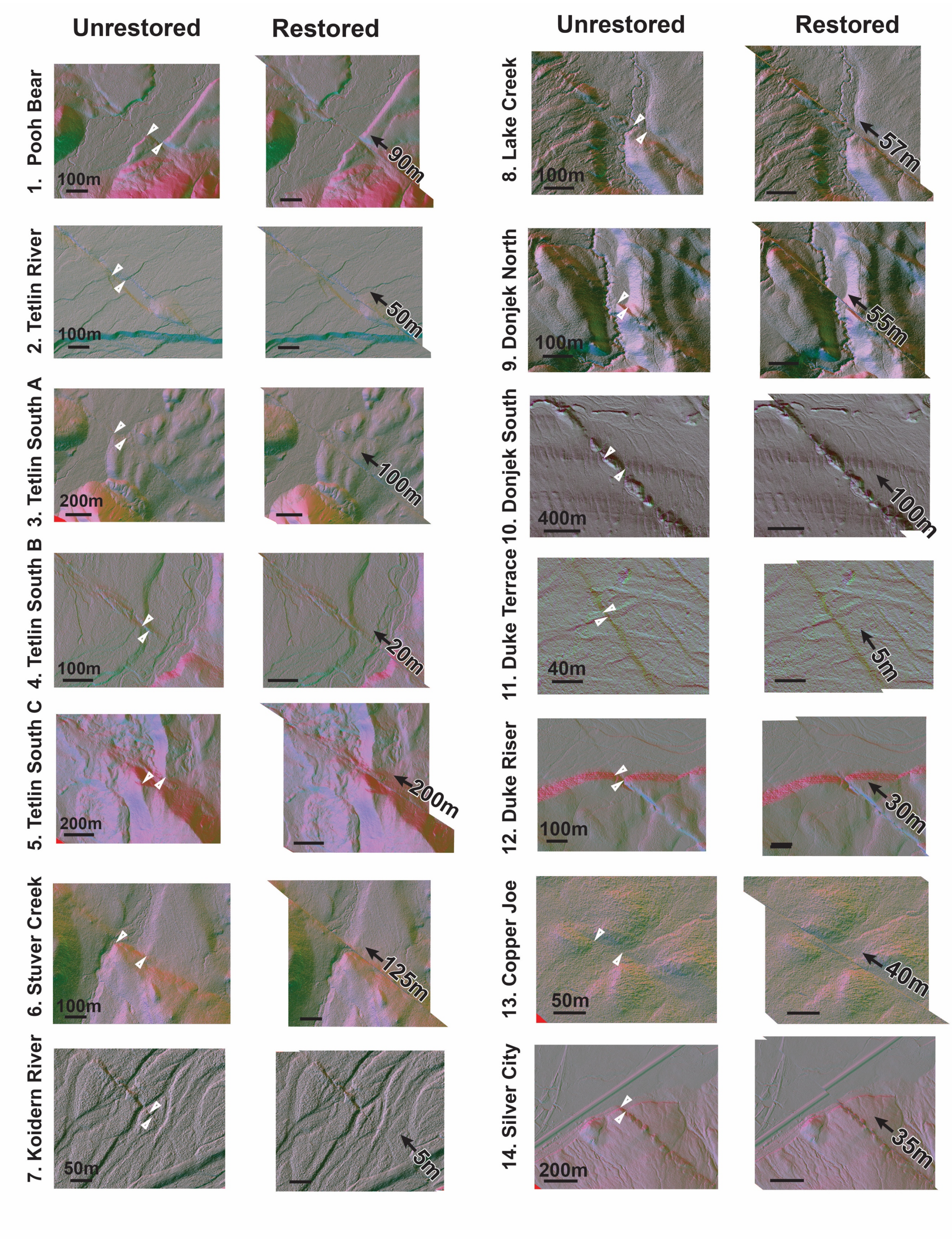

Figure 4.6. LaDiCaoz lateral offset backslipping results from the northwest (1) to southeast (14) end of the EDF. Grey hillshades are overlain by pink slope gradient maps. White arrows indicate the selected piercing point on each unrestored panel. Only the optimal offsets are shown. See Table 4.1 for details for each site.

4.6.3.2 Tetlin River area

There are four locations in the vicinity of the Tetlin River that exhibit evidence of dextral offset. The first is an elevated abandoned fluvial terrace on the north side of the river. Two minor channel risers that cross the EDF trace at high angles are dextrally offset by 50 ± 10 m. We assume this terrace is Holocene in age because the terrace is incised below the glacial surface, but having no direct age control, we do not estimate a slip rate here. Four kilometers to the south (Tetlin South A), a series of hummocky fault-normal ridges, which we interpret to be moraines, are offset by 100 ± 20 m. Using the oldest exposure age nearby (16.45 ± 1.1), we estimate a slip rate of 6.1 (+1.7/-1.5). A further 1.5 km south (Tetlin South B), the riser of a low terrace (presumable Holocene) on a minor creek is offset by 20 ± 5 m, and a further 2.5 km south (Tetlin South C) a prominent lateral moraine is offset by 200 ± 50 m. This latter site was identified by Matmon et al. (2006), who estimated a much lower offset (117 ± 21 m) and obtained several TCN exposure ages from boulders and sediment on the moraines. Exposure ages range from 9.7 ± 0.6 kyr to 16.4 ± 1.1 kyr. Using the oldest exposure age, we estimate a slip rate of 12.2 (+4.1/-3.7) mm/yr.

4.6.3.3 Stuver Creek

A minor creek immediately north of Stuver Creek exhibits clear evidence of lateral offset. The small creek incises an alluvial fan and the southern riser of the creek is offset by 125 ± 25 m. The northern riser has no apparent offset as it has been reworked by the creek. Marechal et al (2018) noted that there is no apparent lateral offset to the main Stuver Creek channel, and concluded that lateral offset continues no farther south along the EDF. However, we suggest the lack of lateral offset to the main channel is simply a preservation issue. This site is located at the limit of Late Pleistocene glaciation, and was likely deglaciated early, between 18.5 and 16.5 ka. We therefore estimate a slip rate of 7.1 (+2/-1.7) mm/yr.

4.6.3.4 Koidern Creek

The Koidern Creek locality (Figure 4.7) was previously examined by Marechal et al. (2018), who used a Pleiades DEM and RTK GPS surveys to measure offsets across a scarp observed crossing the Koidern Creek alluvial fan. In their coarser resolution topographic surveys, they observed no lateral offsets, and this site thus acted as a key constraint on their assertion that the

EDF is dominantly compressional. The lidar, however, reveals an apparent 5 ± 1 m right lateral of offset of two abandoned channels and an interchannel braid bar on the fan surface (Figure 4.7). Aside from a post-glacial age, we have limited constraint on the various terrace levels of the Koidern fan and do not calculate a slip rate here.

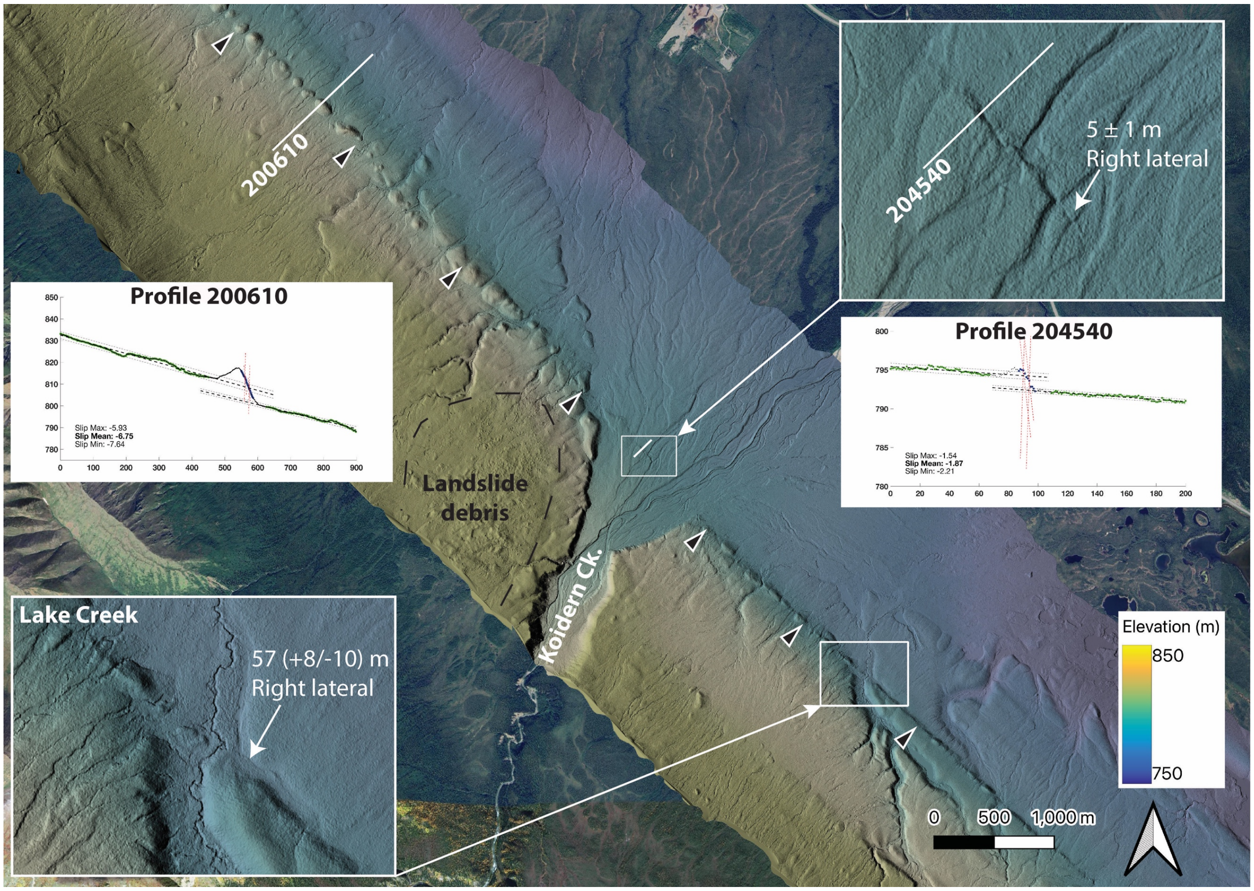

Figure 4.7. Detailed view of fault at Koidern Creek. In the northwest, the fault trace is characterized by a series of circular, aligned mounds. Where the fault crosses the Koidern Creek fan, older terrace levels are offset vertically and laterally. To the southeast, "Lake Creek" has a clear right-lateral offset of 57 (+8/-10).

4.6.3.5 Lake Creek

A minor tributary of Lake Creek, 2.5 km southeast of Koidern Creek, exhibits clear evidence of lateral offset (Figure 4.7). This offset channel was briefly noted by Haeussler et al. (2017) but not measured. An abandoned drainage on the downstream (northeast) side of the scarp is truncated by a shutter ridge, and the stream bank is offset right-laterally by 57 (+8/-10) m. The incision of the stream likely post-dates glaciation, so we use the deglacial age to estimate a minimum slip rate. Two local radiocarbon ages constrain ice free conditions to 12.4 cal kyr B.P (Lowdon and Blake, 1976; Dalton et al., 2023). However, Dalton et al (2023) place deglaciation of this site between 15.5 to 16.5 kyr. Using these upper and lower bounds, we estimate a slip rate of 3.9 (+1.3/-1.1) mm/yr.

4.6.3.6 Dän Zhủr Chù (Donjek River)

A minor creek ~ 1 km northwest of Dän Zhủr Chù (Donjek River) exhibits clear evidence of right-lateral offset; we measure 55 ± 5 m. Ice free conditions are locally constrained to 12.4 ka, and deglaciation is inferred to have occurred between 14.5 and 13.5. Thus, we estimate a minimum slip rate of 4.1 ± 0.7 mm/yr. On the southeast side of Dän Zhủr Chù (the Donjek River), the fault is defined by a prominent series of aligned mounds (Figure 4.8). Unlike most of the EDF trace, which is subparallel to the glacial flow direction, here the fault crosscuts several MGSLs at a ~40° angle, as noted in previous works (Clague, 1979; Haeussler et al., 2017; Blais-Stevens et al., 2020). These MGSLs are dissected by a series of semi-regularly spaced drainages, and the remnants form a series of subtle mounds, similar in horizontal dimension to the fault mounds, but with less vertical relief. We note that two of these dissected MGSLs appear to be right-laterally offset across the fault. Though an imprecise piercing point due to the width of the MGSL and the low angle at which it crosses the fault trace, we estimate 100 ± 50 m of right-lateral offset. Ice free conditions are locally constrained to 12.4 ka, and deglaciation is inferred to have occurred at 13.5 ka. Thus, we estimate a minimum slip rate of 7.7 (+4.3/-4.0) mm/yr.

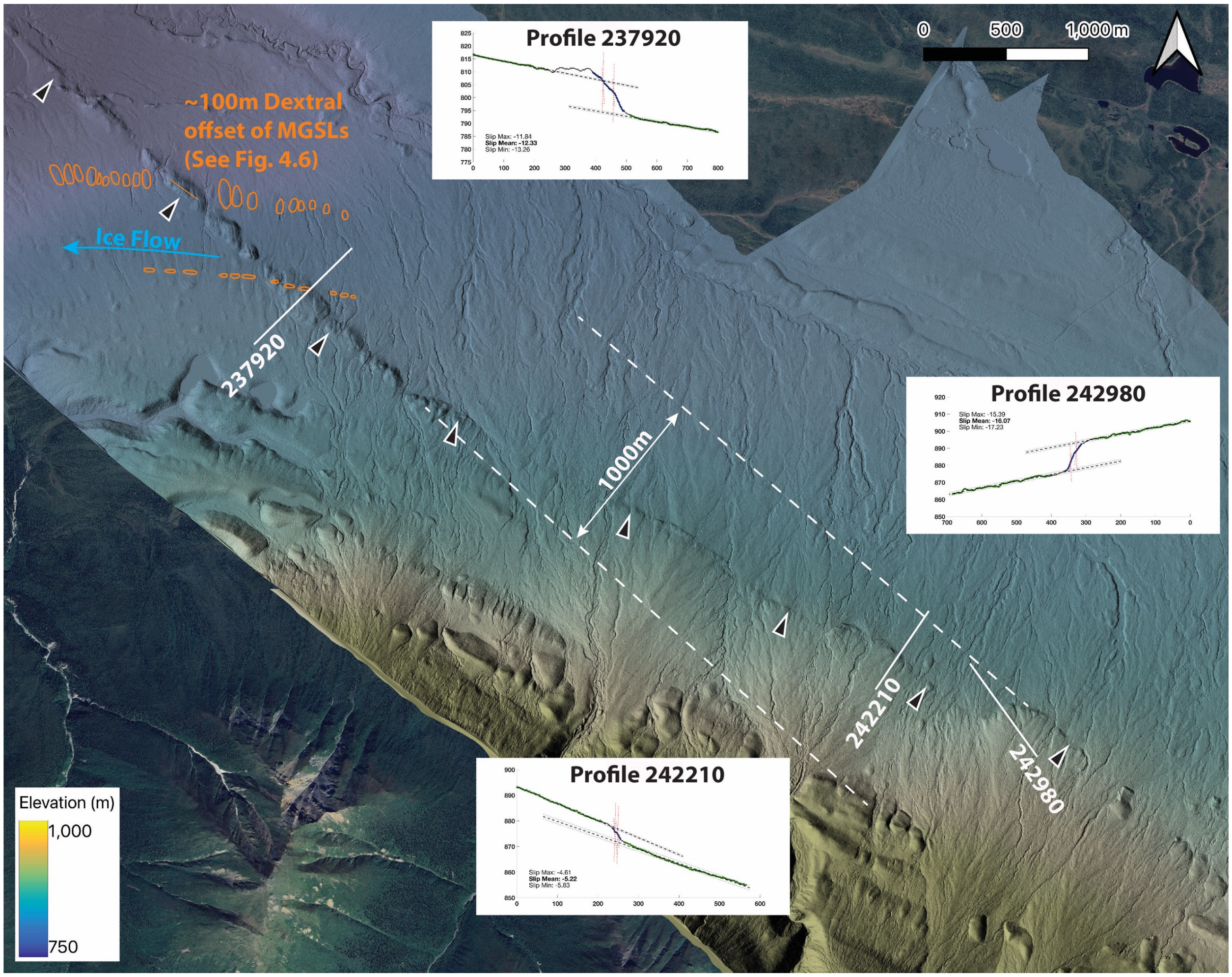

Figure 4.8. Detailed view of glacial surface southeast of Dän Zhǜr Chù (Donjek River). In the northwest, the fault trace is characterized by a series of aligned mounds, and appears to right-laterally offset streamlined glacial landforms. The fault here makes a 1 km wide left-hand step, representing the most significant deviation in fault strike for the entire 354 km fault length.

4.6.3.7 Shắr Ndü Chù (Duke River)

At Shắr Ndü Chù (the Duke River), two lateral offsets are observed (Figure 4.9). The first is on an abandoned floodplain on the southeast side of the river. A minor abandoned channel is apparently offset right-laterally by 5 ± 1 m. We excavated multiple soil pits in the terraces at Shắr Ndü Chù (the Duke River) and observed one layer of tephra, inferred to be the upper White River Ash dated at 1250 years BP (Lerbekmo, 2008). The lower White River Ash (1900 years BP) is not present despite being widespread in the region and conspicuous in other local

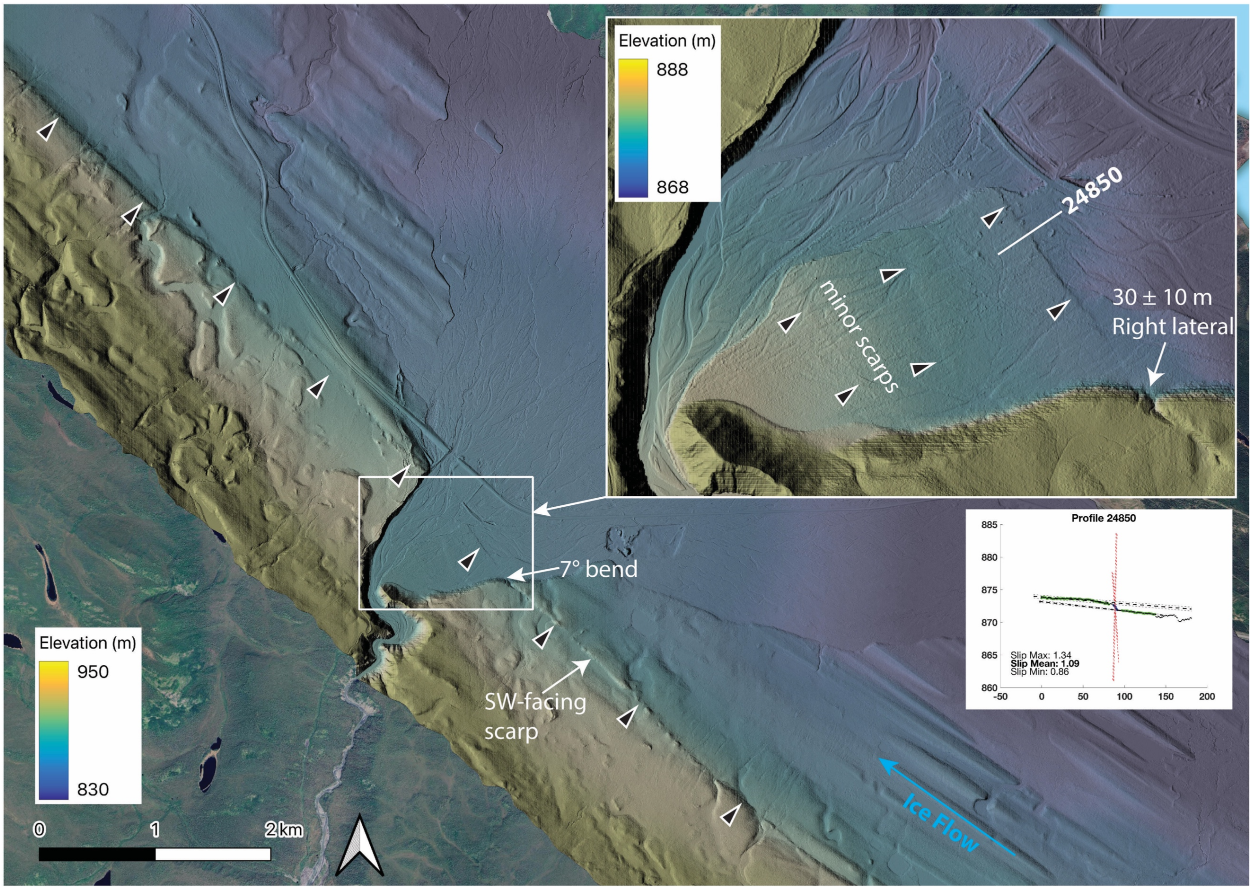

Figure 4.9. Detailed view of Shǟr Ndü Chù (Duke River). The fault strike is locally rotated 7° clockwise from the average fault strike, and the facing direction of the scarp is locally reversed. Inset shows off-fault deformation on the Shǟr Ndü Chù (Duke River) fan.

exposures (e.g., Blais-Stevens et al., 2020). It is therefore possible that the Shǟr Ndü Chù (Duke River) terrace was abandoned sometime between 1900 and 1250 years BP, subsequently blanketed by the upper White River Ash, and then faulted. This age yields a minimum slip rate of 3.2 (+1.8/-1.1) mm/yr, which is consistent with longer term minimum slip rates from glacial features nearby.

The second offset observed at Shǟr Ndü Chù (Duke River) is the main terrace riser on the southeast side of the fan. This offset was noted by Haeussler et al. (2017), but not measured. We estimate a right lateral offset of 30 ± 10 m, but acknowledge a high degree of uncertainty due to the curvature of the terrace riser and its oblique angle to the fault. Ice free conditions are locally recorded by a radiocarbon age of 12.4 ± 0.47, and Dalton et al (2023) place the 14.5 kyr deglacial isochrone at this location. Thus, we estimate a slip rate of 2.2 (+1/-0.8) mm/yr.

4.6.3.8 Copper Joe Creek

The Copper Joe Creek locality has previously served as a significant constraint on the EDF slip rate as it was previously the southernmost lateral offset measured without lidar. On the glacial surface to the northwest of the creek, Haeussler et al., (2017) noted a set of mounds with an apparent right lateral offset of 22.5 (+7.5/–2.5) m, which was used to infer a slip rate of 1.7 (+0.6/-0.2) mm/yr. Haeussler et al (2017) acknowledged low confidence in this measurement because no adjacent mounds exhibit an apparent lateral offset. Additionally, they recognized that the mounds would have had to form first, likely via several earthquake cycles due to their size, before being offset, and their slip rate estimate was likely an underestimate. Ice free conditions are locally constrained to 12.4 ± 0.47, and Dalton et al (2023) place the 14.5 kyr deglacial isochrone at this location. Using LaDiCaoz, we estimate a slightly larger lateral offset of these mounds of 40 ± 5 m and a slip rate of 3 (+0.8/-0.7) mm/yr. Like Haeussler et al. (2017) we consider this a minimum, and we place low confidence on it as an accurate offset marker.

4.6.3.9 Män Shìè’ay (Silver City)

The Män Shìè’aya (Silver City) site (Figure 4.10) offers critical constraint on the geometry, kinematics, and slip rate of the EDF. A series of aligned mounds immediately southeast of the Alaska Highway climb a hillside, maintaining a linear trend, which indicates a vertical dip. The southeast side of the scarp is also upthrown by ~4 to 9 m. Blais-Stevens et al. (2020) noted this site, suggesting that the mounds offset a post-glacial alluvial fan. Our surficial mapping indicates that it is the LGM surface that is offset, rather than an alluvial fan, and we are therefore able to use this site as a key constraint on slip rate. At the base of the hillside, adjacent to the Alaska highway, topographic contours are offset right-laterally across the fault. The base of this slope may represent the 17th century high-stand paleoshoreline of Łù’àn Mä̀n (Kluane Lake; Clague et al., 2006). There is no evidence to suggest the shoreline is deformed by the fault – instead it appears to onlap the offset of the glacial surface. As illustrated in the block diagrams in Figure 4.10, such an apparent lateral offset could be caused by either right-lateral or reverse slip (or some combination of both). However, our structure contour analysis here shows that the fault dip must be >80. Considering the steep dip, the fact that lateral offsets are consistently observed along the fault to the northwest, and the fact that the fault switches facing direction only 5 km south of this location, we believe the apparent right lateral offset is due to true right lateral offset. Additionally, the fact that the scarp height appears to decrease as it climbs the slope is more consistent with strike slip motion, as illustrated in Figure 4.10. Using LaDiCaoz, we estimate a right lateral offset of 35 ± 5 m of topographic contours on the hillside. Ice free conditions are locally constrained to 14.7 ± 0.66 ka, and we therefore calculate a minimum slip rate of 2.4 ± 0.4 mm/yr.

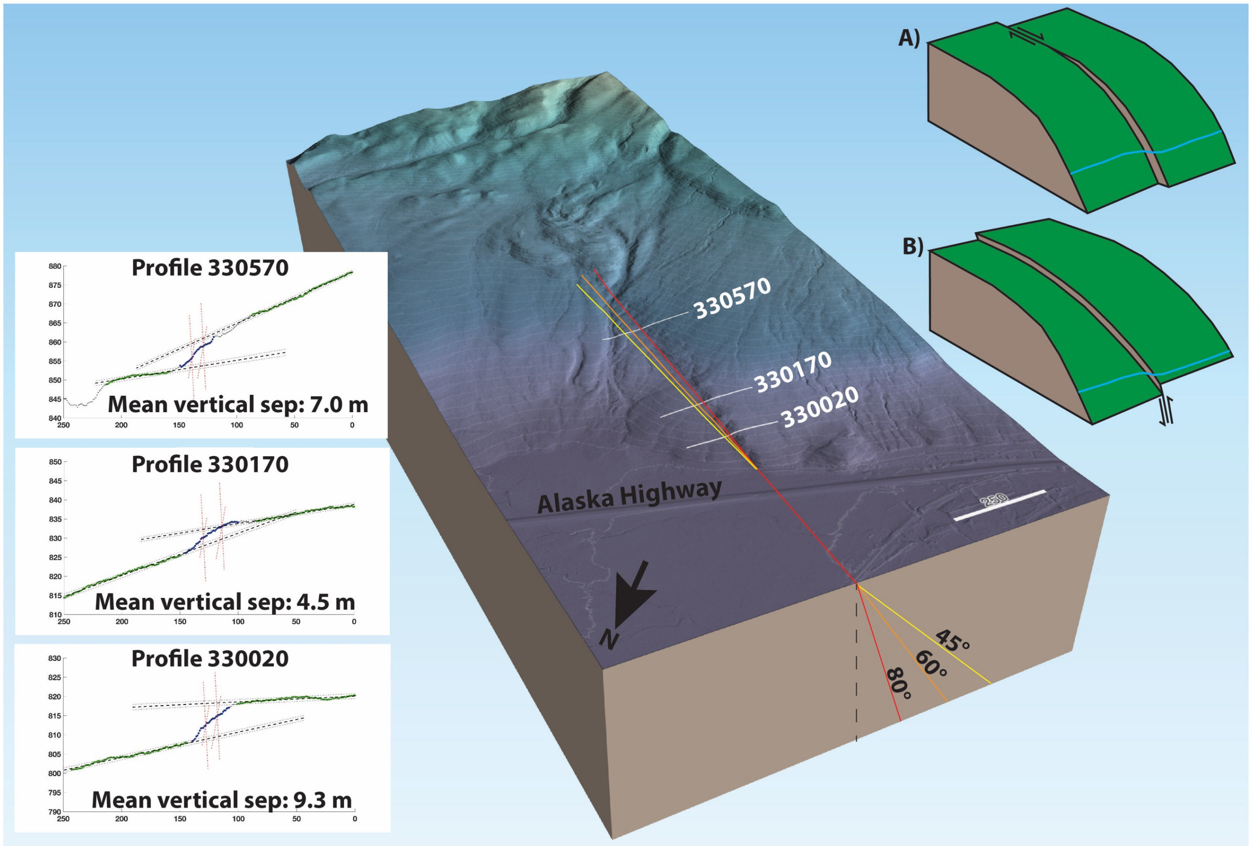

Figure 4.10. Three dimensional view of the fault scarp near Män Shìè'aya (Silver City). Structural contour analysis indicates that the fault must have a dip of at least 80°. Block models (top right) show expected scarp morphology for pure strike-slip and dip slip; model A is more consistent with what is observed. Topographic profiles with MCSST vertical separation measurements across scarp show that the land surface is not well restored by pure vertical slip on the fault.

4.6.3.10 Jarvis River

The EDF scarp appears to terminate on the northwest side of the Jarvis River (Figure 4.11). For the last ~20 km of its length, the scarp is consistently southwest-facing. The switch in facing direction itself provides evidence of predominantly strike-slip motion, and the linearity of the scarp as it crosses topographic contours as it descends into the Jarvis River valley is evidence of a steep dip. Both the change in facing direction and the steep dip are inconsistent with reverse slip. Moreover, the scarp is relatively "fresh" in appearance, and what appear to be Riedel shears rotated ~15 clockwise from the fault strike are evident, and indicative of right-lateral shear (Figure 4.11). However, no laterally-offset piercing points are observed.

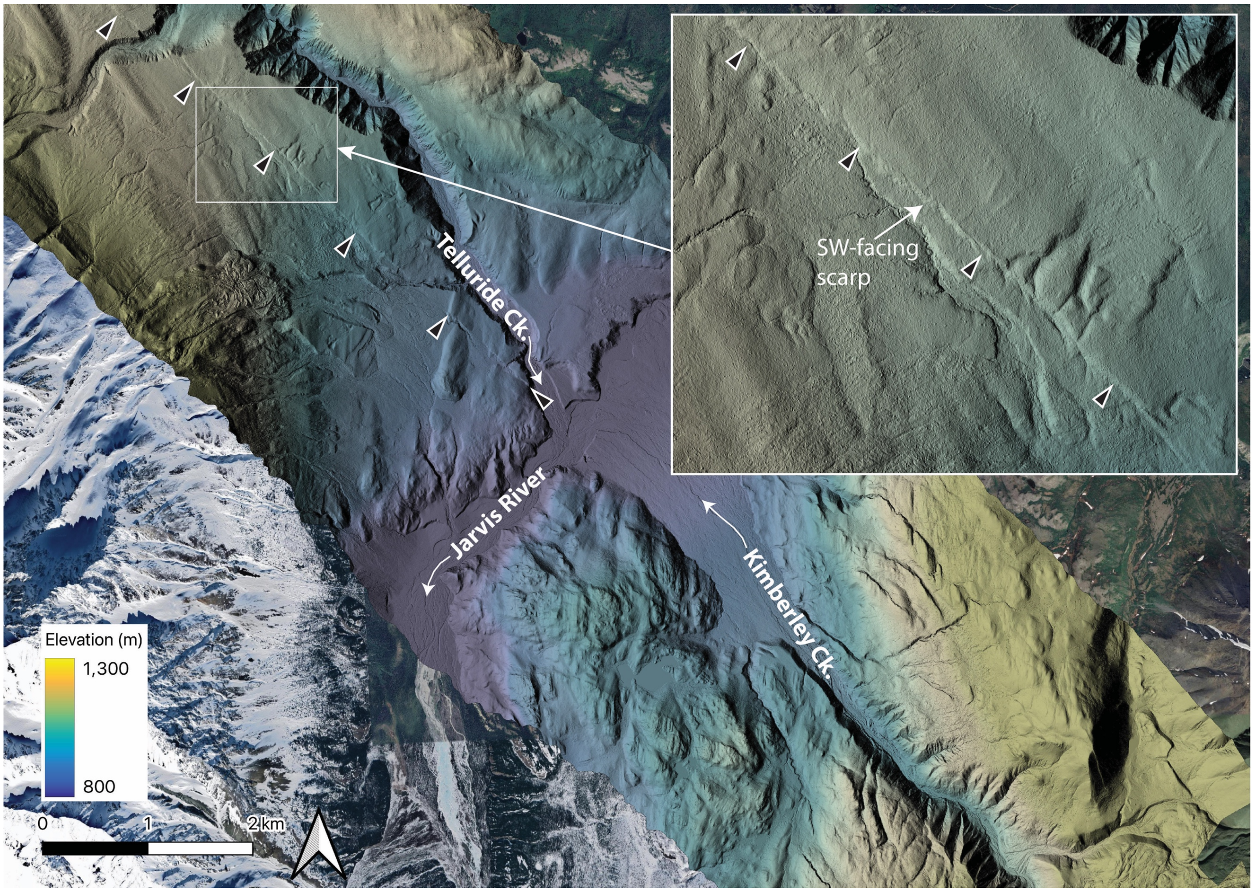

Figure 4.11. Detailed view of Quaternary scarp termination at Jarvis River. The scarp is consistently southwest-facing here and projects into the linear Kimberley Creek drainage, where no surface offsets are observed, but the EDF is observed in bedrock outcrop (Caine et al., 2024).

Table 4.1. Summary of lateral offset observations, geochronological constraints, and slip rate estimates on the EDF, ordered from NW to SE

Site Name	Fault Dist. (km)	Lat.	Long.	Offset (m) min-best-max	Offset Feature	Age Constraint (kyr)	Slip Rate (mm/yr)
1. Pooh Bear	15.3	62.752	-143.076	80-90-100	Terrace riser incising glacial surface	Exposure age 16.45±1.1	5.5 (+1.0/-0.9)
2. Tetlin River	23.1	62.711	-142.946	40-50-60	Braided channels and bars	Holocene	N/A
3. Tetlin South A	27.3	62.692	-142.880	80-100-120	Fault-perpendicular hummocks (Moraines?)	Exposure age 16.45±1.1	6.1 (+1.7/-1.5)
4. Tetlin South B	28.7	62.684	-142.855	15-20-25	River terrace riser	Holocene	N/A
5. Tetlin South C	31.3	62.671	-142.809	150-200-250	Lateral moraines	Exposure age: 16.45±1.1	12.2 (+4.1/-3.7)
6. Stuver Creek	81.4	62.421	-142.005	100-125-150	Terrace riser incising glacial surface	Deglaciated: 16.5-18.5	7.1 (+2/-1.7)
Alaska Segment Ave.							**7.7**
7. Koidern River	204.6	61.783	-140.096	4-5-6	Braided channels and bars	Holocene	N/A
8. Lake Creek	207.2	61.767	-140.062	47-57-65	Creek channel riser	Ice free: 12.5 Deglacial: 16.5	3.9 (+1.3/-1.1)
9. Donjek North	227.1	61.642	-139.793	50-55-60	Creek channel riser	Ice free: 12.5 Deglacial: 14.5	4.1 (+0.7/-0.7)
10. Donjek South	236.9	61.578	-139.655	50-100-150	Mega-scale glacial lineation	Ice free: 12.43 ± 0.32 Deglacial: 13.5	7.7 (+4.3/-4.0)
11. Duke River Bar	267.6	61.370	-139.141	4-5-6	Braided channels and bars	Upper and lower White River Ash: 1.9-1.2	3.2 (+1.8/-1.1)
12. Duke River Terrace	268.1	61.366	-139.136	20-30-40	Terrace riser incising glacial surface	Ice free: 12.4 ± 0.47 Deglacial: 14.5	2.2 (+1/-0.8)
13. Copper Joe Creek	277.3	61.307	-139.016	35-40-45	Sediment mounds and creek channel	Ice free: 12.4 ± 0.47 Deglacial: 14.5	3.0 (+0.6/-0.6)
14. Män Shìè'aya (Silver City)	323.9	61.013	-138.406	30-35-40	Lake shoreline and glacial surface	Ice free: 14.7 ± 0.66	2.4 (+0.4/-0.4)
Yukon Segment Ave.							**3.8**

4.6.4 Crustal Stress and Fault Kinematics

Principal stress orientations derived from earthquake focal mechanisms are relatively consistent along the entire length of the EDF (Figure 4.12); maximum principal stress (σ_1) is generally sub-horizontal, trending north-northeast or south-southwest, σ_2 is generally steeply plunging to subvertical, and σ_3 is gently plunging to the east-southeast or west-northwest. In an Andersonian faulting regime, these orientations are consistent with strike-slip kinematics. The maximum principal stress vector is consistent rotated slightly counterclockwise from fault normal, and the maximum shear stress resolved on the fault plane therefore predicts dextral slip on the EDF.

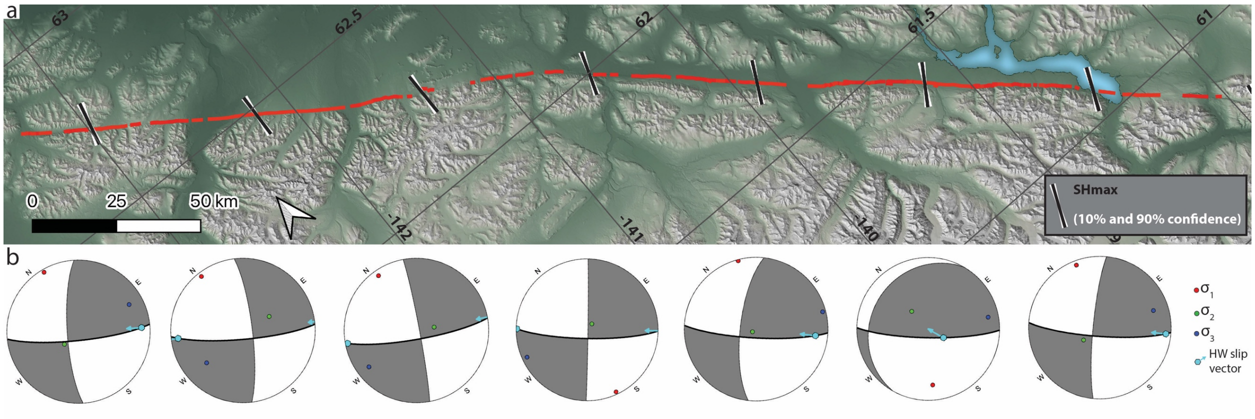

Figure 4.12. A) Fault trace with SHmax at 50 km intervals. B) Pseudo-focal mechanisms representing the slip predicted by resolving the maximum shear stress (slip vector) on a steeply-dipping fault plane at 50 km intervals along the fault.

4.7 Discussion

4.7.1 Is the Eastern Denali Fault Still “Active”?

It is clear from our geomorphic analysis that the EDF should be treated as a Quaternary active fault. While it is apparent from seismological and geodetic studies that a large portion of strain is accommodated on the Totschunda-Fairweather Connector Fault, Duke River fault, and other structures within the St. Elias Mountains (Elliott and Freymueller, 2020; Biegel et al., 2024), the existence of a major scarp exhibiting consistent geomorphic offsets is clear evidence of ongoing strain localization along the EDF. The assertion of Choi et al. (2021) that the EDF fault is no longer active may have some validity in the immediate vicinity of the 2017 earthquake sequence at the far southeastern end of the fault, outside of our lidar footprint (Figure 4.1). Their study was based on a cluster of aftershocks within a ~10 km radius of the mainshocks, and no significant fault scarp is observed nearby. However, we argue that their conclusions should not be extended to the entire EDF.

Several authors have also attempted to reconcile the existence of the Holocene EDF fault scarp and lack of current instrumental strain signature as a migration of strain away from the EDF. However, we contend that there is insufficient temporal resolution in the various datasets to make this claim, and no evidence of a shift in tectonic regime that might cause such a migration of strain accommodation. Only additional paleoseismic studies along the EDF will be able to ascertain whether or not the slip rate has decreased through the Holocene. It should not be surprising that a major active fault exhibits limited seismicity, unfavourable stress conditions for rupture, and a limited geodetic signature. For example, faults that are fully locked may not host any seismicity between large ruptures. Additionally, the San Andreas and Great Sumatran faults - both major active strike slip faults in transpressional settings – are broadly characterized by near-fault-normal maximum principal stress orientations (Mount and Suppe, 1992). Moreover, Wang et al. (2021) showed that for low slip rate faults with relatively long recurrence intervals, the majority of geodetic strain will accumulate early in the interseismic cycle, contributing to underestimation of geodetic slip rate in the decadal time periods of geodetic instrument networks.

4.7.2 Strike-Slip or Dip-Slip Fault?

Our geomorphic analyses and slip-rate estimates strongly indicate that the EDF is predominantly a strike-slip fault with a minor component of dip slip. As discussed above, we document multiple sites with unequivocal evidence of right-lateral offset. Although the fault scarp is dominantly southwest-side-up and lateral offsets are less-commonly observed, we argue that the preservational record is biased towards dip-slip offsets as has been demonstrated by Reitman et al. (2024). Additionally, the sediment mounds along the fault trace resemble the morphology of features developed in sandbox models where strike-slip faulting propagates through weak or unconsolidated cover. Furthermore, these mounds are largest at restraining stepovers, indicating shortening in the fault-parallel direction. Finally, the linearity and length of the fault trace, along with the fact that its facing direction is inverted at several locations, is strong evidence of strike-slip kinematics. Furthermore, through our kinematics analysis, we show that crustal stress orientations are consistent with dextral strike-slip, in contrast to the conclusions of Choi et al., (2021).

Our interpretation of the fault kinematics also differs somewhat from previous geomorphic work. In particular, Marechal et al. (2018) used ArcticDEM to map dip slip and lateral offsets along the fault, but were not able to discern lateral offsets beyond Stuver Creek, 80 km south of the Denali-Totshunda intersection. In contrast, we note strong evidence of lateral offset at Män Shìè'aya (Silver City), ~330 km south of the intersection and at multiple intervening sites. Marechal et al. (2018) also estimated a mean dip slip offset of 13.0 ± 3.7 m along the fault based on 15 topographic profiles. We find this to be an overestimate, likely arising from selection bias of the largest and best expressed scarps, as well as the limitations of ArcticDEM. Our tenfold increase in the number of fault profiles (n=151), along with the higher precision of the lidar data, shows that the average vertical offset, and associated rate of dip-slip motion, is approximately half of that reported by Marechal et al. (2018).

4.7.3 Comparison to Previous Lateral Slip Rate Estimates

For the entire EDF, we calculate an average right-lateral late Quaternary slip rate of 5.2 mm/yr, however, considering the marked decrease in slip rate near the Alaska-Yukon border (Figure 4.5), we prefer to use average values of 7.7 mm/yr for the Alaska segment, and 3.8 mm/yr for the Yukon segment (Table 4.1). Our results on the Alaska segment are generally consistent with past estimates of ~8 mm/yr based on the geomorphic offsets at the Tetlin River (Matmon et al., 2006; Mériaux et al., 2009; Haeussler et al., 2017).

Our lateral slip rates for the Yukon segment of the EDF, however, are higher than many previous estimates. Past attempts to constrain the lateral slip rate from geomorphology include Marechal et al., (2018) who estimate a rate of less than 1 mm/yr, and Haeussler et al. (2017) who report a preferred value of 1.7 mm/yr. These studies were both limited by lower resolution imagery and DEMs. Using GNSS data, Marechal et al. (2015) estimate a strike-slip rate of ~2 mm/yr, and applying a geodetic block model approach, Elliott and Freymueller (2020) calculate a strike-slip rate of 1.8 mm/yr. Using earthquake catalog statistics, Leonard et al., (2008) arrive at a rate of 2 mm/yr. We feel that our geomorphic slip rates using high resolution lidar data are the best reflection of the long term (Holocene) slip rate of the EDF. The lower estimates from past geodetic and seismological studies may be related to transient effects of fault locking, and the fact that on faults with long recurrence intervals, the late interseismic strain field may not fully capture the fault slip rate (Wang et al., 2021).

4.7.4 Surface Rupture Length and Plausible Earthquake Magnitude

The maximum plausible rupture magnitude for the EDF has not previously been considered in detail. Blais-Stevens et al. (2020) inferred that past ruptures were >M 6 solely on the basis of the enigmatic mounds developed along the fault trace. We use empirical earthquake scaling relationships (Wesnousky, 2008) to infer the possible magnitudes of rupture. If the entire 354-km-long fault scarp ruptures together in one earthquake, then earthquakes of moment magnitude 7.7 to 8.0 are plausible. However, we suggest that the lack of observable surface scarp at the fault bend near the Alaska-Yukon border may represent a rupture segment boundary. Both vertical and lateral offsets northwest of the bend are more than double those south of the bend (Figure 4.5), suggesting the two segments have experienced different paleoseismic histories. Additionally, at the Pooh Bear site, Schwartz et al. (2012) excavated a paleoseismic trench and found evidence of four to five paleoearthquakes in the past 2600 to 2800 years. In constrast, trenches at Shä́r Ndü Chù (Duke River) indicate four to five events in the last 6500 to 6800 years (Blais-Stevens et al., 2020). These observations together may indicate that the Yukon segment of the EDF may behave at least somewhat independently of the Alaskan segment. Exactly where the surplus strain between the Alaskan and Yukons segments is accommodated remains unclear, though the network of seismogenic structures identified in the St. Elias Mountains by Biegel et al. (2024) may be possible candidates.

The Yukon segment of the fault is ~180 km-long, and if this ruptured together, a moment magnitude of ~7.5 would be expected. The Yukon segment is highly linear and does not deviate appreciably in strike aside from the one restraining bend south of Dän Zhù̀r Chù (the Donjek River; Figure 4.8). This 1-km-wide step is well below the threshold required to reliably arrest rupture (Wesnousky, 2006; Biasi and Wesnousky, 2016), and the scarp is continuous through the bend. The Alaskan segment of the EDF, where the well expressed scarp ~125 km long, could generate a moment magnitude ~7.4 if it ruptured fully, stopping at the Totshunda-CDF intersection. However, given that the EDF scarp can be traced continuously onto the CDF, we cannot rule out that some larger earthquakes could breach this segment.

We consider it likely that the most recent earthquake alone is preserved on several of the abandoned Holocene fluvial terraces that cross the Yukon segment of the fault, but acknowledge the possibility that a penultimate event is also preserved. The scarps crossing these surfaces appear “fresh” compared to the more diffuse scarps on the glacial surface. Lateral separations preserved at Shä̀r Ndü Chù (Duke River) and Koidern Creek are both 5 ± 1 m. Using empirical scaling relations between average surface slip and surface rupture length, these offset measurements indicate rupture lengths of 400-900 km, which far exceeds the rupture length of most historically observed continental surface ruptures. If these offset measurements instead record the maximum slip along strike (which may explain why preservation of lateral offsets is so limited), they are consistent with a rupture length between 74-174 km, more inline with an independent rupture of the 180 km-long Yukon segment.

These estimates of rupture magnitude are internally consistent with our late Quaternary slip rate estimates. At a rate of 3.8 mm/yr, the Yukon segment will accumulate roughly 5 m of slip deficit over the average 1300 year recurrence interval determined by Blais-Stevens et al. (2020) at Shä̀r Ndü Chù (Duke River). At a rate of 7.7 mm/yr, the Alaska segment will accumulate roughly 5 m of slip deficit over the approximate recurrence interval of 650 years determined by Schwartz et al. (2012) at the Pooh Bear site. Continental strike slip ruptures with surface rupture lengths > 100 km typically have maximum lateral offsets of 5-10 m and average lateral offsets of 2-5 m (Wesnousky, 2008). The past estimates of ~2 mm/yr on the Yukon segment (Leonard et al., 2008; Marechal et al., 2015; Elliott and Freymueller, 2020) imply slip deficits of ~2.6 m, on the lowest end of what is expected for long continental surface ruptures.

4.7.5 Influence of the EDF on Topography and Drainage

Modern activity on the EDF may play a role in shaping topography in the southwestern Yukon. Despite being dominated by strike-slip motion, the southwest-side up dip-slip component on the fault is reflected by the much higher peaks of the Kluane Ranges southwest of the fault relative to the low elevations of the Shakwak Valley to the northeast. The mean elevation in a 5 km swath southwest of the fault is 300 m above that of the scarp, whereas the mean elevation northeast of the fault is 40 m below the elevation of that of the scarp. The highest mean elevation on the southwest side of the fault is adjacent to Łù'àn Mǟn (Kluane Lake), where the maximum compressive stress is at the highest angle to the fault trace and kinematics analyses indicate a greater thrust component (Figure 4.12). At the northwest end of the fault where it connects with the CDF, elevations become more evenly matched on either side of the fault, which is reflected by variable scarp facing directions. Notably, the 2002 Denali earthquake, though overall strike-slip, had a dominantly north-side-up rupture (Haeussler et al., 2004), which is also reflected by higher topography north of that fault section. The strike-slip component of strain may also play a role in controlling topography; in particular, the Nutzotin Mountains are located at the 10º restraining bend in the fault northwest of the White River. Similar to how the Denali massif is exceptionally high due to a restraining bend, their relatively high relief may be related to fault kinematics.

The EDF also appear to influence regional drainage patterns.The majority of rivers flow northeastward across the fault, emanating from the higher elevations of the St. Elias Mountains and entering the Yukon River basin. However, at the south end of the fault, where its facing direction is reversed (northeast side up), the Jarvis River is the first to flow southwest across the fault (Figure 4.11), joining the Tatshenshini River basin and flowing into the Pacific. Thus, we suggest that cumulative offset on the EDF may influence the position of drainage divides between the Bering Sea and the Pacific.

4.7.6 Geothermal Exploration

Our results have some implications for geothermal exploration along the EDF. Being in an overall compressive setting is generally considered unfavourable for fault permeability and fluid circulation as the fault will essentially be clamped shut. Furthermore, the relative simplicity of the fault trace and lack of a wide damage zone may not encourage fluid flow. Modelling studies have shown that geothermal fluids do not ascend as easily along steeply-dipping faults (Moreno et al., 2018); most conceptual models of orogenic fault controlled geothermal systems require that the fault dips beneath the mountain range from which the meteoric fluids are sourced.

However, at Shấr Ndü Chù (Duke River) – a proposed geothermal well site – the EDF fault locally exhibits a right-hand releasing bend and several minor scarps occur up to 800 m southeast of the main fault trace (Figure 4.9), indicating some local fault complexity that may be conducive for geothermal upwelling.

4.7.7 Seismic Hazard and Risk

Southwestern Yukon ranks among the highest seismic hazard zones in Canada (Adams et al., 2019). A major earthquake along the EDF would cause extreme shaking in the communities of Beaver Creek, Burwash Landing, Destruction Bay and Haines Junction, and strong shaking in Whitehorse. In addition to the direct threat to human life, a rupture on the fault threatens the Alaska and Haines Highways (Yukon Highways 1 and 3), which parallel the EDF for a combined length of 450 km. These roads are critical lifelines to many Yukon communities and the Alaska Highway is the sole paved link between Alaska and the rest of the continent, making it of international importance. The two highways cross the fault three times and are within 5 km of the fault trace for most of the shared length. Numerous bridges cross major rivers that emanate from the Saint Elias Mountains and which could be subject to debris flows or liquefaction following an earthquake. Additionally, prehistoric earthquakes are speculated to have caused landslides that have crossed the current path of the highway (Whelan, 2022). Other critical infrastructure could also be damaged by a major EDF earthquake, including pipelines, power lines, dams, and mine facilities.

4.8 Conclusion

Our new lidar analyses provide an improved understanding of the Holocene rupture behaviour of the EDF, one of Canada's largest sources of seismic hazard. By mapping geomorphic offsets, we show that despite being in an overall compressive setting, the kinematics of EDF ruptures are largely strike-slip with only a minor dip-slip component. We show that the maximum shear stress resolved on the steeply dipping fault plane is subhorizontal and consistent with the geomorphically-derived kinematics. We estimate a late Quaternary right-lateral slip rate of ~3.8 mm/yr on the Yukon segment of the EDF, nearly double that of previous studies that employed lower resolution topographic data, GNSS velocities, or seismic catalog statistics. A full rupture of the 354 km-long EDF could produce an earthquake as large as M_w ~8, however, based on previous paleoseismic studies, and our scarp mapping and slip rate estimates, we suggest there may be a rupture segment boundary near the Alaska-Yukon border. The individual 125 to 180 km-long segments might produce Mw 7.4-7.5 ruptures.

4.9 Acknowledgements

This research occurred on the traditional territory of the Kluane, White River, and Champagne & Aishihik First Nations. Place names provided in the Southern Tutchone language are based on research by the Yukon Native Language Centre (Hitch et al., 2012) available through the Yukon Geographical Place Names Board (https://yukonplacenames.ca/dakeyi/maps/). Food, lodging, and research infrastructure were provided by the Kluane Lake Research Station, operated by the Arctic Institute of North America. Thanks are owed to Harry and Kristina Penn for making our stays comfortable. The 2024 airborne lidar survey was funded through an NSERC Alliance grant involving partnerships with, and contributions from, the Yukon Geological Survey, Natural Resources Canada, the Hakai Institute, and Yukon University. Additional fieldwork support was provided by NSERC Discovery grants to E.N. and J.F.C., a Canada Research Chair to E.N., a Polar Knowledge Canada Northern Scientific Training Program award to T.F., and by the Yukon Geological Survey as a part of its geothermal exploration program. Our drone lidar system was developed with funding from the Canada Foundation for Innovation and the BC Knowledge Development Fund.

Chapter 5: Conclusions

5.1 Significance of Findings

Paleoseismic and tectono-geomorphic studies have historically not been common in western Canada. The advent of widespread, publicly available, high-resolution topographic data, has shifted the paradigm, catalyzing a new wave of active fault research. Though there were a handful of paleoseismic studies predating this shift (Clague, 1979; Thompson et al., 1997), the first efforts employing modern, state-of-the-art remote sensing and paleoseismic techniques were those of Morell et al. (2017, 2018) on the Leech River fault in the Cascadia forearc region. These studies were closely followed by Harrichhausen et al. (2021, 2023) and Lynch (2023), also in the forearc, and Blais-Stevens et al. (2020) on the Eastern Denali fault in the Yukon.

This dissertation further capitalizes on the rapidly expanding datasets of high resolution topography, and makes several new and significant contributions to our understanding of active faulting in the Canadian Cordillera. My work moves beyond the Cascadia forearc to the intermontane regions that have thus far received much less scrutiny. Most fundamentally, I have shown that large, surface rupturing earthquakes are possible far inboard of the plate margin, even where tectonic strain rates are relatively low. This finding significantly changes our understanding of seismic hazard in these regions and underscores the utility and importance of high-resolution topographic data in this effort.

5.2 Directions for Future Work

The studies presented herein merely lay the groundwork for further active tectonics research across western Canada. There are still many unanswered questions and unexplored regions that deserve further attention. Below, I summarize a few avenues that I believe to be of high priority for future research.

5.2.1 Paleoseismic Trenching

High priority should be placed on the excavation of paleoseismic trenches across many of the faults identified in this thesis, along with improved geochronological constraint on rupture timing. This thesis was limited to relatively non-invasive methods, due to a combination permitting restrictions, financial considerations, and the wide geographic scope. Though this approach yielded a great deal of novel information, paleoseismic trenches will provide higher quality constraints on fault kinematics, credible earthquake magnitudes, rupture timing, slip rate and recurrence interval, which are all important parameters for seismic hazard assessments. On the Tintina fault (detailed in Chapter 2), a paleoseismic trench will help constrain the frequency and variance of recurrence times between major events. My findings indicate that at least 12 kyr have elapsed since the last earthquake and only a paleoseismic trench will allow us to determine if a large earthquake is imminent. Furthermore, the Tintina fault may represent one of the longest paleoseismic records on Earth and could provide important information about earthquake recurrence on mature, low-slip-rate faults. For the SRMT fault (detailed in Chapter 3), a paleoseismic trench across the scarp on the Warspite Creek fan will test the hypothesis of multiple earthquakes with decreasing frequency since the early Holocene, a finding that is suggestive of glacio-isostatic modulation of tectonic activity. On the EDF (detailed in Chapter 4), although a paleoseismic trench has previously been excavated (Blais-Stevens et al., 2020), the new lidar data may aid in situating additional trenches at additional locations. Given that the EDF is shown to have ruptured in large earthquakes numerous times in the late Holocene, it is critical to understand what stage of the earthquake cycle it is at. Geochronological bounds on the timing of the most recent large event are poor, and a trench located on one of the faulted alluvial fans examined in Chapter 4 may add important constraint. Additionally, multiple trenches on the Canadian and US sides of the border will test the hypothesis of a rupture segment boundary posed in Chapter 4.

5.2.2 Expansion of Lidar Data Coverage

High resolution topographic data coverage is expected to increase rapidly in the coming years, presenting an opportunity to vastly improve our understanding of the tectonic geomorphology of the Canadian Cordillera. It is a stated goal of the British Columbia government to obtain complete coverage by the end of the decade (https://news.gov.bc.ca/releases/2023WLRS0010-000512), and hopefully the Yukon and other territories and provinces will follow close behind. Though northern regions are broadly covered by the ArcticDEM dataset, the increased resolution of lidar data does significantly improve fault identification capability. It will be important to continually review new lidar data as it is released for evidence of Holocene faulting. Particular attention should be paid to known bedrock faults and topographic lineaments, as the majority of fault surface ruptures identified in the Cordillera have been localized on these pre-existing structures.

The role that ultra-high resolution (<1 m) drone lidar will play in this effort to identify faults remains to be seen. As illustrated in this thesis and by Salomon et al. (2024), the restricted areal extent of drone lidar surveys limits the utility for fault discovery and it is unlikely drones will be of much use in finding previously unknown scarps at the vast scales of the Cordillera. However, the higher spatial resolution can be valuable for increased confidence in geomorphic interpretations at targeted sites, especially where ground returns are very low due to thick forest canopies (e.g., Lin et al., 2013). In practice, there is a point of diminishing returns beyond which higher spatial resolution may not yield significant additional information about fault behaviour. Moreover, conventional crewed airborne survey patterns can be adjusted to increase point density (Lin et al., 2013), and new scanners have higher power and pulse rates. It is therefore likely that the true niche for drone lidar is in repeat surveying rather than reconnaissance, as numerous surveys over the same area of interest can be conducted at minimal added cost.

5.2.3 Expanded Seismic and Geodetic Instrumentation

Strategic expansion and densification of seismic and geodetic instrument networks in the Canadian Cordillera will help resolve some of the outstanding questions posed in this thesis. Dense seismograph arrays may be able to detect micro-seismicity, allowing for the delineation of fault planes in the subsurface, as well as the measurement of local stress conditions. Current crustal stress maps based on earthquake focal mechanisms (e.g., Heidbach et al., 2018) are under-constrained in much of the Cordillera, formal stress inversions have not been performed beyond the coastal regions (Balfour et al., 2011; Gosselin et al., 2024), and our current understanding of earthquake stress field in the Cordilleran interior is based on a relatively limited set of centroid moment tensors (Ristau et al., 2007; Kao et al., 2012). Dense seismic network coverage will help improve understanding of regional stresses by lowering the threshold required for accurate focal mechanism determination. For the most part, earthquakes rupture in a manner that is consistent with the regional stress field (McKenzie, 1969), and determining accurate stress orientations thus offers a means to predict the kinematics of a fault.

Improved GNSS station coverage will similarly allow for improved understanding of the patterns (kinematics and rates) of strain accumulation across the cordillera. Current GNSS velocity fields indicate broad patterns of shortening across the Cordillera (Mazzotti et al., 2008; Ojo et al., 2021), which is, in places, inconsistent with geologic and geomorphic evidence (e.g., Tintina fault in Chapter 2 and the SRMT fault in Chapter 3). Denser station coverage may reveal local nuance in the regional strain pattern. Additionally, GNSS stations placed in transects across faults may be able to measure modern fault slip rates, allowing independent corroboration of those measured from geomorphic features.

5.2.4 Measuring and Modelling GIA-induced Stresses

It has been demonstrated in many cases that the effects of GIA can modulate rates of seismicity and tectonism (Thorson, 1996; Brandes et al., 2015; Craig et al., 2016; Damon et al., 2023; Hamilton et al., 2024; Hurtado and Gallen, 2024). Rates of seismicity are thought to increase during the periods of greatest isostatic adjustment immediately following deglaciation when the stress field is most perturbed (Hampel et al., 2007; Hurtado and Gallen, 2024), but the effects can continue into the present (Brandes et al., 2015; Damon et al., 2023). Kinematics of glacially-induced faulting are variable: the majority of faults that have a confirmed glacio-isostatic trigger are either reverse (Muir-Wood, 1989; Craig et al., 2016) or normal (Hetzel and Hampel, 2005; Hampel et al., 2007), and in some cases strike-slip faults may also be brought closer to failure (Damon et al., 2023).

An important implication of GIA-modulated seismicity is that the paleoseismic record may over-represent the modern seismic hazard, as the bulk of slip may have occurred immediately post glaciation. It is therefore important to determine to what extent slip rates may have decreased through time to avoid making potentially unnecessary revisions to seismic building codes that could contribute to increased building costs. However, it is worth highlighting that faults that rupture due to GIA are typically already near failure, and GIA simply temporarily increases the rate of moment release (Craig et al., 2016; Hurtado and Gallen, 2024). Thus, a GIA trigger does not indicate that the fault does not represent an ongoing hazard, just that the hazard may be temporarily reduced. A combination of paleoseismic trenching and numerical ice load modelling have been successfully applied to this problem (e.g., Hurtado and Gallen, 2024) and would be worthwhile in the Canadian Cordillera.

In addition to the temporal changes in strain rates over the Holocene, GIA still appears to control patterns of strain in the present, and it is important to disentangle this effect from tectonic strain. It is common to remove modelled effects of GIA from GNSS velocity fields in order to properly interpret the tectonic signal (Elliott and Freymueller, 2020; Ojo et al., 2021). However, the GIA models themselves are based on geodetic uplift rates, and therefore suffer from the same lack of spatial resolution. A recent PhD thesis (Drooff, 2024) found that by removing a modelled effect of GIA-induced strain from the GNSS velocity field in the northern Cordillera, a previously unresolvable slip rate of ~1 mm/yr is possible across the Tintina fault. This result highlights the importance of careful modelling of GIA strain, and underscores the need for denser GNSS station coverage across the Cordillera.

In terms of the faults studied in this thesis, there are a number of specific questions that could be addressed via paleoseismic trenching alongside numerical modelling and geodetic measurement of GIA-related strain. The Tintina fault (Chapter 2) is positioned near the limit of three successive Quaternary glaciations. Paleoseismic trenching data combined with ice load modelling could potentially demonstrate the long-term modulation of fault slip rate over successive loading and unloading cycles. Additionally, denser GNSS coverage would improve models of current GIA and allow for even further improvement on the estimates of Drooff (2024). The Southern Rocky Mountain Trench fault (Chapter 3) appears to show a decreasing slip rate through the Holocene, but the geochronological constraints are relatively poor. Paleoseismic trenching along with numerical modelling of ice unloading could test this more rigorously. The Eastern Denali fault (Chapter 4) is positioned on the boundary of the late Wisconsinan Ice Sheet, and significant ice remains in the St. Elias mountains, the largest non-polar ice cap in the world. As noted in Chapter 4, the EDF has a consistent southwest-side-up facing direction, which may suggest the slip vector of the fault is at least partially controlled by the removal of ice. In addition to the past effects of unloading on rates of seismicity on the EDF, numerical modelling could explore the potential effects of future climate change and ice sheet melting on rates of seismicity in the region.

5.2.5 Inclusion of Fault Sources in Seismic Hazard Models

The most advanced seismic hazard models around the world include discrete fault sources in addition to area sources, and their inclusion is generally thought to improve the models by making them more representative of the true patterns of strain accommodation (e.g., Field et al., 2014; Hatem et al., 2022b; Seebeck et al., 2023). Canada's National Seismic Hazard Model is currently based mostly on area sources, with only 21 discrete fault segments, the majority of which are major plate boundary (interplate) faults. The Denali, Duke River and Leech River faults are the only fault sources currently included from intraplate regions (Halchuk et al., 2019; Kolaj et al., 2023). As a point of comparison, the 2023 U.S. NSHM includes ~1000 individual fault sections throughout the continental interior (Hatem et al., 2022a). For a fault source to be included in the NSHM, a slip rate is generally required, usually derived from geological/geomorphological constraints and ideally corroborated by other methods (i.e., seismology, geodesy). As discussed throughout this thesis, obtaining this key piece of information for Canadian faults has been challenging for a variety of reasons. However, as a growing number of active faults are identified and characterized, these should be integrated into the Canada's NSHM. Improved constraints on slip rates from geological and geophysical studies will be necessary, as hazard calculations are highly sensitive to this value.

The extent to which the inclusion of fault sources actually alters seismic hazard values remains to be seen and will require case-by-case study. As an example, the inclusion of the Leech River fault in the NSHM caused only marginal changes to hazard values (5-9% increase in PGA) and only in close proximity to the fault (Halchuk et al., 2019; Kukovica et al., 2019). The relatively minor change was due to the fact that southwest BC is already a zone of exceptionally high hazard due to the rates of background seismicity and presence of the Cascadia megathrust. However, Goda and Sharipov (2021) argued that considering the long return periods of crustal faults, the hazard contribution is actually higher (10-30%) if considered over longer periods of time. This is a particularly salient observation considering the finding in Chapter 2 of this thesis – that the Tintina fault has not ruptured in at least 12 thousand years. Moreover, the relative hazard contributions may be a lot larger for faults like the Tintina and SRMT, which currently exist in zones of only moderate hazard covered by large area sources. Specific studies will be necessary to explore the impact of including these faults in the NSHM.

Bibliography

Ackerson, C., Ward, B., and Kennedy, K., 2025, Surficial Geology of the Central Kluane Ranges (parts of NTS 115B/15, 16 and 115G /1, 2, 3, 6 and 7): Yukon Geological Survey Open File Map 2025-2.

Adams, J., 2019, A 65-year history of seismic hazard estimates in Canada, *in* Proceedings 12th World Conference on Earthquake Engineering, Quebec City, The Canadian Association for Earthquake Engineering.

Adams, J., Allen, T., Halchuk, S., and Kolaj, M., 2019, Canada's 6th Generation Seismic Hazard Model, as Prepared for the 2020 National Building Code of Canada, *in* Proceedings 12th World Conference on Earthquake Engineering, Quebec City, The Canadian Association for Earthquake Engineering.

Akciz, S.O., Sançar, T., Kıray, H.N., Zabcı, C., Köküm, M., Balkaya, M., Battogtokh, D., and Akyüz, H.S., 2024, Primary Surface Rupture and Slip Distribution Associated with the Mw 7.6 06 February 2023 Elbistan Earthquake, Turkey, *in* Vienna, Austria, Copernicus Meetings, doi:10.5194/egusphere-egu24-13350.

Allen, D.M., Grasby, S.E., and Voormeij, D.A., 2006, Determining the circulation depth of thermal springs in the southern Rocky Mountain Trench, south-eastern British Columbia, Canada using geothermometry and borehole temperature logs: Hydrogeology Journal, v. 14, p. 159–172, doi:10.1007/s10040-004-0428-z.

Anderson, J.G., Biasi, G.P., and Wesnousky, S.G., 2017, Fault-Scaling Relationships Depend on the Average Fault-Slip Rate: Bulletin of the Seismological Society of America, v. 107, p. 2561–2577, doi:10.1785/0120160361.

Audet, P., Currie, C.A., Schaeffer, A.J., and Hill, A.M., 2019, Seismic Evidence for Lithospheric Thinning and Heat in the northern Canadian Cordillera: Geophysical Research Letters, v. 46, p. 4249–4257, doi:10.1029/2019GL082406.

Avouac, J.-P., Ayoub, F., Wei, S., Ampuero, J.-P., Meng, L., Leprince, S., Jolivet, R., Duputel, Z., and Helmberger, D., 2014, The 2013, Mw 7.7 Balochistan earthquake, energetic strike-slip reactivation of a thrust fault: Earth and Planetary Science Letters, v. 391, p. 128–134, doi:10.1016/j.epsl.2014.01.036.

Balfour, N.J., Cassidy, J.F., Dosso, S.E., and Mazzotti, S., 2011, Mapping crustal stress and strain in southwest British Columbia: Journal of Geophysical Research, v. 116, p. 1–11, doi:10.1029/2010JB008003.

Baljinnyam, I. (Ed.), 1993, Ruptures of Major Earthquakes and Active Deformation in Mongolia and Its Surroundings: Geological Society of America Memoir 181, 70 p.

Ballantyne, C.K., 2002, Paraglacial geomorphology: Quaternary Science Reviews, v. 21, p. 1935–2017, doi:10.1016/S0277-3791(02)00005-7.

Barka, A., and Eyidoğan, H., 1993, The Erzincan earthquake of 13 March 1992 in Eastern Turkey: Terra Nova, v. 5, p. 190–194, doi:10.1111/j.1365-3121.1993.tb00245.x.

BC Department of Recreation and Conservation, 1958, Columbia Lake bathymetry: Fish and Game Branch.

Beaudoin, A.B., and King, R.H., 1994, Holocene palaeoenvironmental record preserved in a paraglacial alluvial fan, Sunwapta Pass, Jasper National Park, Alberta, Canada: CATENA, v. 22, p. 227–248, doi:10.1016/0341-8162(94)90004-3.

Becker, T.W., Lowry, A.R., Faccenna, C., Schmandt, B., Borsa, A., and Yu, C., 2015, Western US intermountain seismicity caused by changes in upper mantle flow: Nature, v. 524, p. 458–461, doi:10.1038/nature14867.

Beierle, B.D., 2002, Late Quaternary glaciation in the Northern Ogilvie Mountains: revised correlations and implications for the stratigraphic record: Canadian Journal of Earth Sciences, v. 39, p. 1709–1717, doi:10.1139/e02-062.

Bello, S., Andrenacci, C., Cirillo, D., Scott, C.P., Brozzetti, F., Arrowsmith, J.R., and Lavecchia, G., 2022, High-Detail Fault Segmentation: Deep Insight into the Anatomy of the 1983 Borah Peak Earthquake Rupture Zone (Mw 6.9, Idaho, USA): Lithosphere, v. 2022, p. 8100224, doi:10.2113/2022/8100224.

Bender, A., and Haeussler, P., 2017, Eastern Denali Fault Surface Trace Map, Eastern Alaska and Yukon, Canada: USGS Open-File Report 2017–1049.

Bense, V.F., Gleeson, T., Loveless, S.E., Bour, O., and Scibek, J., 2013, Fault zone hydrogeology: Earth-Science Reviews, v. 127, p. 171–192, doi:10.1016/j.earscirev.2013.09.008.

Berryman, K.R., Cochran, U.A., Clark, K.J., Biasi, G.P., Langridge, R.M., and Villamor, P., 2012, Major Earthquakes Occur Regularly on an Isolated Plate Boundary Fault: Science, v. 336, p. 1690–1693, doi:10.1126/science.1218959.

Biasi, G.P., and Wesnousky, S.G., 2016, Steps and Gaps in Ground Ruptures: Empirical Bounds on Rupture Propagation: Bulletin of the Seismological Society of America, v. 106, p. 1110–1124, doi:10.1785/0120150175.

Biegel, K.M., Gosselin, J.M., Dettmer, J., Colpron, M., Enkelmann, E., and Caine, J.S., 2024, Earthquake Relocations Delineate a Discrete Fault Network and Deformation Corridor Throughout Southeast Alaska and Southwest Yukon: Tectonics, v. 43, p. e2023TC008140, doi:10.1029/2023TC008140.

Bilham, R., 2009, The seismic future of cities: Bulletin of Earthquake Engineering, v. 7, p. 839–887, doi:10.1007/s10518-009-9147-0.

Blais-Stevens, A., Clague, J.J., Brahney, J., Lipovsky, P., Haeussler, P.J., and Menounos, B., 2020, Evidence for Large Holocene Earthquakes along the Denali Fault in Southwest Yukon, Canada: Environmental and Engineering Geoscience, v. 26, p. 149–166, doi:10.2113/EEG-2263.

Bodtker, J., Cronmiller, D.C., Bond, J.D., and Shugar, D., 2023, The Sunnydale landslide, current understanding and research, Dawson (NTS 116B/3), *in* MacFarlane, K. ed., Yukon Exploration and Geology 2022, Yukon Geological Survey, p. 19–33.

Bollinger, L., Klinger, Y., Forman, S.L., Chimed, O., Bayasgalan, A., Munkhuu, U., Davaasuren, G., Dolgorsuren, T., Enkhee, B., and Sodnomsambuu, D., 2021, 25,000 Years long seismic cycle in a slow deforming continental region of Mongolia: Scientific Reports, v. 11, doi:10.1038/s41598-021-97167-w.

Bostock, H.S., 1952, Geology of the northwest Shakwak Valley, Yukon Territory: Geological Survey of Canada Memoir 267, p. 1–50.

Bott, M.H.P., 1959, The Mechanics of Oblique Slip Faulting: Geological Magazine, v. 96, p. 109–117, doi:10.1017/S0016756800059987.

Brandes, C., Steffen, H., Steffen, R., and Wu, P., 2015, Intraplate seismicity in northern Central Europe is induced by the last glaciation: Geology, v. 43, p. 611–614, doi:10.1130/G36710.1.

Brideau, M.-A., Stead, D., Roots, C., and Orwin, J., 2007, Geomorphology and engineering geology of a landslide in ultramafic rocks, Dawson City, Yukon: Engineering Geology, v. 89, p. 171–194, doi:10.1016/j.enggeo.2006.10.004.

Brooks, G.R., and Adams, J., 2020, A review of evidence of glacially-induced faulting and seismic shaking in eastern Canada: Quaternary Science Reviews, v. 228, p. 106070, doi:10.1016/j.quascirev.2019.106070.

Caine, J.S., Orlandini, O.F., Vollmer, F.W., and Lowers, H.A., 2024, Brittle Regime Slip Partitioned Damage and Deformation Mechanisms Along the Eastern Denali Fault Zone in Southwestern, Yukon: Journal of Geophysical Research: Solid Earth, v. 129, p. e2024JB029506, doi:10.1029/2024JB029506.

Cao, Z., and Liu, L., 2024, Western US intraplate deformation controlled by the complex lithospheric structure: Nature Communications, v. 15, p. 3917, doi:10.1038/s41467-024-48223-2.

Chen, Y., Gu, Y.J., Currie, C.A., Johnston, S.T., Hung, S.-H., Schaeffer, A.J., and Audet, P., 2019, Seismic evidence for a mantle suture and implications for the origin of the

Canadian Cordillera: Nature Communications, v. 10, p. 1–10, doi:10.1038/s41467-019-09804-8.

Choi, M., Eaton, D.W., and Enkelmann, E., 2021, Is the Eastern Denali fault still active? Geology, v. 49, p. 662–666, doi:10.1130/G48461.1.

Choi, J.-H., Klinger, Y., Ferry, M., Ritz, J.-F., Kurtz, R., Rizza, M., Bollinger, L., Davaasambuu, B., Tsend-Ayush, N., and Demberel, S., 2018, Geologic Inheritance and Earthquake Rupture Processes: The 1905 M ≥ 8 Tsetserleg-Bulnay Strike-Slip Earthquake Sequence, Mongolia: Journal of Geophysical Research: Solid Earth, v. 123, p. 1925–1953, doi:10.1002/2017JB013962.

Clague, J.J., 1975, Late Quaternary sediments and geomorphic history of the southern Rocky Mountain Trench, British Columbia: Canadian Journal Earth Sciences, v. 12, p. 595–605.

Clague, J.J., 1979, The Denali Fault System in southwest Yukon Territory - a geologic hazard? Geological Survey of Canada Paper No. 79-1A, p. 169–178, doi:10.4095/104844.

Clague, J.J., 1974, The St. Eugene Formation and the Development of the Southern Rocky Mountain Trench: Canadian Journal of Earth Sciences, v. 11, p. 916–938, doi:10.1139/e74-091.

Clague, J.J., and James, T.S., 2002, History and isostatic effects of the last ice sheet in southern British Columbia: Quaternary Science Reviews, v. 21, p. 71–87, doi:10.1016/S0277-3791(01)00070-1.

Clague, J.J., Luckman, B.H., Van Dorp, R.D., Gilbert, R., Froese, D., Jensen, B.J.L., and Reyes, A.V., 2006, Rapid changes in the level of Kluane Lake in Yukon Territory over the last millennium: Quaternary Research, v. 66, p. 342–355, doi:10.1016/j.yqres.2006.06.005.

Colpron, M., Nelson, J.A.L., and Murphy, D.C., 2007, Northern Cordilleran terranes and their interactions through time: GSA Today, v. 17, p. 4–10, doi:10.1130/GSAT01704-5A.1.

Copley, A., Boait, F., Hollingsworth, J., Jackson, J., and McKenzie, D., 2009, Subparallel thrust and normal faulting in Albania and the roles of gravitational potential energy and rheology contrasts in mountain belts: Journal of Geophysical Research: Solid Earth, v. 114, doi:10.1029/2008JB005931.

Craig, T.J., Calais, E., Fleitout, L., Bollinger, L., and Scotti, O., 2016, Evidence for the release of long-term tectonic strain stored in continental interiors through intraplate earthquakes: Geophysical Research Letters, v. 43, p. 6826–6836, doi:10.1002/2016GL069359.

Craig, J.W., Faulds, J.E., Hinz, N.H., Earney, T.E., Schermerhorn, W.D., Siler, D.L., Glen, J.M., Peacock, J., Coolbaugh, M.F., and Deoreo, S.B., 2021, Discovery and analysis of a blind geothermal system in southeastern Gabbs Valley, western Nevada, USA: Geothermics, v. 97, doi:10.1016/j.geothermics.2021.102177.

Crandall, J.T., and Sadlier-Brown, T.L., 1976, Data on geothermal areas Cordilleran Yukon, Northwest Territories, and Adjacent British Columbia, Canada: Geological Survey of Canada Open File 427.

Crickmay, C.H., 1964, The rocky mountain trench: a problem: Canadian Journal of Earth Sciences, v. 1, p. 184–205, doi:10.1139/e64-011.

Cruden, D., and Varnes, D., 1996, Landslide Types and Processes, *in* Turner, A.K. and Schuster, R.J. eds., Landslides: Investigation and Mitigation, Washington, D. C., Transportation Research Board, National Research Council, National Academy Press, Special Report 247, p. 36–75.

Cui, Y., Miller, D., Schiarizza, P., and Diakow, L.J., 2017, British Columbia Digital Geology: British Columbia Geological Survey Open File 2017-8, http://cmscontent.nrs.gov.bc.ca/geoscience/PublicationCatalogue/OpenFile/BCGS_OF2017-08.pdf (accessed July 2019).

Curewitz, D., and Karson, J.A., 1997, Structural settings of hydrothermal outflow: Fracture permeability maintained by fault propagation and interaction: Journal of Volcanology and Geothermal Research, v. 79, p. 149–168, doi:10.1016/S0377-0273(97)00027-9.

Currie, C.A., Mallyon, D.A., Yu, T.-C., Chen, Y., Schaeffer, A.J., Audet, P., and Gu, Y.J., 2023, Mantle structure and dynamics at the eastern boundary of the northern Cascadia backarc: Journal of Geodynamics, v. 155, p. 101958, doi:10.1016/j.jog.2022.101958.

Currie, C.A., and Yu, T.-C., 2023, Geodynamic studies of southwestern Canada: subduction zone processes and backarc mantle dynamics: Canadian Journal of Earth Sciences, v. 60, p. 1283–1306, doi:10.1139/cjes-2022-0140.

Dalton, A.S. et al., 2023, Deglaciation of the north American ice sheet complex in calendar years based on a comprehensive database of chronological data: NADI-1: Quaternary Science Reviews, v. 321, doi:doi:10.1016/j.quascirev.2023.108345.

Daly, R.A., 1912, Geology of the North American Cordillera at the Forty-Ninth Parallel: Geological Survey of Canada Memoir no. 38, p. 857.

Damon, A., Mazzotti, S., Vernant, P., Vachon, R., Grosset, J., Ego, F., and Baumont, D., 2023, Impact of far-field glacially-induced stresses on fault stability in the eastern Paris Basin: Tectonophysics, v. 864, p. 230035, doi:10.1016/j.tecto.2023.230035.

Dascher-Cousineau, K., Finnegan, N.J., and Brodsky, E.E., 2021, The life span of fault-crossing channels: Science, v. 373, p. 204–207, doi:10.1126/science.abf2320.

Davis, E.E., and Lewis, T.J., 1984, Heat flow in a back-arc environment: Intermontane and Omineca Crystalline belts, southern Canadian Cordillera: Can. J. Earth Sci., v. 21, p. 715–726.

Dawson, G.M., 1885, Preliminary report on the physical and geological features of that portion of the Rocky Mountains, between latitudes 49 and 51: Geological Survey of Canada Annual Report 1.

Demuro, M., Froese, D.G., Arnold, L.J., and Roberts, R.G., 2012, Single-grain OSL dating of glaciofluvial quartz constrains Reid glaciation in NW Canada to MIS 6: Quaternary Research, v. 77, p. 305–316, doi:10.1016/j.yqres.2011.11.009.

Denton, G., and Stuiver, M., 1967, Late Pleistocene Glacial Stratigraphy and Chronology, Northeastern St Elias Mountains, Yukon Territory, Canada: GSA Bulletin, v. 78, p. 485–510, doi:10.1130/0016-7606(1967)78[485:LPGSAC]2.0.CO;2.

Dolan, J.F., and Haravitch, B.D., 2014, How well do surface slip measurements track slip at depth in large strike-slip earthquakes? The importance of fault structural maturity in controlling on-fault slip versus off-fault surface deformation: Earth and Planetary Science Letters, v. 388, p. 38–47, doi:10.1016/j.epsl.2013.11.043.

Dooley, T.P., and Schreurs, G., 2012, Analogue modelling of intraplate strike-slip tectonics: A review and new experimental results: Tectonophysics, v. 574–575, p. 1–71, doi:10.1016/j.tecto.2012.05.030.

Doser, D.I., 2014, Seismicity of Southwestern Yukon, Canada, and its relation to slip transfer between the Fairweather and Denali fault systems: Tectonophysics, v. 611, p. 121–129, doi:10.1016/j.tecto.2013.11.018.

Doser, D.I., 1985, Source parameters and faulting processes of the 1959 Hebgen Lake, Montana, earthquake sequence: Journal of Geophysical Research: Solid Earth, v. 90, p. 4537–4555, doi:10.1029/JB090iB06p04537.

Doser, D.I., and Smith, R.B., 1985, Source parameters of the 28 October 1983 Borah Peak, Idaho, earthquake from body wave analysis: Bulletin of the Seismological Society of America, v. 75, p. 1041–1051, doi:10.1785/BSSA0750041041.

Drooff, C., 2024, Subduction across timescales: geodetic and seismic investigations of ongoing and terminal-stage subduction in Alaska and northwest Canada [PhD Thesis]: Michigan State University.

Drooff, C., and Freymueller, J.T., 2023, New Insights Into the Active Tectonics of the Northern Canadian Cordillera From an Enhanced Earthquake Catalog: Journal of Geophysical Research: Solid Earth, v. 128, p. e2023JB026793, doi:10.1029/2023JB026793.

Duk-Rodkin, A., 1999, Glacial Limits Map of Yukon: Indian & Northern Affairs Canada/Department of Indian & Northern Development: Exploration & Geological Services Division, https://data.geology.gov.yk.ca/Reference/42050#InfoTab.

Duk-Rodkin, A., 1996, Surficial Geology, Dawson, Yukon Territory: Geological Survey of Canada Open File 3288.

Duk-Rodkin, A., Barendregt, R.W., White, J.M., and Singhroy, V.H., 2001, Geologic evolution of the Yukon River: implications for placer gold: Quaternary International, v. 82, p. 5–31, doi:10.1016/S1040-6182(01)00006-4.

DuRoss, C.B. et al., 2020a, Surface Displacement Distributions for the July 2019 Ridgecrest, California, Earthquake Ruptures: Bulletin of the Seismological Society of America, v. 110, p. 1400–1418, doi:10.1785/0120200058.

DuRoss, C.B., Gold, R.D., Briggs, R.W., Delano, J.E., Ostenaa, D.A., Zellman, M.S., Cholewinski, N., Wittke, S.J., and Mahan, S.A., 2020b, Holocene earthquake history and slip rate of the southern Teton fault, Wyoming, USA: GSA Bulletin, v. 132, p. 1566–1586, doi:10.1130/B35363.1.

EBA Engineering Consultants, 2004, Resource Assessment for Heat Potential Study, Haines Junction, YT, 156 p.

Eberhart-Phillips, D. et al., 2003, The 2002 Denali Fault Earthquake, Alaska: A Large Magnitude, Slip-Partitioned Event: Science, v. 300, p. 1113–1118, doi:10.1126/science.1082703.

Egan, J., Staff, R., and Blackford, J., 2015, A high-precision age estimate of the Holocene Plinian eruption of Mount Mazama, Oregon, USA: The Holocene, v. 25, p. 1054–1067, doi:10.1177/0959683615576230.

Elliott, J., and Freymueller, J.T., 2020, A Block Model of Present-Day Kinematics of Alaska and Western Canada: Journal of Geophysical Research: Solid Earth, v. 125, p. 30, doi:https://doi.org/10.1029/2019JB018378.

Elliott, J.R., Nissen, E.K., England, P.C., Jackson, J.A., Lamb, S., Li, Z., Oehlers, M., and Parsons, B., 2012, Slip in the 2010–2011 Canterbury earthquakes, New Zealand: Journal of Geophysical Research: Solid Earth, v. 117, doi:10.1029/2011JB008868.

Enkelmann, E., and Falkowski, S., 2021, Deformation between the highly oblique Yakutat–North American plate boundary and the Eastern Denali fault: Geosphere, v. 17, p. 2123–2143, doi:10.1130/GES02410.1.

Estève, C., Audet, P., Schaeffer, A.J., Schutt, D.L., Aster, R.C., and Cubley, J.F., 2020, Seismic evidence for craton chiseling and displacement of lithospheric mantle by the Tintina fault in the northern Canadian Cordillera: Geology, v. 48, p. 1120–1125, doi:10.1130/G47688.1.

Eyles, N., Arbelaez Moreno, L., and Sookhan, S., 2018, Ice streams of the Late Wisconsin Cordilleran Ice Sheet in western North America: Quaternary Science Reviews, v. 179, p. 87–122, doi:10.1016/j.quascirev.2017.10.027.

Eyles, N., and Kocsis, S., 1988, Sedimentology and clast fabric of subaerial debris flow facies in a glacially-influenced alluvial fan: Sedimentary Geology, v. 59, p. 15–28, doi:10.1016/0037-0738(88)90098-X.

Faccenna, C., and Becker, T.W., 2010, Shaping mobile belts by small-scale convection: Nature, v. 465, p. 602–605, doi:10.1038/nature09064.

Faulds, J., and Hinz, N., 2015, Favorable Tectonic and Structural Settings of Geothermal Systems in the Great Basin Region, Western USA: Proxies for Discovering Blind Geothermal Systems, *in* Proceedings World Geothermal Congress, p. 6.

Faulds, J.E., Hinz, N.H., Coolbaugh, M.F., Shevenell, L.A., Siler, D.L., Wannamaker, P.E., Queen, J.H., and Visser, C.F., 2015, Integrated Geologic and Geophysical Approach for Establishing Geothermal Play Fairways and Discovering Blind Geothermal Systems in the Great Basin Region, Western USA: A Progress Report: GRC Transactions, v. 39, p. 10.

Feng, W., Samsonov, S., Liang, C., Li, J., Charbonneau, F., Yu, C., and Li, Z., 2019, Source parameters of the 2017 Mw 6.2 Yukon earthquake doublet inferred from coseismic GPS and ALOS-2 deformation measurements: Geophysical Journal International, v. 216, p. 1517–1528, doi:10.1093/gji/ggy497.

Field, E.H. et al., 2014, Uniform California Earthquake Rupture Forecast, Version 3 (UCERF3)—The Time-Independent Model: Bulletin of the Seismological Society of America, v. 104, p. 1122–1180, doi:10.1785/0120130164.

Finley, T.D., Johnston, S.T., Unsworth, M.J., Banks, J., and Pana, D.-I., 2022a, Modern dextral strain controls active hydrothermal systems in the southeastern Canadian Cordillera: GSA Bulletin, doi:10.1130/B36500.1.

Finley, T., Nissen, E., Cassidy, J., Salomon, G., and Stephen, R., 2024, Drone lidar surveys of the Tintina Fault, Yukon, Canada, September 2023, doi:10.5069/G9MG7MR9.

Finley, T., Salomon, G., Nissen, E., Stephen, R., Cassidy, J., and Menounos, B., 2022b, Preliminary results and structural interpretations from drone lidar surveys over the Eastern Denali fault, Yukon, *in* MacFarlane, K. ed., Yukon Exploration and Geology 2021, Yukon Geological Survey, p. 83–105.

Finley, T., Salomon, G., Nissen, E., Stephen, R., and Clark, B., 2023, Drone lidar survey of the eastern shore of Columbia Lake, East Kootenays, doi:10.5069/G9PK0DCW.

Finzel, E.S., Flesch, L.M., and Ridgway, K.D., 2014, Present-day geodynamics of the northern North American Cordillera: Earth and Planetary Science Letters, v. 404, p. 111–123, doi:10.1016/j.epsl.2014.07.024.

Foo, W.K., 1979, Evolution of Transverse Structures Linking the Purcell Anticlinorium to the Western Rocky Mountains Near Canal Flats, British Columbia [PhD Thesis]: Queens University.

Fraser, K.I., Enkelmann, E., Jess, S., Gilbert, H., and Grieco, R., 2021, Resolving the Cenozoic History of Rock Exhumation Along the Central Rocky Mountain Trench Using Apatite Low-Temperature Thermochronology: Tectonics, v. 40, p. e2021TC006847, doi:10.1029/2021TC006847.

Friele, P.A., Ekes, C., and Hickin, E.J., 2000, Evolution of Cheekye fan, Squamish, British Columbia: Holocene sedimentation and implications for hazard assessment: Canadian Journal of Earth Sciences, v. 36, p. 2023–2031, doi:10.1139/e99-090.

Froese, D.G., 2005a, Surficial Geology, Flat Creek, Yukon Territory: Geological Survey of Canada Open File 4592.

Froese, D.G., 2005b, Surficial Geology, Medrick Creek, Yukon Territory: Geological Survey of Canada Open File 4593.

Froese, D.G., Barendregt, R.W., Enkin, R.J., and Baker, J., 2000, Paleomagnetic evidence for multiple Late Pliocene - Early Pleistocene glaciations in the Klondike area, Yukon Territory: Canadian Journal of Earth Sciences, v. 37, p. 863–877, doi:10.1139/e00-014.

Fu, B., Awata, Y., Kano, K., Lin, A., and Tsukuda, E., 2003, Coseismic surface deformation and engineering damage associated with the large strike-slip faulting: Lessons from the 2001 Mw 7.8 Central Kunlun earthquake: Annual Report on Active Fault and Paleoearthquake Researches, v. 3, p. 191–209.

Fulton, 1971, Radiocarbon geochronology of southern British Columbia: Geological Survey of Canada Paper 71-37.

Gabrielse, H., 1985, Major dextral transcurrent displacements along the Northern Rocky Mountain Trench and related lineaments in north-central British Columbia: Bulletin of the Geological Society of America, v. 96, p. 1–14, doi:10.1130/0016-7606(1985)96<1:MDTDAT>2.0.CO;2.

Gabrielse, H., Murphy, D.C., and Mortensen, J.K., 2006, Cretaceous and Cenozoic dextral orogen-parallel displacements, magmatism, and paleogeography, north-central Canadian Cordillera, *in* Haggart, J.W., Enkin, R.J., and Monger, J.W.H. eds., Paleogeography of the North American Cordillera: Evidence For and Against Large-Scale Displacements, p. 255–276.

Gal, L.P., and Ghent, E.D., 1990, Metamorphism in the Solitude Range, southwestern Rocky Mountains, British Columbia: comparison with adjacent Omineca Belt rocks and tectonometamorphic implications for the Purcell Thrust: Canadian Journal of Earth Sciences, v. 27, p. 1511–1520.

Gaudreau, E., Audet, P., and Schneider, D., 2019, Mapping Curie Depth Across Western Canada From a Wavelet Analysis of Magnetic Anomaly Data: Journal of Geophysical Research: Solid Earth, v. 124, doi:10.1029/2018JB016726.

Gledhill, K., Ristau, J., Reyners, M., Fry, B., and Holden, C., 2011, The Darfield (Canterbury, New Zealand) Mw 7.1 Earthquake of September 2010: A Preliminary Seismological Report: Seismological Research Letters, v. 82, p. 378–386, doi:10.1785/gssrl.82.3.378.

Goda, K., and Sharipov, A., 2021, Fault-Source-Based Probabilistic Seismic Hazard and Risk Analysis for Victoria, British Columbia, Canada: A Case of the Leech River Valley Fault and Devil's Mountain Fault System: Sustainability, v. 13, p. 1440, doi:10.3390/su13031440.

Goldberg, D.E. et al., 2023, Rapid Characterization of the February 2023 Kahramanmaraş, Türkiye, Earthquake Sequence: The Seismic Record, v. 3, p. 156–167, doi:10.1785/0320230009.

Gosselin, J.M., Biegel, K.M., Dettmer, J., Gilbert, H., Colpron, M., and Enkelmann, E., 2024, Crustal stress near the Yakutat microplate collision from probabilistic earthquake focal mechanisms: Canadian Journal of Earth Sciences, doi:10.1139/cjes-2024-0095.

Government of Yukon Lidar collection, https://maps.mcelhanney.com/Vertisee/YukonGovLidar/ (accessed October 2024).

Graham, A., 2018, Geometry, kinematics, and Quaternary activity of the brittle Leech River fault zone, southern Vancouver Island, British Columbia, Canada [PhD Thesis]: University of Victoria.

Grasby, S.E. et al., 2012, Geothermal Energy Resource Potential of Canada: Geological Survey of Canada Open File 6914, 322 p.

Grasby, S.E., and Hutcheon, I., 2001, Controls on the distribution of thermal springs in the southern Canadian Cordillera: Canadian Journal of Earth Sciences, v. 38, p. 427–440, doi:10.1139/e00-091.

Griffin, J.D., Stirling, M.W., and Wang, T., 2020, Periodicity and Clustering in the Long-Term Earthquake Record: Geophysical Research Letters, v. 47, p. e2020GL089272, doi:10.1029/2020GL089272.

Haddon, E.K., Amos, C.B., Zielke, O., Jayko, A.S., and Bürgmann, R., 2016, Surface slip during large Owens Valley earthquakes: Geochemistry, Geophysics, Geosystems, v. 17, p. 2239–2269, doi:10.1002/2015GC006033.

Haeussler, P.J. et al., 2004, Surface Rupture and Slip Distribution of the Denali and Totschunda Faults in the 3 November 2002 M 7.9 Earthquake, Alaska: Bulletin of the Seismological Society of America, v. 94, p. S23–S52, doi:10.1785/0120040626.

Haeussler, P.J., Bender, A.M., Powers, P.M., Koehler, R.D., and Brothers, D.S., 2024, Updating the Crustal Fault Model for the 2023 National Seismic Hazard Model for Alaska, *in* Ruppert, N., Jadamec, M., and Freymueller, J. eds., Tectonics and Seismicity of Alaska and Western Canada: Earthscope and Beyond, Wiley, AGU Geophysical Monograph Series.

Haeussler, P.J., Matmon, A., Schwartz, D.P., and Seitz, G.G., 2017, Neotectonics of interior Alaska and the late Quaternary slip rate along the Denali fault system: Geosphere, v. 13, p. 1445–1463, doi:10.1130/GES01447.1.

Halchuk, S., Allen, T., Adams, J., and Onur, T., 2019, Contribution of the Leech River Valley - Devil’s Mountain Fault System to Seismic Hazard in Victoria, B.C., *in* Proceedings 17th World Conference on Earthquake Engineering, Quebec City.

Halchuk, S., Allen, T.I., Rogers, G.C., and Adams, J., 2015, Seismic Hazard Earthquake Epicentre File (SHEEF2010) used in the fifth generation seismic hazard maps of Canada: Geological Survey of Canada Open File 7724, doi:10.4095/296908.

Hamilton, T.S., Enkin, R.J., Li, Z., Bednarski, J.M., Stacey, C.D., McGann, M.L., and Jensen, B.J.L., 2024, Where ice gave way to fire: deglacial volcanic activity at the edge of the Coast Mountains in Milbanke Sound, BC: Canadian Journal of Earth Sciences, v. 61, p. 58–85, doi:10.1139/cjes-2023-0080.

Hampel, A., Hetzel, R., and Densmore, A.L., 2007, Postglacial slip-rate increase on the Teton normal fault, northern Basin and Range Province, caused by melting of the Yellowstone ice cap and deglaciation of the Teton Range? Geology, v. 35, p. 1107–1110, doi:10.1130/G24093A.1.

Harrichhausen, N. et al., 2023, Discovery of an Active Forearc Fault in an Urban Region: Holocene Rupture on the XEOLXELEK-Elk Lake Fault, Victoria, British Columbia, Canada: Tectonics, v. 42, doi:10.1029/2023TC008170.

Harrichhausen, N., Morell, K.D., Regalla, C., Bennett, S.E.K., Leonard, L.J., Lynch, E.M., and Nissen, E., 2021, Paleoseismic Trenching Reveals Late Quaternary Kinematics of the Leech River Fault: Implications for Forearc Strain Accumulation in Northern Cascadia: Bulletin of the Seismological Society of America, v. 111, p. 1110–1138, doi:10.1785/0120200204.

Hatem, A.E., Collett, C.M., Briggs, R.W., Gold, R.D., Angster, S.J., Field, E.H., and Powers, P.M., 2022a, Simplifying complex fault data for systems-level analysis: Earthquake geology inputs for U.S. NSHM 2023: Scientific Data, v. 9, p. 506, doi:10.1038/s41597-022-01609-7.

Hatem, A.E., Reitman, N.G., Briggs, R.W., Gold, R.D., Thompson Jobe, J.A., and Burgette, R.J., 2022b, Western U.S. Geologic Deformation Model for Use in the U.S. National Seismic

Hazard Model 2023: Seismological Research Letters, v. 93, p. 3053–3067, doi:10.1785/0220220154.

Haugerud, R.A., Harding, D.J., Johnson, S.Y., Harless, J.L., Weaver, C.S., and Sherrod, B.L., 2003, High-Resolution Lidar Topography of the Puget Lowland, Washington — A Bonanza for Earth Science: GSA Today, v. 4, p. 4–10.

Heidbach, O. et al., 2018, The World Stress Map database release 2016: Crustal stress pattern across scales: Tectonophysics, v. 744, p. 484–498, doi:10.1016/j.tecto.2018.07.007.

Henderson, G.G.L., 1954, Geology of the Stanford Range of the Rocky Mountains: British Columbia Department of Mines Bulletin, v. 35, p. 93.

Hetzel, R., and Hampel, A., 2005, Slip rate variations on normal faults during glacial–interglacial changes in surface loads: Nature, v. 435, p. 81–84, doi:10.1038/nature03562.

Hidy, A.J., Gosse, J.C., Froese, D.G., Bond, J.D., and Rood, D.H., 2013, A latest Pliocene age for the earliest and most extensive Cordilleran Ice Sheet in northwestern Canada: Quaternary Science Reviews, v. 61, p. 77–84, doi:10.1016/j.quascirev.2012.11.009.

Hitch, D., Ritter, J., and Workman, M., 2012, Dákeyi Teaching Guide: Athapaskan Language Course - Southern Tutchone Place Names: Yukon Native Language Centre.

Hofmann, M.H., Hendrix, M.S., Sperazza, M., and Moore, J.N., 2006, Neotectonic evolution and fault geometry change along a major extensional fault system in the Mission and Flathead Valleys, NW-Montana: Journal of Structural Geology, v. 28, p. 1244–1260, doi:10.1016/j.jsg.2006.03.030.

Humphreys, E.D., and Coblentz, D.D., 2007, North American dynamics and western U.S. tectonics: Reviews of Geophysics, v. 45, doi:10.1029/2005RG000181.

Hurtado, C., and Gallen, S.F., 2024, Exploring the impact of deglaciation on fault slip in the Sangre de Cristo Mountains, Colorado, USA: Geology, doi:10.1130/G52661.1.

Hyndman, R.D., Currie, C.A., and Mazzotti, S.P., 2005, Subduction zone backarcs, mobile belts, and orogenic heat: GSA Today, v. 15, p. 4–10, doi:10.1130/1052-5173(2005)015<4:SZBMBA>2.0.CO;2.

Hyndman, R.D., and Lewis, T.J., 1999, Geophysical consequences of the Cordillera-Craton thermal transition in southwestern Canada: Tectonophysics, v. 306, p. 397–422, doi:10.1016/S0040-1951(99)00068-2.

Isenburg, M., 2021, LAStools - efficient LiDAR processing software, https://lastools.github.io/.

Jaya, A., Nishikawa, O., and Jumadil, S., 2019, Distribution and morphology of the surface ruptures of the 2018 Donggala–Palu earthquake, Central Sulawesi, Indonesia: Earth, Planets and Space, v. 71, p. 144, doi:10.1186/s40623-019-1126-3.

Jobin, D.M., Véronneau, M., and Miles, W.F., 2017, Gravity anomaly map, Canada: Geological Survey of Canada Open File 8081.

Johnson, K.L., Nissen, E., and Lajoie, L., 2018, Surface Rupture Morphology and Vertical Slip Distribution of the 1959 Mw 7.2 Hebgen Lake (Montana) Earthquake From Airborne Lidar Topography: Journal of Geophysical Research: Solid Earth, v. 123, p. 8229–8248, doi:10.1029/2017JB015039.

Kanamori, H., 2003, 72 - Earthquake Prediction: An Overview, *in* Lee, W.H.K., Kanamori, H., Jennings, P.C., and Kisslinger, C. eds., International Geophysics, Academic Press, International Handbook of Earthquake and Engineering Seismology, Part B, v. 81, p. 1205–1216, doi:10.1016/S0074-6142(03)80186-9.

Kanaori, Y., and Kawakami, S., 1996, The 1995 7.2 magnitude Kobe earthquake and the Arima-Takatsuki tectonic line: implications of the seismic risk for central Japan: Engineering Geology, v. 43, p. 135–150, doi:10.1016/0013-7952(96)00056-7.

Kao, H., Shan, S.-J., Bent, A., Woodgold, C., Rogers, G., Cassidy, J.F., and Ristau, J., 2012, Regional Centroid-Moment-Tensor Analysis for Earthquakes in Canada and Adjacent Regions: An Update: Seismological Research Letters, v. 83, p. 505–515, doi:10.1785/gssrl.83.3.505.

Kaufman, D.S., Young, N.E., Briner, J.P., and Manley, W.F., 2011, Chapter 33 - Alaska Palaeo-Glacier Atlas (Version 2), *in* Ehlers, J., Gibbard, P.L., and Hughes, P.D. eds., Developments in Quaternary Sciences, Elsevier, Quaternary Glaciations - Extent and Chronology, v. 15, p. 427–445, doi:10.1016/B978-0-444-53447-7.00033-7.

Kayen, R., Thompson, E., Minasian, D., Moss, R.E.S., Collins, B.D., Sitar, N., Dreger, D., and Carver, G., 2004, Geotechnical Reconnaissance of the 2002 Denali Fault, Alaska, Earthquake: Earthquake Spectra, v. 20, p. 639–667, doi:10.1193/1.1778389.

Kennedy, K., 2013, Surficial geology of Burwash Landing and Destruction Bay (parts of NTS 115G/2, 6 and 7), Yukon: Yukon Geological Survey Open File 2013-14.

Kennedy, K., and Ellis, S., 2020, Surficial geology of the northern Kluane Ranges (parts of NTS 115G/5, 6, 11, 12): Yukon Geological Survey Open File 2020-5.

KGS Group, 2016, Yukon Energy Corporation Geothermal Review and Site Inventory.:

Klinger, Y., Etchebes, M., Tapponnier, P., and Narteau, C., 2011, Characteristic slip for five great earthquakes along the Fuyun fault in China: Nature Geoscience, v. 4, p. 389–392, doi:10.1038/ngeo1158.

Klinger, Y., Xu, X., Tapponnier, P., Van der Woerd, J., Lasserre, C., and King, G., 2005, High-Resolution Satellite Imagery Mapping of the Surface Rupture and Slip Distribution of the Mw ~7.8, 14 November 2001 Kokoxili Earthquake, Kunlun Fault, Northern Tibet, China: Bulletin of the Seismological Society of America, v. 95, p. 1970–1987, doi:10.1785/0120040233.

Koch, J., Clague, J., and Blais-Stevens, A., 2014, Debris Flow Chronology and Potential Hazard Along the Alaska Highway in Southwest Yukon Territory: Environmental and Engineering Geoscience, v. 20, p. 25–43.

Kolaj, M., Adams, J., and Halchuk, S., 2020, The 6th Generation Seismic Hazard Model of Canada: 17th World Conference on Earthquake Engineering, p. 12 p.

Kolaj, M., Halchuk, S., and Adams, J., 2023, Sixth Generation seismic hazard model of Canada: final input files used to generate the 2020 National Building Code of Canada seismic hazard values.: Geological Survey of Canada, Open File 8924,.

Kozaci, O., Altunel, E., Koehler, R., Yildirim, C., and Clahan, K., 2024, M7.8 Kahramanmaras Earthquake Surface Fault Rupture and Near-fault Effect Observations: Japanese Geotechnical Society Special Publication, v. 10, p. 276–281, doi:10.3208/jgssp.v10.SS-6-03.

Kukovica, J., Ghofrani, H., Molnar, S., and Assatourians, K., 2019, Probabilistic Seismic Hazard Analysis of Victoria, British Columbia: Considering an Active Fault Zone in the Nearby Leech River Valley: Bulletin of the Seismological Society of America, v. 109, p. 2050–2062, doi:10.1785/0120180330.

Lee, B., Unsworth, M., Finley, T., Kong, W., and Cordell, D., 2024, Electrically anisotropic structure of the Rocky Mountain Trench near Valemount, British Columbia inferred from magnetotellurics: implications for geothermal exploration: Canadian Journal of Earth Sciences, doi:10.1139/cjes-2023-0086.

Leonard, L.J., Hyndman, R.D., Mazzotti, S., Nykolaishen, L., Schmidt, M., and Hippchen, S., 2007, Current deformation in the northern Canadian Cordillera inferred from GPS measurements: Journal of Geophysical Research: Solid Earth, v. 112, p. 1–15, doi:10.1029/2007JB005061.

Leonard, L.J., Mazzotti, S., and Hyndman, R.D., 2008, Deformation rates estimated from earthquakes in the northern Cordillera of Canada and eastern Alaska: Journal of Geophysical Research: Solid Earth, v. 113, p. 1–18, doi:10.1029/2007JB005456.

Lerbekmo, J.F., 2008, The White River Ash: largest Holocene Plinian tephra: Canadian Journal of Earth Sciences, v. 45, p. 693–700, doi:10.1139/E08-023.

Levander, A., and Miller, M.S., 2012, Evolutionary aspects of lithosphere discontinuity structure in the western U.S.: Geochemistry, Geophysics, Geosystems, v. 13, doi:10.1029/2012GC004056.

Lian, O., and Hickin, E., 1996, Early Postglacial Sedimentation of Lower Seymour Valley, Southwestern British Columbia: Géographie physique et Quaternaire, v. 50, p. 95–102, doi:10.7202/033078ar.

Lin, A., Guo, J., and Fu, B., 2004, Co-seismic mole track structures produced by the 2001 Ms 8.1 Central Kunlun earthquake, China: Journal of Structural Geology, v. 26, p. 1511–1519, doi:10.1016/j.jsg.2004.01.005.

Lin, Z., Kaneda, H., Mukoyama, S., Asada, N., and Chiba, T., 2013, Detection of subtle tectonic–geomorphic features in densely forested mountains by very high-resolution airborne LiDAR survey: Geomorphology, v. 182, p. 104–115, doi:10.1016/j.geomorph.2012.11.001.

Lipovsky, P.S., Seitz, G., Haeussler, P.J., Crone, A.J., Schwartz, D.P., Clague, J.J., Mazotti, S., and Cobbett, R., 2009, Neotectonic investigations in southwest Yukon, *in* Canadian Quaternary Association Meeting, Vancouver, BC, Canada.

Little, T.A., Morris, P., Hill, M.P., Kearse, J., Van Dissen, R.J., Manousakis, J., Zekkos, D., and Howell, A., 2021, Coseismic deformation of the ground during large-slip strike-slip ruptures: Finite evolution of “mole tracks”: Geosphere, v. 17, p. 1170–1192, doi:10.1130/GES02336.1.

Lowdon, J.A., and Blake, W., 1976, Geological Survey of Canada radiocarbon dates XVI: Paper 76-7.

Lowry, A.R., and Smith, R.B., 1995, Strength and rheology of the western U.S. Cordillera: Journal of Geophysical Research: Solid Earth, v. 100, p. 17947–17963, doi:10.1029/95JB00747.

Lund Snee, J.-E., and Zoback, M.D., 2020, Multiscale variations of the crustal stress field throughout North America: Nature Communications, v. 11, p. 1951, doi:10.1038/s41467-020-15841-5.

Lynch, E.M., 2023, Strain Accommodation on Forearc Faults: A Case Study on the Beaufort Range Fault, an Active Crustal Fault in the Northern Cascadia Forearc, Vancouver Island, BC, Canada [PhD Thesis]: Northern Arizona University, 254 p.

Mackenzie, D., and Elliott, A., 2017, Untangling tectonic slip from the potentially misleading effects of landform geometry: Geosphere, v. 13, p. 1310–1328, doi:10.1130/GES01386.1.

Manighetti, I., Campillo, M., Bouley, S., and Cotton, F., 2007, Earthquake scaling, fault segmentation, and structural maturity: Earth and Planetary Science Letters, v. 253, p. 429–438, doi:10.1016/j.epsl.2006.11.004.

Manighetti, I., Mercier, A., and De Barros, L., 2021, Fault Trace Corrugation and Segmentation as a Measure of Fault Structural Maturity: Geophysical Research Letters, v. 48, p. e2021GL095372, doi:10.1029/2021GL095372.

Manighetti, I., Perrin, C., Gaudemer, Y., Dominguez, S., Stewart, N., Malavieille, J., and Garambois, S., 2020, Repeated giant earthquakes on the Wairarapa fault, New Zealand, revealed by Lidar-based paleoseismology: Scientific Reports, v. 10, p. 2124, doi:10.1038/s41598-020-59229-3.

Marechal, A., Mazzotti, S., Elliott, J.L., Freymueller, J.T., and Schmidt, M., 2015, Indentor-corner tectonics in the Yakutat-St. Elias collision constrained by GPS: Journal of Geophysical Research: Solid Earth, v. 120, p. 3897–3908, doi:10.1002/2014JB011842.

Marechal, A., Ritz, J.-F., Ferry, M., Mazzotti, S., Blard, P.-H., Braucher, R., and Saint-Carlier, D., 2018, Active tectonics around the Yakutat indentor: New geomorphological constraints on the eastern Denali, Totschunda and Duke River Faults: Earth and Planetary Science Letters, v. 482, p. 71–80, doi:10.1016/j.epsl.2017.10.051.

Marrett, R., and Allmendinger, R.W., 1990, Kinematic analysis of fault-slip data: Journal of Structural Geology, v. 12, p. 973–986, doi:10.1016/0191-8141(90)90093-E.

Matmon, A., Schwartz, D.P., Haeussler, P.J., Finkel, R., Lienkaemper, J.J., Stenner, H.D., and Dawson, Te., 2006, Denali fault slip rates and Holocene–late Pleistocene kinematics of central Alaska: Geology, v. 34, p. 645, doi:10.1130/G22361.1.

Mazzotti, S., and Hyndman, R.D., 2002, Yakutat collision and strain transfer across the northern Canadian Cordillera: Geology, v. 30, p. 495–498, doi:10.1130/0091-7613(2002)030<0495:YCASTA>2.0.CO;2.

Mazzotti, S., James, T.S., Henton, J., and Adams, J., 2005, GPS crustal strain, postglacial rebound, and seismic hazard in eastern North America: The Saint Lawrence valley example: Journal of Geophysical Research: Solid Earth, v. 110, doi:https://doi.org/10.1029/2004JB003590.

Mazzotti, S., Leonard, L.J., Cassidy, J.F., Rogers, G.C., and Halchuk, S., 2011, Seismic hazard in western Canada from GPS strain rates versus earthquake catalog: Journal of Geophysical Research: Solid Earth, v. 116, p. 1–17, doi:10.1029/2011JB008213.

Mazzotti, S., Leonard, L.J., Hyndman, R.D., and Cassidy, J.F., 2008, Tectonics, dynamics, and seismic hazard in the Canada-Alaska Cordillera: Washington DC American Geophysical Union Geophysical Monograph Series, v. 179, p. 297–319, doi:10.1029/179GM17.

McCalpin, J., 1999, Criteria for Determining the Seismic Significance of Sackungen and Other Scarplike Landforms in Mountainous Regions: U.S. Nuclear Regulatory Commission.

McCalpin, J.P., Bruhn, R.L., Pavlis, T.L., Gutierrez, F., Guerrero, J., and Lucha, P., 2011, Antislope scarps, gravitational spreading, and tectonic faulting in the western Yakutat microplate, south coastal Alaska: Geosphere, v. 7, p. 1143–1158, doi:10.1130/GES00594.1.

McClay, K., and Bonora, M., 2001, Analog Models of Restraining Stepovers in Strike-Slip Fault Systems: AAPG Bulletin, v. 85, p. 233–260, doi:10.1306/8626C7AD-173B-11D7-8645000102C1865D.

McConeghy, J., Flesch, L., and Elliott, J., 2022, Investigating the Effect of Mantle Flow and Viscosity Structure on Surface Velocities in Alaska Using 3-D Geodynamic Models: Journal of Geophysical Research: Solid Earth, v. 127, p. e2022JB024704, doi:10.1029/2022JB024704.

McDermott, R.G., Ault, A.K., Caine, J.S., and Thomson, S.N., 2019, Thermotectonic History of the Kluane Ranges and Evolution of the Eastern Denali Fault Zone in Southwestern Yukon, Canada: Tectonics, v. 38, p. 2983–3010, doi:10.1029/2019TC005545.

McDonough, M.R., and Simony, P.S., 1988, Structural evolution of basement gneisses and Hadrynian cover, Bulldog Creek area, Rocky Mountains, British Columbia: Canadian Journal of Earth Sciences, v. 25, p. 1687–1702, doi:10.1139/e88-159.

McKenna, K., and Lipovsky, P., 2014, Surficial Geology, Dawson Region, Yukon, Parts of NTS 115O/14 & 15 and 116B/1, 2, 3 & 4: Yukon Geological Survey Open File 2014-12.

McKenzie, D.P., 1969, The relation between fault plane solutions for earthquakes and the directions of the principal stresses: Bulletin of the Seismological Society of America, v. 59, p. 591–601.

McMechan, M.E., 2000, Walker Creek fault zone, central Rocky Mountains, British Columbia-southern continuation of the Northern Rocky Mountain Trench fault zone: Canadian Journal of Earth Sciences, v. 37, p. 1259–1273, doi:10.1139/e00-038.

Meigs, A., 2013, Active tectonics and the LiDAR revolution: Lithosphere, v. 5, p. 226–229, doi:10.1130/RF.L004.1.

Meixner, J., Schill, E., Grimmer, J.C., Gaucher, E., Kohl, T., and Klingler, P., 2016, Structural control of geothermal reservoirs in extensional tectonic settings: An example from the Upper Rhine Graben: Journal of Structural Geology, v. 82, p. 1–15, doi:10.1016/j.jsg.2015.11.003.

Menounos, B. et al., 2017, Cordilleran Ice Sheet mass loss preceded climate reversals near the Pleistocene Termination: Science, v. 358, p. 781–784, doi:10.1126/science.aan3001.

Mériaux, A.-S., Sieh, K., Finkel, R.C., Rubin, C.M., Taylor, M.H., Meltzner, A.J., and Ryerson, F.J., 2009, Kinematic behavior of southern Alaska constrained by westward decreasing postglacial slip rates on the Denali Fault, Alaska: Journal of Geophysical Research: Solid Earth, v. 114, doi:10.1029/2007JB005053.

Mihindukulasooriya, L.N., Ortiz, J.D., Pompeani, D.P., Steinman, B.A., and Abbott, M.B., 2015, Reconstruction of late Quaternary paleohydrologic Conditions in southeastern British

Columbia using visible derivative spectroscopy of Cleland Lake Sediment: Quaternary Research, v. 83, p. 531–544, doi:10.1016/j.yqres.2015.02.003.

Miller, B.G.N., Iverson, R.M., Clague, J.J., Geertsema, M., and Roberts, N.J., 2021, Channel-amphitheatre landforms resulting from liquefaction flowslides during rapid drawdown of glacial Lake Fraser, British Columbia, Canada: Geomorphology, v. 392, p. 107898, doi:10.1016/j.geomorph.2021.107898.

Mira Geoscience, 2015, Ross River geothermal exploration project: Review of the 2014 work program: Yukon Geological Survey Miscellaneous Report MR-18, 141 p.

Moeck, I.S., 2014, Catalog of geothermal play types based on geologic controls: Renewable and Sustainable Energy Reviews, v. 37, p. 867–882, doi:10.1016/j.rser.2014.05.032.

Morell, K.D., Regalla, C., Amos, C., Bennett, S., Leonard, L., Graham, A., Reedy, T., Levson, V., and Telka, A., 2018, Holocene Surface Rupture History of an Active Forearc Fault Redefines Seismic Hazard in Southwestern British Columbia, Canada: Geophysical Research Letters, v. 45, p. 11,605-11,611, doi:10.1029/2018GL078711.

Morell, K.D., Regalla, C., Leonard, L.J., Amos, C., and Levson, V., 2017, Quaternary Rupture of a Crustal Fault beneath Victoria, British Columbia, Canada: GSA Today, v. 27, p. 1–7, doi:10.1130/GSATG291A.1.

Morell, K.D., Styron, R., Stirling, M., Griffin, J., Archuleta, R., and Onur, T., 2020, Seismic Hazard Analyses From Geologic and Geomorphic Data: Current and Future Challenges: Tectonics, v. 39, p. 47, doi:https://doi.org/10.1029/2018TC005365.

Moreno, D., Lopez-Sanchez, J., Blessent, D., and Raymond, J., 2018, Fault characterization and heat-transfer modeling to the Northwest of Nevado del Ruiz Volcano: Journal of South American Earth Sciences, v. 88, p. 50–63, doi:10.1016/j.jsames.2018.08.008.

Mortensen, J., and Von Gaza, P., 1992, Application of Landsat TM thermal imagery to structural interpretations of the Tintina Trench in west-central Yukon, *in* Yukon Geology, Exploration and Geological Services Division, Yukon, Indian and Northern Affairs Canada, v. 3, p. 214–222.

Mount, V.S., and Suppe, J., 1992, Present-day stress orientations adjacent to active strike-slip faults: California and Sumatra: Journal of Geophysical Research: Solid Earth, v. 97, p. 11995–12013, doi:10.1029/92JB00130.

Mueller, C.S., 2018, Earthquake Catalogs for the USGS National Seismic Hazard Maps: Seismological Research Letters, v. 90, p. 251–261, doi:10.1785/0220170108.

Muir-Wood, R., 1989, Extraordinary Deglaciation Reverse Faulting in Northern Fennoscandia, *in* Gregersen, S. and Basham, P.W. eds., Earthquakes at North-Atlantic Passive Margins: Neotectonics and Postglacial Rebound, Dordrecht, Springer Netherlands, NATO ASI Series, p. 141–173, doi:10.1007/978-94-009-2311-9_10.

Murphy, D.C., 1990, Direct evidence for dextral strike-slip displacement from mylonites in the southern Rocky Mountain Trench near Valemount, British Columbia: Geological Survey of Canada Current Research, Paper 90-1E.

Natural Resources Canada, 2024, Canadian National Earthquake Database: Earthquakes Canada, https://www.earthquakescanada.nrcan.gc.ca/stndon/NEDB-BNDS/index-en.php (accessed October 2024).

Neyamadpour, A., Wan Abdullah, W.A.T., Taib, S., and Neyamadpour, B., 2010, Comparison of Wenner and dipole–dipole arrays in the study of an underground three-dimensional cavity: Journal of Geophysics and Engineering, v. 7, p. 30–40, doi:10.1088/1742-2132/7/1/003.

Nicol, A., Robinson, R., Van Dissen, R., and Harvison, A., 2016, Variability of recurrence interval and single-event slip for surface-rupturing earthquakes in New Zealand: New Zealand Journal of Geology and Geophysics, v. 59, p. 97–116, doi:10.1080/00288306.2015.1127822.

Noh, M.-J., and Howat, I.M., 2017, The Surface Extraction from TIN based Search-space Minimization (SETSM) algorithm: ISPRS Journal of Photogrammetry and Remote Sensing, v. 129, p. 55–76, doi:10.1016/j.isprsjprs.2017.04.019.

North, F.K., and Henderson, G.G.L., 1954, The Rocky Mountain Trench, *in* Alberta Society of Petroleum Geologists, v. Guide Book, Fourth Annual Field Conference Banff-Golden-Radium, p. 82–100.

Ojo, A.O., Kao, H., Jiang, Y., Craymer, M., and Henton, J., 2021, Strain Accumulation and Release Rate in Canada: Implications for Long-Term Crustal Deformation and Earthquake Hazards: Journal of Geophysical Research: Solid Earth, v. 126, p. e2020JB020529, doi:10.1029/2020JB020529.

Ostenaa, D.A., Levish, D.R., and Klinger, R.E., 1995, Mission Fault Study: U.S. Bureau of Reclamation Seismotectonic Report 94-8.

Özalaybey, S., Ergin, M., Aktar, M., Tapirdamaz, C., Biçmen, F., and Yörük, A., 2002, The 1999 İzmit Earthquake Sequence in Turkey: Seismological and Tectonic Aspects: Bulletin of the Seismological Society of America, v. 92, p. 376–386, doi:10.1785/0120000838.

Palacky, G.J., 1987, Resistivity Characteristics of Geologic Targets, *in* Nabighian, M.N. and Corbett, J.D. eds., Electromagnetic Methods in Applied Geophysics: Volume 1, Theory, Society of Exploration Geophysicists, v. 3, p. 0, doi:10.1190/1.9781560802631.ch3.

Petersen, M.D., Cao, T., Campbell, K.W., and Frankel, A.D., 2007, Time-independent and Time-dependent Seismic Hazard Assessment for the State of California: Uniform California Earthquake Rupture Forecast Model 1.0: Seismological Research Letters, v. 78, p. 99–109, doi:10.1785/gssrl.78.1.99.

Porter, C., 2023, ArcticDEM, Version 4.1, doi:https://doi.org/10.7910/DVN/3VDC4W.

Purba, J.C.S., Gilbert, H., and Dettmer, J., 2021, Structure and Dynamics of the Southern Rocky Mountain Trench near Valemount, British Columbia, Inferred from Local Seismicity: Seismological Research Letters, v. 92, p. 13.

Reavely, L., 1985, The Borah Peak, Idaho Earthquake of October 28, 1983—Summary: Earthquake Spectra, v. 2, doi:10.1193/1.1585297.

Reimer, P.J. et al., 2020, The IntCal20 Northern Hemisphere Radiocarbon Age Calibration Curve (0–55 cal kBP): Radiocarbon, v. 62, p. 725–757, doi:10.1017/RDC.2020.41.

Reitman, N.G., Klinger, Y., Briggs, R.W., and Gold, R.D., 2022, Climatic influence on the expression of strike-slip faulting: Geology, p. 18–22.

Reitman, N.G., Klinger, Y., Briggs, R.W., and Gold, R.D., 2024, Limited Preservation of Strike-Slip Surface Displacement in the Geomorphic Record: Journal of Geophysical Research: Solid Earth, v. 129, p. e2024JB028692, doi:10.1029/2024JB028692.

Ren, J., Xu, X., Zhang, G., Wang, Q., Zhang, Z., Gai, H., and Kang, W., 2022, Coseismic surface ruptures, slip distribution, and 3D seismogenic fault for the 2021 Mw 7.3 Maduo earthquake, central Tibetan Plateau, and its tectonic implications: Tectonophysics, v. 827, p. 229275, doi:10.1016/j.tecto.2022.229275.

Resop, J.P., Lehmann, L., and Hession, W.C., 2019, Drone Laser Scanning for Modeling Riverscape Topography and Vegetation: Comparison with Traditional Aerial Lidar: Drones, v. 3, p. 35, doi:10.3390/drones3020035.

Richard, P., Mocquet, B., and Cobbold, P.R., 1991, Experiments on simultaneous faulting and folding above a basement wrench fault: Tectonophysics, v. 188, p. 133–141, doi:10.1016/0040-1951(91)90319-N.

Rippe, D., Unsworth, M.J., and Currie, C.A., 2013, Magnetotelluric constraints on the fluid content in the upper mantle beneath the southern Canadian Cordillera: Implications for rheology: Journal of Geophysical Research: Solid Earth, v. 118, p. 5601–5624, doi:10.1002/jgrb.50255.

Risbøl, O., and Gustavsen, L., 2018, LiDAR from drones employed for mapping archaeology – Potential, benefits and challenges: Archaeological Prospection, v. 25, p. 329–338, doi:10.1002/arp.1712.

Ristau, J., Rogers, G.C., and Cassidy, J.F., 2007, Stress in western Canada from regional moment tensor analysis: Canadian Journal of Earth Sciences, v. 44, p. 127–148, doi:10.1139/e06-057.

Rizza, M. et al., 2015, Earthquake Geology of the Bulnay Fault (Mongolia): Bulletin of the Seismological Society of America, v. 105, p. 72–93, doi:10.1785/0120140119.

Rodgers, D.W., and Little, T.A., 2006, World's largest coseismic strike-slip offset: The 1855 rupture of the Wairarapa Fault, New Zealand, and implications for displacement/length scaling of continental earthquakes: Journal of Geophysical Research: Solid Earth, v. 111, doi:10.1029/2005JB004065.

Roed, M.A., and Wasylyk, D.G., 1973, Age of Inactive Alluvial Fans—Bow River Valley, Alberta: Canadian Journal of Earth Sciences, v. 10, p. 1834–1840, doi:10.1139/e73-178.

Rogers, G., Cassidy, J., and Ellis, R., 1990, The Prince George, British Columbia, Earthquake of 21 March 1986: Bulletin of the Seismological Society of America, v. 80, p. 1144–1161.

Rogers, G.C., and Ellis, R.M., 1979, The eastern British Columbia earthquake of February 4, 1918: Canadian Journal of Earth Sciences, v. 16, p. 1484–1493, doi:10.1139/e79-131.

Rogers, G.C., Ellis, R.M., and Hasegawa, H.S., 1980, The McNaughton Lake Earthquake of May 14, 1978: Bulletin of the Seismological Society of America, v. 70, p. 1771–1786.

Ryan, J., Hayward, N., and Jackson, L.E., Jr., 2017, Landscape antiquity and Cenozoic drainage development of southern Yukon, through restoration modeling of the Tintina Fault: Canadian Journal of Earth Sciences, v. 54, p. 1085–1100, doi:10.1139/cjes-2017-0053.

Ryder, J.M., 1971a, Some Aspects of the Morphometry of Paraglacial Alluvial Fans in South-central British Columbia: Canadian Journal of Earth Sciences, v. 8, p. 1252–1264, doi:10.1139/e71-114.

Ryder, J.M., 1971b, The Stratigraphy and Morphology of Para-glacial Alluvial Fans in South-central British Columbia: Canadian Journal of Earth Sciences, v. 8, p. 279–298, doi:10.1139/e71-027.

Ryder, J., Fulton, R., and Clague, J., 1991, The Cordilleran Ice Sheet and the Glacial Geomorphology of Southern and Central British Colombia: Géographie physique et Quaternaire, v. 45, p. 365–377, doi:10.7202/032882ar.

Salomon, G., Finley, T., Nissen, E., Stephen, R., and Menounos, B., 2024, Mapping fault geomorphology with drone-based lidar: Seismica, v. 3, doi:10.26443/seismica.v3i1.1186.

Sawicki, O., 1990, Geomorphology of Glacial Lake Invermere, upper Columbia Lake Valley, British Columbia [MSc Thesis]: University of Calgary, 133 p.

Sawicki, O., and Smith, D.G., 1992, Glacial Lake Invermere, upper Columbia River valley, British Columbia: a paleogeographic reconstruction: Canadian Journal of Earth Sciences, v. 29, p. 687–692, doi:10.1139/e92-059.

Schaeffer, A.J., and Lebedev, S., 2014, Imaging the North American continent using waveform inversion of global and USArray data: Earth and Planetary Science Letters, v. 402, p. 26–41, doi:10.1016/j.epsl.2014.05.014.

Schellart, W.P., and Nieuwland, D.A., 2003, 3D evolution of a pop-up structure above a double basement strike-slip fault: some insights from analogue modelling: Geological Society, London, Special Publications, v. 212, p. 169–179, doi:10.1144/GSL.SP.2003.212.01.11.

Schmeelk, D., Bendick, R., Stickney, M., and Bomberger, C., 2017, Kinematic evidence for the effect of changing plate boundary conditions on the tectonics of the northern U.S. Rockies: Tectonics, v. 36, p. 1090–1102, doi:10.1002/2016TC004427.

Schwartz, D.P., Haeussler, P.J., Seitz, G.G., and Dawson, T.E., 2012, Why the 2002 Denali fault rupture propagated onto the Totschunda fault: Implications for fault branching and seismic hazards: Journal of Geophysical Research: Solid Earth, v. 117, p. 1–25, doi:10.1029/2011JB008918.

Seebeck, H. et al., 2023, The New Zealand Community Fault Model – version 1.0: an improved geological foundation for seismic hazard modelling: New Zealand Journal of Geology and Geophysics, p. 1–21.

Seitz, G., Haeussler, P.J., Crone, A.J., Lipovsky, P.S., and Schwartz, D.P., 2008, Eastern Denali fault slip rate and paleoseismic history, Kluane Lake area, Yukon Territory, Canada, *in* American Geophysical Union Fall Meeting, San Francisco, CA, USA.

Sella, G.F., Stein, S., Dixon, T.H., Craymer, M., James, T.S., Mazzotti, S., and Dokka, R.K., 2007, Observation of glacial isostatic adjustment in “stable” North America with GPS: Geophysical Research Letters, v. 34, p. 2006GL027081, doi:10.1029/2006GL027081.

Smith, R., and Sbar, M., 1974, Contemporary Tectonics and Seismicity of the Western United States with Emphasis on the Intermountain Seismic Belt: GSA Bulletin, v. 85, p. 1205–1218, doi:10.1130/0016-7606(1974)85<1205:CTASOT>2.0.CO;2.

Smith, L.N., Sohbati, R., Buylaert, J.-P., Lian, O.B., Murray, A., and Jain, M., 2018, Timing of lake-level changes for a deep last-glacial Lake Missoula: optical dating of the Garden Gulch area, Montana, USA: Quaternary Science Reviews, v. 183, p. 23–35, doi:10.1016/j.quascirev.2018.01.009.

Smith, C., Tarnocai, C., and Hughes, O., 1986, Pedological Investigations of Pleistocene Glacial Drift Surfaces in the Central Yukon: Géographie Physique et Quaternaire, v. 40, p. 29–37, doi:10.7202/032620ar.

Spotila, J.A., and Berger, A.L., 2010, Exhumation at orogenic indentor corners under long-term glacial conditions: Example of the St. Elias orogen, Southern Alaska: Tectonophysics, v. 490, p. 241–256, doi:10.1016/j.tecto.2010.05.015.

Steffen, R., and Steffen, H., 2021, Reactivation of Non-Optimally Orientated Faults Due to Glacially Induced Stresses: Tectonics, v. 40, p. e2021TC006853, doi:10.1029/2021TC006853.

Steffen, R., Steffen, H., Wu, P., and Eaton, D.W., 2014, Stress and fault parameters affecting fault slip magnitude and activation time during a glacial cycle: Tectonics, v. 33, p. 1461–1476, doi:10.1002/2013TC003450.

Stewart, N., Gaudemer, Y., Manighetti, I., Serreau, L., Vincendeau, A., Dominguez, S., Mattéo, L., and Malavieille, J., 2018, "3D_Fault_Offsets," a Matlab Code to Automatically Measure Lateral and Vertical Fault Offsets in Topographic Data: Application to San Andreas, Owens Valley, and Hope Faults: Journal of Geophysical Research: Solid Earth, v. 123, p. 815–835, doi:10.1002/2017JB014863.

Stroeven, A.P., Fabel, D., Codilean, A.T., Kleman, J., Clague, J.J., Miguens-Rodriguez, M., and Xu, S., 2010, Investigating the glacial history of the northern sector of the Cordilleran Ice Sheet with cosmogenic 10Be concentrations in quartz: Quaternary Science Reviews, v. 29, p. 3630–3643, doi:10.1016/j.quascirev.2010.07.010.

Styron, R., 2019, The impact of earthquake cycle variability on neotectonic and paleoseismic slip rate estimates: Solid Earth, v. 10, p. 15–25, doi:10.5194/se-10-15-2019.

Tarnocai, C., Smith, S., and Hughes, O.L., 1985, Soil development on Quaternary deposits of various ages in the central Yukon Territory, *in* Current Research, Part A, Geological Survey of Canada, Paper 85-1A, p. 229–238.

Tetra Tech, 2017, Overarching Yukon Source Water Supply and Protection Study - Summary Report.

Thakur, P., and Huang, Y., 2021, Influence of Fault Zone Maturity on Fully Dynamic Earthquake Cycles: Geophysical Research Letters, v. 48, p. 1–11, doi:10.1029/2021GL094679.

Thomas, R.D., and Rampton, V.N., 1982, Surficial Geology and Geomorphology North Klondike River, Yukon Territory: Geological Survey of Canada Preliminary Map 6-1982, https://doi.org/10.4095/119397.

Thompson, S., Clague, J., and Evans, S., 1997, Holocene Activity of the Mt. Currie Scarp, Coast Mountains, British Columbia, and Implications for its Origin: Environmental & Engineering Geoscience, v. III, p. 329–348, doi:10.2113/gseegeosci.III.3.329.

Thompson, S.C., Weldon, R.J., Rubin, C.M., Abdrakhmatov, K., Molnar, P., and Berger, G.W., 2002, Late Quaternary slip rates across the central Tien Shan, Kyrgyzstan, central Asia: Journal of Geophysical Research: Solid Earth, v. 107, p. 1–32, doi:10.1029/2001JB000596.

Thorson, R.M., 1996, Earthquake recurrence and glacial loading in western Washington: GSA Bulletin, v. 108, p. 1182–1191, doi:10.1130/0016-7606(1996)108<1182:ERAGLI>2.3.CO;2.

Thorson, R.M., 2000, Glacial tectonics: a deeper perspective: Quaternary Science Reviews, v. 19, p. 1391–1398, doi:10.1016/S0277-3791(00)00068-8.

Tschirhart, V., Colpron, M., Craven, J., Ghalati, F.H., Enkin, R.J., and Grasby, S.E., 2022, Geothermal Exploration in the Burwash Landing Region, Canada, Using Three-Dimensional Inversion of Passive Electromagnetic Data: Remote Sensing, v. 14, p. 1–22, doi:10.3390/rs14235963.

U.S. Geological Survey, 2017, Quaternary fault and fold database for the United States:, doi:10.5066/F7S75FJM.

Vasyura-Bathke, H., Dettmer, J., Steinberg, A., Heimann, S., Isken, M.P., Zielke, O., Mai, P.M., Sudhaus, H., and Jónsson, S., 2020, The Bayesian Earthquake Analysis Tool: Seismological Research Letters, v. 91, p. 1003–1018, doi:10.1785/0220190075.

Vavryčuk, V., 2014, Iterative joint inversion for stress and fault orientations from focal mechanisms: Geophysical Journal International, v. 199, p. 69–77, doi:10.1093/gji/ggu224.

van der Velden, A.J., and Cook, F.A., 1996, Structure and tectonic development of the southern Rocky Mountain trench: Tectonics, v. 15, p. 517–544, doi:10.1029/95TC03288.

van der Wal, W., Braun, A., Wu, P., and Sideris, M.G., 2009, Prediction of decadal slope changes in Canada by glacial isostatic adjustment modelling: Canadian Journal of Earth Sciences, v. 46, p. 587–595, doi:10.1139/E09-044.

Wahrhaftig, C., Turner, D.L., Weber, F.R., and Smith, T.E., 1975, Nature and timing of movement on Hines Creek strand of Denali fault system, Alaska: Geology, v. 3, p. 463–466, doi:10.1130/0091-7613(1975)3<463:NATOMO>2.0.CO;2.

Wald, D.J., Kanamori, H., Helmberger, D.V., and Heaton, T.H., 1993, Source study of the 1906 San Francisco earthquake: Bulletin of the Seismological Society of America, v. 83, p. 981–1019, doi:10.1785/BSSA0830040981.

Waldien, T.S., Roeske, S.M., and Benowitz, J.A., 2021, Tectonic Underplating and Dismemberment of the Maclaren-Kluane Schist Records Late Cretaceous Terrane Accretion Polarity and 480 km of Post-52 Ma Dextral Displacement on the Denali Fault: Tectonics, v. 40, p. e2020TC006677, doi:10.1029/2020TC006677.

Wallace, R., 1951, Geometry of Shearing Stress and Relation to Faulting: Journal of Geology, v. 59, p. 118-130, doi:10.1086/625831.

Wang, K., Zhu, Y., Nissen, E., and Shen, Z.-K., 2021, On the Relevance of Geodetic Deformation Rates to Earthquake Potential: Geophysical Research Letters, v. 48, p. e2021GL093231, doi:10.1029/2021GL093231.

Ward, B.C., Bond, J.D., Froese, D., and Jensen, B., 2008, Old Crow tephra (140 ± 10 ka) constrains penultimate Reid glaciation in central Yukon Territory: Quaternary Science Reviews, v. 27, p. 1909–1915, doi:10.1016/j.quascirev.2008.07.012.

Wesnousky, S.G., 2008, Displacement and Geometrical Characteristics of Earthquake Surface Ruptures: Issues and Implications for Seismic-Hazard Analysis and the Process of Earthquake Rupture: Bulletin of the Seismological Society of America, v. 98, p. 1609–1632, doi:10.1785/0120070111.

Wesnousky, S.G., 2006, Predicting the endpoints of earthquake ruptures: Nature, v. 444, p. 358–360, doi:10.1038/nature05275.

Whelan, N., 2022, Geochronology of landslides in the Kluane Lake Region, Southwest Yukon [MSc Thesis]: Simon Fraser University.

Witter, J., 2022, Analysis of geoscience data for geothermal exploration along the Tintina fault near Watson Lake, Yukon: Yukon Geological Survey Open File 2022-8, p. 50 p.

Witter, J.B., 2020, Early-stage exploration for geothermal energy resources along the Denali fault near Duke River, Yukon: Yukon Geological Survey Open File 2020-3, 70 p.

Witter, J., Miller, C., Friend, M., and Colpron, M., 2018, Curie Point Depths and Heat Production in Yukon, Canada, *in* Proceedings, 43rd workshop on Geothermal Reservoir Engineering, Stanford University, Stanford, California.

Wolfe, F.D., Stahl, T.A., Villamor, P., and Lukovic, B., 2020, Short communication: A semiautomated method for bulk fault slip analysis from topographic scarp profiles: Earth Surface Dynamics, v. 8, p. 211–219, doi:10.5194/esurf-8-211-2020.

Youngs, R.R. et al., 2003, A Methodology for Probabilistic Fault Displacement Hazard Analysis (PFDHA): Earthquake Spectra, v. 19, p. 191–219, doi:10.1193/1.1542891.

Youngs, R.R., and Coppersmith, K.J., 1985, Implications of fault slip rates and earthquake recurrence models to probabilistic seismic hazard estimates: Bulletin of the Seismological Society of America, v. 75, p. 939–964, doi:10.1785/BSSA0750040939.

Yu, T.-C., Currie, C.A., Unsworth, M.J., and Chase, B.F.W., 2022, The Structure and Dynamics of the Uppermost Mantle of Southwestern Canada From a Joint Analysis of Geophysical Observations: Journal of Geophysical Research: Solid Earth, v. 127, p. e2022JB024130, doi:10.1029/2022JB024130.

Yuan, Z., Liu-Zeng, J., Wang, W., Weldon, R.J., Oskin, M.E., Shao, Y., Li, Z., Li, Z., Wang, P., and Zhang, J., 2018, A 6000-year-long paleoseismologic record of earthquakes along the Xorkoli section of the Altyn Tagh fault, China: Earth and Planetary Science Letters, v. 497, p. 193–203, doi:10.1016/j.epsl.2018.06.008.

Zielke, O., and Arrowsmith, J.R., 2012, LaDiCaoz and LiDARimager—MATLAB GUIs for LiDAR data handling and lateral displacement measurement: Geosphere, v. 8, p. 206–221, doi:10.1130/GES00686.1.